The Radio Science Bulletin

ISSN 1024-4530

INTERNATIONAL
UNION OF
RADIO SCIENCE

UNION
RADIO-SCIENTIFIQUE
INTERNATIONALE

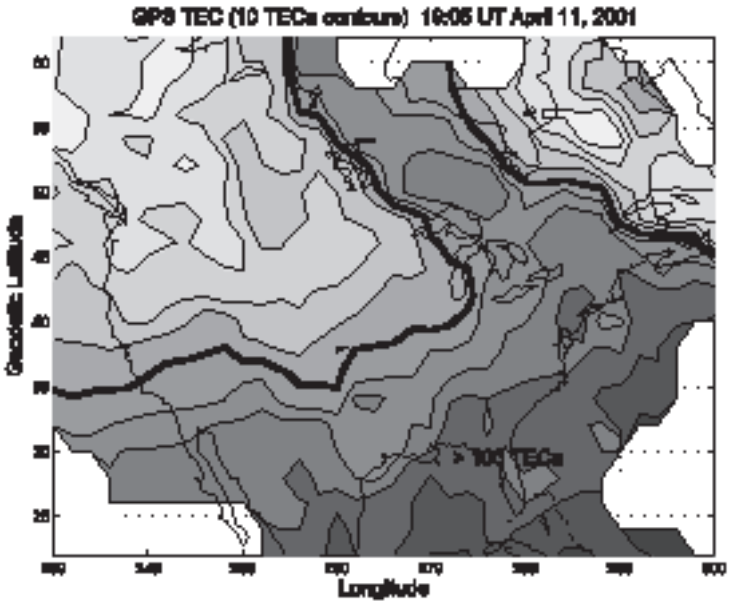

No 311
December 2004

Publié avec l'aide financière de l'ICSU
URSI, c/o Ghent University (INTEC)
St.-Pietersnieuwstraat 41, B-9000 Gent (Belgium)

Contents

Front cover: Observations of a sub-auroral plasma stream (SAPS) during a large magnetic storm. This panel shows a jet of enhanced total electron content derived from GPS measurements. See the paper by Robert Robinson, pp. 79-94

For information, please contact :
The URSI Secretariat
c/o Ghent University (INTEC)
Sint-Pietersnieuwstraat 41, B-9000 Gent, Belgium
Tel.: (32) 9-264 33 20, Fax: (32) 9-264 42 88
E-mail: ursi@intec.rug.ac.be
http://www.ursi.org

Editorial

Happy New Year! Unfortunately, you should be receiving this issue in December, but instead you are getting it after the start of the new year.

We have the second Special Section on Space Solar Power Systems (SPSS) in this issue, with six invited papers, and we have four invited contributions from the *Reviews of Radio Science*.

The Second Special Section on SPSS

The Special Section on SPSS in this issue is the second of two such special sections. The first appeared in the September, 2004, issue of the *Radio Science Bulletin.* These papers were invited by the organizing committee of the 2003 Japan-United States Joint Workshop on Space Solar Power Systems (JUSPS'03), held July 3-4, 2003, at Kyoto University, Japan, from among those presented at the workshop. Very special thanks go to the co-Chairs of the workshop, Hiroshi Matsumoto and Tatsuo Itoh, and to the members of the organizing committee, Kozo Hashimoto, Shigeo Kawasaki, Tomohiko Mitani, Tamotsu Nishino, Naoki Shinohara, and Haruo Tanaka, for providing us with these very interesting papers.

The excellent work of John Volakis in coordinating the reviews of the papers in both special sections is gratefully recognized.

Several different approaches for designing a space solar power system are being considered. In their paper, Michael Steer, Linda Katehi, Saeed Mohammadi, John Whitaker, and Alexander Yakovlev present an overview of an approach based on using arrays of solid-state sources to generate the microwave beam used to transmit the solar power captured by the satellite to the Earth. In this approach the sources are optically controlled, and the microwave power is spatially combined. The paper describes the basic architecture, along with solutions addressing a number of issues related to this design. It also discusses the need for a virtual prototyping laboratory, and the important process of technology integration.

A key component in an SSPS is the antenna to be used for transmitting the solar power from the satellite to the ground. In their paper, Tadashi Takano, Akira Sugawara, and Susumu Sasaki examine the requirements for such a space-based antenna. They consider three possible configurations: a very large parabolic dish, of the order of 1 km in diameter; an array of parabolic antennas, each with dimensions of about 100 wavelengths; and an array consisting of a very large number of half-wavelength radiators. They look at the system considerations and tradeoffs for these three approaches, and draw conclusions that address issues relevant to any proposed design.

Another approach to the space-based antenna for an SPSS is to use an active antenna. Such antennas integrate active components – amplifiers, mixers, and oscillators – into the antenna. This is the approach considered by Kevin Leong, Younkyu Chung, Weijun Yao, Yuanxun Wang, and Tatsuo Itoh in their paper. They also look at the use of such an active integrated antenna as a retrodirective array. This solves the very significant problem of keeping the beam from the satellite pointed at the receiving antenna on the Earth. Several retrodirective array designs are considered. In addition, a new method for self-calibration of an antenna array is introduced. This utilizes reference sources that are positioned in close proximity to the array, and allows correcting for position and circuit errors in the elements of the array.

A method for controlling the beam carrying power from the SPSS satellite to the Earth is the topic of the paper by Kozo Hashimoto, Koji Tsutsumi, Hiroshi Matsumoto, and Naoki Shinohara. A pilot signal from the Earth is used to determine the direction in which to point the beam, based on the phase difference in the pilot signal at two or more elements of the antenna in space. The result is a form of retrodirective array. The pilot signal, which is at the same frequency as the microwave power transmission, is modulated using spread-spectrum techniques. This allows the use of the same antenna(s) for both receiving the pilot signal and for transmitting power. It also provides a method of separating the pilot signal from interference. The results of an experiment demonstrating the ability to steer a beam using such a system are reported.

In their paper, F. E. Little, S. J. Kokel, C. T. Rodenbeck, K. Chang, G. D. Arndt, and P. H. Ngo describe a retrodirective phased-array antenna for an SPSS. It is based on a series of 1 m by 1 m subarrays, each subarray powered by a solid-state power amplifier. The phase of the output of each power amplifier can be individually determined based on the conjugated phase of a pilot signal from the receiving location on the Earth. The approach has many potential advantages, but there are also challenges. The authors report the results of demonstration experiments with two such subarrays.

Jonghoon Choi and Amir Mortazawi consider another approach to the problem of transmitting the microwave power from the satellite of an SPSS to the Earth. They consider an array of solid-state oscillators employing spatial power combing. A key requirement for the success of such a system is the ability to get such an array of coupled oscillators to operate in resonance. The authors employ external injection locking and an extended resonance technique to accomplish this. They also show how the power beam can be scanned by controlling the phases of the subarrays that make up the array of oscillators.

Reviews of Radio Science

As always, Phil Wilkinson deserves our thanks for his coordination of the *Reviews*.

The science of photodetectors plays a key role in modern optical communications, which, in turn, is at the core of most modern data and telecommunication systems. The initial design of photodetectors was based on what can be characterized as lumped-element devices, in which the response is basically determined by the total device area. Such devices have bandwidth, efficiency, and power limitations in meeting modern communication requirements. Less than 15 years ago, distributed – or traveling-wave – photodetectors were proposed. These combine a transmission line with a distributed photodetector, resulting in significant improvements in bandwidth, efficiency, and power-handling capabilities. In their review, G. Rangel-Sharp, R. E. Miles, and S. Iezekiel provide a very understandable explanation of the theory of such devices. They go on to explain a number of practical considerations in the design and manufacture of traveling-wave photodetectors. They then describe several new implementations of such devices, and their importance for modern communication systems. The efforts of Fréderique de Fornel in bringing us this *Review* from Commission D are greatly appreciated.

Electromagnetic compatibility (EMC) measurements are an important practical part of the development of almost every electronic device in use today. Such measurements allow the determination of the emissions (both intentional and unintentional) of such devices, they help in determining the susceptibility of such devices to the electromagnetic environment in which they must operate, and they enable an understanding of the radiation and interference coupling characteristics of such devices. In his review, Perry Wilson looks at the variety of radiated EMC measurement techniques available today. He begins by looking at a number of theoretical and practical considerations for such measurements on electrically large objects. He then provides a very readable discussion of the use of a variety of EMC measurement facilities, including open-area test sites, anechoic chambers, transmission lines, reverberation chambers, and near-field methods. He explains the advantages and limitations of each, and describes ongoing research and development activities related to such measurements. He also provides a very extensive set of references to the field. Flavio Canavero is the Associate Editor for Commission E, and his efforts in bringing us this *Review* are greatly appreciated.

Incoherent scatter radar has been an important method of gathering information about the ionosphere and upper atmosphere for more than 40 years. Robert Robinson provides a review of this technique, how it is being used around the world, and what is planned in the field for the future. He begins with a survey of the existing incoherent scatter radars in the world, looking at both what they have in common and what makes each unique. He then reviews improvements in incoherent scatter radar technology, including digital signal processing, transmitter waveform techniques, innovative methods of using antennas, coherent radar experiments carried out with incoherent radars, coordinated observations, and long-duration experiments. A detailed look at the future of incoherent scatter radar is then provided, centered on the recently funded Advanced Modular Incoherent Scatter Radar. Potential new uses of incoherent scatter radar are examined, and the scientific information that might be obtained from such uses is discussed. Paul Cannon is the Associate Editor for Commission G, and his efforts in bringing us this *Review* are gratefully acknowledged.

There is evidence for non-thermal magnetic effects of extremely low frequency (<300 Hz) fields on biological systems. There are also a variety of proposed mechanisms by which potentially observable effects might be produced. Stefan Engström provides us with a very readable review of this topic. The review begins with a careful discussion of what the term "non-thermal" really means, and how it should be used in connection with such effects. A variety of candidate physical mechanisms for such effects are then considered, including magnetic induction of electric fields and currents; magneto-mechanical effects, in which a torque is induced on a magnetic dipole moment; mechanisms whereby forces could be induced on a magnetic dipole moment; anisotropic diamagnetic effects; magnetite in biological systems; magnetic resonance; and several other possible mechanisms. A critical examination of the evidence for the various mechanisms is provided, followed by consideration of how future work might be directed to clarify what is known in the field. The result is a very interesting paper on a fascinating area of the field of bioelectromagnetic effects. We appreciate the efforts of Frank Prato, Associate Editor for Commission K, in bringing us this *Review*.

Our Other Contributions

In his column on "Radio Frequency Radiation Safety and Health," Jim Lin describes a new research program of the Italian government. This is concerned with the impact of electromagnetic-field-emitting systems – including cell phones – on humans and the environment. Similar studies are also being undertaken in other European countries. A

recent conference held in connection with the Italian study is described, and the importance and need for such work is discussed.

URSI's Scientific Committee on Telecommunications (SCT), chaired by Martin Hall, is at an important point in its development. You need to become involved. In his contribution in this issue, Martin Hall describes several ways in which you can become involved. One is simply by contacting the SCT representative of the URSI Commission in which you are active or the SCT Chair and letting them know that you wish to become active. Another way is to download the leaflet describing its activities that the SCT has prepared, and to read and distribute the leaflet. There are also opportunities involving associated meetings with "user organizations," and an SCT Lecture Team.

Frank Olyslager, Ann Franchois, and Ari Sihvola have provided us with a very interesting and even entertaining report on the Bianisotropics 2004 meeting. This was the tenth in the series of such meetings, and it was very well attended. There was a strong emphasis on the new and exciting field of metamaterials.

A workshop on "Active Protection of Passive Radio Services" was held in October of last year. Although this was not sponsored by URSI, the topic is one of considerable interest to many in the URSI community, and many of the participants are active in URSI. Jim Cohen has provided a good summary of the workshop, and his report also indicates a number of steps that those concerned with such activities can take.

Your Help is Needed!

About a month ago, one of the largest earthquakes on record occurred near Sumatra, Indonesia, triggering tsunamis that have killed at least 160,000 people. Several million more lives are at risk because of the lack of safe water, food, shelter, and the likely onset of diseases. I hope and pray that none of our colleagues is directly involved. Regardless, a disaster of this magnitude affects all of us, wherever we are. I hope you will join me with your prayers and thoughts supporting those who have been directly affected, and those involved in the disaster relief efforts underway. I also hope you will give to and do what you can to support these efforts. Donations are being accepted by the United Nations Foundation. Information about making a donation can be found at http://www.unfoundation.org/. A link from that page leads to the UN news page reporting on UN relief efforts.

In Memoriam

PIERRE CUGNON
1940-2004

It is with great sadness that we must inform you of the sudden death of Pierre Cugnon on October 18, due to complications following heart surgery.

Pierre Cugnon was born on April 17, 1940, in Bertrix, a small city in the Belgian Ardennes. He conducted nearly his whole scientific career in the Solar Physics Department of the Royal Observatory of Belgium (ROB). After studies at the University of Liège, where he obtained his PhD in the field of interstellar polarization, he obtained a position in the Department in 1968. Working first on photometric and chromospheric observations from the Uccle station, he then developed a program of coronal polarimetry that led him to participate personally to 4 total solar eclipse expeditions from 1980 to 1998. In 1990, Pierre played a key role in promoting the Belgian participation to the SOHO EIT instrument, allowing the ROB solar team to become, over the last decade, the prominent group that it is now in solar space research.

In 1994, Pierre Cugnon became simultaneously Head of the Department, as well as the Director of the SIDC, hosted by the ROB since 1981. Over the last decade, he spent most of his time and energy leading his team and services with dedication, leaving his personal imprint and vision. For instance, he developed, jointly with K. Denkmayr, the Combined Method still used now to improve the sunspot index forecasts and he introduced a quality control for the SIDC data products. A major step was the addition to the SIDC of the European Regional Warning Center of the ISES, previously hosted by Paris-Meudon. Since then, this operational center has continuously expanded its services under a new name, "Solar Influences Data analysis Center".

He was also in charge of the Humain station and its solar radiotelescopes, which he tried to promote and to modernize, but with unfortunately severe underfunding problems. In the framework of those activities, Pierre Cugnon was also an active member of several committees and organizations (including IAU Commission 10, ISES, FAGS and of course the URSI and the CRAF, for what concerns radioastronomy).

He will be also remembered for his rich culture and his humble, gentle and patient manner of interacting with colleagues and leading his team. Pierre Cugnon leaves a wife and two daughters.

VACLAV ZIMA
1925-2004

Sadly, on April 11, 2004 died Václav Zima. Born February 15, 1925 as a son of professor of the forestry school in Písek (Southern Bohemia), Václav Zima frequented industrial secondary school in Prague and in 1945 entered university. After a short time spent studying physics at the Faculty of Natural Sciences, he transferred to the Electrotechnical Faculty which he finished in 1948. He then joined the Army; as an officer he began, in 1950, working in the Army Technological Institute, like a number of other top-level specialists in that time. He was doing research in ballistics and acoustics and worked out exact methods for measuring time intervals. This was the basis of a monograph published in 1962 in Czech and in 1965 in Russian in Moscow. At that time he also studied electromagnetic waves propagation, identification methods for metallic objects imbedded in earth, and properties of concatenated two-ports. The latter subject he elaborated in a monograph published in 1968.

In 1963 he was appointed to direct the Institute of Radio Engineering and Electronics of the Czechoslovak Academy of Sciences. He turned his attention to methods of frequency synthesis, a theme studied in the Institute. He made significant contributions to this field which was translated into enhanced stability of the middle-wave transmitters in Czechoslovakia.

His favoured discipline was the circuit theory. He worked out an original theory of the general two-port based on the power flow and on non-euclidean geometry. The results constitute the main part of monograph (1976) he prepared jointly with some of his collaborators.

The late (1989-1990) activity of Professor Zima was devoted to the constant-wave underground radars and slotted cables. Besides the obvious application facets of this research, he pursued mode propagation problems in parallel transmission lines which he regarded as concatenated four-ports, as well as concepts of reciprocity and semi-reciprocity. In addition to his scientific and administrative activities, Professor Zima gave lectures at Universities in Prague and Pilsen. He took part in organisation of a number of international conferences and supervised graduate students.

In 1967 the Doctor of Sciences (DrSc) degree was conferred to him at the Czech Technical University; in 1983 he habilitated as a professor at the same institution.

In 1966, the URSI National Committee (NC) was restored due to initiative of the Academy of Sciences. (Originally, it was founded in 1948.) At that time, Czechoslovakia was the sole member of the Eastern Alliance where a NC existed. This fact is due, in large part, to the efforts of Václav Zima. It was symbolic, that chairman of the NC was Professor Stránský, who occupied this post at the very beginning. When Professor Stránský died in 1984, Václav Zima took over and remained in the chairman position till 1992. On the international URSI scene, Professor Zima was elected vice-chairman of the Commission C at the XVIIIth URSI General Assembly (GA) in Lima in 1975 and, subsequently, a chairman of this Commission (1981-1984). At the URSI GA in Florence, 1984, he became vice-president of URSI. In period 1981-1984 he was member of the financial commission. The 1990 URSI GA was held in Prague, thanks to his initiative and efforts. It took place in an atmosphere of radical political changes in the country.

Václav Zima stimulated many younger colleagues by his enthusiasm, dedication and breadth of his interests. He educated a number of salient specialists. He led the Institute until he was 65 years old and continued scientific work up to his death.

In his capacity as director of the Institute he contributed a great deal to its renown. He initiated the introduction of important new topics to the research program, such as technology of semiconductor lasers and LEDs. His mindset was one of a scientist with broad erudition and great power of exact reasoning on one hand and of an engineer capable of solving, in an original fashion, practical problems of disheartening complexity on the other.

As the father of three children, he always found time for his gradually expanding family, notwithstanding his numerous duties and engagements. Vice versa, the family life, thanks foremost to his wife, constituted a harmonious background, full of comprehension for his obligations.

Professor Zima was one of the rare personalities that mastered the three fundamental pillars of radioscience: field theory, circuit theory and signal theory. He is one of the founding fathers of modern electronics in the Czech Republic. His bibliography counts over one hundred original contributions. For his work he was awarded three highest distinctions.

Václav V. Cížek

Architectures and Prototyping Laboratory for the Development of Space-Based Microwave Power Transmission Systems

M.B. Steer
L.P.B. Katehi
S. Mohammadi
J.F. Whitaker
A.B. Yakovlev

Abstract

A vision is presented for the generation of enormous (terawatt) power levels using solid-state sources arranged in arrays of devices that are opto-electronically controlled to produce a microwave beam that can be safely directed towards terrestrial receptors. The performance and capabilities of discrete technologies will increase tremendously over the next three or four decades (when SSP systems should be economically feasible), and will be driven both by unrelated technology pulls and by the identification of necessary technologies. Critical are architecture studies for microwave beam forming, which will enable the identification of technology directions and basic feasibility of concepts. Even with a few orders-of-magnitude increase in the power available from solid-state sources (or even alternative devices), the ability to generate terawatt power levels will demand innovative developments in combining power in an inherently safe manner, beaming the power to Earth from low-Earth orbit, and in safe and reliable beam steering using structures that are adaptive, self-monitoring, and self-healing.

1. Introduction

The concept of harvesting energy in space for terrestrial use has captured political, engineering, and scientific imaginations for around three decades. Many system concepts have been proposed and explored, and the economics of solar space power (SSP) have been explored, with feasibility primarily dependent on the amount of power that can be generated for specific weight, and thus launch cost. Many lessons have been learned about the required attributes of such a SSP system [1, 2]. The focus of this paper is the presentation of a vision for an environment

Figure 1. The essential components of a space solar power-collection system. Terrestrial issues must be addressed at early system concept stages.

Michael B. Steer is with North Carolina State University, Electrical and Computer Engineering Department, Raleigh North Carolina, USA, NC27695-07911; Tel: +1 (919) 522-2610; Fax: +1 (919) 513-1979; E-mail: mbs@ncsu.edu. Linda P. B. Katehi and Saeed Mohammadi are with Purdue University, College of Engineering, 400 Centennial Mall Drive, West Lafayette, Indiana, USA 47907-2016; Tel: +1 (765) 494-5346 (LPBK); E-mail: katehi@purdue.edu; Tel: +1 (765) 494-3557 (SM); E-mail: saeedm@ecn.purdue.edu. John F. Whitaker is with the University of Michigan, Center for Ultrafast Optical Science, Ann Arbor, Michigan, USA MI 48109; Tel: +1 (734) 763-1324; Fax: +1 (734) 763-4876; E-mail: whitaker@umich.edu. Alexander B. Yakovlev is with the University of Mississippi, Department of Electrical Engineering, University, Mississippi, USA MI 48109; Tel: +1 (662) 915-7196; Fax: +1 (662) 915-7231; E-mail: yakovlev@olemiss.edu.

This invited paper is part of the Special Section on Space Solar Power Systems. An oral version was originally presented at the 2003 Japan-US Joint Workshop on Space Solar Power System (JUSPS'03), July 3-4, 2003, Kyoto University, Uji, Kyoto, Japan.

that enables future directions of technology investment to be identified. The core elements of an SSP system, Figure 1, are a solar collection mechanism, a space power management and distribution system, and a mechanism for transmitting the energy to Earth. It is essential that we address health and safety issues in a manner with which people can identify. The most promising candidates for the components of the SSP system are semiconductor solar cells (for solar collection) and semiconductor-based microwave transmitters (for energy transportation). Technologies must be developed for ultra-low-weight microwave circuits, optically injection-locked distributed spatial power-combining systems, and, we believe, a virtual prototyping laboratory that will facilitate system exploration, as fielding prototypes is a very expensive undertaking.

2. Prime Directives

The challenge in SSP system research is creating developments that will benefit SSP research in the long term, without being wedded to a particular collection of components that is sure to evolve as technologies evolve. We believe that there are five prime directives for SSP systems: 1) safety and system stability, 2) low weight (optimum performance-to-weight ratio), 3) maximum efficiency, 4) long lifetime, and 5) low cost to first power.

It is abundantly clear that for the foreseeable future, the power from numerous solid-state sources will need to be combined to achieve tens to hundreds of gigawatts from each satellite installation. It is natural to think of using amplifiers in a phased-array architecture to achieve this, as this approach has been successful in fielding radar systems. SSP and radar systems are similar to spatial power combiners. However, with spatial power combining systems (see [3, 4]), the emphasis is on integrating antennas with active devices to achieve what amounts to an array of active antennas. Phased-array concepts are based on modules that are connected to antennas and so have higher losses. In the case of military radars, these losses can be 3 dB or more. These losses result in greatly enhanced system stability, but, of course, at the price of reduced efficiency. Spatial power-combining systems are much more difficult to design, but the much lower output losses clearly place them as a prime consideration. Beam control in spatial combining systems is of paramount importance. The most attractive option is to amplify a precise frequency source, but narrowband amplification can also be effectively achieved by using injection locking of oscillators, which achieve higher efficiencies than do amplifiers.

3. Virtual Prototyping Laboratory and Technology Integration

There is a mandatory requirement to develop revolutionary enabling technologies and to explore radically new system concepts for space solar power (SSP) generation. A virtual prototyping environment will allow concepts to be explored even before enabling technologies have been brought to maturity. We will use physically-based modeling of components and advanced simulation technology to achieve realistic physically-connected system simulation, incorporating complete thermal, circuit, mechanical and electromagnetic analyses. This approach is termed *technology integration* [5], and is an alternative to technology transfer, which more closely described the process of developing basic technologies and seeing where they can be applied (see Figure 2).

Today's power systems are some of the largest engineered systems, and yet they are operated with a high degree of reliability. One of the main reasons for this

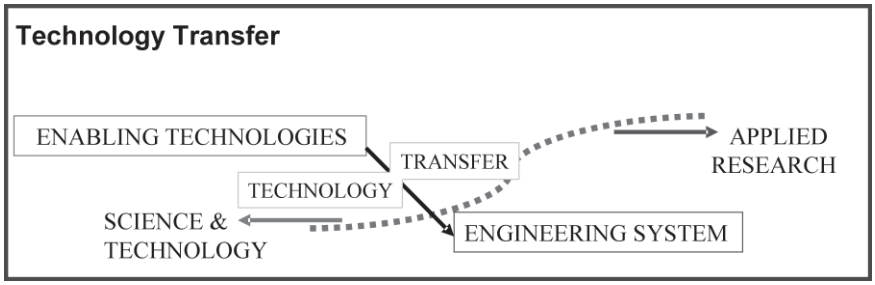

Figure 2a. The traditional approach of technology transfer.

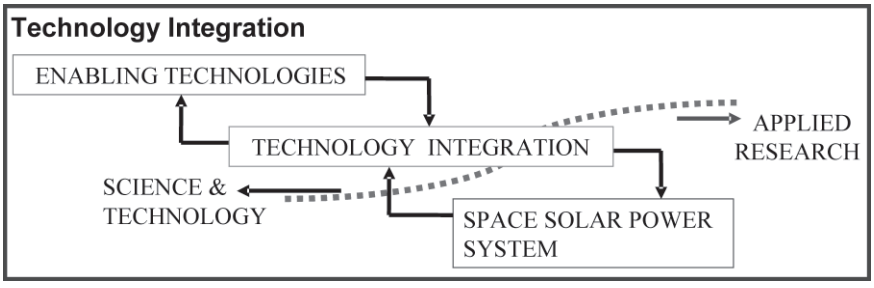

Figure 2b. The research and development process of technology integration, to be contrasted with the approach of Figure 2a.

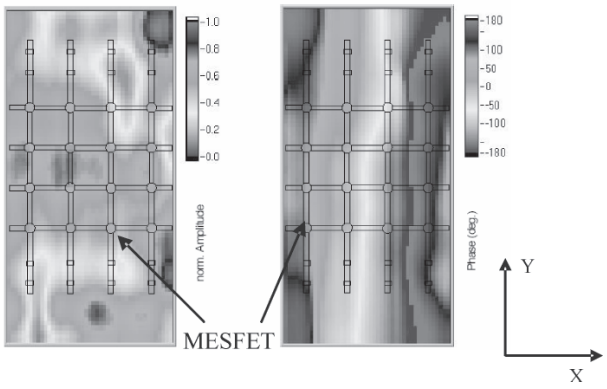

Figure 3. A mapping of the electric field immediately above a free-running quasi-optical oscillator array. The array was designed by Prof. Wilson Pearson and his group at Clemson University, and measured by us at the University of Michigan using electro-optic sampling.

success is the adoption of a well-defined system architecture, which allows the integration of system components into the system with ease, and which provides a high degree of robustness against variations in the system's operating conditions. Thus, for the envisioned SSP systems to be commercially viable, they should have similar features: they should have an architecture that facilitates system integration and management, and a high degree of robustness for handling varying operating conditions. Since the SSP system will provide the base load generation for terrestrial systems, the SSP system should be as easy to manage as the terrestrial generation systems (which consist of power generation stations), and should provide the same level of reliability. For reliability, the SSP must consist of many units that can be independently operated, and must be able to feed the terrestrial system at various locations.

4. Spatial Power Combining

Considerable experience has been gained in spatial power combining, including development of systems, analytic investigation technologies, and global modeling activities. A key insight is that free-running oscillator arrays are problematic, and very low levels of feedback adversely affect the performance of the systems. Amplifier arrays have a similar effect, but this is also manifested as variations of output power and phase across the array.

Figure 3 shows the field above a free-running quasi-optical grid oscillator. The prominent features here are the dramatic variations in amplitude and phase of the output signals, and the consequently poor control of the created beam. This, we believe, is due to low-level feedback effects. This does serve to lock the oscillators, but as feedback is not uniform, amplitudes and phase of each unit cell adjust to create just the right oscillation conditions.

Other experiences with spatial power combining systems indicate rather finicky stability issues. Stability and good efficiencies can be achieved in practice, but only after careful manipulation of the structures. For this reason, we undertook a number of system-level studies to determine their basic attributes. Figure 4 shows plots of the output amplitudes immediately above a spatial power combining amplifier array. Here can be seen the effect of low-level feedback from amplifier to amplifier, which principally results from the output of one amplifier being injected into the output of another amplifier. Amplifier mismatch was also considered. In all of our investigations that involved any level of feedback, the variations across the array were much greater than would be expected from the individual

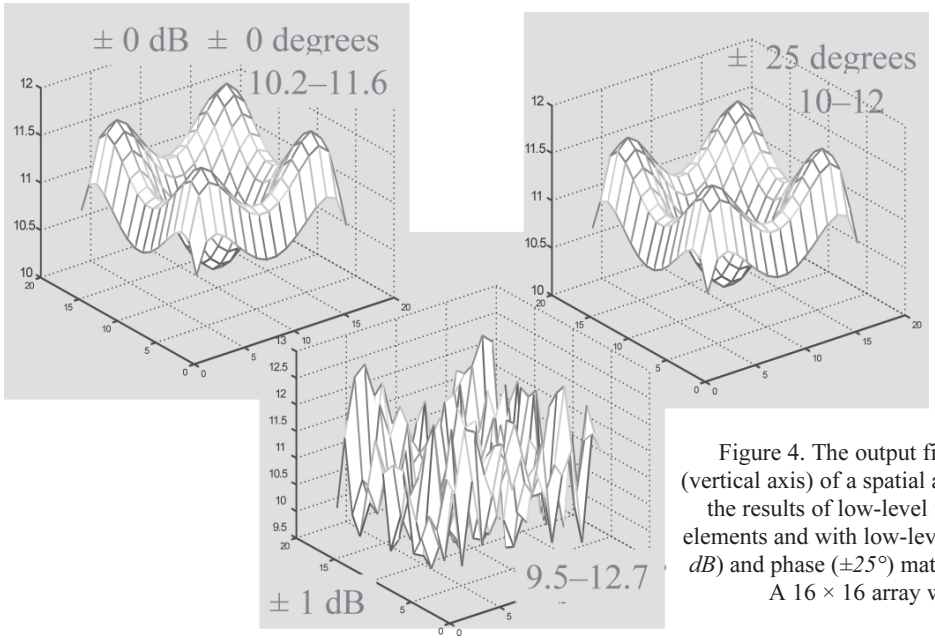

Figure 4. The output field amplitude levels (vertical axis) of a spatial amplifier array, showing the results of low-level feedback between the elements and with low-level variations in gain (*±1 dB*) and phase (*±25°*) matching of the amplifiers. A 16 × 16 array was considered.

amplifier variations. There were even significant variations when the amplifiers were matched. These affects will have an affect on stability, overall system efficiencies, and on beam integrity.

Our conclusions from these studies are that high-power spatial power combining necessitates the use of injection-locked oscillators in a spatial power combining structure with near as well as remote detection of beam characteristics, and with feedback to control the phase of (possibly) an optical injection locking signal applied to each unit cell.

5. Architecture Proposals

We present two possible architectures, based on collections of unit radiators. In essence, we envision arrays of microwave oscillators, with a fiber-optic feed to each oscillator unit cell for an optically injection-locked oscillator. The phase of the unit oscillators will be controlled optically to direct the beam to a terrestrial site.

5.1 Unit Radiators

The number of unit radiators in the system is determined by both the total power requirements and the power available from individual microwave sources. We can expect developments in the primary power-limiting factor: breakdown voltage. With alternative semiconductor technologies (yet to be developed), we could achieve an order-of-magnitude increase in breakdown voltage. This could result from extremely-wide-bandgap semiconductors, which will also enable operation at elevated temperatures, dramatically improving the extraction of waste heat. We then could very reasonably expect 10 kW per device. With circuit-level combining (with circuit-board-like interconnections), we could combine 64 devices, which, in round numbers, would yield an output power of 1 MW per oscillator unit. (Circuit-level combining above 64 units is extremely difficult to achieve.) A panel with 100 oscillating units would produce 100 MW of power. If we were limited to 100 orbiting clusters to provide reliable uninterrupted power of 4 TW, then there would need to be 400 panels per cluster. Each panel would have to operate independently: therefore, we foresee two more means of combining power. We see frequency division combining, where a panel operates at 2.58 GHz (for example), and a neighbor operating at a frequency separated by 1 kHz. A further level of combining would be time-division combining, much the same as is achieved with mode-locked lasers. In this scenario, a panel would generate microwave energy in a cavity formed by a reflector and the vacuum of space, and would periodically dump the energy into an Earth-bound beam.

5.2 Panel Architecture

We envision a system that transmits energy to Earth in a microwave beam, formed using spatial power combining to combine the power from multiple transmitters (see Figure 5). Each panel comprises one hundred individual radiators, directly driven by microwave oscillators. The limited number of discrete sources is determined from stability considerations. Also, each discrete source is optically controlled, adapting the circuit configuration for maximum efficiency and achieving self-healing. At the same time, electro-optical modulation injection locks each unit. Opto-electronics will also be used for self-diagnosis and self-healing. Each panel will be powered by its own solar collector, to minimize weight and the losses associated with power distribution. A large number of panels will be grouped in a cluster, and a number of clusters will orbit the Earth, with each terrestrial unit receiving power from just one cluster (although a cluster could serve more than one terrestrial unit). A cluster in low Earth orbit will direct the microwave beam, using electronic steering with phase control of individual oscillators realized by the opto-electronic injection-lock system. A failsafe mechanism would result in a random phasing of the individual oscillators and a diffused microwave beam. This would also be an aid in safely switching power from one terrestrial site to another.

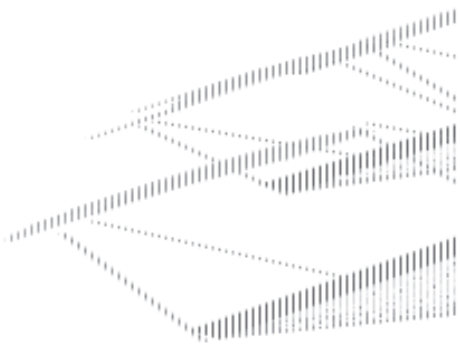

Figure 5a. The microwave beamforming components of an SSP system: a cluster of multiple panels forming one orbiting unit.

Figure 5b. Multiple clusters per Figure 5a, each directing power at specific terrestrial sites. Oceanic sites could be used for liquid fuel production. Not shown is the solar-collection apparatus.

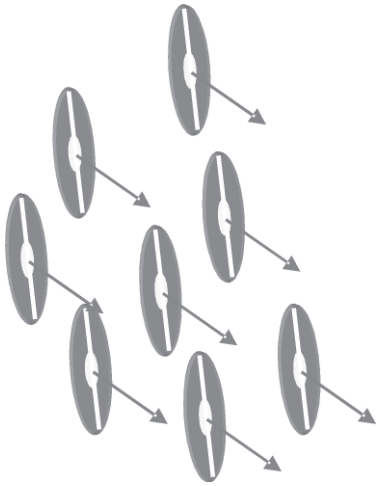

Figure 6a. The microwave beamforming components of an SSP system: a cluster of a multitude of independent sources, each positionally aware of each other, and implementing a distributed phase-locked oscillator control.

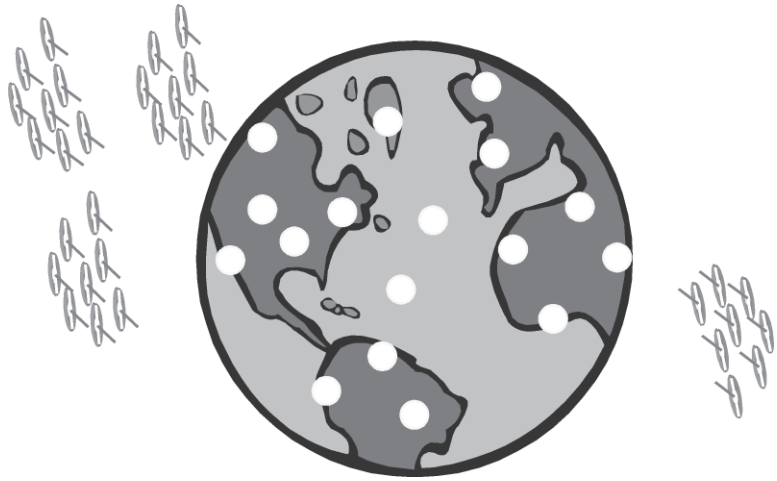

Figure 6b. Multiple clusters of the components shown in Figure 6a, each directing power at specific terrestrial sites.

Efficiency is paramount, and we see the development of microwave electronics that do not need power conditioning (in much the way that RF transmitters in cellular phones are powered directly from the battery). Ideally, there would be no dc/dc converters or voltage regulators in the system. Opto-electronic control will present optimum microwave circuit conditions, and will enable efficient harmonic control without using output filtering.

This system design has another attribute. A system could be fielded with just one panel per cluster, with subsequent panels parked as required. The initial panels would not need to use exotic time-division combining. Terrestrial receiving antenna (rectenna) farms would not need to be fully deployed, as the defocusing mechanism would enable microwave power to be directed away from the Earth during non-receive periods. As we rely on opto-electronic sensing and control of the panels rather than array-level combining (through coupled neighbors) with structure-determined dimensions, even a panel could evolve over time, with additional segments subsequently linked into position, or removed from service for maintenance.

5.3 Point Architecture

Figure 6 shows an architecture similar to the panel architecture, but now the system is composed of a large number of point sources. The concept here is that of minimizing the transfer of power via dc current, and using microwave radiation to achieve power distribution. Each unit contributes to the evolving beam. We envision a system where each unit radiator has intelligence and is position-aware of all other components, including other unit radiators of the system. The system is not arranged in a plane, but in three-dimensional space with laser positioning, for example, precisely locating each radiator and adjusting the optical locking reference appropriately. Even a supposed planar arrangement cannot be assumed to be sufficiently planar for array-combining purposes. We suppose that in the next two decades, there will be great developments in the engineering system complexity that can be handled.

6. Electro-Optics for System Diagnosis, Optimization, and Beam Control

There are four main diagnostic and control measurement functions that need to be addressed, as enumerated below. Together, they demand a novel approach to the characterization of RF signals, one that will allow amplitude, phase, and frequency to be distinguished separately, at different locations, and then utilized to ensure proper operation of the power-combining array. The four measurement categories can be summarized as follows:

1. Determine amplitude, phase, and frequency in the near field of individual unit-cell radiators, and compare with expected values in order to verify correct initial beam strength, beam direction, and injection-locking frequency. Incorrect values would prompt the creation of error signals that would be used in a feedback loop to adjust array gain, injection-locking-modulation phase, or injection-locking-modulation amplitude (see Figure 7).
2. Measure the same quantities at crucial points in the far field of the array, in order to confirm that the combined power has formed as expected.
3. Investigate cross-talk effects from neighboring unit cells and their influence on injection locking.
4. Monitor microwave radiation in the proximity of crops that may be part of an environment that is impacted by high-power microwave radiation from space. Electric-field and temperature can be sensed simultaneously, with the same probe, under unusual and harsh conditions,

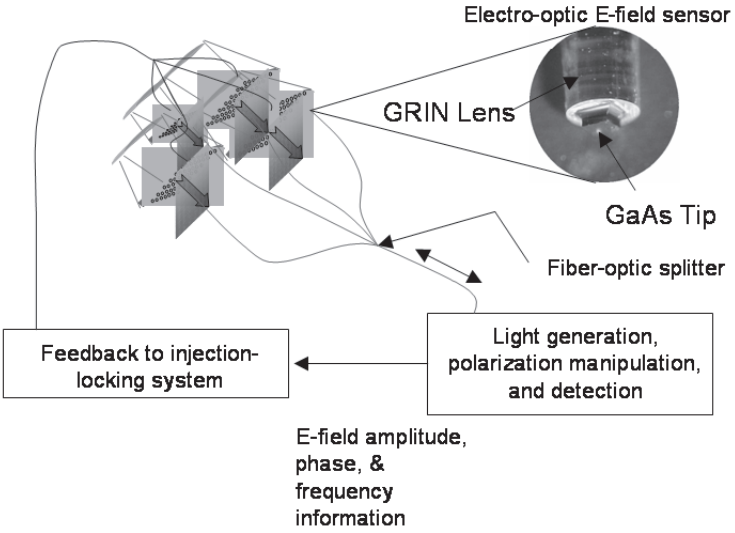

Figure 7. A cluster with an opto-electronic sensor and control system for phase control of oscillators, self diagnosis, and self-healing. The insert shows a low-perturbation field sensor on the end of a fiber that we have developed. This is an electric-field diagnostic-testing and array-correction concept. An optically-based field-sensing system will monitor the amplitude and phase output of the unit cells of the array, in order to maintain the power and directional integrity of the array.

such as in high humidity, within dense foliage, and under the surface of the soil.

Electro-optic (EO) field sensing has attracted attention as a beneficial near-field measurement technique that can extract a great deal of information from micro- and mm-wave integrated circuits [6], antennas, and complex arrays [7]. Electro-optic field sensing was initially suggested as a diagnostic tool for antennas and arrays using free-space-propagating optical beams around 1994 [8]. However, the coupling of a laser pulse train and electro-optic sensors to fibers would be essential for networking a large number of sensors that are spread apart by perhaps hundreds of meters. While it will not be necessary to scan an electric-field sensor and extract maps of electric field from the injection-locked unit cells of a high-power microwave array, it will be desirable to utilize the same laser as a sampling-beam source for all of the individual, fixed electro-optic probes monitoring the array. In sampling the field from different unit cells, the input laser beam will then be split among the fibers leading to the various probes, so that one near-field probe per unit cell and one far-field probe per array can be accessed by the same optical source. This will require a fiber-optic, voltage-controlled switch, which transfers light quickly among different fibers leading to the electro-optic sensors. It will also need to allow light to pass in both directions, so that the modulated light returning from the electro-optic sensors is routed to the photodetector. In the first-generation system, a rotating mirror or a translating fiber-holder can be used to demonstrate flexible access for one laser to a variety of probes. In subsequent embodiments – and certainly by the time such a system was implemented in space – commercial fiber-optic switches or the application of optical MEMS (micro-electromechanical systems) for steering the beam with small, moveable mirrors will be required.

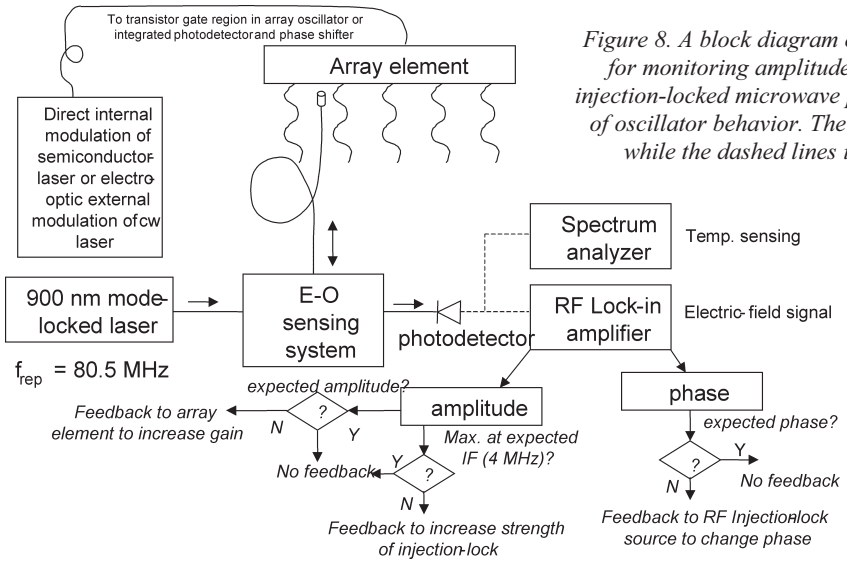

Figure 8. A block diagram of a proposed electro-optic technique for monitoring amplitude, phase, and frequency of a single, injection-locked microwave power source, and subsequent control of oscillator behavior. The red lines represent the optical fiber, while the dashed lines indicate an electrical connection.

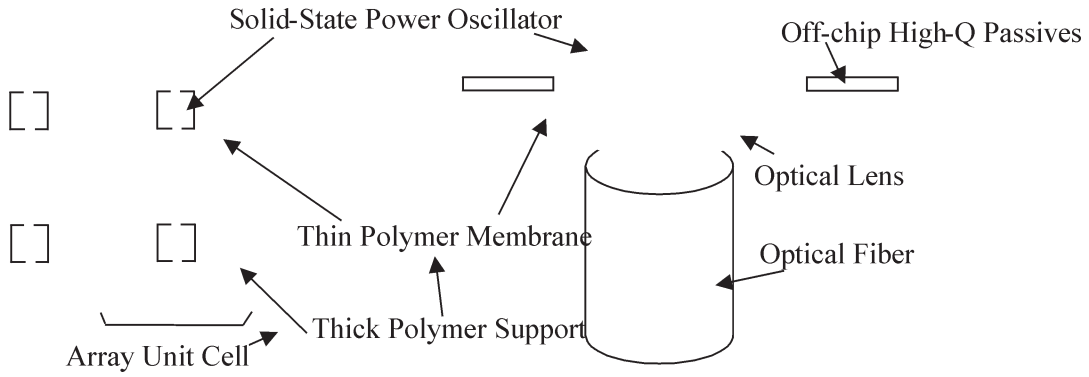

Figure 9. A proposed polymer membrane fabrication technology.

A schematic of the optical and electrical system that could be used to monitor and control one radiating microwave power element is shown in Figure 8. Since the microwave frequency to be used is set at a value of 2.58 GHz – and if we wish to set our IF at 4 MHz – it will be necessary to adjust the laser repetition frequency to 80.5 MHz by slightly decreasing the cavity length, so that we can use the 32nd harmonic of 80.5 MHz (i.e., 2.576 GHz) as the "local oscillator" frequency. This should be easily accomplished, due to the presence of a piezoelectric translation stage on the end mirror of the Ti:sapphire laser used as the mode-locked optical source. If the laser repetition frequency varies from 80.5 MHz, an error signal will be generated, and the cavity will be returned to the correct length. In order to maintain a high degree of synchronization between the laser and the electric-field signal it will be used to measure, both the 80.5 MHz and the 2.58 GHz microwave signal (that will either directly or externally modulate the injection-locking laser) will need to be synthesized from the same 10-MHz RF signal. This 10 -MHz reference signal is available from the same driver that controls the laser piezoelectric translation stage.

In addition to the near-field measurements, the same optical system will be employed to sense other electric fields at a variety of locations. For instance, as the probe is moved increasing distances from the radiating plane it will enter the far field of the antenna. By strategically placing fiber-coupled sensors in the far field, we will be able to detect the direction of the beam's propagation in a fashion that would also allow confirmation that a combined, high-power space-based beam was proceeding towards its target location.

7. Microwave Beam-Forming Structures

A critical aspect of the beam-forming structure is low weight. Membrane polymer processing technology [9, 10] provides a low-weight functional package for the array, as shown in Figure 9. It consists of the following functions: a lens for optical wave-guiding, which is de-embedded in this structure (the lens focuses the light on the high-speed opto-electronic injection-locked oscillator); a thin polymer membrane that supports the solid-state power oscillator and also provides off-chip high-Q passive elements; and a thick polymer support structure that can be partially metallized to reduce coupling between array elements.

8. Electromagnetic Modeling of Large Arrays for Space Applications

The analysis, modeling, and design of quasi-optical power-combining systems has much in common with an SSP system. The theoretical understanding of the operation of spatial combiners started with the open-cavity resonator structure, which contained a planar array of filamentary current sources radiating into a plano-concave open resonator (spherical reflector) [11-16]. The analysis was based on the Method of Moments with the electric Green's dyadic obtained for the open-cavity resonator. The Green's function was derived in terms of paraxial and non-paraxial components, where the paraxial components described the quasi-optical modes. Later, this analysis was extended to the development of a dyadic Green's function for a quasi-optical grid amplifier system with lenses [17-19]. An electromagnetic model of this structure incorporated full electromagnetic coupling, and integrated the EM model into a circuit-level simulation of the amplifier array elements [20, 21]. Similar results have been obtained with other types of power-combining structures, in particular, waveguide-based amplifier arrays [22-32]. The amplifier arrays were placed in an oversized layered waveguide in close proximity to receiving/ transmitting horn antennas. The electromagnetic modeling environment for the complete characterization of waveguide-based spatial-power-combining systems was based on the Generalized Scattering Matrix (GSM) approach, to obtain an overall response of the system by cascading the individual responses of simple modules [22, 23]. The integral-equation formulation for planar antenna arrays with dyadic Green's functions obtained for a multilayered waveguide was discretized using the Method of Moments projection technique [22-27]. This resulted in a complete characterization of finite antenna arrays operating in a waveguide environment, and modeling of all possible resonance, coupling, multimoding, and surface-wave effects. Recently, a global model was

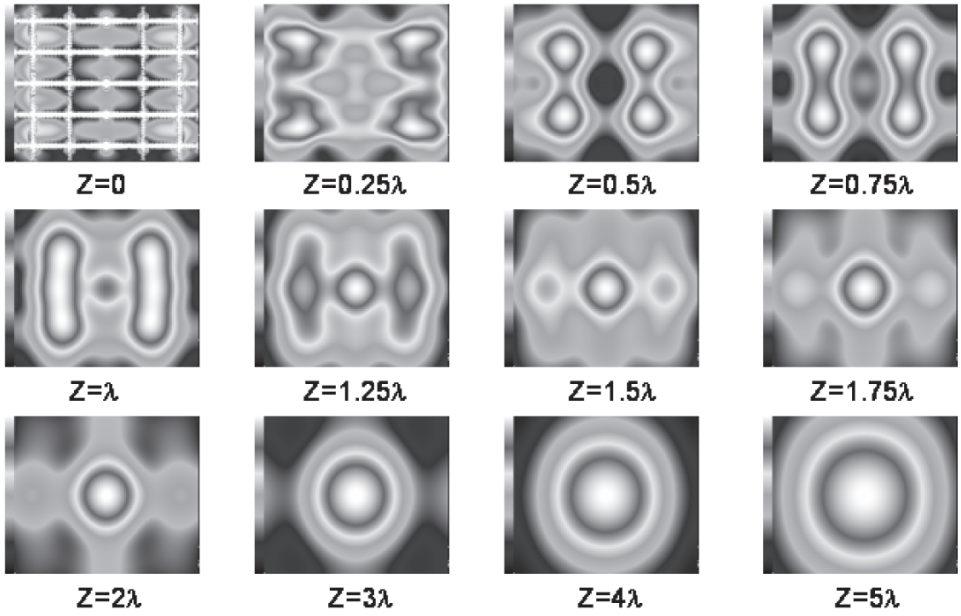

Figure 10. A microwave beam evolving above an antenna array. The plot shows the magnitude of the E field at different distance, z, from the square grid array.

developed for an aperture-coupled patch amplifier array in a multilayered waveguide [32]. This included an interacting electromagnetic-electric-thermal simulation of the power-combining system.

We believe that this integrated level of modeling is essential if we are to understand the dynamics and design criteria of the SSP microwave radiators. For example, we have considered a 5 × 5 grid array with circuit-level models of the active devices. We were able to predict edge and coupling effects, as shown in Figure 10. One issue that is clear here is that edge and coupling effects are important. In this case, the beam produced was not circular due to the nonuniform distribution of charges on the array, which can only be predicted based on the circuit-field interactions and the influence of edge and coupling effects. As was shown in the section on SSP architectures, coupling effects limit the size of the array, as even low-level coupling seriously affects the radiated uniformity.

9. Conclusion

Capturing solar power in orbit and beaming it to Earth will be the grandest engineering endeavor of the 21st century. We envision the generation of enormous (terawatt) power levels, using solid-state sources arranged in arrays of devices that are opto-electronically controlled to produce a microwave beam that can be safely directed towards terrestrial receptors. The performance and capabilities of discrete technologies will increase tremendously over the next three or four decades (when SSP systems should be economically feasible), and will be driven both by unrelated technology pulls and by the identification of necessary technologies. Even with a few orders-of-magnitude increase in the power available from solid-state sources (or even alternative devices), the ability to generate terawatt power levels will demand innovative developments in combining power in an inherently safe manner, beaming the power to Earth from low-Earth orbit, and in safe and reliable beam steering using structures that are adaptive, self-monitoring, and self-healing. Evaluation of the effects of microwave beaming on life needs careful exploration at this early stage of research to frame development and garner the political and public support for future developments.

10. Acknowledgements

M. Steer gratefully acknowledges the National Science Foundation, which supported his work through grant ECS-0107740.

11. References

1. National Research Council, *Laying the Foundation for Space Solar Power, An assessment of NASA's Space Solar Power Investment Strategy,* National Academy Press, 2001.

2. J. C. Lin, "Space Solar-Power Stations, Wireless Power Transmissions, and Biological Implications," *IEEE Microwave Magazine*, **3**, March 2002, pp. 36-42.

3. J. W. Mink, "Quasi-Optical Power Combining of Solid-State Millimeter-Wave Sources," *IEEE Transactions on Microwave Theory and Techniques*, **MTT-34**, February 1986, pp. 273-279.

4. R. A. York and Z. B. Popovic (eds.), *Active and Quasi-Optical Arrays for Solid-State Power Combining*, New York, John Wiley, 1997.

5. E. M. Iansiti, *Technology Integration: Making Critical Decisions in a Dynamic World*, Boston, Harvard Business School Press, 1998.

6. K. Yang, G. David, S. Robertson, J. F. Whitaker, and L. P. B. Katehi, "Electro-Optic Mapping of Near-Field Distributions in Integrated Microwave Circuits," *IEEE Transactions on*

Microwave Theory and Techniques, **MTT-46**, 1998, pp. 2338-2343.

7. K. Yang, T. Marshall, M. Forman, J. Hubert, L. Mirth, Z. Popovic, L. P. B. Katehi, and J. F. Whitaker, "Active-Amplifier-Array Diagnostics Using High-Resolution Electro-Optic Field Mapping," *IEEE Transactions on Microwave Theory and Techniques*, **MTT-49**, 2001, pp. 849-857.

8. Y. Imaizumi, M. Shinagawa, and H. Ogawa, "Electric Field Distribution Measurement of Microstrip Antennas and Arrays Using Electro-Optic Sampling," *IEEE Transactions on Microwave Theory and Techniques*, **MTT-43**, 1995, pp. 2402-2407.

9. W. Y. Liu, D. P. Steenson and M. B. Steer, "Membrane-Supported Copper E-plane Circuits," *2001 IEEE International Microwave Symposium Digest*, *Volume* 3, May 2001, pp. 539-541.
10. W. Y. Liu, D. P. Steenson and M. B. Steer, "Membrane-supported CPW, with Mounted Active Devices," *IEEE Microwave and Guided Wave Letter*s, **11**, April 2001, pp. 167-171.

11. P. L. Heron, F. K. Schwering, G. P. Monahan, J. W. Mink, and M. B. Steer, "A Dyadic Green's Function for the Plano-Concave Quasi-Optical Resonator," *IEEE Microwave Guided Wave Letters*, **3**, August 1993, pp. 256-258.

12. P. L. Heron, G. P. Monahan, J. W. Mink, F. K. Schwering, and M. B. Steer, "Impedance Matrix of an Antenna Array in a Quasi-Optical Resonator," *IEEE Transactions on Microwave Theory and Techniques*, **MTT-41**, October 1993, pp. 1816-1826.

13. P. L. Heron, G. P. Monahan, J. E. Bird, M. B. Steer, F. K. Schwering, and J. W. Mink, "Circuit Level Modeling of Quasi-Optical Power Combining Open Cavities," *1990 IEEE International Microwave Symposium Digest*, June 1993, pp. 433-436.

14. P. L. Heron, G. P. Monahan, F. K. Schwering, J. W. Mink, and M. B. Steer, "Multiport Circuit Model of an Antenna Array in an Open Quasi-Optical Resonator," *Proc. URSI*, June 1993, p. 84.

15. G. P. Monahan, P. L. Heron, M. B. Steer, J. W. Mink, and F. K. Schwering, "Mode Degeneracy in Quasi-Optical Resonators," *Microwave and Optical Technology Letters*, **8**, April 1995, pp. 230-232.

16. T. W. Nuteson, G. P. Monahan, M. B. Steer, K. Naishadham, J. W. Mink, and F. K. Schwering, "Use of the Moment Method and Dyadic Green's Functions in the Analysis of Quasi-Optical Structures," *1995 IEEE International Microwave Symposium Digest*, May 1995, pp. 913-916.

17. T. W. Nuteson, G. P. Monahan, M. B. Steer, K. Naishadham, J. W. Mink, K. Kojucharow, and J. Harvey, "Full-Wave Analysis of Quasi-Optical Structures," *IEEE Transactions on Microwave Theory and Techniques*, **MTT-44**, May 1996, pp. 701-710.

18. T. W. Nuteson, M. B. Steer, K. Naishadham, J. W. Mink, and J. Harvey, "Electromagnetic Modeling of Finite Grid Structures in Quasi-Optical Systems," *1996 IEEE International Microwave Symposium Digest*, June 1996, pp. 1251-1254.

19. T. W. Nuteson, *Electromagnetic Modeling of Quasi-Optical Power Combiner*, PhD dissertation, North Carolina State University, 1996.

20. T. W. Nuteson, M. B. Steer, S. Nakazawa, and J. W. Mink, "Near-Field and Far-Field Prediction of Quasi-Optical Grid Arrays," *IEEE Transactions on Microwave Theory and Techniques*, **MTT-47**, January 1999, pp. 6-13.

21. T. W. Nuteson, H. Hwang, M. B. Steer, K. Naishadham, J. W. Mink, and J. Harvey, "Analysis of Finite Grid Structures with Lenses in Quasi-Optical Systems," *IEEE Transactions on Microwave Theory and Techniques*, **MTT-45**, May 1997, pp. 666-672.

22. A. B. Yakovlev, S. Ortiz, M. Ozkar, A. Mortazawi, and M. B. Steer, "A Waveguide-Based Aperture-Coupled Patch Amplifier Array: Full-Wave System Analysis and Experimental Validation," *IEEE Transactions on Microwave Theory and Techniques*, **MTT-48**, 12, December 2000, pp. 2692-2699.

23. A. B. Yakovlev, A. I. Khalil, C. W. Hicks, A. Mortazawi, and M. B. Steer, "The Generalized Scattering Matrix of Closely Spaced Strip and Slot Layers in Waveguide," *IEEE Transactions on Microwave Theory and Techniques*, **MTT-48**, 1, January 2000, pp. 126-137.

24. A. I. Khalil, A. B. Yakovlev, and M. B. Steer, "Efficient Method of Moments Formulation for the Modeling of Planar Conductive Layers in a Shielded Guided-Wave Structure," *IEEE Transactions on Microwave Theory and Techniques*, **MTT-47**, 9, September 1999, pp. 1730-1736.

25. A. B. Yakovlev, S. Ortiz, M. Ozkar, A. Mortazawi, and M. B. Steer, "Electric Green's Dyadics for Modeling Resonance and Surface Wave Effects in a Waveguide-Based Aperture-Coupled Patch Array," *IEEE International Symposium on Antennas and Propagation and USNC/URSI National Radio Science Meeting*, July, 2001, pp. 236-239.

26. S. Ortiz, M. Ozkar, A. B. Yakovlev, M. B. Steer, and A. Mortazawi, "Fault Tolerance Analysis and Measurement of a Spatial Power Amplifier," *2001 IEEE International Microwave Symposium Digest*, Phoenix, Arizona, June 2001, pp. 1827-1830.

27. A. I. Khalil, A. B. Yakovlev, and M. B. Steer, "Efficient MOM-Based Generalized Scattering Matrix Method for the Integrated Circuit and Multilayered Structures in Waveguide," *1999 IEEE International Microwave Symposium Digest*, *Volume 4*, Anaheim, CA, June 1999, pp. 1707-1710.

28. A. B. Yakovlev, S. Ortiz, M. Ozkar, A. Mortazawi, and M. B. Steer, "Electric Dyadic Green's Functions for Modeling Resonance and Coupling Effects in Waveguide-Based Aperture-Coupled Patch Arrays," *ACES Journal*, **17**, 2, July 2002, pp. 123-133.

29. A. B. Yakovlev, M. V. Lukich, A. Z. Elsherbeni, C. E. Smith, and M. B. Steer, "Broadband Printed Antennas for Waveguide-Based Spatial Power Combiners," *IEEE International Symposium on Antennas and Propagation and USNC/URSI National Radio Science Meeting*, San Antonio, Texas, June 2002, pp. 420-423.

30. M. V. Lukich, A. B. Yakovlev, A. Z. Elsherbeni, and C. E. Smith, "Electromagnetic Modeling and Design of Broadband Spatial Power Combiners," *Proceedings of the Thirty-Fourth South Eastern Symposium on System Theory (SSST)*, Huntsville, Alabama, March 2002, pp. 108-112.

31. A. B. Yakovlev, M. V. Lukich, A. Z. Elsherbeni, C. E. Smith, and M. B. Steer, "Meander-Slot and U-Slot Antenna Arrays for Wideband Spatial Power Combiners," *IEEE Microwave Wireless Components Letters*, 2002, pp. 125-127.

32. W. Batty, C. E. Christoffersen, A. B. Yakovlev, J. F. Whitaker, M. Ozkar, S. Ortiz, A. Mortazawi, R. Reano, K. Yang, L. P. B. Katehi, C. M. Snowden, and M. B. Steer, "Global Coupled EM-Electrical-Thermal Simulation and Experimental Validation for a Spatial Power Combining MMIC Array," *IEEE International Microwave Symposium Digest*, Seattle, WA, June 2002, pp. 2177-2180.

System Considerations of Onboard Antennas for SSPS

T. Takano
A. Sugawara
S. Sasaki

Abstract

A gigantic antenna aboard a Space Solar Power System (SSPS) satellite – a space-tenna – is one of the most challenging devices to build. The space-tenna is considerably larger in size and weight than conventional onboard antennas use for other microwave applications, such as communications. Also, microwave power handled in the SSPS is much higher than that of other microwave applications. As a result, the space-tenna has the greatest influence on the system design, including measures against environmental hazards. This paper describes the requirements for a space-tenna for an SSPS, and the system considerations for the configuration of space-tennas. Three kinds of configurations are presented and compared from the viewpoint of their realization.

1. Introduction

A Space Solar Power System (SSPS) is composed of a satellite with a huge solar-cell paddle and a gigantic antenna (space-tenna), and a ground station with a huge antenna (rectenna). The dc power generated on the satellite is converted to microwaves and transmitted from the space-tenna to the rectenna. The rectenna rectifies the received microwave power, and supplies the power to commercial electrical power grids. The SSPS is expected to help rescue the world from energy shortage. Several concepts for the SSPS have been proposed and studied [1-3], but they still remain in the research phase, due to technological, economic, and social difficulties. The space-tenna is one of the most important and difficult devices to build. The antenna itself is a huge and complicated system. The total satellite system itself is on a larger scale, consisting of solar-cell paddles, huge electric power feeders, structures, thermal control subsystem, etc., in addition to the antenna. The functions and characteristics and, eventually, the structure and size depend on whether the SSPS is operated in geosynchronous Earth orbit (GEO) [2] or a low Earth orbit (LEO) [3].

The space-tenna is considerably larger in size and weight than conventional onboard antennas for other microwave applications, such as communications. Also, the microwave power handled in an SSPS is considerably higher than in other microwave applications. The antennas that have been realized for space use are of 10 m diameter at most [4], and handle a microwave power of about one kW in a modulated wave. The SSPS antenna should exceed these values by several orders of magnitude. The USA Reference Model for an SSPS in geosynchronous orbit requires a diameter of 1 km and a microwave power of 107 kW [2], and SPS 2000 in low Earth orbit requires an area of 132 m × 132 m and 104 kW [3]. Both systems assume the use of a microwave frequency of 2.45 GHz, which is allotted to so-called ISM uses and popular for microwave ovens. As a result, the space-tenna has the greatest influence on the system design, including measures against environmental hazards.

This paper first describes the requirements for a space-tenna for an SSPS. The electrical and mechanical characteristics of the space-tenna are presented, with relevant studies. Then, focusing on the electrical characteristics, the power transmission capability of the total system is analyzed, considering the radiation patterns of a space-tenna and a rectenna. Sections 5 and 6 are dedicated to the antenna from the view points of improvement and testing its characteristics.

2. Requirement of SSPS for Onboard Antennas

In the case of a geosynchronous SSPS, the space-tenna points to a rectenna on the ground at all times. The size of the space-tenna is determined by the allowable footprint of the transmitted beam on the ground, which is equivalent to the size of the rectenna. If the rectenna size, D_{rec}, is given, the space-tenna size, D_s, is roughly calculated by Equation (1), which is valid for a uniform field distribution on the space-tenna's aperture and for a narrow beamwidth:

Tadashi Takano and Susumu Sasaki are with the Institute of Space and Astronautical Science, JAXA, 3-1-1 Yoshino-dai, Sagamihara, 229-8510 Japan; Tel: +81-42-759-8315; Fax: +81-42-759-8320; E-mail: ttakano@radionet.isas.jaxa.jp, sasaki@newslan.isas. jaxa.jp.
Akira Sugawara is with the University of Electro-Communications, 1-5-1 Cyoufugaoka, Cyoufu, 182-8585 Japan; E-mail: sugawara@radionet.isas. jaxa.jp.

This invited paper is part of the Special Section on Space Solar Power Systems. An oral version was originally presented at the 2003 Japan-US Joint Workshop on Space Solar Power System (JUSPS'03), July 3-4, 2003, Kyoto University, Uji, Kyoto, Japan.

1. Transportation: Weight and size of a unit
2. Temperature:
   Solar irradiated side: +100° C
   Shadow side: –100° C
3. Vibration conditions
4. Examination and test
   – Mechanical accuracy and electrical properties
   – Characteristics in 1G and 0G
   – To cope with flexible nature

Table 1: Mechanical and Thermal Conditions

Concept	Element Size	Number of Elements	Phase Control
1. Single aperture	1000 m	1	N. A.
2. Array of apertures	10 m	10000	Possible
3. Array of small apertures	0.1 m	2×10^8	Necessary

Table 2: Composition of a gigantic antenna (1km diameter, 2.45GHz)

$$D_s = 1.2R\lambda / D_{rec} \ , \qquad (1)$$

where R is the distance between the space-tenna and the rectenna and λ is the wavelength. If the rectenna's size is 5 km, the space-tenna's size may be 1 km at 2.45 GHz.

On the contrary, a low-Earth-orbit SSPS flies over a rectenna, so the beam of the space-tenna should be scanned, and the generated power should be switched from one rectenna to another. As the rectenna receives power intermittently for a short time, power storage is inevitable for power to be used while the SSPS is out of sight.

For both the low-Earth-orbit and geosynchronous cases, sidelobes should be suppressed to avoid interference with other systems, most importantly grating lobes. The direction of the main beam should be adjusted according to even the slight changes in the satellite's attitude.

The mechanical and thermal requirements for a space-tenna are also stringent, as summarized in Table 1. Item 1 in the table will be discussed in Section 3. Items 2 to 4 are important, but have been considered in detail in other articles [4, 12].

3. Mechanical and Structural Considerations

Several methods for constructing antennas have been proposed. These are classified as follows:

1. An ultra-large parabola of 1 km diameter, used as a single dish.
2. Parabolic antennas of about 100 wavelengths are arrayed, the shape of which may be non-circular [5].
3. Radiating elements of a half wavelength are arrayed in large numbers [3, 6].

The structure of a gigantic antenna is designed to realize large size and stability in orbit, considering its launching rocket. Mechanical conditions are imposed to keep the antenna's characteristics through the severe vibrations experienced during launch, and for a long life in orbit.

The most fundamental factor is the type of radiator. The configurations of three types of antennas are shown in Figure 1. Rough estimates of the radiator's size and of the number of radiators are given in Table 2. The single dish antenna may be constructed by assembling thousands of reflector panels, and a huge subreflector and a horn. The accuracy of the assembly should be better than $\lambda/30$, which is 4 mm rms at 2.45 GHz. Considering the ratio of the diameter and the height of a parabolic reflector, its height should be about 300 m, which may impose severe difficulties on the attitude control of the satellite.

The array of small radiating elements may be formed with flat panels that contain hundreds of the elements in each panel. The accuracy of mutual alignment could be relaxed, due to an electrical phase-adjustment capability. However, the number of elements is enormous: 2×10^{10}.

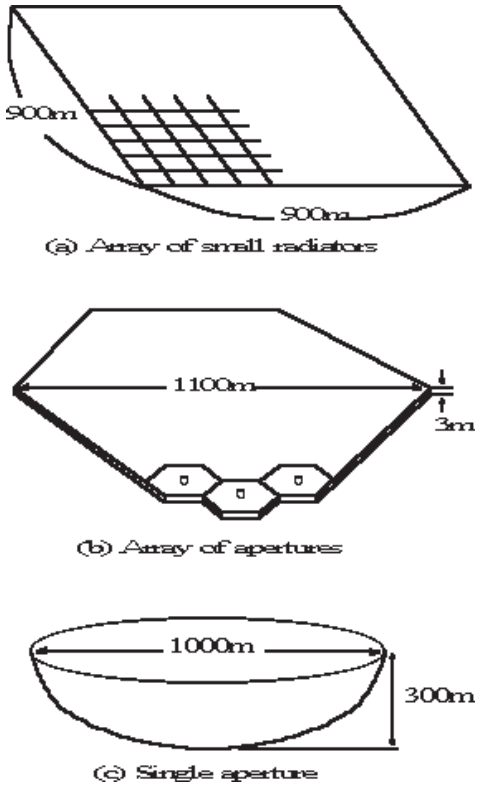

Figure 1. Three concepts of gigantic antennas.

Figure 2. The structure of the HALCA antenna (deployed state).

The array of large radiating elements or small apertures is formed by assembling thousands of aperture antennas. The accuracy of mutual alignment could be relaxed due to an electrical phase-adjustment capability, although each aperture should be manufactured and maintained with sufficient accuracy.

From the viewpoint of transportation, the single dish has to be divided into thousand of panels that are assembled in space with the aid of huge jigs. This method of assembling is well established for antennas for terrestrial uses. On the other hand, a small aperture can be transported and deployed in space automatically, on the basis of current technologies. All apertures are fixed at the designated positions. Figure 2 shows the deployable antenna for the HALCA satellite, as an example. In the case of an array of half-wavelength elements, the total antenna will be divided into several flat panels, each of which can be transported by a single launch. The subsequent deployment procedure was well investigated in the SPS 2000 project [6].

4. Beam Transmission and Reception Characteristics

The transmitted beam makes a large footprint on the ground, which should be almost completely included within the rectenna. Therefore, the efficiency of power transmission is evaluated by the received power, P_r, through integrating the power flux, $p(\vec{r}_r)$, over the area of the rectenna, as follows:

$$P_r = \iint_S p(\vec{r}_r)\,dS\,, \qquad (2)$$

where

$$p(\vec{r}_r) = \frac{P_t}{4\pi R^2} G_t(\vec{r}_r)\,. \qquad (3)$$

P_t is the transmitted power and $G_t(\vec{r}_r)$ is the directional gain at the point $\vec{r}_r$ in the rectenna. Note that the antenna gain of the space-tenna cannot be assumed constant over the rectenna, because $G_t(\vec{r}_r)$ will be designed to have a small value, or to even be zero, on the rectenna's edge.

If $G_t(\vec{r}_r)$ is constant over the rectenna, Equation (2) reduces to Friis's equation. Therefore, the equation of power-transmission efficiency proposed in the CCIR document [7] cannot be applied to a practical SSPS.

Murao et al. analyzed the power-transmission efficiency in the above-mentioned method, and obtained optimization conditions for the space-tenna [8]. The efficiency can be maximized not by a uniform field distribution on the space-tenna's aperture, but by a Gaussian distribution. Reference [5] shows, in Figure 5, that the optimum distribution is a Gaussian distribution with a –5.5 dB taper, for a 100 m space-tenna and a 10 km rectenna. This fact shows the significant difference between transmission antennas for SSPS and for communications, and is clearly presented in Figure 3. The situation is the

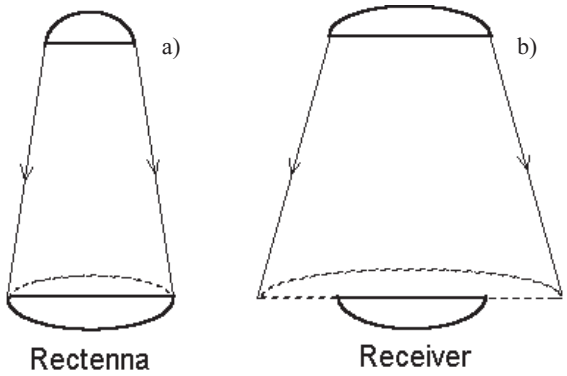

Figure 3. The relationship of a transmitted beam to a receiving antenna: (a) Power transmission; (b) Communications.

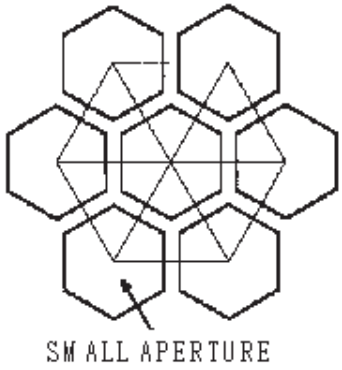

Figure 4. A densely-packed array of apertures.

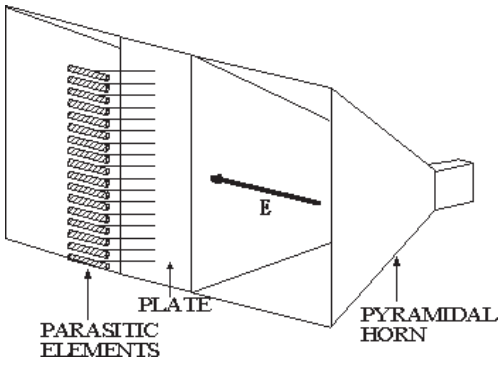

Figure 5. Constitution of the model antenna.

same for an array of small elements and for an array of apertures as for a single dish antenna.

5. Improvements of the Radiation Characteristics of a Space-Tenna

The space-tenna should satisfy the radiation characteristics described in the former section. A single dish antenna has little problem in this regard, because design methods are well established for terrestrial uses, except for difficulties due to the huge size. A similar situation exists for an array of small elements.

An array of apertures, however, has many technical problems to be solved, as follows:

1. suppressing the grating lobes,
2. electrically patching the gaps between the small apertures,
3. illuminating the reflector by a primary radiator with a pattern matched to the reflector shape.

For problem 1, the total antenna should not have un-illuminated areas in the aperture, so small apertures should be packed as closely as possible. One solution is a reflector with a hexagonal shape, as shown in Figure 4, which can fill a plane without any gaps, unlike the case of circular apertures [9].

Problem 2 arises because the above-mentioned hexagonal apertures need gaps between them for the sake of structural and mechanical margins. A practical means of using parasitic elements was proposed, as shown in Figure 5. Both tips of each parasitic element are illuminated by the radiated wave from two horns so that the current is induced on the element to radiate the wave. With a space adjustment between the element and the reflector, the re-radiated wave can be in-phase with the wave radiated from the horns. Accordingly, the degradation of the antenna's gain and the grating lobes – both due to un-illuminated areas in the total space-tenna aperture – can be reduced. The validity of this concept was shown experimentally, as in Figure 6, and analytically [10].

A normal conical horn radiates a beam with a circular or elliptical cross section. Therefore, the above-mentioned hexagonal reflector suffers from a spillover loss or an under-illumination loss, depending on the size relationship between the beam and the reflector, as shown in Figure 7. Problem 3 arises from the need to reduce these losses [11]. A primary radiator that radiates a matched beam, namely, a beam with a cross section similar to the reflector's shape, can solve the problem. Figure 8 shows a hexagonal horn for radiating a hexagonal beam in the near field [11].

6. Tests

After transportation and assembly, the antenna has to be tested. This is also a more important and difficult task than that experienced previously for large antennas [12]. The test items are summarized in Table 3.

The basic factors are the gain, the radiation pattern, and the input impedance for each element and for the total space-tenna. The near-field measurement of a space-tenna as a whole is impossible. As the PIM (passive inter-modulation) waves probably have significant radiation over a wide range of angles, measurements should be

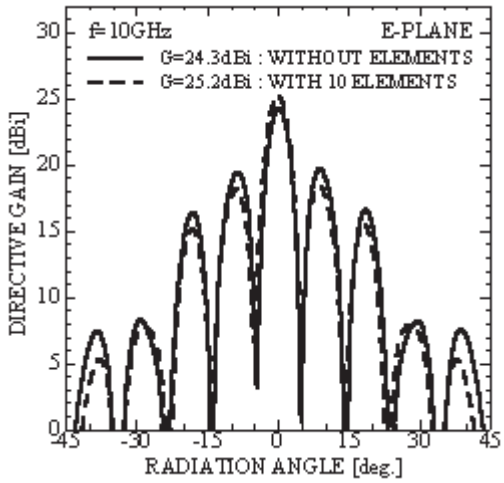

Figure 6. A comparison of the radiation patterns.

1. Patterns of element apertures
2. Pattern of the total space-tenna
3. Input impedance from the microwave circuit to the space-tenna
4. Switch-off function to be used in an emergency
   - pattern of wasted power
   - transient phenomena
5. Passive inter-modulation (PIM)
6. Combined characteristics of a space-tenna and a rectenna
   - input to the space-tenna and output from the rectenna
7. Functions of retrodirective phased array

Table 3: Items for Test and Calibration

carried out over a much wider area than the footprint at the transmitted frequency. For that purpose, movable test equipment on a van with deployable antennas is needed, although a dedicated satellite may be used for measurements at the research stage [12].

7. Conclusions

1. Space-tennas on a SSPS are quite different in their functioning and characteristics, depending on whether they are in geosynchronous orbit or low Earth orbit.
2. The space-tenna design should be compatible with the total SSPS concept, with many compromises.
3. The efficiency of power transmission can be maximized by an optimized design for the space-tenna.
4. An array of apertures seems to be a superior candidate for geosynchronous use.
5. The realization of a space-tenna requires many research activities and offers many research topics.
6. Tests should be studied for both the antenna itself and for its application system.
7. Collaboration of electrical and mechanical engineers is inevitable.

8. References

1. P. E. Gleser, "Power from the Sun: Its Future," *Science*, **162**, 1968, pp. 857-886.

2. G. M. Hanley, "Satellite Power Systems (SPS) Concept Definition Study: Vol. I – Executive Summary," NASA CR-3317, 1980.

3. M. Nagatomo, S. Sasaki, and Y. Naruo, "Conceptual Study of a Solar Power Satellite SPS 2000," 19th International Symposium on Space Technology and Science, ISTS-94-e-04, May 1994.

4. T. Takano, K. Miura, M. Natori, E. Hanayama, T. Inoue, T. Noguchi, N. Miyahara, and H. Nakaguro, "Deployable Antenna with 10 m Maximum Diameter for Space Use," *IEEE Transactions on Antennas and Propagation*, **AP-52**, 1, 2004, pp. 2-11.

5. Tadashi Takano, "Investigation on Antennas in the Concept of the Most-Dense Packing," Symposium on SPS Technologies of Power Transmission and Reception, November 1994 (in Japanese).

6. M. Nagatomo and K. Itoh, "An Evolutionary Satellite Power System for International Demonstration in Developing Nations," 2nd International Symposium on SPS, Paris, 1991.

7. CCIR, "Characteristics and Effects of Radio Techniques for the Transmission of Energy from Space," Rep. 679-2, 1986, pp. 106-112.

8. Y. Murao and T. Takano, "An Investigation on the Design of a Transmission Antennas and a Rectenna with Arrayed Apertures for Microwave Power Transmission," *Transactions of the Institute of Electronics, Information and Communication Engineers*, **J81-B-II**, 1, 1998, pp. 46-53 (in Japanese); *Electronics and Communications in Japan*, **83**, 2, 2000, pp. 1-9 (translated into English).

9. Y. Murao and T. Takano, "Proposal and Analysis of Ultra-Large Aperture Array Antennas," *Transactions of the Institute of Electronics, Information and Communication Engineers*, **J80-B-II**, 6, 1997, pp. 501-506 (in Japanese).

10. A. Sugawara, T. Takano, E. Hanayama, and Y. Kami, "Investigation on an Electrical Patching Method of a Gap between Apertures by Loading Parasitic Elements," *Transactions of the Institute of Electronics, Information and Communication Engineers*, **J86-B**, 3, 2003, pp. 519-526 (in Japanese).

11. E. Hanayma, K. Asari, and T. Takano, "Investigation on the Radiation Characteristics of a Horn Antenna with Hexagonal Beam," IEICE Com. Soc. Convention, B-69, 1995 (in Japanese).

12. NASA CP-2368, Part 1 – Large Space Antenna Systems Technology 1984, 1984.

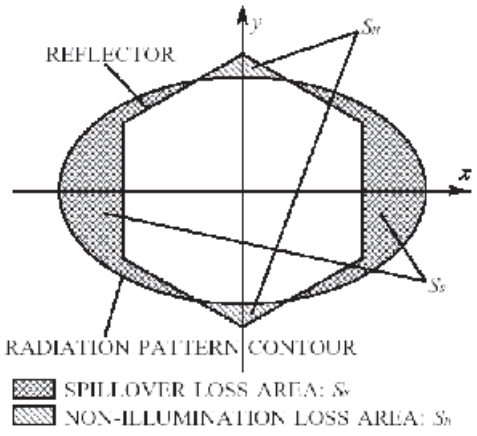

Figure 7: The losses due to mismatches between a reflector's shape and a horn's radiation pattern

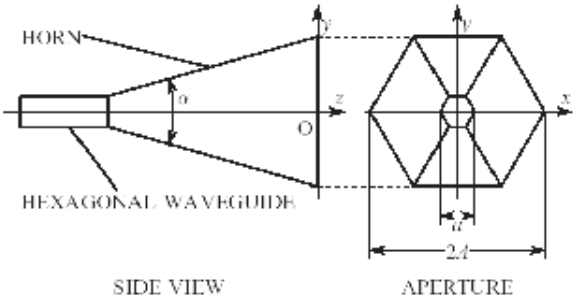

Figure 8. A horn to match a hexagonal reflector.

Active Antenna Approach for Power Transmission

K. M.K.H. Leong, Y. Chung
W. Yao, Y. Wang, T. Itoh

Abstract

Active integrated antennas (AIAs) represent a new class of microwave and millimeter-wave front-end circuitry. They offer several attractive features, such as compact circuit implementation, light weight, better efficiency, and multi-functionality. We believe that these features will be beneficial in the design of front ends for solar power satellites (SPS). Several examples of this technology are demonstrated, including a high-efficiency AlGaN/GaN-based transmitter and a frequency-doubling transmitter. The self-steering behavior of retrodirective arrays and their use for beam-control applications for SPS is also presented. This technique can be used to achieve accurate beam pointing directed to the Earth power reception site. Implementations of various retrodirective arrays are presented, including a reconfigurable retrodirective/ digital beamforming array and a frequency autonomous retrodirective array. In addition, a new antenna array self-calibration scheme, which uses reference sources positioned in close proximity to the array, is also introduced. This technique is used to detect and correct for element position errors as well as circuit errors, which can be used to minimize SPS beam-pointing errors.

1. Introduction

Active integrated antennas (AIA) are an emerging technology in which antennas are combined with active circuits – such as oscillators, mixers, and amplifiers – to form a single entity [1]. Often, the antenna is used to provide additional functions, such as harmonic suppression, signal combining, and mode filtering, in addition to its traditional radiating function. Since the antenna and circuit are designed as one unit, this new design method offers high efficiency and compact overall circuit size.

When receiving a signal from an unspecified direction, retrodirective arrays are able to transmit a signal response to that same direction, without any previous knowledge of the source direction. This function is performed automatically, without the use of phase shifters or digital circuitry. The capability to automatically perform high-gain antenna pointing makes the retrodirective array an attractive candidate for advanced digital mobile communication systems.

For the most part, interest in the development of wireless technologies is structured for the transmission of information. However, wireless power transmission (WPT) has gained added interest in the last two decades [2-4]. Although many early scientists foresaw wireless power transmission as one of the major applications of radiowave transmission, only recently have RF and space technology been mature enough to support such claims. It is envisioned that solar power satellites (SPS) can provide a limitless energy resource, acting as conduit between the sun and the Earth. The SPS will first harvest energy from the sun's rays using solar cells, and will then transmit power down to Earth using wireless power transmission.

There are many technical issues that must be overcome in order in implement a successful SPS. Two major concerns that must be addressed are power efficiency and accurate beam pointing. This paper summarizes several aspects of active integrated antennas, which may be applied as a component technology, and retrodirective antenna arrays, which may be used as a beam-control technique for future solar power satellite applications. To date, both classes of technology described here have been explored for sensor (radar)/transponder and communication applications by the authors, as well as by several other groups. However, these techniques posses several strong points that will prove useful in improving transmitter control and efficiency for SPS.

Implementations of active integrated antenna front ends, capable of providing high output power and including an AlGaN/GaN power amplifier and an AlGaN/GaN-based frequency doubler, are presented. The self-steering behavior of retrodirective arrays and their use for beam-control

---

Kevin M. K. H. Leong, Younkyu Chung, Weijun Yao, Yuanxun Wang, and Tatsuo Itoh are with the Department of Electrical Engineering, University of California, Los Angeles, 405 Hilgard Avenue, Los Angeles, CA 90095, USA; E-mail: kleong@ee.ucla.edu.

This invited paper is part of the Special Section on Space Solar Power Systems. An oral version was originally presented at the 2003 Japan-US Joint Workshop on Space Solar Power System (JUSPS'03), July 3-4, 2003, Kyoto University, Uji, Kyoto, Japan.

applications for SPS are also be discussed. Implementations of this technology are presented, including a reconfigurable retrodirective/ digital beamforming array and a frequency autonomous retrodirective array. Lastly, a novel antenna array self-calibration technique is introduced and demonstrated. This technique is especially useful for space-deployable arrays built on inflatable surfaces.

2. High-Efficiency AlGaN/GaN HEMT AIA Power Amplifier

In most transmitter designs, the power amplifier (PA) is the active component that precedes the antenna. It is also the most power-hungry circuit in the transmitter chain. Therefore, much effort has been spent on maximizing the efficiency and output power of power amplifiers. One method of accomplishing this is to incorporate output harmonic tuning in the amplifier design. In practice, this is often realized by adding resonators at the amplifier output, which act as reactive terminations for the upper harmonic frequencies generated by the power amplifier. Because such resonators always have some inherent loss, the addition of these components cannot lead to the maximum achievable amplifier efficiency.

The active-integrated-antenna approach to this problem is to design an antenna that intrinsically rejects all harmonic frequencies generated by the amplifier. Moreover, the antenna input impedance need not be 50 Ω, which adds more flexibility in the design of the output-matching circuit of the power amplifier. This technique was used to design a class-F GaAs amplifier [5]. More recently, a similar approach was used in the design of an AlGaN/GaN HEMT (high-electron-mobility transistor) active integrated antenna power amplifier [6]. Wide-bandgap semiconductor devices, such as GaN-based and SiC-based HEMTs, have shown much promise for use in high-power applications at microwave and millimeter-wave frequencies, due to their high breakdown voltage, high current density, and fast carrier characteristics.

For this design, a modified circular-sector microstrip antenna, which was designed to resonate at 2.45 GHz and to reject both second and third harmonics, was integrated with an AlGaN/GaN HEMT with a gate width of 1 mm and a gate length of 0.8 ìm (Figure 1). As opposed to a simple rectangular patch antenna, the circular-sector antenna's resonant frequencies depend on the roots of Bessel functions, rather than multiples of the fundamental frequencies. This allows it to be designed to suppress both second and third harmonics. The input matching network was fabricated on alumina, with a dielectric constant of 9.8 and a thickness of 0.375 mm. The radiating antenna was built on a Duroid substrate, with a dielectric constant of 2.33 and a thickness of 0.775 mm. For more accurate modeling of the structure, we have also considered the effect of Au bonding wires, with an equivalent inductance of 0.5 nH/mm, for connecting circuit components. The fabricated active integrated antenna power amplifier was mounted on a metal fixture for heat sinking.

Measurements were done in an anechoic chamber. The amplifier characteristics can be determined by using the Friis transmission equation:

$$P_{rec} = \left(1-|\Gamma_{trans}|^2\right) G_t \frac{P_{in}}{4\pi R^2} \left(1-|\Gamma_{rec}|^2\right) \frac{\lambda^2}{4\pi} G_r \,. \quad (1)$$

Radiated power from a passive antenna was measured in the broadside direction to calibrate out the antenna's gain. In Equation (1), P_{rec} and P_{in} are the received power and the input power from the output of the HEMT to the antenna, and Γ_{trans} and Γ_{rec} are the reflection coefficients of the transmitting and receiving sides, respectively. G_t and G_r are the transmitting and receiving antenna gains, and $\lambda^2/4\pi R^2$ represents the free-space loss. This allows us to get the output power just before the antenna, after de-embedding the receiving and the passive antenna gains.

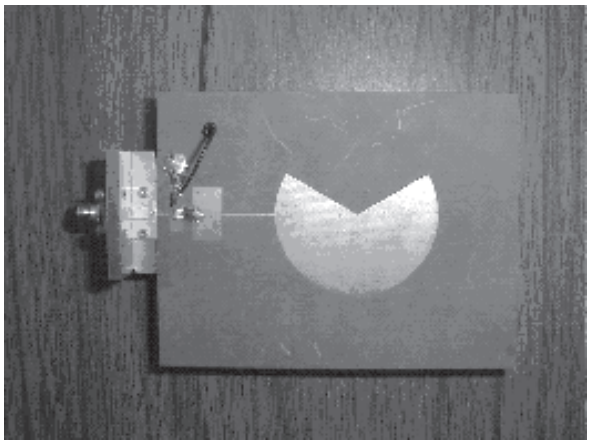

Figure 1. A photograph of an AlGaN/GaN power amplifier, integrated with a circular-sector antenna.

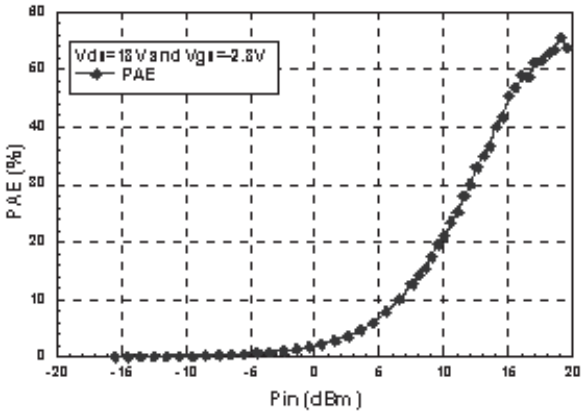

Figure 2. The measured PAE performance for an AlGaN/GaN power amplifier integrated with a circular-sector antenna (frequency: 2.45 GHz).

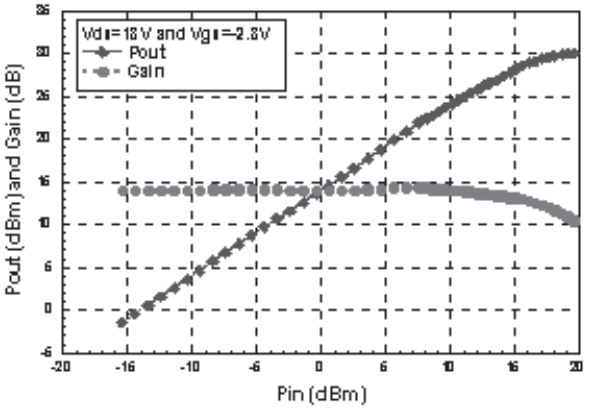

Figure 3. The measured output power (P_{out}) and gain for an AlGaN/GaN power amplifier integrated with a circular- sector antenna (frequency: 2.45 GHz).

Figure 2 shows the measured PAE (power- amplifier efficiency) as a function of the input power (P_{in}) of the class-AB-biased power amplifier (V_{ds} of 18 V and V_{gs} of –2.8 V) at 2.45 GHz. The measured P_{out} and power gain are shown in Figure 3 as functions of P_{in} . A peak PAE of 55% at an input power level of 19 dBm, a P_{out} of 30 dBm, and a power gain of 14 dB were obtained.

Harmonic terminations reduce radiating power at harmonic frequencies and increase the PAE. This effect was observed through the measured radiation patterns of the second and third harmonic frequencies, as shown in Figure 4 and Figure 5 for the H and E planes, respectively. Note that the radiation power at the fundamental frequency of 2.45 GHz was normalized to 0 dB. Due to the harmonic termination characteristic of a circular-sector antenna, the radiation powers at the second and third harmonic frequencies were below –30 dB and –20 dB, respectively, for each polarization in the broadside direction. If needed, further suppression of harmonic radiation can be achieved by using an additional filter. However, since harmonic

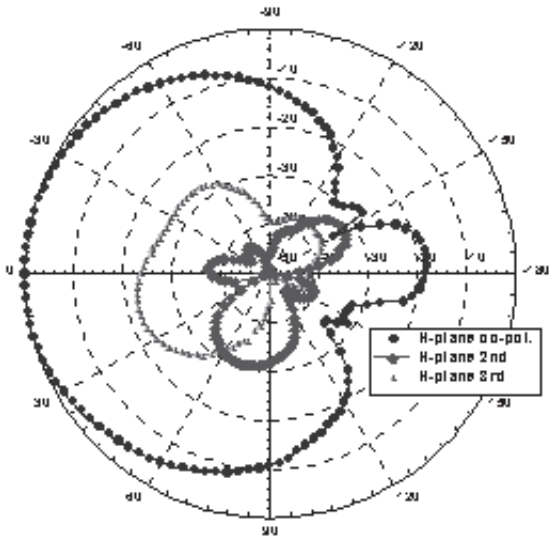

Figure 4. The measured radiation patterns at the fundamental, second, and third harmonic frequencies in the H plane.

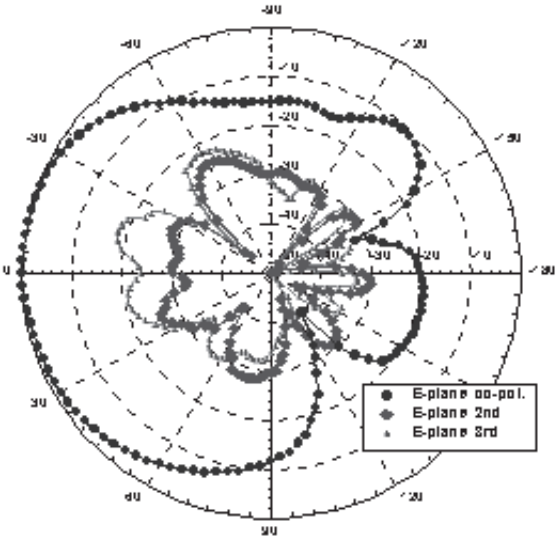

Figure 5. The measured radiation patterns at the fundamental, second, and third harmonic frequencies in the E plane.

suppression is already provided by the active-integrated-antenna approach, the filter rejection requirements become less stringent.

3. AlGaN/GaN HEMT AIA Frequency Doubler

The conventional design of frequency doublers includes a filtering element – such as an open-circuited stub (at the fundamental frequency) – which is used to suppress the fundamental frequency signals while passing the second harmonic at the circuit output. By applying the active-integrated-antenna design approach for this component's design, we were able to propose a new doubler circuit [7, 8]. This circuit configuration is shown in Figure 6. Note that the antenna's resonant frequency corresponds to the second harmonic of the input frequency. The antenna operates as an equivalent fundamental frequency reflector in the conventional frequency doubler by only radiating the second harmonic power generated by the active device, while efficiently suppressing the fundamental-frequency signal power. This eliminates the need for an additional fundamental-frequency reflector, as well as eliminating additional cable and feed-line losses incurred when an external antenna is used. Also, because the antenna plays a double role in this design scheme, both the size and the transmission-line loss can be reduced.

As shown in Figure 7, the single-ended AlGaN/GaN HEMT frequency doubler consists of AlGaN/GaN HEMT and a microstrip rectangular patch antenna. The antenna was designed at the second harmonic frequency of 8 GHz. In the input matching network, a second-harmonic reflector using a $\lambda/4$ open-circuited stub (at the second harmonic) was employed, with an input-matching network designed at the fundamental frequency of 4 GHz. The device was biased in the pinch-off region (V_{ds} of 12 V and V_{gs} of –5 V), and the circuit characteristics were measured in a

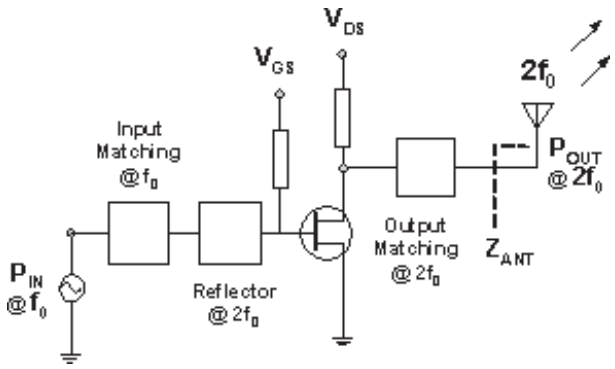

Figure 6. The architecture of a new frequency doubler using the active-integrated-antenna (AIA) design approach.

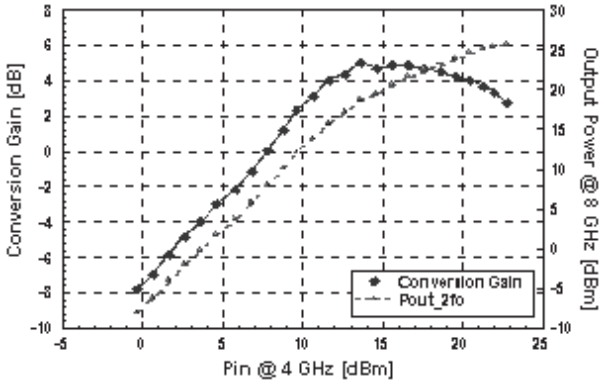

Figure 8. The measured output power (P_{out}) and conversion gain for the AlGaN/GaN frequency doubler integrated with the rectangular patch antenna.

manner similar to the active-integrated-antenna amplifier in Section 2. The measured conversion gain and output power at the second-harmonic frequency are shown in Figure 8 as a function of the input power. Note that the output power is defined at the end of the frequency doubler. This embeds antenna gain, taking into account cable loss. A maximum conversion gain of 5 dB at an input power level of 14 dBm and a saturated P_{out} of 25 dBm were obtained. In Figure 9, the measured suppression characteristics of the fundamental frequency and the third harmonic at the output of the AlGaN/GaN HEMT frequency doubler, integrated with the rectangular patch antenna, are shown. The suppression was better than 10 dB and 25 dB for the fundamental and the third-harmonic frequencies, respectively. As with the active-integrated-antenna power amplifier demonstrated in Section 2, additional suppression of the fundamental and harmonic tones can be achieved by inserting an external filter.

4. Retrodirective Arrays

Retrodirective arrays are antenna arrays that are able to perform automatic beam pointing and tracking, without the use of digital phase shifters. The uses of such arrays include enhanced-gain transponders and beacons. This beam-control technique can be adapted and used to help direct the high power generated on the SPS toward the intended landing point on Earth, by sending a pilot signal from the Earth target.

Retrodirective behavior can be induced using a number of different techniques. The technique for achieving retrodirectivity that has been the focus of research at UCLA uses phase-conjugating mixers. Phase conjugation with heterodyne mixing uses an LO (local oscillator) signal at twice the RF frequency (Figure 10). In this scheme, the lower sideband product has the same frequency as the RF, but with conjugated phase. The phase-conjugated signal from each antenna element in an array is re-radiated towards the source direction. The following subsections discuss different retrodirective array architectures, and provide some insight on how they might be applied to SPS.

4.1. Active Retrodirective Arrays

In order to observe retrodirective radiation behavior, we need only conjugate the incoming wave's phase. However, to make this technology more practical, we

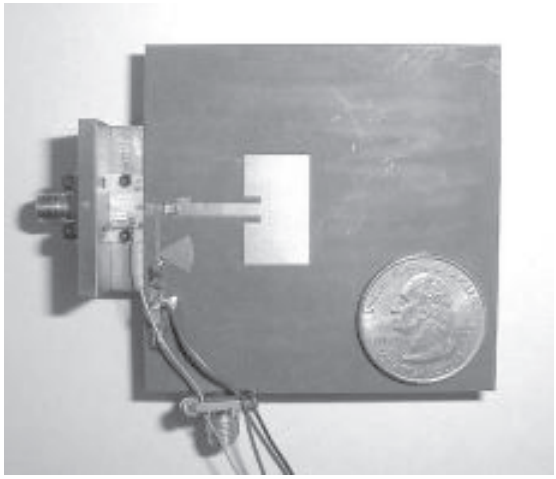

Figure 7. A photograph of an AlGaN/GaN frequency doubler integrated with the rectangular patch antenna.

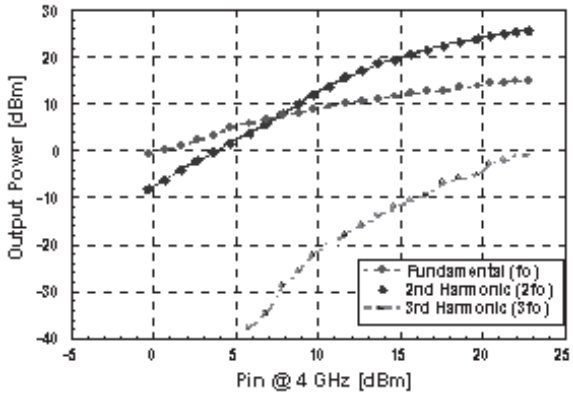

Figure 9. The measured output power (P_{out}) at the fundamental, second, and third harmonics for the AlGaN/GaN frequency doubler integrated with the rectangular patch antenna.

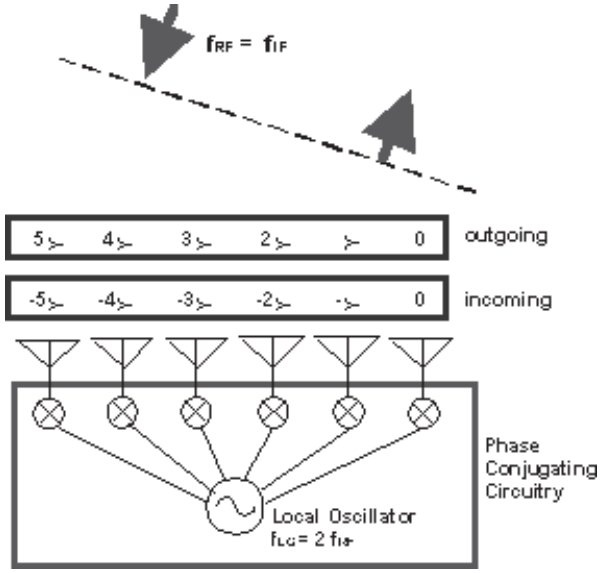

Figure 10. A schematic of the phase-conjugating retrodirective array.

would also like to amplify the outgoing wave. To this end, active devices such as MESFETs are attractive, since they can provide conversion gain as well as a mixing operation. This allows the array to send amplified signals towards the source location without including additional amplifiers, which would increase the size and cost of the circuit [9].

A compact active phase-conjugation circuit is presented in [9]. One challenge in the design of phase-conjugation circuits is to provide isolation between the RF and the IF (intermediate frequency). This cannot be done using filters, since the frequencies are often very close together, or can even be the same frequency. Instead, a balanced mixer design is used to provide isolation. As shown in Figure 11, the signal paths are identical except for the addition of a 90° phase-delay line (at the RF frequency) in one circuit branch. This delay line is used for cancellation of the returned RF signal at the RF/IF port, for isolation. Since the LO frequency is twice the RF frequency, the LO power from the two channels will experience a 180° delay when combined at the RF/IF port, thereby canceling the LO leakage to provide good LO isolation. The IF signals are phase conjugated and combined in-phase with conversion gain.

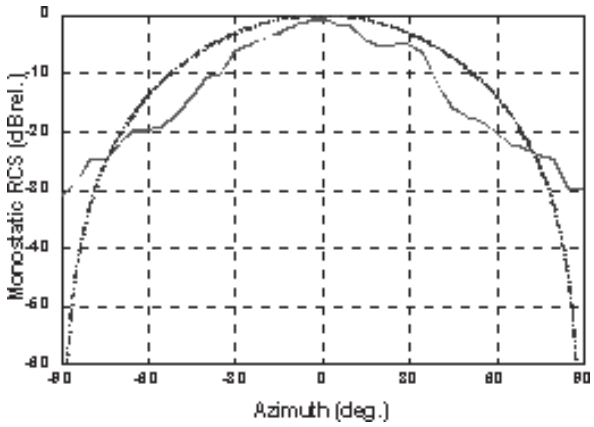

Figure 12. The monostatic radar cross section pattern.

The retrodirective radiative nature of an array of phase-conjugation mixers, described in Figure 11, was measured. Due to the array's unique retrodirective behavior, we expect that the peak of the array factor will always be in the direction of the source. Since the source point is always tracked by the peak of the radiation pattern, the monostatic radar cross section (RCS) pattern should have no nulls (see Figure 12). The measured results agreed reasonably well with the theoretical predictions based on the measured element pattern.

The radiation patterns of the array were measured with sources at different angles. Figures 13 and 14 show the bistatic radar cross section with the source at 0° and at +45°. The results were comparable with the theoretical results. The retrodirectivity of the array was clearly observed. Note that no grating lobe was observed in all cases, with pointing errors that were less than +/–6°. Errors in beam pointing come as a result of circuit unbalance between antenna elements. These can be minimized by element calibration. Under ideal circumstances, there will be no pointing errors.

4.2. Reconfigurable Retrodirective Array

The capability of performing high-gain antenna pointing automatically makes the retrodirective array an

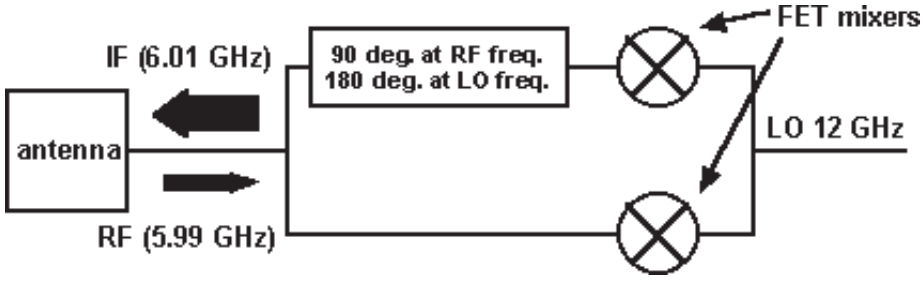

Figure 11. A schematic of the compact active phase conjugation circuit.

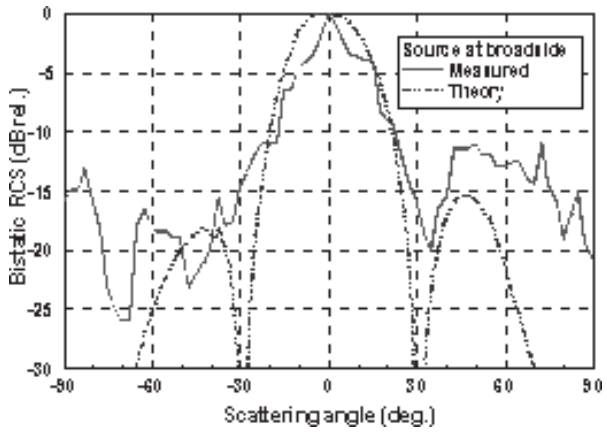

Figure 13. The bistatic radar cross section with the source at broadside (0°).

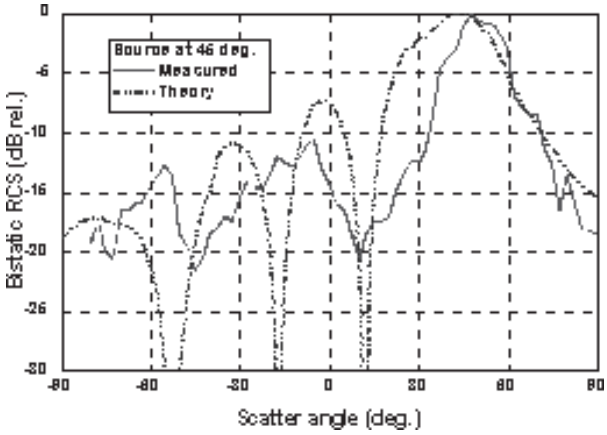

Figure 14. The bistatic radar cross section with the source at 45°.

attractive candidate for advanced digital mobile communication systems. This technology is mainly envisioned to be used as a transponder that can be used to relay data to moving interrogators. As a natural extension to this idea, we implemented a built-in receiver function in the retrodirective array. This allows the antenna array to receive data from multiple remote sources, and to then relay all of the collected data to the moving interrogator, acting as a kind of data hub.

This design ideology was applied to develop a reconfigurable retrodirective/direct down-conversion receiver array [10]. Both types of arrays generally rely on front-end mixers to perform phase conjugation and down conversion, respectively. The two functions have been combined into a single mixer that is dynamically reconfigured by simply changing the LO frequency. This architecture may also be useful in SPS applications, allowing for the reuse of hardware for multiple tasks, such as for beam control and receiving control commands from the Earth station.

A proposed wireless server system, using a reconfigurable active retrodirective/direct-conversion receiver array, is shown in Figure 15. In the receiving mode, Figure 15a, the array system functions as a direct-conversion receiver and stores data received from remote sensors. Next, upon receiving an instruction signal from an interrogator, the system operates as a retrodirective transponder (Figure 15b), and sends the stored data to the interrogator. This switching can be initiated by the header code contained in the signal from the interrogator. Then, after a prescribed time limit, the retrodirective array reverts back to receiver mode.

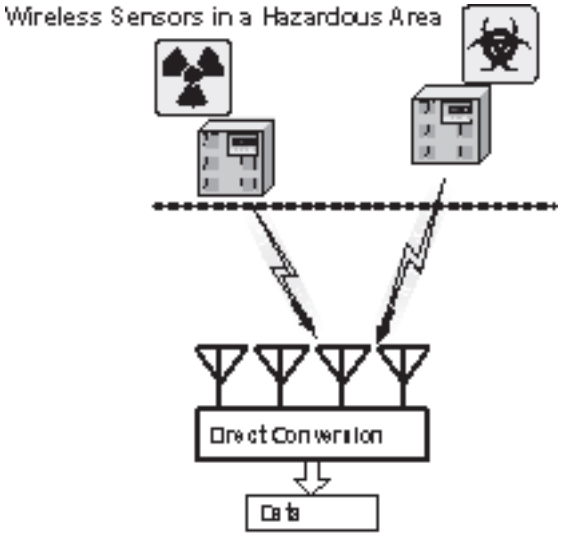

Figure 15a. A wireless sensor system using a reconfigurable array: the direct-conversion receiver mode.

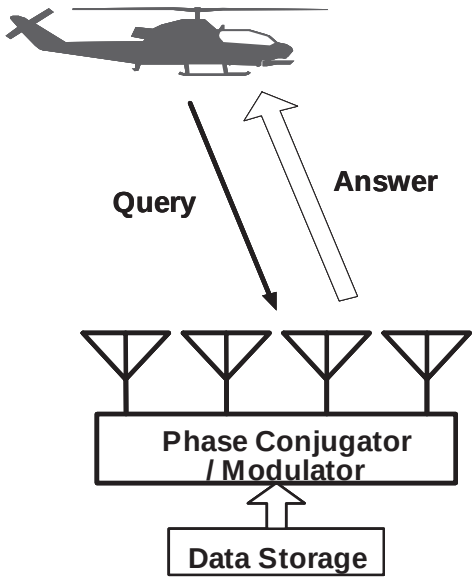

Figure 15b. A wireless sensor system using a reconfigurable array: the retrodirective transponder mode.

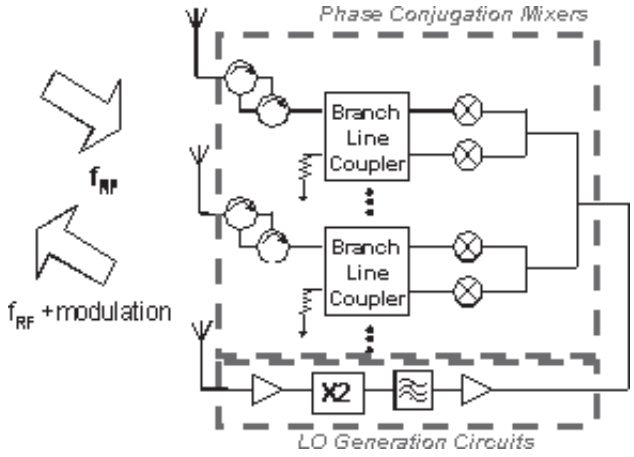

Figure 16. A schematic of a frequency autonomous retrodirective array.

4.3. Frequency Autonomous Retrodirective Array

Retrodirective arrays are able to automatically perform beam pointing and tracking. Recently, a new architecture that enables the retrodirective array to automatically respond to an interrogator at the same transmitted frequency, with no previous knowledge of the transmission frequency, was reported [11]. This enhances the covert nature of the retrodirective array, and also eliminates the possibility of beam-pointing error due to Doppler shifts. A higher degree of beam stabilization is a very attractive feature that may be used for SPS control applications.

In this array, shown in Figure 16, phase conjugation is accomplished by first doubling the RF signal, and then using this doubled frequency to mix with the incoming RF. The result is the generation of a phase-conjugated form of the incoming RF. The phase-conjugated signal is always exactly the same as the incoming RF.

Bistatic radar cross section pattern measurements of the array were done at 5.2 and 5.8 GHz, as shown in Figures 17 and 18, respectively. The frequency-agile prototype array showed excellent retrodirectivity at various

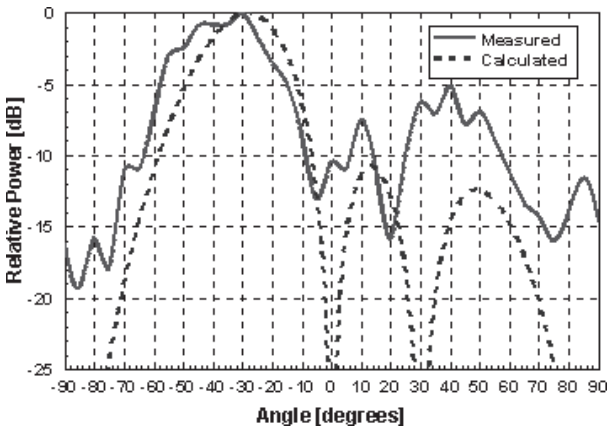

Figure 17. The bistatic radar cross section with the source at –30°, RF = 5.2 GHz.

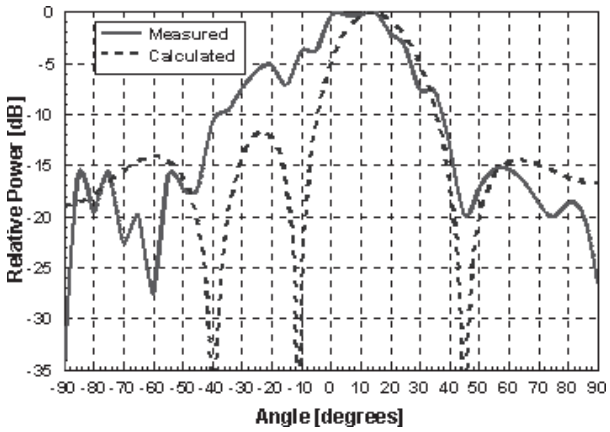

Figure 18. The bistatic radar cross section with the source at 15°, RF = 5.8 GHz.

frequencies. Again, we observed pointing errors as a result of circuit unbalance between antenna elements. These can be minimized by element calibration.

5. Antenna Array Self-Calibration Technique

Because of the importance of the beam-pointing accuracy needed by the SPS, array-calibration techniques are another area that needs to be studied. Generally, the error existing in the phased-array system comes from two parts: circuit error, and element-location error or position error. Most of the work in this area has been toward calibrating and correcting circuit errors. The element-position error usually only exists in non-rigid antenna arrays, such as inflatable arrays, where the antennas are made on a flexible surface. A combination of circuit and element position errors causes large beam-pointing errors. Some previously introduced calibration techniques include those in [12-13].

A self-calibration scheme for both the position error and circuit error is introduced in this section [14]. The main idea is to use reference sources – placed in the near field of the array but still in the far field of each antenna element – to calibrate each element's relative position and circuit error. The calibration process is divided into two steps. First, an estimation algorithm is used to estimate the position error. The basic principle is somewhat like that of a Global Positioning Satellite (GPS) receiver. A special technique is employed in this algorithm so that the circuit error's effect can be cancelled out. The second step includes a circuit error calibration.

The key technique of this system is to separate the position error and the circuit error with near-field sources. An orthogonal coding technique makes it possible for the near-field sources to share one frequency channel. Finally, the output information from the calibration system can update the old weighting coefficients to restore the correct far-field pattern.

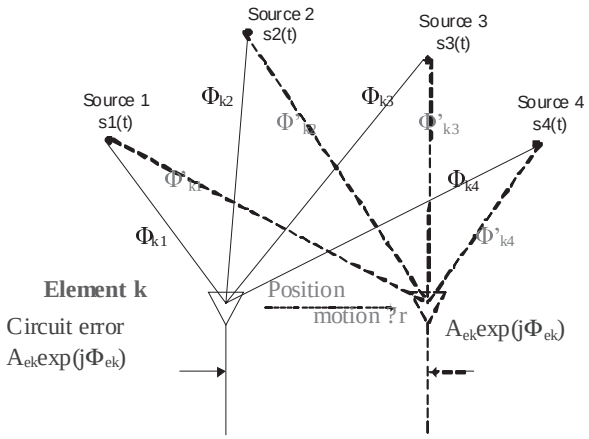

Figure 19. The geometry of the array calibration scheme.

Figure 19 describes the basic idea of this three-dimensional position-calibration algorithm. The four calibration sources are fixed in the positions close to the receiving antenna array. Element *k* is the *k*th element in the smart antenna array, and because of mechanical motion, this element has a three-dimensional position motion Δr. Furthermore, there is circuit phase error, Φ_{ek}, in the branch *k*. $\Phi_{k\xi}$, where $\xi = 1,2,3,4$, is the phase shift created by the distance between sources and element *k*. The calibration scheme operates on three basic assumptions:

1. Four calibration sources are fixed in the near field of the antenna array, but still in the far field of each antenna.
2. Four sources are synchronized, or their phase differences are known.
3. The position motion is very small compared with the distance between sources and the element.

The purpose of this algorithm is to use the phase information to calibrate the position. However, the circuit phase error, Φ_{ek}, always exists in the receiving signals. Here, the phase difference between two sources' signal at the receiving element *k* is calculated so that Φ_{ek} is cancelled.

$$\Delta\Phi_{k\xi} = \left(\Phi_{k\xi} + \Phi_{ek}\right) - \left(\Phi_{k\xi+1} + \Phi_{ek}\right) = \Phi_{k\xi} - \Phi_{k\xi+1}, \tag{2}$$

$$\Delta\Phi'_{k\xi} = \left(\Phi'_{k\xi} + \Phi_{ek}\right) - \left(\Phi'_{k\xi+1} + \Phi_{ek}\right) = \Phi'_{k\xi} - \Phi'_{k\xi+1},$$

where $\xi = 1,2,3$. $\Delta\Phi_{k\xi}$ and $\Delta\Phi'_{k\xi}$ represent the phase differences before and after motion. Due to assumption 3, a linear relationship can be easily found:

$$\left(\Delta\Phi_{k\xi} - \Delta\Phi'_{k\xi}\right) + n_{k\xi} \propto \Delta r\ ,\ \xi = 1,2,3. \tag{3}$$

Clearly, the position motion is proportional to the difference of the phase differences.

Circuit calibration can be realized after position calibration. Since the position error has been calibrated – which means $\Phi'_{k\xi}$ is known, the circuit error information, $A_{ek}\exp\left(j\Phi_{ek}\right)$ can be extracted. Finally, the weighting coefficients can be adjusted for pattern compensation.

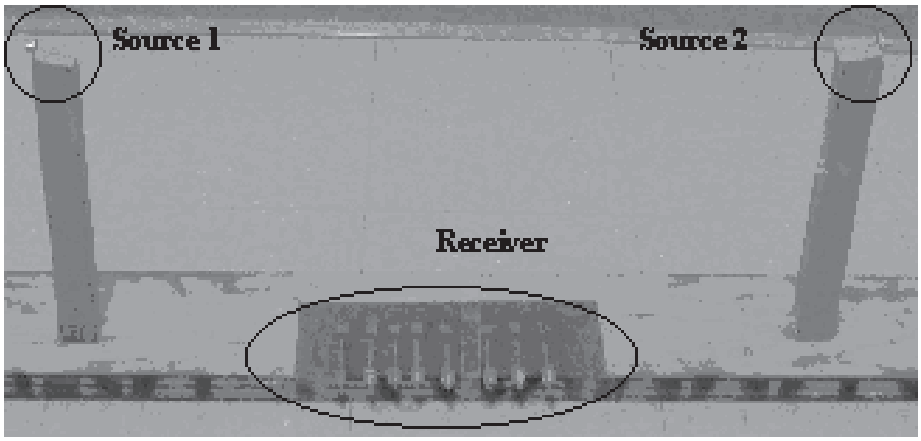

Figure 20. The location of the calibration sources and array.

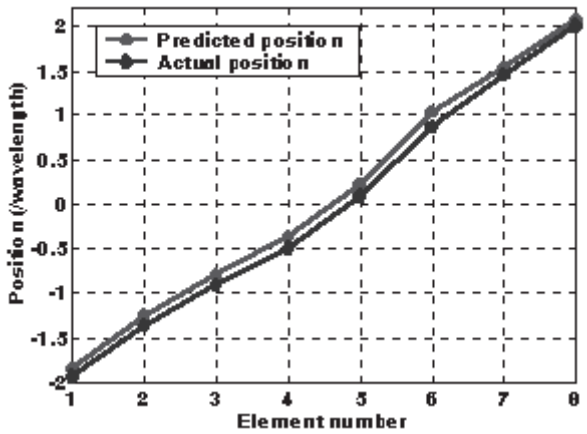

Figure 21. The predicted position and the actual position of each element.

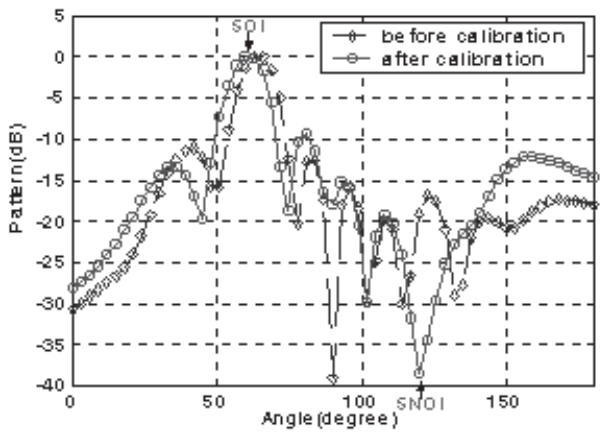

Figure 23. The synthesized beamforming result (SOI: +30°, SNOI: –30°).

As a demonstration of this concept, a system including a receiver and two calibration sources was constructed. This let us determine the one-dimensional position error as well as the circuit error. We assumed that mechanical motion caused the smart-antenna receiver to be distorted from a uniform half-wavelength array to a non-uniform array. As a result, the original weighting coefficients, which were calculated from the uniform array, were no longer suitable for the distorted array. With the two fixed near-field sources, the element spacing error of the non-uniform array could be detected. Then, the new weighting coefficients could be calculated to calibrate the main-beam direction and the null direction.

The two synchronized digital sources generated 100 KHz orthogonal sequences: "0101" and "1010." This was done so that the receiver could distinguish the transmission from each source, independently. These two digital signals were modulated with a synchronized LO carrier at 5.828 GHz. Each receiver element consisted of a 20 dB gain block and a sub-harmonic I/Q mixer. The two near-field calibration sources were fixed 0.483 m away and 0.156 m above of the uniform array's center (see Figure 20).

Figure 21 shows the predicted and actual positions of each element. A common position error existed in each element, and this error was caused by the position error of

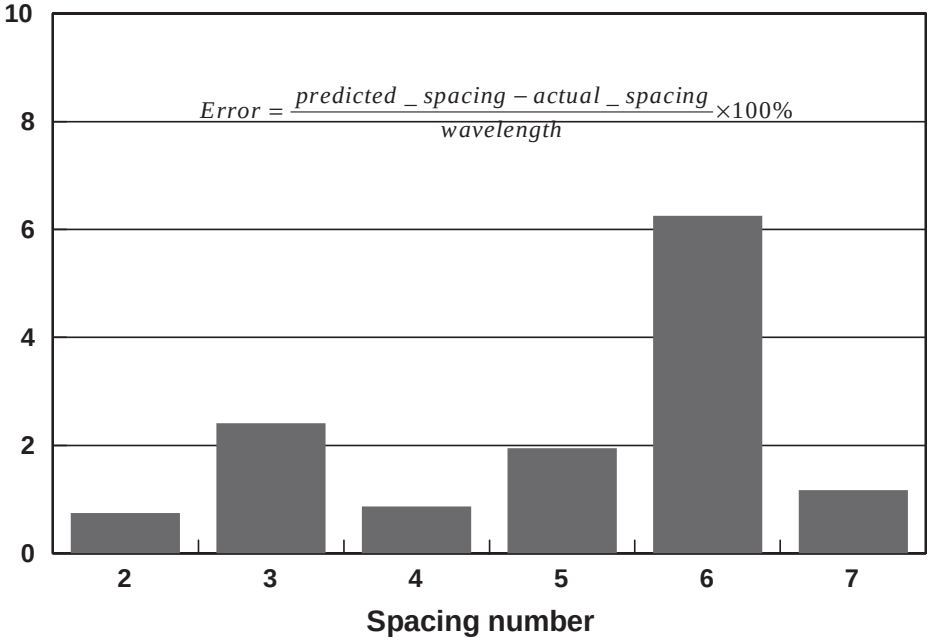

Figure 22. The array spacing error.

the sources. However, this error did not affect the array spacing, which showed that our calibration algorithm is robust enough to determine the calibration sources' position error. Figure 22 shows the spacing error of each element, normalized by the free-space wavelength. The maximum error was only about 6% of the wavelength. Figure 23 shows a synthesized pattern with two far-field signals from 30° and –30°, respectively. Because of the element position error, the original pattern was highly distorted, with the main-beam and null positions shifted. After the position calibration and the new weighting coefficients were applied, the pattern was restored.

Although this calibration technique was demonstrated in just one dimension, it is readily adapted to three dimensions. This can be done by adding calibration sources at different planes, as suggested in Figure 19. Large-scale implementation is also possible by strategically placing calibration sources throughout the large array while satisfying the three conditions mentioned earlier in this section. It is important that the relative positions between calibration sources be known.

6. Conclusion

The active-integrated-antenna design approach has been demonstrated to be an effective concept in modern microwave and millimeter-wave front-end applications. We believe that this technology will also prove useful in the design of highly efficient SPS front-end components.

In addition, an overview of two essential array-control technologies has been presented. Automatic retrodirective beam-pointing technology has been discussed, and several examples were presented. Finally, a novel antenna array calibration scheme has been proposed and tested. This scheme is especially applicable to inflatable antennas deployed in space.

7. References

1. Y. Qian and T. Itoh, "Progress in Active Integrated Antennas and their Applications," *IEEE Transactions on Microwave Theory and Techniques*, **MTT-46**, 1998, pp. 1891-1900.

2. H. Mastumoto, "Research on Solar Power Satellites and Microwave Power Transmission in Japan," *IEEE Microwave Magazine*, **3**, December 2002, pp. 36-45.

3. W. C. Brown, "The History of Power Transmission by Radio Waves," *IEEE Transactions on Microwave Theory and Techniques*, **MTT-**32, September 1984, pp. 1230-1242.

4. W. C. Brown and E. E. Eves, "Beamed Microwave Power Transmission and its Application to Space," *IEEE Transactions on Microwave Theory and Techniques*, **MTT-**40, 6, June 1992, pp. 1239-1250.

5. V. Radisic, S. T. Chew, Y. Qian, and T. Itoh, "High-Efficiency Power Amplifier Integrated with Antenna," *IEEE Microwave and Guided Wave Letters*, **7**, 2, 1997, pp. 39-41.

6. Y. Chung, C. Y. Hang, S. Cai, Y. Qian, C. P. Wen, K. L. Wang, and T. Itoh, "Output Harmonic Termination Techniques for AlGaN/GaN HEMT Power Amplifiers using Active Integrated Antenna Approach," *IEEE MTT-S International Microwave Symposium Digest*, **1**, 2002, pp. 33-436.

7. Y. Chung and T. Itoh, "A New Architecture for AlGaN/GaN HEMT Frequency Doubler Using Active Integrated Antenna Design Approach," Asian Pacific Microwave Conference, 2002.

8. Y. Chung, K. M. K. H. Leong, and T. Itoh, "AlGaN/GaN HEMT X-Band Frequency Doublers with Novel Fundamental Frequency Reflector Scheme," *IEICE Trans. Electron.*, **E86-C**, 8, 2003, pp. 1416-1421.

9. R. Y. Miyamoto, Y. Qian, and T. Itoh, "An Active Integrated Retrodirective Transponder for Remote Information Retrieval-on-Demand," *IEEE Transactions on Microwave Theory and Techniques*, **MTT-49**, 9, September 2001.

10. R. Y. Miyamoto, Y. Qian, and T. Itoh, "A Reconfigurable Active Retrodirective/Direct Conversion Receiver Array for Wireless Sensor Systems," *IEEE MTT-S International Microwave Symposium Digest*, Phoenix, AZ, May 2001, pp. 1119-1122.

11. K. M. K. H. Leong, R. Y. Miyamoto, S.-S. Jeon, Y. Wang, and T. Itoh, "A Frequency Autonomous Retrodirective Array Transponder," *IEEE MTT-S International Microwave Symposium Digest*, **2**, 2002, pp. 1349-1352.

12. A. J. Weiss and B. Friedlander, "**Array Shape Calibration using Eigenstructure Methods,"** *Signals, Systems and Computers, Twenty-Third Asilomar Conference*, **2**, November, 1989, pp. 925-929.

13. B. P. Flanagan and K. L. Bell "Array Self Calibration with Large Sensor Position Errors," *Signals, Systems and Computers, Asilomar Conference*, **1,** October 1999, pp. 925-929.

14. B. C. Ng and C. M. Samson See, "Sensor-Array Calibration Using a Maximum-Likelihood Approach", *IEEE Transactions on Antennas and Propagation*, **AP-44**, 6, June 1996, pp. 827-835.

15. W. Yao, Y. Wang, and T. Itoh, "A Self-Calibration Antenna Array System with Moving Apertures," *IEEE MTT-S International Microwave Symposium Digest*, **3**, June 2003, pp. 1541-1554.

Space Solar Power System Beam Control with Spread-Spectrum Pilot Signals

K. Hashimoto
K. Tsutsumi
H. Matsumoto
N. Shinohara

Abstract

A beam-control system for microwave power transmission with spread-spectrum (SS) pilot signals is developed for the Space Solar Power System (SSPS). The spread-spectrum modulation is used to differentiate pilot signals sent from power receiving sites from other interference signals. The arrival direction is estimated from the phase difference between two antenna elements after despreading the spread-spectrum modulation. This system is a kind of software retrodirective array. This does not respond to fake or wrong signals, and is more reliable for power transmission.

We propose a new system where a single frequency can be used for both monochromatic power transmission and as a carrier of the pilot signal. Antennas are shared for both power transmission and pilot-signal reception. Band-elimination filters (BEFs) and a software synchronization detection are used in this system. The fundamental characteristics of the phase-difference detection are evaluated. The phase-detecting circuit has been shown to work well, and the direction of arrival has been successfully detected while transmitting power from the same antennas. We can use this system to transmit energy in SSPS if we have band-elimination filters that have high attenuation, and amplifiers that have high dynamic range and low noise.

1. Introduction

A Space Solar Power System (SSPS) needs to correctly send a microwave power beam to a receiving site. A pilot signal is sent from the receiving site to the SSPS, and then the power is beamed back to its original arrival direction. This function is the same as a retrodirective antenna system [1, 2]. This type of beam control is one of the most important techniques for the microwave power transmission system used on an SSPS [3, 4]. The objective of this paper is to develop a new microwave power transmission system using a spread spectrum (SS) pilot signal [5-7] with a single frequency for the power transmission and the pilot signal, and to evaluate this system through experiments. This system is based on a software retrodirective response (e.g. [8]). The antennas for power transmission and for the pilot signal share a common frequency band. If the transmitting antennas were removed for the receiving antennas, this could increase the sidelobe levels because of the elements that were removed. However, sharing the antenna makes it possible to set the receiving antennas without removing transmitting antennas. Although dual-frequency antennas could also be used, another frequency spectrum for a pilot signal would be necessary, which might be difficult to obtain.

The SSPS sends a microwave beam from a distance of about 40,000 km in a geostationary orbit to a rectenna (rectifying antenna) site that is a few kilometers in diameter. The required accuracy of the beam control is less than 10^{-4} radian. This cannot be achieved by mechanical attitude control, but it could be achieved by a retrodirective array. A software retrodirective system is adopted, since an accurate direction-finding system and a flexible beam-forming system can be used, and the necessary response speed is not as fast as that for mobile communications.

A new improved spread-spectrum pilot signal receiver was designed. This system has band-elimination filters at the center frequency, before the despread circuit, and a software synchronous detection system. The fundamental characteristics of phase-difference detection between the two channels of the pilot signal have been evaluated.

Kozo Hashimoto, Hiroshi Matsumoto, and Naoki Shinohara are with the Radio Science Center for Space and Atmosphere, Kyoto University, Uji, Kyoto 611-0011, Japan; Tel: +81-774-38-3807; Fax: +81-774-31-8463; E-mail: kozo@kurasc.kyoto-u.ac.jp.
Koji Tsutsumi is now at the Information Technology R&D Center, Mitsubishi Electric Corporation, 5-1-1 Ofuna, Kamakura, Kanagawa 247-0056, Japan.

This invited paper is part of the Special Section on Space Solar Power Systems. An oral version was originally presented at the 2003 Japan-US Joint Workshop on Space Solar Power System (JUSPS'03), July 3-4, 2003, Kyoto University, Uji, Kyoto, Japan.

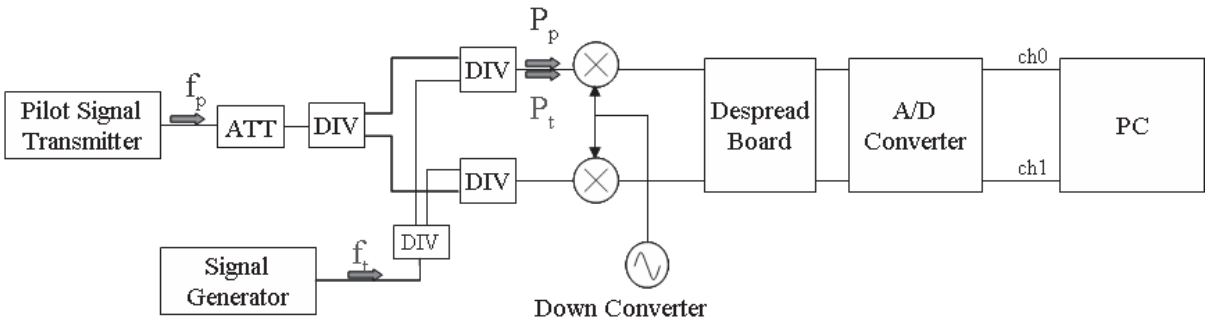

Figure 1. A block diagram of the wired experiment on interference effects.

We have experimented using an eight-element array antenna. In this experiment, the direction of arrival was successfully detected, even while transmitting power from the same receiving antennas. Application of this system to a model SSPS is also discussed.

2. Interference Characteristics of Spread-Spectrum Pilot-Signal Receiver

The effects of monochromatic interference on spread-spectrum signal reception was tested as shown in the diagram in Figure 1. An M-series pseudo-noise (PN) code with a length of 1023 bits was used for spreading at the chip rate of 1.25 M chips/s (Mcps). Although the carrier frequency of this pilot signal, f_p, was 904 MHz in this experiment, this was not essential. The spread-spectrum pilot signal was attenuated (ATT: attenuator) and divided into two (DIV: divider), and each signal was connected to one of the two inputs of each down-converter. The output of a signal generator – which simulated a transmitter with a frequency f_t as interference – was divided into two, and each component was connected to the other input of each down-converter, as interference. They were down-converted to 10.7 MHz, despread, down-converted to 10 kHz, and A/D converted for processing by a PC (personal computer). The second down-converter was used before the A/D converter in order to decrease the sampling frequency, although this is not shown in the figure. The attenuators determined the intensity difference between the pilot signal and the transmitter. The phase difference between the two gave information about the direction of arrival (DOA). The two inputs were in phase in the present test. The phase difference was measured by Fourier analysis of the A/D-converted signals. Figure 2 shows the despread circuit, the center frequency of which was 10.7 MHz. The pseudo-noise code for the despreading could be shared by more than two inputs if their time difference was much smaller than the length of one bit of the code. This would simplify the system. The sliding correlator and DLL (delay locked loop) were used for initial synchronization and tracking, respectively.

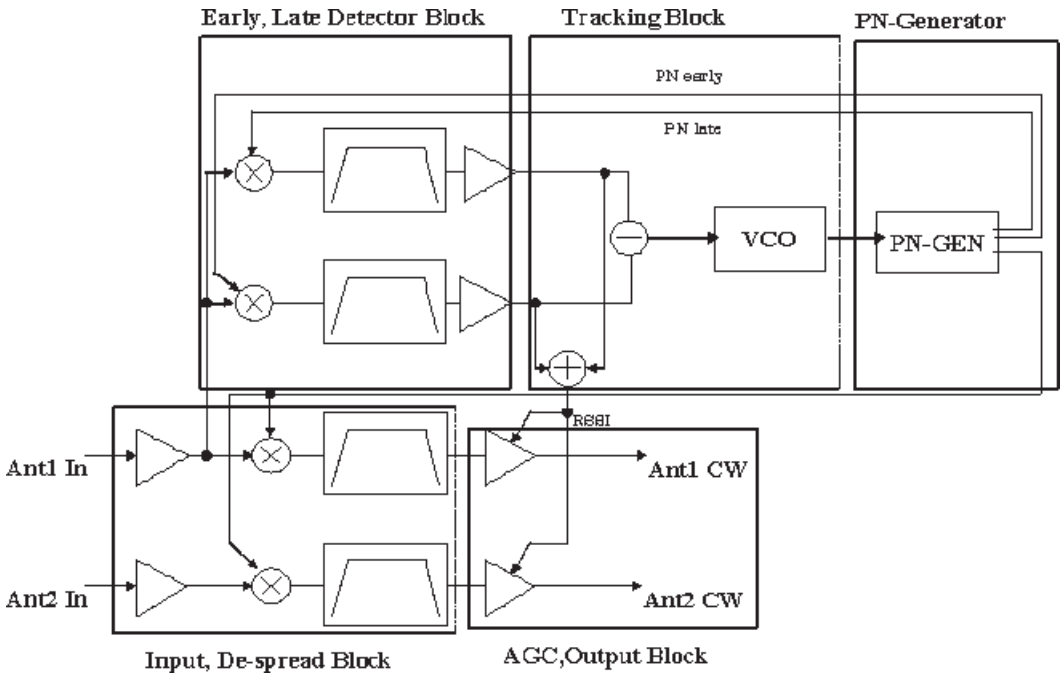

Figure 2. The despreading board for a spread-spectrum signal.

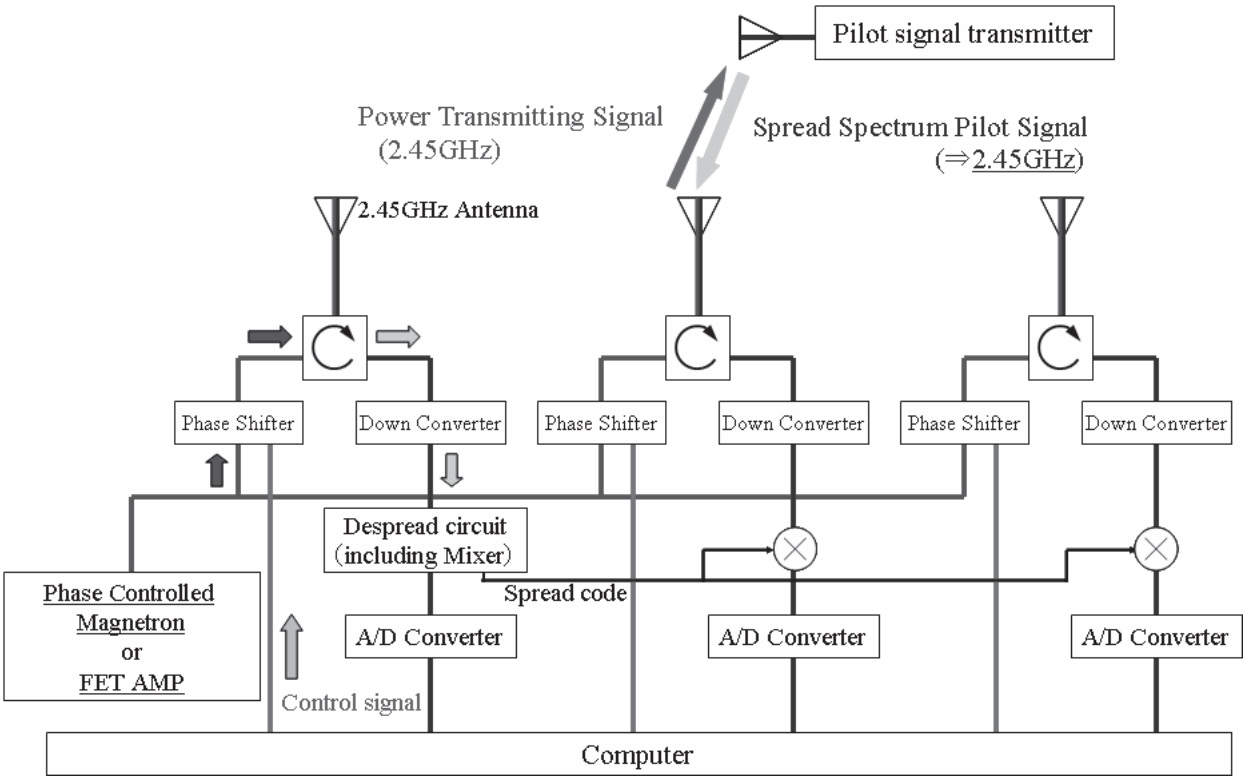

Figure 3. The system configuration.

3. Spread-Spectrum Retrodirective Transmission System

Figure 3 shows a retrodirective transmitting system. Three out of eight channels of the system are shown. This system receives a spread-spectrum pilot signal, detects the direction of arrival, and transmits a power beam in the desired direction by software control. Both the power transmitting and receiving frequencies are equal to 2.45 GHz. This frequency is selected since most SSPS models use the ISM frequency band for energy transmission. The transmitting power is basically generated by a phase-controlled magnetron (PCM) [9] or sent from FET amplifiers. This is sent to each antenna through a phase shifter, for beam steering, and to a circulator. A signal generator is used as the transmitter, since quite low phase noise is required for better phase-difference measurements. The transmission direction is fixed to the broadside in the present experiment.

The received signal goes through the circulator, is down-converted to 10.7 MHz, despread, down-converted to 10 kHz, and A/D converted to measure the phase difference by Fourier analysis. Because a direct-sequence spread spectrum is used for the pilot signal, it does not respond to erroneous signals and is more reliable under noise. The despread circuit supplies the PN code for despreading to other mixers that share the code. This works under multiple pilot signals [6, 7], and is a useful technique even for a single receiving site. M-series pseudo noise codes up to a length of 1023 ($= 2^{10} - 1$) bits can be used.

4. Basic Characteristics in a Wired Experiment

The basic characteristics of the phase-difference detection were evaluated by applying both spread-spectrum pilot and transmitter signals to the down-converters through combiners (DIVs were used). In order to make the phase differences one of the pilot signals was put through a phase shifter. The root-mean-square error (RMSE) of the phase difference between the two outputs was measured as a function of the ratio of the transmitting power to the pilot

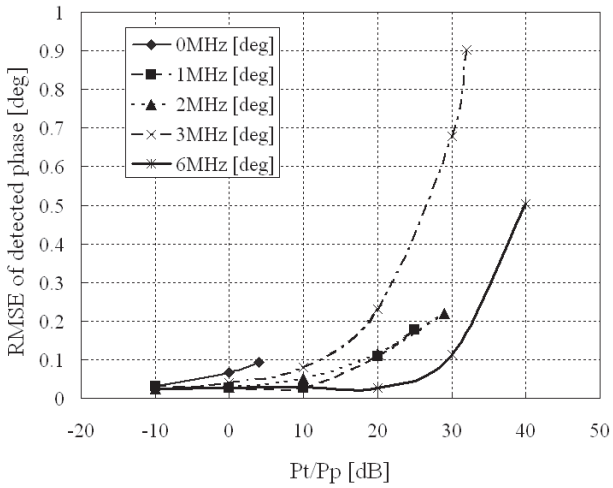

Figure 4. The root mean square errors (RMSE) of the phase difference as a function of the power ratio.

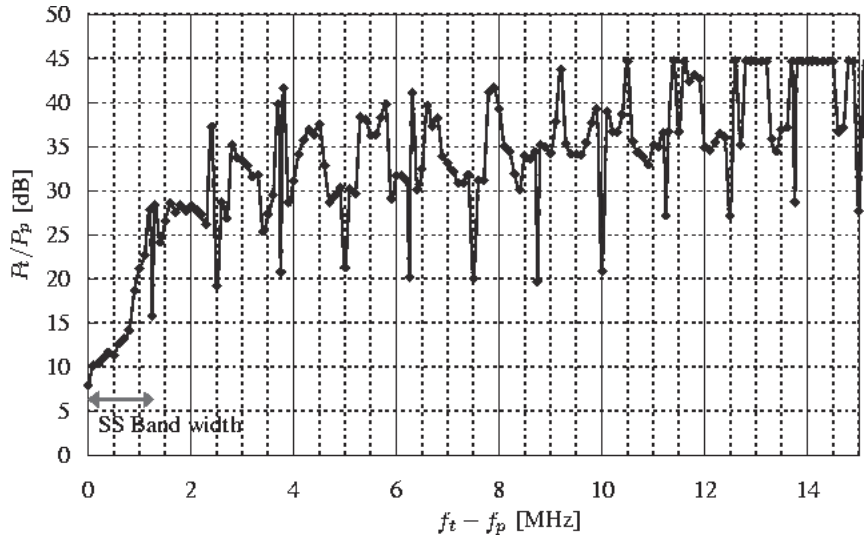

Figure 5. The limits of the spread-spectrum synchronization.

power (P_t/P_p). This ratio was controlled by the attenuator. The results are shown in Figure 4. The parameters were the frequency differences ($f_t - f_p$) of 0, 1, 2, 3, and 6 MHz, as indicated in the legend. The RMSE was generally less than 0.1°. This became larger as P_t increased. The lines stop after the limit where spread-spectrum synchronization could not be locked. The threshold power ratio of the interference (transmitter) power, P_t, over the pilot-signal power, P_p, is shown in Figure 5, as a function of the frequency difference. The vertical axis shows P_t/P_p, which was limited to 45 dB due to the output limit of the oscillator used. P_t/P_p was less than 10 dB if the frequency was close, but this was more than 25 dB if the difference was larger than the chip rate (1.25 Mbps). This became smaller, however, if the difference was equal to one of the harmonics of the chip rate.

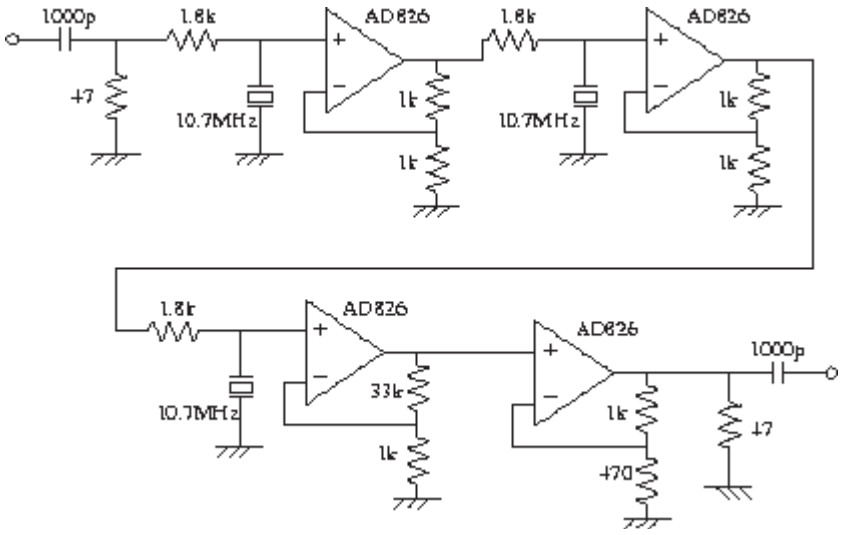

Figure 6a. The band-elimination filter.

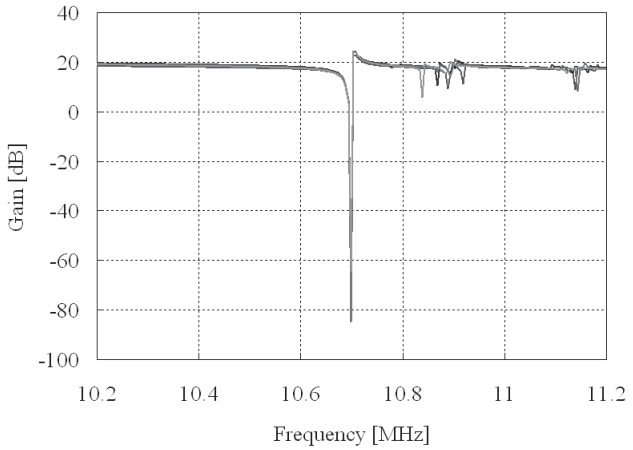

Figure 6b. The band-elimination filter's characteristics.

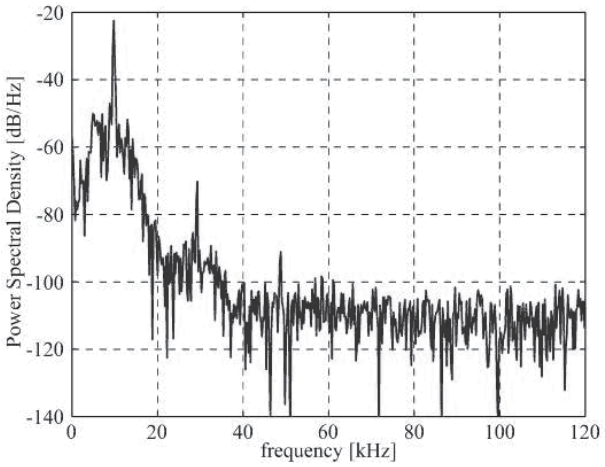

Figure 7a. The spread-spectrum signal spectra when the system is synchronized.

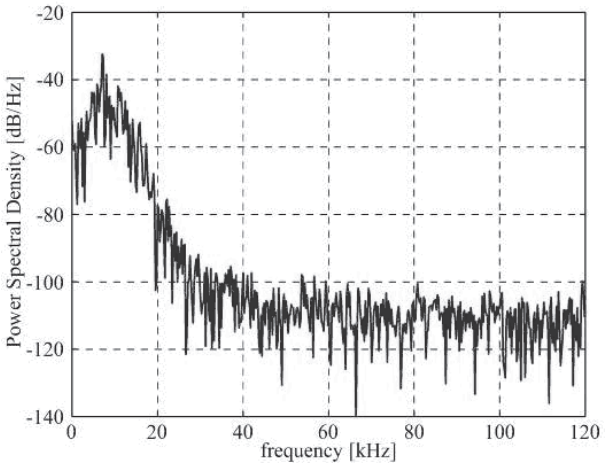

Figure 7b. The spread-spectrum signal spectra when the system is not synchronized.

5. Band-Elimination Filters and Software Synchronization Detection System

Band-elimination filters at 10.7 MHz were inserted between the down-converter and the despread circuit in each channel. The circuit is simple and convenient, as shown in Figure 6a. The series resonance of a crystal oscillator was used as a filter. The total gain was 20 dB, and the attenuation at the center was 60 dB, as shown in Figure 6b. The noise figure of this circuit was not so good, since the loss of the attenuator caused by the crystal oscillator was large.

When the intensity of the interference signal is large, the indicator of the synchronization in the tracking circuit (the delay locked loop, DLL) is reset and the sliding correlator starts to slide, since the received signal-strength indicator (RSSI) is used as a lock indicator. The software synchronous detection system which was used as a better lock indicator works as follows. The despread signals at 10.7 MHz were A/D converted after down conversion to 10 kHz. Figures 7a and 7b show the frequency spectra of A/D-converted signals when the system was synchronized and not synchronized, respectively. A sharp peak at 10 kHz was observed in Figure 7a, but not in Figure 7b. As a criterion for synchronization detection, the maximum value of the spectrum and the ratio of the first two peak levels were used.

Figure 8 shows the effect of these revisions. The two lines starting from RMSE < 0.1 show the RMSE without the band-elimination filter for $f_t - f_p = 0$ and 6 MHz, for reference. The other two lines, marked with ¦ and ?, show the RMSE with the band-elimination filter, and with the band-elimination filter and the software-synchronization detection

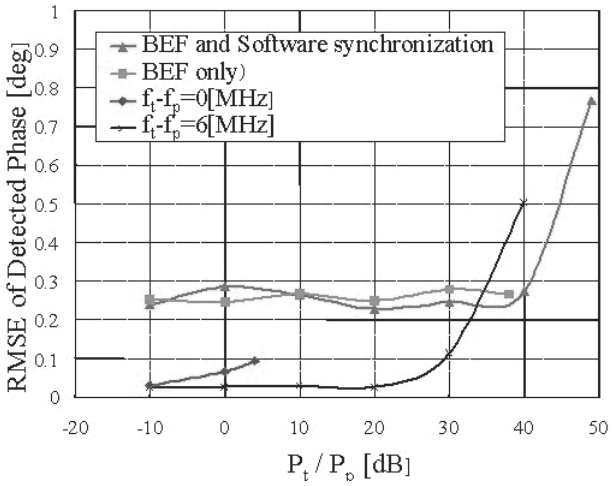

Figure 8. The effect of the band-elimination filer (BEF) on the root mean square error (RMSE).

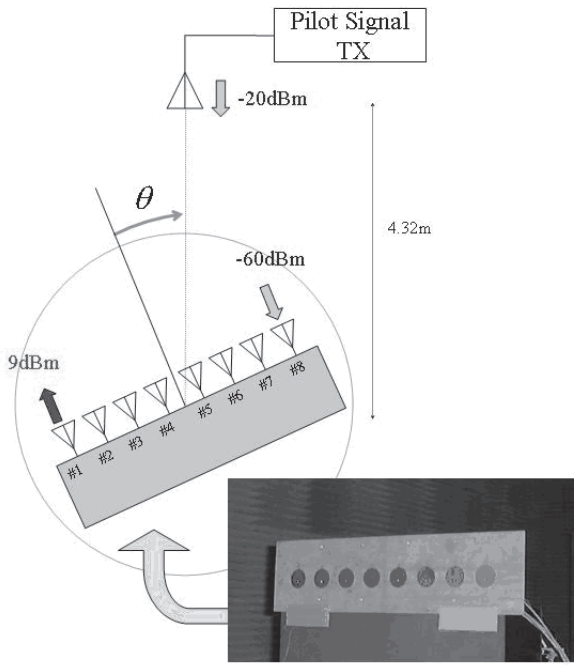

Figure 9. The setup for the direction-of-arrival (DOA) measurement.

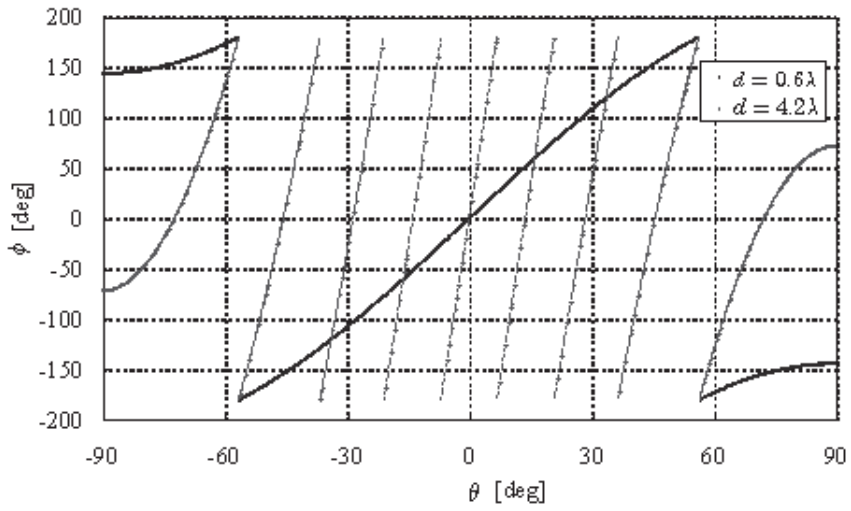

Figure 10. The relationship between the arrival direction and the phase difference.

system, respectively. The lines stop after the limit where spread-spectrum synchronization could not be locked. Synchronization was attained up to a ratio of 40 dB if software synchronization was used. The bad noise figure caused the increase in the RMSE.

6. Direction-of-Arrival Detection

The direction of arrival (DOA) was measured using an eight-element CMSA (circular microstrip antenna) array with 0.6λ spacing, as shown in Figure 9. The system block diagram is shown in Figure 3. The distance between the pilot transmitter and the system was 4.32 m. Both the pilot signal and the power transmission used the same center frequency of 2.45 GHz. The output power of the pilot was –20 dBm from a dipole, and the M-series pseudo-noise code with a length of 1023 bits was used. The power of the transmitting signal was 9 dBm at each antenna. The reflected powers were from –7 to –12 dBm, and the received power of the pilot signal was about –60 dBm at each input of the down-converter. The difference was about 50 dB.

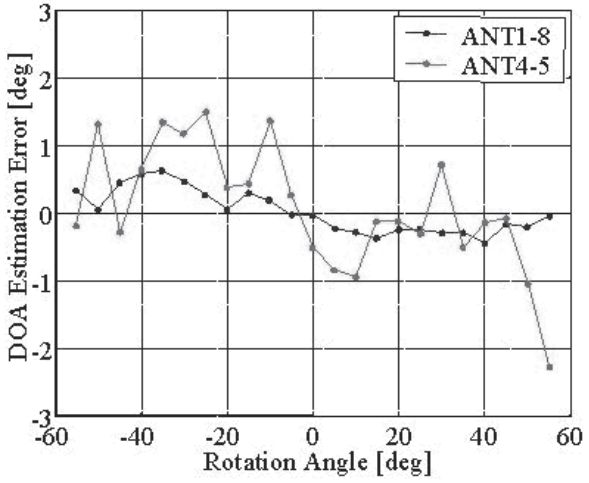

Figure 11. The direction-of-arrival measurement.

The relationship between the arrival direction, θ, and the phase difference, ϕ, is shown in Figure 10. They have the following relationship if the distance between the two antennas is d and the wavelength is λ:

$$\sin\phi = (2\pi d/\lambda)\sin\theta \cdot$$

For $d = 4.2\lambda$ (#1 and #8), the arrival direction was obtained with high resolution, but ambiguities existed. On the other hand, for $d = 0.6\lambda$ (#4 and #5), no ambiguities existed, but the resolution was low [10]. Figure 11 shows the direction-of-arrival estimation error as a function of the rotation angle or arrival direction. When two adjacent antennas, #4 and #5, were used, the errors were about ±1.5°. On the other hand, when #1 and #8 were used, the errors were about ±0.4° and they became much better, as expected. Although the latter antenna distance was so large that an ambiguity of angles could exist, this could be removed using the result of the former case.

7. Discussion and Conclusions

It was shown that the direction of arrival could be correctly measured even if power was transmitted at the same frequency as that of the pilot signal. This system worked well even in the presence of an interference signal with an intensity that was 50 dB higher than the received pilot signal. The angular accuracy of the detected direction was about ±0.4°. We can use this system to transmit energy in an SSPS when we use a band-elimination filter that has a high attenuation, and an amplifier that has a large dynamic range, say, more than 80 dB. The problem of the present system is a bad noise figure, due partly to the very simple circuit. More sophisticated filters are shown in [11]. It is expected that a better P_t/P_p ratio could be attained by optimizing the circuit. Although the band-elimination filters were inserted in the IF stage in the present experiments, the filtering should be done in an earlier stage at a microwave frequency.

P_t (Transmitter power)	60 dBm
G_t (Antenna gain, Diameter $D = 10$ m, $\eta = 0.7$)	54 dBi
EIRP	114 dBm
Free-space loss (GEO, 5.8 GHz	119 dB

Table 1. Pilot signal levels.

This system can be scaled to any size where the plane of the antenna can be assumed to be flat and the antenna's distortion is negligible, say less than 0.1λ . The number of receiving antennas for the pilot signal would be much smaller than the number of transmitting antennas for this size. The large array would be composed of a lot of medium-sized units, say with a diameter of several meters.

In an SSPS model proposed by NASDA (National Space Development Agency of Japan) [12], a 1 kW pilot signal is transmitted from a 10 m dish to the SSPS in geostationary orbit (GEO). The EIRP (effective isotropic radiated power) of the pilot signal is 114 dBm, and the expected power at the geostationary orbit is –80 dBm under the gain of 6 dBi by a circular microstrip antenna (CMSA), as shown in Table 1. The transmitted power from each antenna element is small, although the total power is quite large (1 GW). This is because the number of elements can be as large as 8 billion, when the diameter of the array is 2 km, the frequency used is 5.8 GHz, and the element spacing is 0.5λ . The effects of surrounding antennas are difficult to calculate since their phases are not necessarily the same, and they are in the end-fire direction. Only one output is taken into consideration in the present analysis. If the transmitting power is 22.4 dBm (0.175 W) per antenna, P_t/P_p is 102.5 dB, and so a revision of 33.5 dB is necessary. It is expected that this system will be used after further improvement. Although two polarizations could be used for transmission and reception, a dual-polarization antenna would have to be used. It would be much simpler if the frequencies are different in a frequency band and diplexers can be used.

8. Acknowledgments

We appreciate the careful reading of the manuscript by Prof. Patrick Collins. This research was partially supported by the Ministry of Education, Science, Sports and Culture, Grant-in-Aid for Scientific Research and the 21st COE program "Establishment of COE on Sustainable Energy System" at Kyoto University.

9. References

1. D. L. Margerum, "Self Phased Arrays," in R. C. Hansen (ed.), *Microwave Scanning Antennas, Volume III, Array Systems*, New York, Academic Press, 1966.

2. R. Y. Miyamoto and T. Itoh, "Retrodirective Arrays for Wireless Communications," *IEEE Microwave Magazine*, **3**, 1, March 2002, pp. 71-79.
3. H. Matsumoto, "Microwave Power Transmission from Space and Related Nonlinear Plasma Effects," *Radio Science Bulletin*, No. **273**, June, 1995, pp. 11-35.

4. H. Matsumoto, "Research on Solar Power Station and Microwave Power Transmission in Japan: Review and Perspectives," *IEEE Microwave Magazine*, **3**, 4, 2002, pp. 36-45.

5. Y. Fujino, M. Ishii, and M. Fujita, "Fundamental Experiment of an Incident Angle Detection System for Power Transmission Beam Control of a Stratosphere Radio Relay System," *Trans. IEICE B-II*, **J80-B-II**, 9, 1997, pp. 800-804 (in Japanese).

6. K. Hashimoto and M. Iuchi, "Direction Finding System for Spread Spectral Pilot Signals from Multiple Microwave Power Receiving Sites," *Proceedings ISAP2000*, Volume 3, 2000, pp. 1199-1202.

7. K. Hashimoto, K. Tsutsumi, and H. Matsumoto, "Direction Finding System for Multiple Microwave Power Receiving Sites by Spread Spectral Pilot Signals," *IEICE Trans. Commun.*, 2004 (submitted).

8. M. Omiya and K. Itoh, "A Fundamental System Model of the Solar Power Satellite, SPS2000," *Proceedings of ISAP1996*, Volume 2, 1996, pp. 417-420.

9. N. Shinohara, J. Fujiwara, and H. Matsumoto, "Development of Active Phased Array with Phase-Controlled Magnetrons," *Proceedings of ISAP2000*, Volume 2, 2000, pp. 713-716.

10. S. E. Lipsky, *Microwave Passive Direction Finding*, New York, John Wiley & Sons, 1987.

11. L. B. Milstein, "Interference Rejection Techniques in Spread Spectrum Communications," *Proc. IEEE*, **76**, 6, 1988, pp. 657-671.

12. H. Nagayama, Y. Saito, M. Mori, and H. Matsumoto, "Summary of Studies on Space Solar Power Systems of the National Space Development Agency of Japan," IAF Congress, IAF-01-R.1.04, Toulouse, France, 2001.

Development of a Retrodirective Control Transmitter for Wireless Power Transmission

F.E. Little, S.J. Kokel
C.T. Rodenbeck
K. Chang, G.D. Arndt
P.H. Ngo

1. Background

In 1990, the world demand for power exceeded 10 terawatts (10×10^{12} W) thermal, with about 30% of the thermal energy being used to produce electricity [1]. In 1990, the nations of the Organization for Economic Cooperation and Development (OECD) used more than two-thirds of the world's total electrical power of >10.5 terawatt-hours [2]. However, beginning in 2015, the United States Department of Energy (DOE) has forecast that the non-OECD countries' share of electric power usage will exceed 50%, and will continue to rise [2]. It is estimated that energy demand will increase by more than 60% from the present 382 quads (1999) to 612 quads in 2020 [1 quad $=10^{15}$ Btu $=2.93\times10^{11}$ kilowatt-hours]. Electricity, with an annual growth rate of 2.7% between 1999 and 2020, will outpace the growth of other energy use, reaching more than 22.4 terawatt-hours [2].

Solar power is a reality. Apart from nuclear fission (including geothermal energy, mostly a regional energy source), virtually all energy produced is, or was, dependent wholly or partly on solar energy. Fossil fuels, such as coal, oil, and natural gas, are all derived from the conversion of biological material originally created by organisms using sunlight to power photosynthetic storage of energy in chemical reactions. Hydroelectric power depends on the thermal conversion of sunlight to evaporate water from oceans, and to provide rain or snow runoff at higher elevations. Winds arise from differential solar heating of the Earth's surface. Obtaining sufficient energy for economic development for the future means concentrating on those sources with guarantees of continuing availability. In addition to the source, the quality of energy is important. In general, the highest quality and most useful energy is electrical.

Today, increasing numbers of photovoltaic and other solar-powered installations are in service around the world and in space. These uses range from primary electric power sources for satellites, remote site scientific experiments, and villages in developing countries, to supplementing the commercial electric grid and providing partial power for individual businesses and homeowners in developed countries. In space, electricity generated by photovoltaic conversion of solar energy is the mainstay of power for low-Earth and geostationary satellite constellations. Still, for all its acceptance as a benign and environmentally friendly energy source, terrestrial solar power has yet to be seriously considered as a viable technology for providing base electrical-generating capacity. The obvious reason is that sunshine on Earth is too unreliable. In addition to the diurnal and seasonal cycles, inclement weather reduces the average daily period and intensity of insolation. However, the sun shines constantly in space. The challenge is to harvest and transmit the energy from space to Earth.

The Solar Power Satellite (SPS) has been hailed by proponents as the answer to future global energy security, and dismissed by detractors as impractical and uneconomic. The idea for a solar power satellite that would help meet the growing energy needs of developed and developing nations was conceived by Dr. Peter Glaser in 1968 [3]. Dr. Glaser's

F. E. Little is with the Center for Space Power, MS3118, Texas A&M University, College Station, TX 77843-3118 USA; Tel: +1 (979) 845-8768; Fax: +1 (979) 847-8857; E-mail:f-little@tamu.edu
S. J. Kokel (MS3128; Tel: +1 (979) 845-5409; Fax: +1 (979) 845-6259; E-mail: samuel-kokel@tamu.edu), C. T. Rodenbeck (MS3128; Tel: +1 (979) 845-5409; Fax: +1 (979) 845-6259; E-mail: croden@ee.tamu.edu), and K. Chang (MS3128; Tel: +1 (979) 845-5485; Fax: +1 (979) 845-6259; E-mail: chang@ee.tamu.edu) are with the Electrical Engineering Department at Texas A&M University. G. D. Arndt (Tel: +1 (281) 483-1438; Fax: +1 (281) 483-5830; E-mail: g.d.arndt@nasa.gov.) and P. H. Ngo (Tel: +1 (281) 483-7990; Fax: +1 (281) 483-5830; E-mail: phong.h.ngo1@jsc.nasa.gov) are with the Lyndon B. Johnson Space Center, Code EV4, 2101 NASA Road 1, Houston, TX 77058 USA.

This invited paper is part of the Special Section on Space Solar Power Systems. An oral version was originally presented at the 2003 Japan-US Joint Workshop on Space Solar Power System (JUSPS'03), July 3-4, 2003, Kyoto University, Uji, Kyoto, Japan.

concept was for orbiting satellites converting solar energy and transmitting the energy to Earth via a radio-frequency energy beam. Solar power satellites, placed in geosynchronous equatorial orbit 35,800 km above Earth's surface, would be continuously illuminated for most of the year. As a result of the orbit location, the amount of sunlight shining on the satellite during the year would be five times more than is available to any terrestrial location. At geosynchronous orbit, satellites have the same rotational period as the Earth and are therefore fixed over one location at all times, which would enable the satellite to deliver almost uninterrupted power to a ground receiving site.

Because the Earth's axis tilts 23° from the plane of the ecliptic, the satellites would pass either above or below the Earth's shadow, except during the spring and fall equinox periods. During the 22 days prior to equinox, the satellite would experience a lengthening daily period of eclipse to a maximum of 72 minutes. The period of eclipse would then fall during the 22 days following equinox. The eclipse period would occur near local midnight, when energy demand is at a minimum. The equinox eclipses would result in about a 1% decrease in the amount of solar radiation reaching the solar power satellite and, hence, a 1% scheduled outage rate during the year.

Wireless power transmission is an enabling technology that permits energy users to be physically decoupled from energy generators. The most obvious and ubiquitous example of wireless electromagnetic energy transmission is the solar radiation that is harvested in space for satellite use, as well as here on Earth. Recent solar power satellite system designs have included laser power transmission as an option [4]. This paper will concentrate on microwave energy transmission from space for the production of electricity on Earth.

2. Major Technical Hurdles to Microwave Power Beaming

Several important technical hurdles to the commercial (i.e., cost-competitive) application of wireless power transmission are beyond the scope of this paper. This paper will concentrate on those technical hurdles directly related to the transmission, reception, and retrodirective control of wireless power.

Two issues directly related to microwave power transmission are more of a political than a technical nature, but will have a major impact, particularly on space-to-Earth and near-Earth space-to-space wireless power transmitting systems. These are allocation of radio-frequency spectrum for microwave power beaming (with the attendant harmonic and near-frequency interference issues), and allowable energy density of the power beam. In the case of frequency allocation, for instance, creation of a base power-beaming frequency with allocated harmonic bands at integer spacing above the fundamental would eliminate the necessity for higher harmonic suppression to avoid interference with astronomy or communications bands. Then, harmonic suppression becomes a cost tradeoff instead of a mandate. Such a reallocation of spectrum would necessitate great inconvenience and economic hardship to those already using the desired frequencies.

The issue of beam energy density has implications for total energy throughput and transmitting and receiving antenna size, and, hence, economic viability. The maximum power density at the ionosphere (to avoid ionosphere heating) of 230 W/m^2, proposed for the 1978 system definition study [5], was an arbitrary limit defined by the transmitted power, aperture dimensions, and beam characteristics (10 dB Gaussian taper, <10 W/m^2 at the rectenna edge, and <1 W/m^2 at the edge of the exclusion fence). The limit was considered to be "safe" for transient biota, and was deemed low enough to not interact significantly with the ionosphere. Subsequent research and computer simulations have shown this limit to be very conservative [6]. This limit could pose severe constraints on aperture sizing and energy throughput to a ground station. In addition to being a potential hazard to the atmosphere and biota, the electric field created by the microwave beam could affect electronic systems. At low-Earth orbit, for example, a 5.8 GHz power transmission beam would have a power flux density of >90 W/cm^2 for an electric field strength of ~ 180 V/m, compared to the NASA ISS test level of 60 V/m [7].

2.1 Beam Control and Steering

Because it is necessary to capture the transmitted beam (both for economic and for health and safety reasons), it is necessary to be able to accurately aim it at the target. This is done by sending a pilot beam from the receiving antenna, which can be used as a "guide" for the transmitted beam. For high operating efficiency, it is also necessary that the beam be transmitted as a spherical converging wavefront (the individual transmitting elements that form the beam must be in proper phase). Such a system is called a retrodirective phased array. Although much of the technology for such a system has been developed, a beam-steering retrodirective phasing system, which takes phase information from the incoming pilot beam and uses the information to control (shift) the phase of each transmitting element in the array to produce a phased return power beam, has not been developed and demonstrated at pilot scale for wireless power transmission applications.

In addition to active control of the direction and quality of the beam during transmission, it may become necessary during emergency conditions to interrupt the beam to assure the safety of people and equipment (aircraft and satellites) that pass through the beam. A system to safeguard people and spacecraft or aircraft during an emergency intrusion into the beam-exclusion zone might be handled in several ways. These range from interrupting power to the transmitting array (very hard on the satellite

power management and distribution systems, and on the transmitting array electronics) to defocusing the beam through dispersing the beam by disrupting the phase conjugation provided through the retrodirective phase shifters by the pilot beam.

One of the lessons learned from the Solar Power Satellite (SPS) studies in the late 1970s and early 1980s was that the ability to automatically prevent beam wander from the center of the rectenna was very important for public acceptance. The concept of a retrodirective phase-control system was both technically and publicly acceptable.

2.2 Transmission System Efficiency

The challenge to high transmission efficiency is to assure that the greatest percentage of the energy radiated is at a useful frequency and falls within the physical rectenna. This is accomplished through an appropriate distribution of transmitting elements and of the energy density over the antenna (antenna spacing and taper) to reduce physical beam losses (sidelobe, backlobe, and grating-lobe losses), and efficient filtering of the power amplifier to eliminate enough of the high-frequency harmonics to satisfy international radio wave interference regulations, while maintaining a high percentage of power in the fundamental frequency (insertion losses). In addition to decreasing transmission efficiency, the physical beam losses present a safety and an electromagnetic interference hazard to people and electronics at a distance from the receiving site. Higher-order harmonics might possibly interfere with other spectrum use, such as telecommunications and radio astronomy. While not dangerous, such interference could lead to suspension of broadcast rights with attendant severe economic loss.

2.3 Conversion Efficiency

The transmitted microwave power will be captured and converted to electric power [8, 9]. Experiments conducted in the 1970s by Mr. William Brown at 2.45 GHz demonstrated greater than 90% conversion efficiency for a small rectenna array under ideal laboratory conditions [8], and greater than 85% conversion efficiency during a large multi-kilowatt field demonstration [10]. Laboratory experiments have been conducted on higher-frequency rectenna elements with reported efficiencies of greater than 80% at 5.8 GHz [11, 12], and 74% at 35 GHz [13, 14]. Canadian researchers have investigated methods to suppress re-radiation (particularly of harmonics) from the rectenna at 2.45 GHz [15]. Japanese researchers have shown that locating the rectifying diode and filter circuit behind the antenna's ground plane gives a substantial reduction in harmonics [16, 17], and have studied the effect of different element connection schemes on overall rectenna efficiency [18, 19]. In addition to further work on individual element efficiency and harmonic suppression, research must be conducted to develop the most efficient method to efficiently harvest power from the nonuniform energy density field in the transmitted beam, and to convert it to electricity. Being able to transmit a beam with a more uniform power density at the rectenna could simplify conversion.

2.4 Retrodirective System Design Criteria

A major consideration for the design of the transmitter system is to deliver the beam reliably to the ground station. For most geostationary solar power satellite designs, the transmitter is fixed in a nadir-pointing configuration, with the solar collector arranged north-south (relative to the Earth) and free to rotate to track the sun. The antenna can be roughly aligned to point at the ground station, and the retrodirectively controlled phased array can be used to center the beam on the target, and to prevent beam wander. To be commercially successful, the SPS must be able to deliver electrical energy at a cost that is competitive with terrestrial generation. Thus, the design of a transmitting system should be optimized to be as efficient as possible, while meeting the requirements for beam quality (reduced higher harmonics, low sidelobes and grating lobes, etc.), and safety.

Areas where technical tradeoffs affect cost and efficiency are beam shape and the unit size and the number of phase-shifted transmitting elements. Beam shape (power distribution over the transmitter) will affect antenna coupling and conversion efficiency, and sidelobe levels. The size and number of phase-shifted transmitting units will affect cost and design complexity, as well as beam steering and grating-lobe formation. In general, the more elements that are phase-controlled, and the closer their spacing, the greater the steering angle that can be achieved while maintaining low grating lobes. However, that is achieved at a cost to system efficiency, because phase shifters, particularly those that operate on the antenna element after the power amplifier, can cause significant insertion loss and overall beam attenuation.

2.5 Antenna and Subarray Effects on Sidelobe and Grating-Lobe Levels

The beamwidth of the downlink power beam is approximately 1 arc minute, and it is always focused at the center of the ground rectenna, using the retrodirective phasing scheme. This phasing technique prevents the power beam from wandering as the transmitting antenna goes through normal variations in attitude. An uplink pilot beam is transmitted from the center of the rectenna to the satellite. Each subarray has its own RF receiver and associated electronics for processing the uplink pilot beam. A phase reference signal, which is distributed to each subarray from

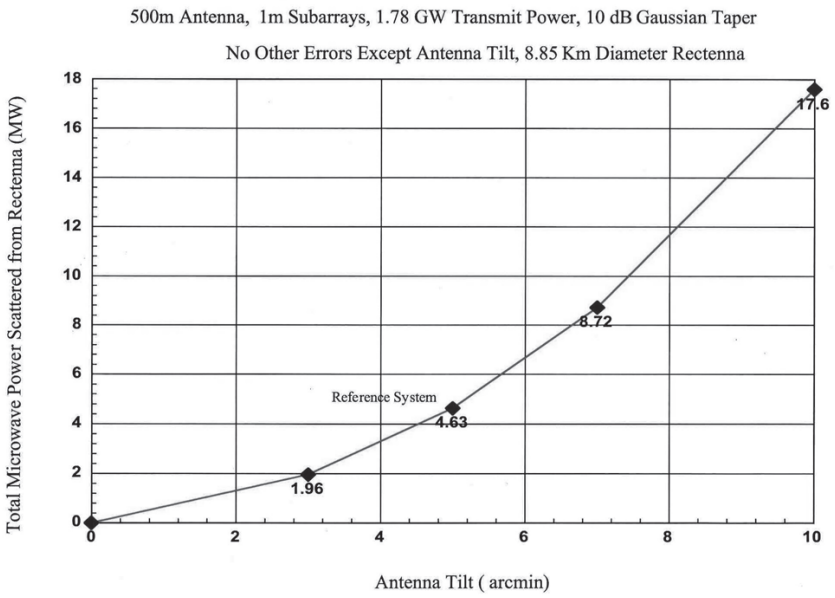

Figure 1. The scattered power due to antenna tilt.

a central processor, allows the phase angle of the pilot beam to be measured and its conjugate formed. This phase conjugate, which is unique to each subarray, is applied to the RF power amplifier within the subarray. The individual downlink beams from each subarray arrive in phase at the center of the rectenna, hence the term retrodirective.

Without electronic beam steering, it would be impossible to hold the transmitter antenna in an attitude to maintain the main beam focused on the rectenna. Even with retrodirective phase control for beam steering, there are still very stringent requirements for the allowable antenna tilt and subarray tilts within the antenna. These tilts are determined by the microwave system parameters. From system studies over the past several years, a reference system has been developed, as follows:

- 500 m diameter antenna
- 10 dB Gaussian Taper
- 1 m subarrays
- 1.78 GW of transmit power
- Frequency = 5.8 GHz (in a 150 MHz Industrial, Scientific and Medical (ISM) band
- Rectenna diameter = 8.85 km
  - Rectenna collection efficiency (coupling efficiency) = 95.5% (with no errors)
  - Collection efficiency with errors = 88%
- Error Parameters
  - Phase jitter = 10° rms
  - Amplitude error = ±1 dB
  - Number of subarray failures = 2%
- Tilts: the allowable tilts for an allowable grating-lobe power-density level of 0.01 mW/cm^2 are determined mainly by the antenna tilt
  - Antenna = 5 arc minutes
  - Subarray = 10 arc minutes

The effects of these system parameters upon allowable antenna and subarray tilts as misalignments have been

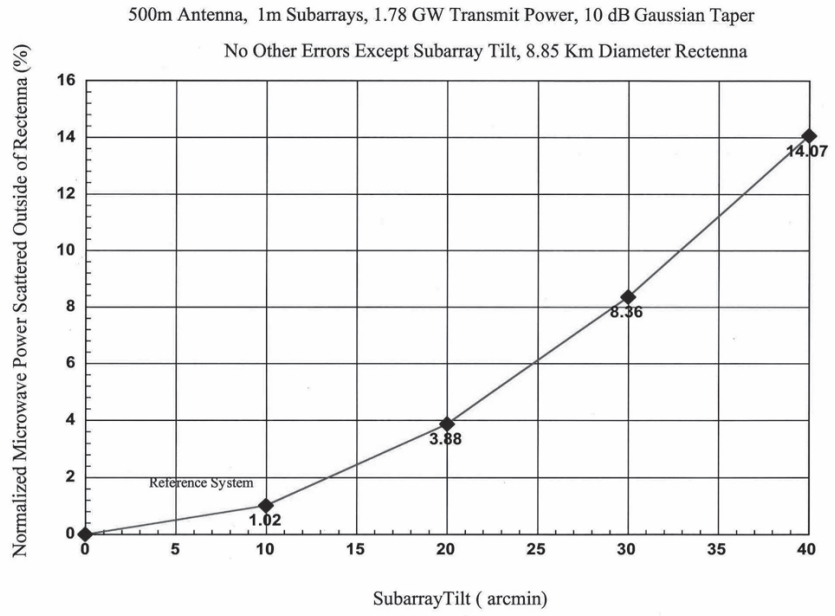

Figure 2. The scattered power due to subarray tilt.

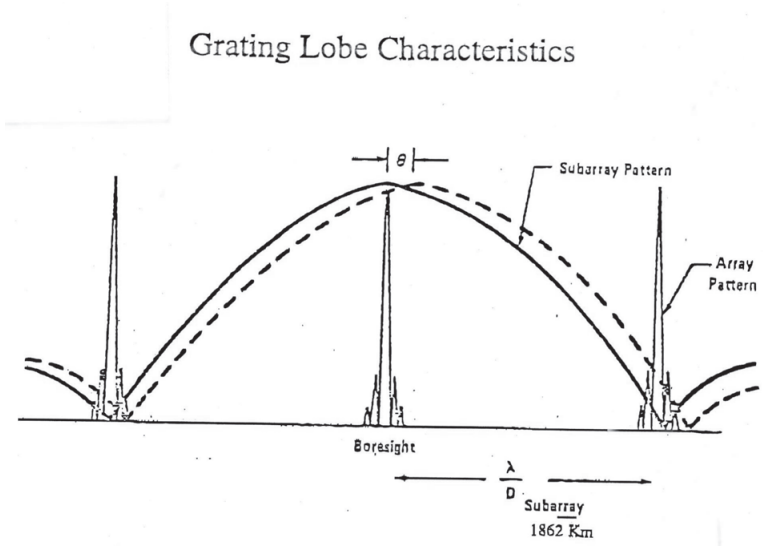

Figure 3. The grating lobe characteristics.

determined. Subarray tilt mainly affects the amount of scattered power from the main beam, while antenna tilt determines the power in the grating lobes.

2.6 Scattered Power

Overall antenna tilt has little effect on scattered power, even for the 1 arc minute main beam, because the retrodirective phase-control system continues to point the beam at the center of the rectenna. The scattered power as a function of antenna tilt in arc minutes is shown in Figure 1. A 5 arc minute antenna tilt results in only 4.6 MW of scattered power. The retrodirective phase-control system makes the antenna tilt affect scattering from the subarray pattern rather than from the full array pattern.

There will be random subarray tilt across the antenna surface due to thermal distortions of the antenna structure, screwjack misalignments of the individual subarrays, etc. The scattered power as a function of subarray misalignments in arc minutes is shown in Figure 2. The reference system has a budget of 10 arc minutes for subarray tilt, which results in 18 MW of scattered power.

2.7 Grating Lobes

The transmitting antenna is made up of 196,000 independent subarrays, each of which transmits a downlink power beam, the phase of which is determined by its path-link distance to the pilot-beam transmitter at the center of the rectenna. Each subarray can be treated as a single-point phase source with electromagnetic amplitude E_0, spaced X_D meters apart. The electric fields from each of the subarrays add in-phase at the pilot-beam transmitter, and also at all spatial angles where the path lengths vary by multiples of 2π. The distance between grating lobes, i.e.,

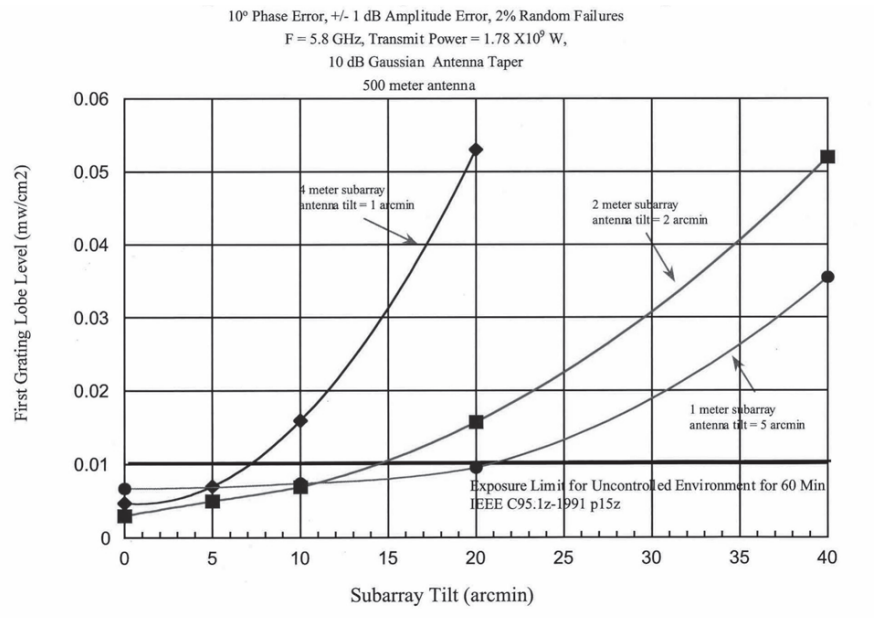

Figure 4. The effect of subarray tilt on the first grating-lobe level for 1-, 2- and 4-m subarrays.

where the subarrays add in phase, is determined by X_D, the subarray spacing.

The grating-lobe characteristics, as shown in Figure 3, are given by

$$R_{GL} = R_0 \sin\theta_{GL} \tag{1}$$

and

$$n(2\pi) = \frac{2\pi}{\lambda} X_D \sin\theta_{GL}, \tag{2}$$

where R_{GL} is the range from the rectenna to the first grating lobe, R_0 is the range from the satellite to the rectenna (3.6×10^7 km), X_D is the distance between phase centers on subarrays, λ is the wavelength of the microwave transmission, θ_{GL} is the grating-lobe angle when the outputs from each subarray add in-phase. Solving Equations (1) and (2) for a 1 m subarray, $R_{GL} = 1862$ km.

The characteristics of the grating lobes (GL) for the reference system are as follows. They are widely spaced (1862 km) due to the small subarray size (1 m). They are greatly enhanced by antenna tilt/beam steering and by spacing (gaps) between subarrays. Individual subarray tilts are random, and have much less effect on grating lobes. Grating-lobe levels are independent of the amplitude taper across the array. For example, uniform illumination and 10 dB Gaussian taper produce approximately the same grating-lobe levels as functions of subarray gap width and antenna tilt. Grating lobe levels are dominant on the *x* and *y* axes. Off-axis grating-lobe levels are attenuated by the deep nulls in the subarray patterns. A 0.1 mW/cm^2 maximum power density level is suggested for the grating lobes.

The location of grating lobes is determined by the subarray sizing, but the magnitude is determined mainly by antenna tilt. The first grating lobe levels in mW/cm^2 are shown in Figure 5 for 1 m, 2 m, and 4 m subarray sizes. The reference system has an antenna tilt budget of 5 arc minutes and a subarray tilt budget of 10 arc minutes, resulting in first grating lobe levels less than 0.01 mW/cm^2 for a 1 m by 1 m subarray.

3. Retrodirective Transmitter Development

Since calculations show that a 1 m by 1 m subarray satisfies the requirements for reduced grating levels, that size was chosen as the starting point for the design of a retrodirective transmitter array.

Almost all retrodirective transmitter development has been aimed at the transmission of information (e.g., data and voice communication), not energy [20]. For the application to information transmission, efficiency is not as important a consideration as maintaining bit integrity, and the antennas are relatively small. However, for energy transmission, efficiency is of primary concern, and the antennas are of the order of hundreds of meters to kilometers in diameter. The challenge is magnified by scale.

Three types of microwave power amplifiers have been proposed for energy transmission. The original DOE/NASA study [5] concentrated on klystron tubes, with each tube producing thousands of watts of power. Other studies [21-24] have included magnetron tubes, each producing hundreds to several thousand watts, and solid-state devices, each producing tens to around one hundred watts. Little actual design work was done for a klystron-based retrodirective transmitter. Retrodirective arrays based on phase-locked magnetrons have been proposed at 2.45 GHz [25] and at 5.8 GHz [26].

The simplest form of retrodirective beam steering (and one used in laser ranging by NASA and others) is the passive "corner cube," in which an incoming beam is directed back to its origin through multiple reflections. It is a passive system in that the beam is essentially the original beam, which has been directed (reflected) back on itself. Active retrodirective systems are those that use phase information from the incoming (usually microwave) pilot beam, detected at multiple elements of the transmitter, to steer a beam generated at the pilot-beam receiving site (transmitter) back to the pilot-beam origination site. The application of retrodirective antennas to space was proposed by Hansen in 1964 [27] for communications satellites, and by Chernoff in 1979 [28] for solar power satellites. Recent work on retrodirective transmitter antennas for power transmission has occurred primarily at the Universities of Kyoto and Kobe in Japan, and at the University of Alaska, Fairbanks in the United States. The Alaska researchers [29] have demonstrated beam steering (but not retrodirective steering with a pilot) in one plane with two magnetron-fed 64-element slotted-waveguide transmitters. The beam was manually steered ± 7.5°. Lobe patterns that agreed with analytic predictions were measured. The group at Kyoto University has developed several retrodirectively controlled wireless power transmitters. One prototype, developed in 1987, [6] used a heterodyne technique, and was unique in using two asymmetric pilot signals to eliminate 2π ambiguities in phase comparison. More recently, work at Kyoto University [6] has concentrated on magnetron-based power transmission systems in which the power from each computer-controlled phase-lock-loop magnetron is divided to feed several antennas. Each antenna element is individually phase shifted to minimize the formation of grating lobes. One retrodirective phase control circuit has been developed based on a subharmonic pilot signal (815 MHz pilot for 2.45 GHz beam with hardware phase conjugation) [6], and another is based on a spread spectrum (software control of phase conjugation) [30]. Prof. Kaya at Kobe University developed a solar power satellite demonstrator for exhibition at the World Space Congress in 2002 that included retrodirective transmission elements [31].

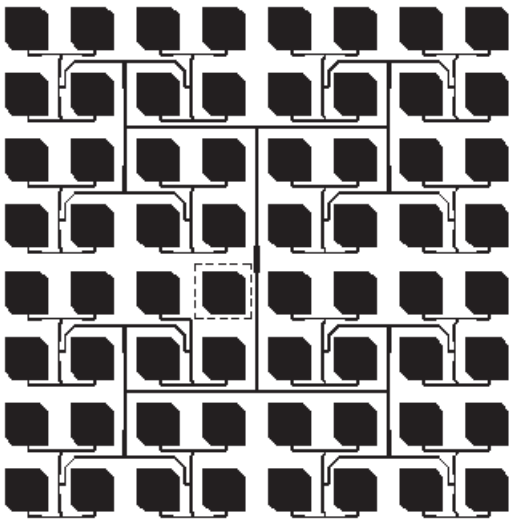

Figure 5. A diagram of the antenna subarray. The receive element is enclosed in dashed lines.

The transmitter design work described here is based on solid-state amplifiers. There are several important considerations when choosing solid-state amplifiers versus tubes (magnetrons or klystrons). First, because the power of the solid-state device is lower, each amplifier will feed only one subarray. This eliminates the need for power dividers and inline phase shifters, which are needed with the higher-power tube devices. Second, although magnetrons have demonstrated higher efficiency (>85% at 2.45 GHz [29] and >50% at 5.8 GHz [30]) than currently available solid-state amplifiers, experimental class E devices have demonstrated greater than 70% efficiency at low power, [31, 32], thus giving the expectation of achieving efficiency comparable to tubes. Because these devices produce higher harmonics, they would have to be combined with a harmonically tuned circuit (class F) for SPS application [33]. Third, tube devices run at and can tolerate higher operating temperatures than current solid-state devices (although here, again, recent improvements in semiconductor devices have closed the gap somewhat), which means higher temperature radiators and easier thermal management. The use of solid-state devices was chosen based primarily on the fact that one radiating subarray per amplifier leads to simpler and more efficient phase control.

4. Demonstration System

The system developed in this work and reported here is a software-controlled system. It was implemented as a low-power demonstration for the World Space Congress in 2002. Due to constraints of time and money, the implementation consisted of only two transmitter panels. Thus, the demonstration was only steerable in one plane. However, the principle of retrodirective control was demonstrated. A 2.9 GHz pilot-beam signal was projected from the rectenna site back to the transmitter site. The pilot signal was captured by patch-antenna receiving elements, located at each subarray within the transmitting antenna array. The received pilot signal was compared at each subarray with a reference phase that was distributed within the array via fiber-optic link. Digital electronics were used to generate a phase conjugate to that of the incoming pilot beam at each transmitter subarray. If the location of the

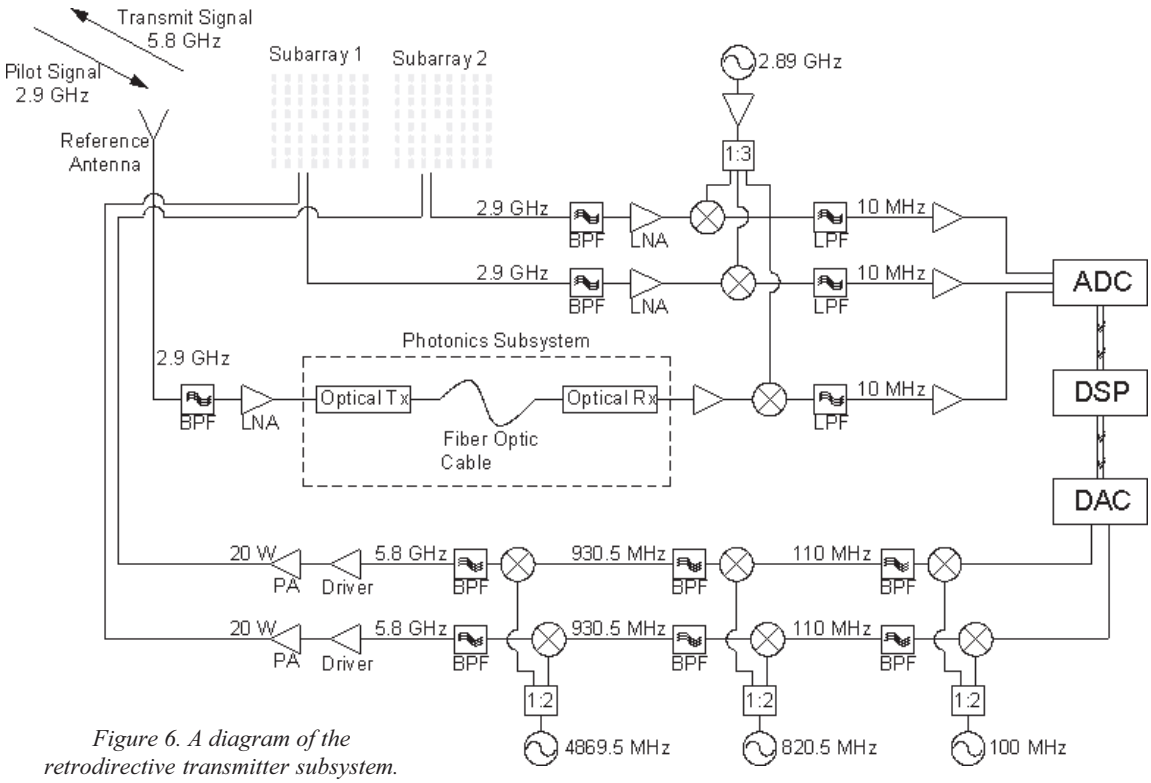

Figure 6. A diagram of the retrodirective transmitter subsystem.

transmitting or receiving site drifted over time, the resulting phase-control system spatially steered the power beam back to the rectenna.

4.1 Transmitting Antenna Subarray

Figure 5 illustrates the layout of the transmitting antenna subarray. Sixty-three CP truncated microstrip patch antennas were etched on a 60-mil substrate of RT-Duriod 5870 ($\varepsilon_r = 2.33$). The inter-element spacing was 25.9 mm. At the 5.8 GHz transmitting frequency, the return loss was –13.2 dB and the gain was 20.2 dB. The axial ratio was 0.70 dB, the 3 dB beamwidth was 12.2°, and sidelobes were more than 13 dB below the main beam. The receiving element (enclosed in dashes in Figure 5) was designed to receive a pilot-beam signal at 2.9 GHz. To reduce the size of this antenna, it was fabricated on a substrate of $\varepsilon_r = 10.2$, and inserted into a hole cut in the transmitting antenna subarray. The isolation between the transmitting and receiving antennas was –33.5 dB.

In this demonstration design, two subarrays were used. The electrically large spacing between subarrays restricted beam steering at 5.8 GHz to about ±5°, which was acceptable given that the ultimate application of this technology is for power transmission across long distances and the drift is normally small.

4.2 Retrodirective Phased Array

The retrodirective phased-array system included a pilot-signal receiver at each subarray, a reference channel distributed to each subarray by fiber-optic link, digital circuitry that produced a phase-conjugated intermediate-frequency (IF) signal, and a transmitting channel that up-converted the IF signal for wireless transmission.

Figure 6 illustrates the retrodirective phased-array system in detail. Two subarrays were used to demonstrate the feasibility of the system. The 2.9 GHz pilot-beam signal was received by patch antennas located at the center of each subarray. The signal was filtered, amplified, and mixed with a signal from a local oscillator to produce an IF signal that was fed to an analog-to-digital converter (ADC). A third receiving antenna acted as a reference channel. After filtering and amplification, this signal was routed through a photonics subsystem before also being down-converted to IF and digitized at the analog-to-digital converter. A digital signal processor (DSP) produced digital output signals with phase information for the separate subarrays. A digital-to-analog converter (DAC) generated two analog IF signals, one for each transmitting channel. These signals were filtered and up-converted in three stages to produce the 5.8 GHz transmitted signal. The phase of each signal was controlled at the IF frequency so that phase conjugation was maintained at 5.8 GHz. The two signals were amplified to about 20 W each, and injected into the CP transmitting subarray panels.

5. Results

The design parameters for a retrodirective power transmission stem have been studied. Efficient, highly focused beam tapers, which maintain acceptably low sidelobe levels and provide more-benign thermal profiles at the transmitter, are available. Grating-lobe levels can be maintained at a sufficiently low level with 1 m by 1 m subarrays. A software controlled retrodirective system has been designed and implemented in one plane, for a demonstration.

6. Conclusions

A practical retrodirective phased-array antenna for power beaming using solid-state microwave power amplifiers is feasible, based on 1 m by 1 m subarrays, with each subarray powered by a single solid-state power amplifier that is individually phase shifted, based on phase conjugation of a pilot-beam signal. Although the state-of-the-art efficiency for solid-state power amplifiers is lower than that of magnetron devices, the research is encouraging. A transmitting array based on individually powered subarrays would have the advantage that no losses would be incurred from the power dividers and inline phase shifters necessary with higher-power tubes. The economic viability of the design will depend largely on improving the efficiency of the solid-state power devices. Even though it offers advantages in flexibility, the software phase-control circuitry is very complex and probably too expensive to build economically, even in large quantities. A simplified hardware-controlled phase-control scheme should be developed.

7. References

1. D. R. Criswell. and R .D. Waldron, "Results of Analysis of a Lunar-Based Power System to Supply Earth with 20,000 GW of Electric Power," *SPS 91 Power from Space*, Paris/Gif-sur-Yvette, August 27-30, 1991, pp. 186-193.

2. US Department of Energy, Energy Information Administration, "International Energy Outlook 2002," Report No. DOE/EIA 0484 (2001), March 2002.

3. P. E. Glaser, "Power from the Sun: Its Future," *Science*, **162**, 1968, p. 857.

4. M. H. Smith, R. L. Fork, and S. T. Cole, "Safe Delivery of Optical Power from Space" *Optics Express*, **8**, 10, 2001, pp. 537-546.

5. DOE 1978, "Satellite Power System (SPS) Concept Development and Evaluation Program (CDEP) Reference System Report," DOE/ER-0023, October 1978.

6. H. Masumoto, "Research on Solar Power Satellites and Microwave Power Transmission in Japan," *IEEE Microwave Magazine*, **3**, 4, December 2002, pp. 36-45.

7. R. M. Dickinson, personal communication.

8. R. M. Dickinson and W. C. Brown, "Radiated Microwave Power Transmission System Efficiency Measurements," Tech Memo 33-727, Jet Propulsion Laboratory of California Institute of Technology, March 15, 1975.

9. V. A. Vanke, H. Matsumoto, N. Shinohara, and A. Kita, "Cyclotron Wave Converter of Microwaves into DC," *IEICE Transactions on Electronics*, **E81-C**, 7, July 1998, pp. 1136-1142.

10. R. M. Dickinson, "Evaluation of a Microwave High-Power Reception-Conversion Array for Wireless Power Transmission," Tech Memo 33-741, Jet Propulsion Laboratory of California Institute of Technology, September 1, 1975.

11. S. S. Bharj, R. Camisa, S. Grober, F. Wozniak, and E. Pendleton, "High Efficiency C-Band 1000 Element Rectenna Array For Microwave Powered Applications," 1992 IEEE MTT-S International Microwave Symposium *Digest*, pp. 301-303.

12. J. O. McSpadden, L. Fan and K. Chang, "Design and Experiments of a High-Conversion-Efficiency 5.8 GHz Rectenna," *IEEE Transactions on Microwave Theory and Techniques*, **MTT-46**, 12, December 1998, pp. 2053-2059.

13. P. Koert and J. T. Cha, "35 GHz Rectenna Development," *WPT-93: First Annual Wireless Power Transmission Conference*, Center for Space Power, Texas A&M University, College Station, Texas, 1993, pp. 457-466.

14. T. Yoo and K. Chang, "Theoretical and Experimental Development of 10 and 35 GHz Rectennas," *IEEE Transactions on Microwave Theory and Techniques*, **MTT-40**, 6, June 1992, pp. 1259-1266.

15. J. J. Schlesak, A. Alden, and T. Ohno, "A Microwave Powered High Altitude Platform," IEEE MTT-S International Microwave Symposium *Digest*, 1988, pp. 283-286.

16. T. Ito, Y. Fujino, and M. Fujita, "Fundamental Experience of a Rectenna Array for Microwave Power Reception," *IEICE Transactions on Communications*, **E76-B**, 12, December 1993, pp. 1508-1513.

17. Y. Fujino, N. Kaya and T. Saka, "Development of a C Band Rectenna for Microwave Power Transmission Toward a Space Robot," 49th International Astronautical Congress, Melbourne, Australia, September 28 - October 2, 1998.

18. N. Shinohara and H. Matsumoto, "Dependence of dc Output of a Rectenna Array on the Method of Interconnection of its Array Elements," *Electrical Engineering in Japan*, **125**, 1, 1998 pp. 9-17.

19. T. Miura, N. Shinohara and H. Matsumoto, "Experimental Study of Rectenna Connection for Microwave Power Transmission," *Electronics and Communications in Japan, Part 2*, **84**, 2, 2001, pp. 27-36.

20. R. Y. Miyamoto and T. Itoh, "Retrodirective Arrays for Wireless Communications," *IEEE Microwave Magazine*, **3**, 1, March 2002, pp. 71-79.

21. S. Sasaki, Y. Naruo, and M. Nagatomo, "Engineering Research for Solar Power Satellite SPS 2000," *Proceedings SPS '97 Conference*, Montréal, Canada, August 24-28, 1997, pp. 73-77.

22. H. Feingold et al., "Space Solar Power – A fresh Look at the Feasibility of Generating Solar Power in Space for Use on Earth," Science Applications International Corporation Report SAIC-97/1005, Science Applications International Corporation, Schaumberg, Illinois, 1997.

23. H. Feingold et al., "Space Solar Power 1998 Concept Definition Study," Report Number SAIC-99/1016, Science Applications International Corporation, Schaumburg, Illinois, 1999.

24. N. Kaya, "A New Concept of SPS With a Power Generator/Transmitter of a Sandwich Structure and a Large Solar Collector," *Space Energy and Transportation*, **1**, 3, 1996, pp. 205-213.

25. W. C. Brown, "Development of Electronically Steerable Phased Array Module (ESPAM) with Magnetron Directional Amplifier (MDA) Power Source," Final Report, Microwave Power Systems, Weston, MA, Texas A&M Research Foundation Subgrant No. L300060, Project RF-2500-95, September 1995.

26. N. Shinohara, H. Matsumoto, and K. Hashimoto, "Solar Power Station/Satellite (SPS) with Phase Controlled Magnetrons," *IEICE Transactions on Electronics*, **E86-C**, 8, August 2003, pp. 1-7.

27. R. C. Hansen, "Preface to the Special Issue on Active and Adaptive antennas," *IEEE Transactions on Antennas and Propagation*, **AP-12**, March 1964, pp. 140-141.

28. R. C. Chernoff, "Large Active Retrodirective Arrays for Space Applications," *IEEE Transactions on Antennas and Propagation*, **AP-27**, 4, July 1979, pp. 489-496.

29. M. C. Hatfield and J. G. Hawkins, "Design of an Electronically-Steerable Phased Array for Wireless Power Transmission Using a Magnetron Directional Amplifier," IEEE MTT-S International Microwave Symposium *Digest*, **1**, Anaheim, CA, 1999, pp. 341-344.

30. K. Hashimoto, H. Matsumoto, N. Shinohara, and K. Tsutsumi, "SSPS Beam Control with Spread Spectrum Pilot Signals," *2003 Japan-United States Joint Workshop on Space Solar Power system (JUSPS'03) Proceedings*, Kyoto University, Uji Japan, July 3-4, 2003, pp. 124-130.

31. N. Kaya, personal communication, 2003.

32. Richard Dickinson, personal communication, 2002.

33. N. Shinohara, H. Matsumoto, N. Tanaka, and Y. Takahashi, "Development of Small and Light Phase Controlled Magnetron for Space Use," *Proceedings of the 1st International Symposium on Sustainable Energy System*, Kyoto, Japan, March 13-14, 2003, p. 129.

34. F. N. Sechi, "High Efficiency Microwave FET Amplifiers," *Microwave Journal*, November 1981, pp. 59-66.

35. T. B. Mader, *Quasi-Optical Class-E Power Amplifiers*, PhD Dissertation, 1995, University of Colorado, Boulder.

36. J. McSpadden and J. C. Mankins, "Space Solar Power Programs and Microwave Wireless Power Technology," *IEEE Microwave Magazine*, **3**, 4, December 2002, pp. 46-57.

Free-Space Power-Combining Oscillator Array for Solar Power Transmission

J. Choi
A. Mortazawi

Abstract

This paper addresses wireless power transmission by means of spatial-power-combining oscillator arrays that employ high-power semiconductor devices. The main goal is to design a highly stable, efficient, and multimode-free oscillator array that is tolerant to multiple device failures. The proposed solar power transmitting system consists of optical-link distribution networks, phase-correction loops, and extended resonance oscillator arrays. The beam-scanning capabilities of the large array antenna are investigated. The extended resonance technique is applied to the design of coupled oscillator subarrays, and external injection locking is employed in order to create a more stable and coherent power beam.

1. Introduction

The demand for power usage will increase at least 2.5 times in the next 50 years, according to a prediction [1]. Based on the need for clean, non-polluting sources of energy, and a trend to abandon nuclear power generation, the solar power source appears to be an attractive alternative energy source. However, Earth-based solar-cell power generation would require an unrealistically large Earth surface area (about one-fifth of the entire United States). Instead, the concept of Solar Power Satellite (SPS) systems has been presented to solve this problem. One of the key technologies for the SPS system is the wireless power transmission system, which includes dc/RF converters in the transmitters, the retrodirective beam-control system, and the receiving rectenna [2]. In this paper, the overall transmitting system and its components will be discussed.

The techniques for generating and transmitting a high-intensity microwave beam for solar power transmission can be divided into the centralized and the distributed approaches. The centralized approach relies on microwave tubes that are capable of generating kilowatts of power at microwave frequencies. However, microwave tubes are heavy and require extensive cooling systems. They are not as reliable as solid-state devices, and therefore the system is prone to single-point failure.

A more practical approach for solar power transmission via microwaves is to adopt a distributed approach with high-power solid-state devices. The distributed approach will provide a lightweight, fault-tolerant system. Moreover, it will not need active cooling systems and power distribution networks. In this approach, the dc power collected from solar cells would be converted into the form of RF power, using a distributed oscillator array employing high-power and efficient oscillators. Microstrip patch antenna arrays with low cost and a low profile would transmit the converted microwave power to the Earth.

This paper discusses the theoretical and practical aspects of designing a very large, low-profile, printed, self-oscillating injection-locked antenna array to generate a powerful coherent microwave beam. First, we describe the entire distributed system, including the active antenna array. A beam-scanning scheme to direct the microwave beam to a precise target area is also discussed. We then describe the extended resonance technique for combining spatial power, and the injection-locking technique to increase the coherence and stability of the oscillator array.

2. System Description

A diagram of the proposed concept for constructing a large active array by synchronizing many subarrays is shown in Figure 1. The whole solar power transmitting array is composed of numerous subarrays, and each subarray is made of an extended resonance oscillator array with radiating patch antennas. Because the extended resonance oscillator is a free-running coupled oscillator array, it needs to be externally injection locked to improve the frequency coherence. For this purpose, the proposed system is composed of optical-link distribution networks, phase-

Jonghoon Choi and Amir Mortazawi are with the University of Michigan, Department of Electrical Engineering and Computer Science, 1301 Beal Avenue, Ann Arbor, MI 48109-2122, USA;
Tel: +1 (734) 936-2597; Fax: +1 (734) 647-2106;
E-mail: jonghoon@umich.edu, amirm@eecs.umich.edu.

This invited paper is part of the Special Section on Space Solar Power Systems. An oral version was originally presented at the 2003 Japan-US Joint Workshop on Space Solar Power System (JUSPS'03), July 3-4, 2003, Kyoto University, Uji, Kyoto, Japan.

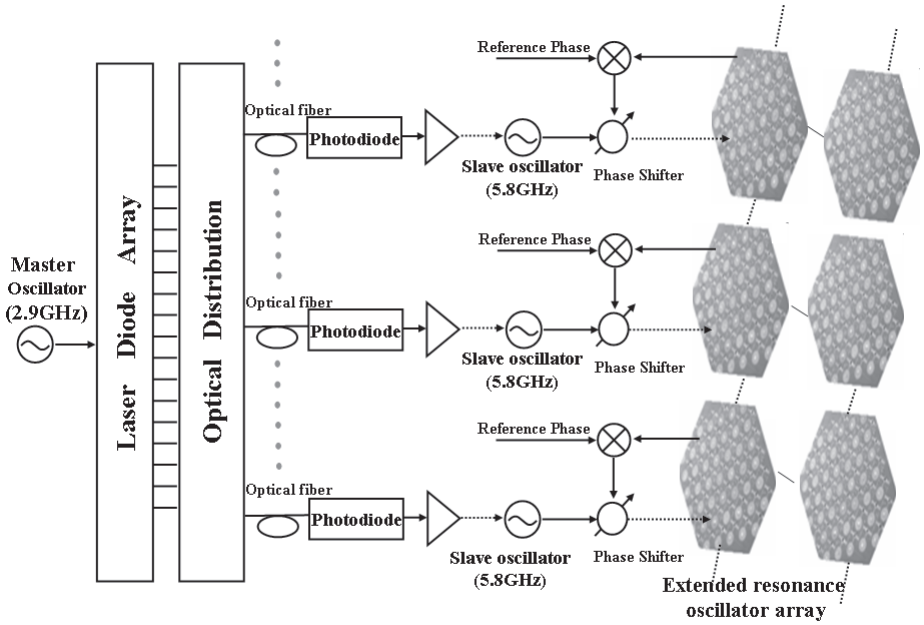

Figure 1. A schematic of the sub-harmonic injection-locked large array containing many active antenna subarrays (the dashed lines represent the injection locking).

correction loops, and the extended-resonance oscillator arrays [3-5].

In this system, the reference RF signal from the master oscillator at 2.9 GHz is converted into an optical signal through a laser diode, and is distributed via optical fiber with low loss and compactness. These distributed optical signals are detected by photodiodes and converted back into RF signals. The converted RF reference signal is inputted into the nonlinear amplifier, which generates the second-harmonic component, and boosts up the amplitude of the reference signal for increasing the injection-locking bandwidth. From the nonlinear amplifier, the second-harmonic reference signal (5.8 GHz) is injected into the free-running slave oscillator at 5.8 GHz, which leads to the sub-harmonic injection locking. The signal from the sub-harmonically injection-locked oscillator then goes into the extended-resonance oscillator array, resulting in the second external injection locking. Through the second injection locking, the frequency in the extended-resonance oscillator array in a subarray is locked to twice the reference frequency. Consequentially, all subarrays can be synchronized with each other, and the frequency coherency and the power-combining efficiency will improve.

In the process of the second injection locking, a phase shift could occur – according to Adler's equation [15] – due to the frequency difference between the reference signal and the free-running oscillator subarray signal. This phase shift leads to the loss of phase control in the oscillator array, causing control of the power beam to become difficult. In order to keep the phase control, one can employ a feedback loop consisting of a phase detector and a phase shifter. In this feedback loop, the phase in the oscillator subarray and the reference phase are applied to two inputs of the phase detector. The reference phase is set for the power beam control. The phase detector compares two input phases, and generates an output voltage that is a measure of their phase difference. The output voltage from the phase detector changes the time delay in the phase shifter, which corrects the phase of the subarray by means of the external injection locking. As a result, this feedback loop enables the phase in the subarray to approach the reference phase and the precise beam control.

The antenna size must be carefully chosen in order to maximize the power-transmission efficiency in the Fresnel region. For this purpose, we employed Goubau's analysis, which explains the relationship among the sizes of the receiving and transmitting antennas and the power transmission efficiency between the receiving and transmitting antennas [8, 9]. To determine the antenna size, the following is assumed:

1. The transmitting antenna array and the rectenna are square in shape.
2. The array antenna is approximated to the aperture antenna considering the densely located unit antenna elements.
3. The size of the receiving antenna is ten times that of the transmitting antenna, in order to reduce the burden and cost of installing and maintaining the transmitting array antenna in space.

Considering only the power-transmission efficiency between the transmitting array antenna and the rectenna, the target transmission efficiency can be set at 99%. In this case, the calculated sizes of the transmitting and receiving antennas become approximately 700 m x 700 m and 7 km x 7 km, respectively. Under the conditions that the operation frequency is 5.8 GHz and the spacing between adjacent antennas is $\lambda/2$, the number of unit antennas in one row of the whole array is approximately calculated as follows:

$$N = \frac{L}{\lambda/2} \approx 27000\,, \qquad (1)$$

where L is the length of one side in the transmitting antenna (700 m) and λ is the wavelength at 5.8 GHz. Consequently, the required number of antennas in the transmitting array antenna is $27000 \times 27000 = 7.29 \times 10^8$, in order to achieve the 99% transmission efficiency from the transmitting array antenna to the rectenna.

3. Power Beam Scanning

Beam scanning of substantial radiated power levels is critical in the system design, which would allow for the maximum level of collected power at the rectenna. The transmitting beam must be oriented in the direction coinciding with the center of the receiving rectenna to obtain the best power transfer efficiency.

In the case where the transmitting antenna covers the whole visible region on the Earth's surface, the required scan angle is calculated to be ±8.7° [11]. However, from a practical standpoint, the required maximum scan angle can be reduced significantly because the solar power transmitting satellite will orbit at the same speed as the revolution of the Earth. Therefore, in our system, a scan angle of ±1°, covering ±630 km on the Earth's surface, seems to be sufficient so that the power beam is accurately directed to the target rectenna.

Based on the above facts, we propose a beam-scanning method that provides more stable and economical operation. The conventional beam-scanning technique requires a phased array with linear phase progression between adjacent antennas. Hence, the phase of each unit antenna needs to be controlled by a phase shifter, and many phase shifters are therefore required. However, in our scheme, many unit antennas are grouped to constitute a single subarray [12]. All antennas in a subarray have the same phase, so only one phase shifter is required per subarray. Therefore, this scheme enables the in-phase operation that enhances the stability of the subarrays, and allows for the ease of beam-scanning control.

In order to simplify the array analysis, a one-dimensional (1D) array, corresponding to one side of the whole array, is investigated. The one-dimensional array has 27000 unit antennas, and the number of antennas in each one-dimensional subarray is arbitrarily chosen as 50, which makes the whole one-dimensional array contain 540 subarrays. Also, we assume that the resolution of the phase shifter is seven bits (2.8°), in order to investigate the performance of the proposed scheme with coarse resolution.

The procedure of determining the phase distribution of a subarray is described as follows. Generally, in order to produce a scan angle of θ_1 degrees, the phase difference between two adjacent antennas is given by

$$\alpha = -kd \sin\theta_1\,, \qquad (2)$$

where α is the phase difference and d is the spacing between adjacent antennas. Therefore, the Mth unit antenna requires the following phase to obtain a scan angle of θ_1:

$$\phi_M = M\alpha = -Mkd \sin\theta_1\,. \qquad (3)$$

In the proposed scheme, we selected the 25th unit antenna located in the center of a subarray as a representative antenna in the subarray. The phase for this representative antenna is calculated using Equation (3). The calculated phase is substituted for the phases of all unit antennas in the same subarray. Therefore, the resulting phase, given by Equation (4), is the same for all unit antennas in the Nth subarray:

$$\phi_N = -\left[50(N-1)+25\right]\alpha\,. \qquad (4)$$

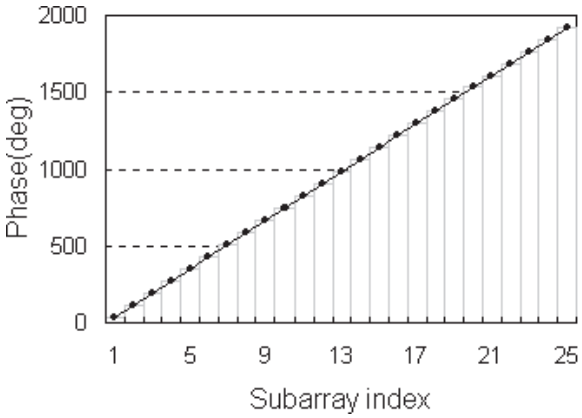

Figure 2a. The continuous phase distribution (line) and quantized phase distribution (bar) of the first 25 subarrays for a target scan angle of 0.5°.

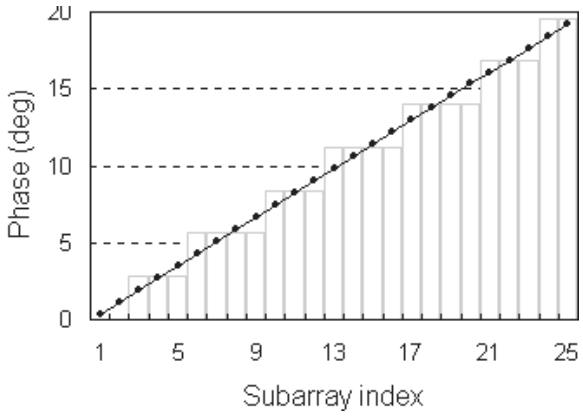

Figure 2b. The continuous phase distribution (line) and quantized phase distribution (bar) of the first 25 subarrays for a target scan angle of 0.005°.

Finally, the calculated phases of the subarrays need to be rounded off to multiples of 2.8° for the seven-bit phase-shifting resolution.

Figure 2 shows the phase distributions when the target scan angles are 0.5° and 0.005°. To show the phase distributions clearly, the phase distributions of only the first 25 subarrays in the whole one-dimensional array are depicted. The solid line represents the phase distribution in the conventional scheme, having a linear phase progression. The bar represents the phase distribution in the proposed scheme, showing the staircase shape. In the case of a target angle of 0.005°, the required phase difference between two adjacent subarrays is very small: 0.785°. This small phase difference causes an identical phase to be distributed to several subarrays. In other words, several subarrays are consequentially grouped in terms of their phases. In Figure 2b, it is shown that three or four subarrays have the same phase and are therefore grouped.

With the calculated phase, the array factor can be determined. Since our analysis is based upon the Fresnel region, the distance between each unit antenna and the receiving antenna is given by

$$R = r - x'\sin\theta + \frac{1}{r}\left(\frac{x'^2}{2}\cos^2\theta\right), \qquad (5)$$

where r is the distance between the center of the transmitting antenna and the receiving antenna, x' is the distance between the unit antenna and the center of the transmitting antenna, and θ is the scan angle.

Since the scanning range is within ±1° and the distance between the center of the transmitting antenna and the receiving antenna (r) is almost constant, the last term in Equation (5) is only dependent on the distance between the unit antenna and the center of the transmitting antenna (x'). If one can design a fixed feeding network with different time delays depending on the locations of the subarrays, the dependence on x' is removed and we can ignore the last term, which simplifies our analysis from the Fresnel approximation to the far-field approximation.

A Gaussian-tapered excitation is recommended on the transmitting antenna array, in order to achieve maximum power-transfer efficiency [10]. Depending upon the distances between the center point of the whole array and the subarrays, the subarrays may have different power levels, and a digitized Gaussian excitation will be achieved. Taking into account all aforementioned facts, the array factor for the whole one-dimensional array can be expressed as

$$F(\theta) = \sum_{n=1}^{540}\sum_{m=1}^{50} I_0 \exp\left[-\frac{\sigma\left(x_n - \ell/2\right)^2}{\left(\ell/2\right)^2}\right]$$

$$\exp\left[j\left(m+50n\right)kd\sin\theta\right]\exp\left(j\phi_n\right), \quad (6)$$

where ℓ is the size of the whole array (700 m), x_n is the location of the center antenna in the nth subarray, ϕ_n is the phase of the nth subarray, and σ is the coefficient that determines the illumination shape.

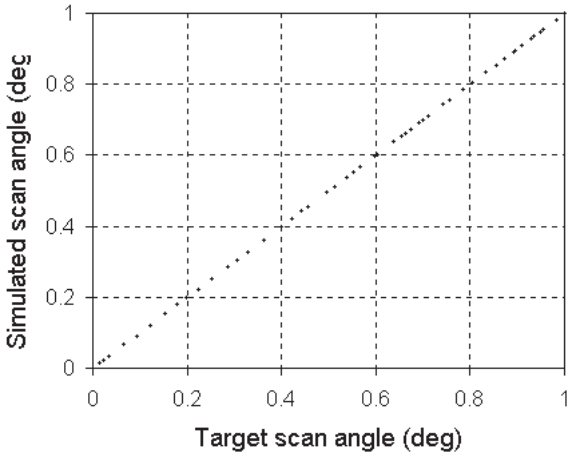

Figure 3. The beam-scanning simulation result.

To demonstrate the performance of the above scheme, 50 target scan angles were randomly sampled within ±1°, and the array factor for each target scan angle was obtained by calculating the phases of the subarrays. The scan angles were determined from the simulated antenna radiation pattern, and are depicted in Figure 3. The x axis represents the sampled target scan angles, and the y axis represents the scan angles obtained from the simulation. Good agreement is observed, and the maximum error is 0.00005°. This angle error is equivalent to a distance of 40 m on the Earth. This degradation of performance is negligible, because the corresponding distance is very small compared with the proposed size of the rectenna (7 km). In addition, it should be mentioned that the use of more-refined phase shifters will improve the beam-scanning precision.

4. Design of Subarray

The spatial-power-combining technique of combining microwave power from distributed solid-state sources can be applied to the design of the subarray in the SPS system. In spatial-power-combining oscillators, many oscillators are connected to each other to provide mutually coherent operation, and are designed to strongly interact through strong and weak coupling networks. In this paper, an approach based on the extended-resonance technique is explored and analyzed, based on strong coupling networks.

4.1 Extended-Resonance Technique

The concept of the extended-resonance technique employing two-terminal devices is illustrated in Figure 4 [5]. Many active devices are connected via a network of cross-configuration transmission lines of length L. Active

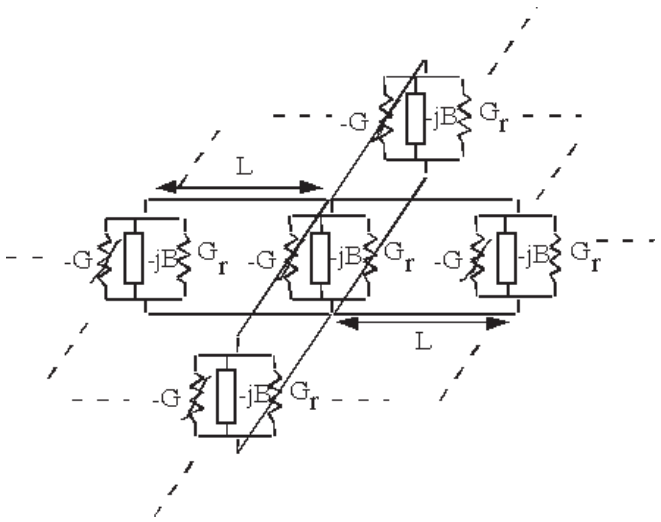

Figure 4. The equivalent circuit for a spatial-power-combining oscillator, based on the extended-resonance technique.

devices can be modeled as $-G - jB$, and G_x represents the radiation conductance of the antenna connected to each port. In the steady state, this G_x should be equal to the conductance of each device to satisfy the oscillation condition. The important feature of the extended-resonance technique is that each device can not resonate alone. Through a transmission line of length L, one-quarter of each device's susceptance $(-jB/4)$ is transformed to the susceptance with the same magnitude but the opposite sign $(+jB/4)$ at the adjacent port. By means of this transformation of the device's susceptance, the midway point of the transmission line of length L becomes virtually open, leading to exciting an eigenvector of (1,1). This eigenvector results in in-phase operation between adjacent devices.

Three-terminal devices can be incorporated into the extended-resonance structure by providing an appropriate feedback. Figure 5 shows an implemented extended-resonance oscillator with 47 GaAs MESFET devices [13].

A short stub is connected to the gate, and provides series feedback in order to create the negative resistance. The radiation conductance of the antenna is chosen to satisfy the oscillation condition. Circular patch antennas are used, and the chip resistor in the middle of the interconnecting transmission line suppresses the excitation of any undesired mode.

4.2 Extended-Resonance Theory

For coherent operation in the extended-resonance subarray, phase coherency and frequency coherency should be simultaneously satisfied. In-phase operation in an extended-resonance oscillator can be verified using equivalent-circuit equations for the case where the susceptance of the devices is inductive. The equivalent circuit for an extended-resonance oscillator with two devices is represented in Figure 6. Using the transmission-line model, the equation for the equivalent circuit becomes [14]

$$\begin{pmatrix} -Y_{D1} & \overline{V}_1 \\ -Y_{D2} & \overline{V}_2 \end{pmatrix} = \begin{pmatrix} Y_{11} & Y_{12} \\ Y_{21} & Y_{22} \end{pmatrix} \begin{pmatrix} \overline{V}_1 \\ \overline{V}_2 \end{pmatrix}. \qquad (7)$$

Assuming that any losses in the transmission line are considered as part of the conductance, G_x, we can use Y parameters for lossless transmission lines:

$$Y_{11} = Y_{22} = -jY_0 \cot 2\theta, \qquad (8)$$

$$Y_{12} = Y_{21} = jY_0 \csc 2\theta \cdot$$

Assuming that two devices are identical, Y_{D1} can be set equal to Y_{D2}:

$$Y_{D1} = Y_{D2} = Y_D = (G_r - G_d) + 1/j\omega L + j3Y_0 \tan\theta \cdot \qquad (9)$$

By manipulating Equations (7), (8), and (9), the ratio of two

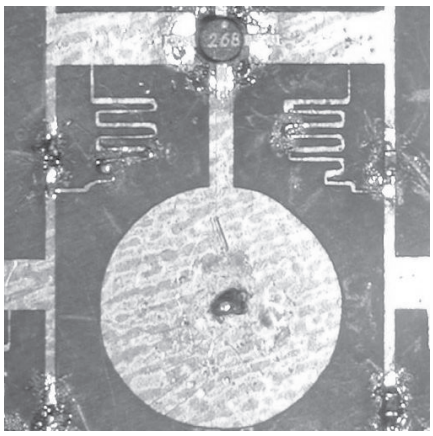

Figure 5a. A circuit implementation of the extended-resonance technique: the unit cell.

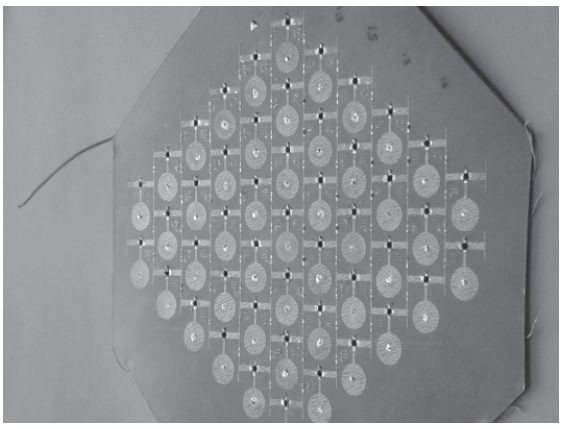

Figure 5b. A circuit implementation of the extended-resonance technique: an oscillator array with 47 devices.

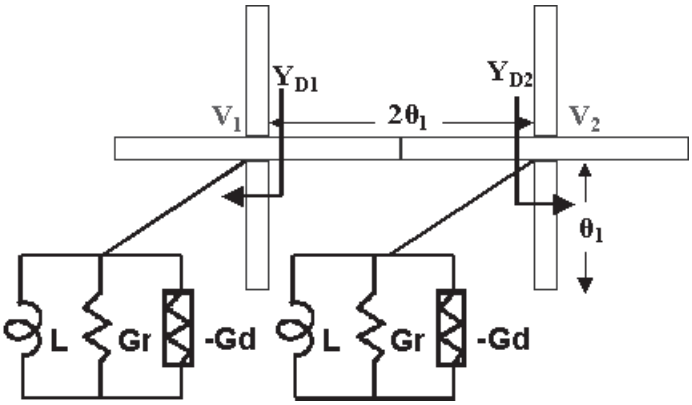

Figure 6. An equivalent circuit for an extended-resonance oscillator with two devices.

adjacent voltages is given by

$$\frac{\overline{V_1}}{\overline{V_2}} = -\frac{Y_{12}}{Y_{11}+Y_D}$$

$$= \frac{-jY_0 \csc 2\theta}{-jY_0 \cot 2\theta + (G_r - G_d) + j3Y_0 \tan\theta + 1/j\omega L} . \quad (10)$$

The electrical length of the transmission line that satisfies the condition of extended resonance becomes

$$\theta_1 = \tan^{-1}\frac{1}{4Y_0\omega_0 L} , \quad (11)$$

where ω_0 is the designated frequency.

Under the steady state at the designated oscillation frequency (ω_0), the absolute value of the device conductance becomes equal to the radiation conductance, and the voltage relation is found to be

$$\frac{\overline{V_1}}{\overline{V_2}} = \left.\frac{-jY_0 \csc 2\theta}{-jY_0 \cot 2\theta + (G_r - G_d) + j3Y_0 \tan\theta + 1/j\omega L}\right|_{\theta=\theta_1}$$

$$= 1 \cdot \quad (12)$$

The above result means that the adjacent phase difference and the amplitude difference are zero. In other words, the adjacent devices operate in phase with the same amplitude. When the extended-resonance oscillator is injection locked to the external injection signal with frequency (ω_1), the free-running frequency becomes shifted to the injection frequency. For this condition, the chosen electrical length of the transmission lines (θ_1) changes into

$$\theta = \Omega\theta_1 , \quad (13)$$

where

$$\Omega = \frac{\omega_1}{\omega_0} = \frac{\omega_0 + \Delta\omega}{\omega_0} .$$

Since the locking bandwidth is relatively small, the magnitudes of the device conductance and the load conductance are approximated to be equal within the locking bandwidth, $\Delta\omega_{lock}$.

$$G_L - G_d \approx 0 , \quad |\omega| \le \Delta\omega_{lock} . \quad (14)$$

Under the above assumption, Equation (10) becomes

$$\left.\frac{\overline{V_1}}{\overline{V_2}}\right|_{\theta=\theta_1} = \frac{-Y_0 \csc 2\Omega\theta_1}{-Y_0 \cot 2\Omega\theta_1 + 3Y_0 \tan\Omega\theta_1 + 1/(\omega + \Delta\omega_0)L} . \quad (15)$$

The above voltage ratio is plotted in Figure 7 for the case where the locking bandwidth is 40 MHz. It is observed that the amplitude difference between two adjacent oscillators is negligibly small and there is no phase difference, indicating that two devices in the extended-resonance oscillator operate in phase, even at a slightly perturbed frequency. This robust in-phase operation in the extended-resonance oscillator can enhance the stability of the overall SPS system.

Basically, the extended-resonance oscillator array operates at a single frequency with the same phase. However, due to fabrication errors, temperature sensitivity, and other circuitry and environmental factors, the operating frequency of each subarray is likely to be slightly different. To compensate for this difference, the external injection-locking technique can be adopted. As mentioned earlier, the reference signals from the master oscillator are injected into each subarray, causing the extended-resonance oscillator array

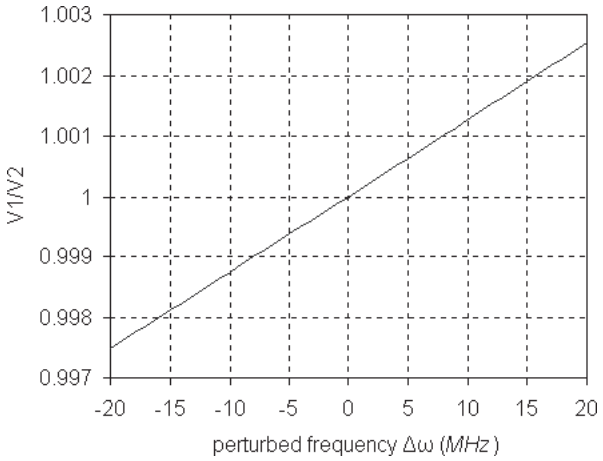

Figure 7. The ratio of the voltage at port 1 to the voltage at port 2 as a function of the perturbed frequency.

in each subarray to operate at twice the reference frequency. As a result, the frequency coherency in the subarrays will improve.

4.3. Stability of Extended-Resonance Oscillator Array

The extended-resonance oscillator array has the inherent property of being tolerant to multi-device failure. The effect of single and multiple device failures on synchronization and the power-combining efficiency was investigated for a nine-device extended-resonance oscillator array through time-domain simulations, using the Van der Pol oscillator model and experimental measurements [5]. The experimental result showed that single device failure does not disturb in-phase operation, but results in a shift in the operating frequency of 0.01%, and a drop in the total power (11.4%) in the nine-device extended-resonance oscillator array. This result indicates that the extended-resonance oscillator is a system that is very tolerant to device failures.

In addition, since the extended-resonance oscillator array in a subarray for the SPS consists of over 1000 unit elements, it is expected that it would be much more tolerant to multiple device failures than the nine-device extended-resonance oscillator array.

However, multiple device failures shift the operating frequency of the free-running oscillator array [5]. If the frequency shift due to multiple device failures in the subarray is within the injection-locking bandwidth, then this issue is rectified by externally injection locking the array. If the frequency shift is outside the injection-locking bandwidth, then external injection locking will not be helpful. In this case, degradation in the power-combining efficiency and the array pattern will occur. Also, the power reduction in a subarray due to multiple device failures will deteriorate the radiation pattern.

5. Conclusion

Based on the distributed approach for generating a high-intensity microwave beam, a free-space power-combining oscillator array for the SPS system has been presented and analyzed. Our calculations suggested that the proposed array is capable of directing a microwave power beam to a target rectenna by controlling the phases of the subarrays. With this method, we could alleviate the need for mechanical systems for beam steering, and also significantly reduce the number of phase shifters. We employed the extended resonance technique in designing an individual subarray. Our analysis supported the theory that the extended-resonance technique provides stable in-phase operation in a subarray due to its strong dependence between the adjacent devices. We also suggested that the external injection-locking technique could be useful in order to provide a coherent frequency to all subarrays. As a result of these techniques, coherent power beam and beam scanning capability can be obtained in the SPS system.

6. References

1. H. Matsumoto, "Research on Solar Power Satellites and Microwave Power Transmission in Japan," *IEEE Microwave Magazine*, **3**, December 2002, pp. 36-45.

2. J. O. McSpadden and J. C. Mankins, "Space Solar Power Programs and Microwave Wireless Power Transmission Technology," *IEEE Microwave Magazine*, **3**, December 2002, pp. 46-57.

3. A. S. Daryoush, "Optical Synchronization of Millimeter-Wave Oscillators for Distributed Architectures," *IEEE Transactions on Microwave Theory and Techniques*, **MTT-38**, May 1990, pp. 467-476.

4. A. S. Daryoush, M. Francisco, R. Saedi, D. Polifko, and R. Kunath, "Phase Control of Optically Injection Locked Oscillators for Phased Arrays," IEEE MTT-S International Microwave Symposium *Digest*, **3**, May 1990, pp. 1247-1250.

5. A. Mortazawi and B. C. De Loach, Jr., "Spatial Power Combining Oscillators Based on an Extended Resonance Technique," *IEEE Transactions on Microwave Theory and Techniques*, **MTT-42**, December 1994, pp. 2222-2228.

6. R. W. Bickmore and R. C. Hansen, "Antenna Power Densities in the Fresnel Region," *Proceedings of the IRE*, **47**, December 1959, pp. 2119-2120.

7. B. Z. Katsenelenbaum, "Microwave Power Transmission by a Long Beam," *DIPED-99 Proceedings*, December 1999, pp. 17-21.

8. W. C. Brown, E. E. Eves, "Beamed Microwave Power Transmission and its Application to Space," *IEEE Transactions on Microwave Theory and Techniques*, **MTT-40**, June 1992, pp. 1239-1250.

9. G. Goubau and F. Schwering, "On the Guided Propagation of Electromagnetic Wave Beams," *IRE Transactions on Antennas and Propagation*, **AP-9**, May 1961, pp. 248-256.

10.Y. Murao and T. Takano, "An Investigation on the Design of a Transmission Antenna and a Rectenna with Arrayed Apertures for Microwave Power Transmission," *Elec. Commun. Japan I*, **83**, 2000, pp. 1-9.

11.F. T. Ulaby, *Fundamentals of Applied Electromagnetics*, Englewood Cliffs, New Jersey, Prentice Hall, 2001.

12.A. Abbaspour-Tamijani and K. Sarabandi, "Planar Implementation of the Partially Overlapped Subarrays for Milimeterwave Beam Steerable Antenna Applications," IEEE MTT-S International Microwave Symposium *Digest*, **1**, June 2002, pp. 53-56.

13.M. Rahman, T. Ivanov, and A. Mortazawi, "A 26-MESFET Spatial Power-Combining Oscillator," *IEEE Microwave and Guided Wave Letters*, **7**, April 1997, pp. 100-102.

14.K. S. Ang, M. J. Underhill, and I. D. Robertson, "Balanced Monolithic Oscillators at K- and Ka- Band," *IEEE Transactions on Microwave Theory and Techniques*, **MTT-48**, February 2000, pp. 187-193.

15.R. Adler, "A Study of Locking Phenomena in Oscillations," *Proceedings of the IRE*, **34**, 1946, pp. 351-357.

UTC Time Step

On n'introduira pas de seconde intercalaire à la fin de juin 2005.
La différence entre UTI et le Temps Atomique International TAI est :
du 1er janvier 1999, 0h UTC, jusqu'à nouvel avis : UTC - TAI = -32 s
Des secondes intercalaires peuvent être introduites à la fin des mois de décembre ou de juin, selon l'évolution de UT1-TAI. Le Bulletin C est diffusé deux fois par an, soit pour annoncer un saut de seconde, soit pour confirmer qu'il n'y aura pas de saut de seconde à la prochaine date possible.

No positive leap second will be introduced at the end of June 2005.
The difference between UTC and the International Atomic Time TAI is :
from 1999 January 1, 0 h UTC, until further notice : UTC - TAI = -32 s
Leap seconds can be introduced in UTC at the end of the months of December and June, depending on the evolution of UT1-TAI. Bulletin C is mailed every six months, either to announce a time step in UTC, or to confirm that there is no time step at the next possible date.

Daniel GAMBIS
Director, Earth Orientation Center of IERS
Fax: +33 1-40 512291
E-mail: iers@obspm.fr

Traveling-Wave Photodetectors: A Review

G. Rangel-Sharp
R.E. Miles
S. Iezekiel

Abstract

The development and theory of traveling-wave photodetection is presented, along with examples of fabricated devices – both fully distributed and periodic – that have been developed since the early 1990s. Distributed photodetectors show tremendous potential for overcoming bandwidth-efficiency-power tradeoffs that are common with lumped devices. Traveling-wave devices are ultimately limited by velocity mismatch. However, other considerations, such as microwave loss and transit-time limitations, must be taken into account for a high-performance device.

1. Introduction

With current trends in communication calling for ever increasing data rates, long-range, high-speed links are a necessity. Optical technologies have been well proven to cope with the increasing demands, whereas purely electrical solutions cannot cope with the long distances and high bit rates involved in worldwide communications. A typical electro-optical link consists of a laser source, an external modulator, an optical amplifier link, and a photodetector. Additional elements, such as EDFAs (erbium-doped fiber amplifiers), low-noise electrical amplifiers, and signal conditioning elements, may also be employed. Therefore, there is much interest in the development of high-speed electro-optic/opto-electric devices, primarily modulators and photodetectors.

Vertically illuminated devices, such as the p-i-n photodiode, introduce a tradeoff between efficiency and bandwidth. In these devices, light is coupled in through the upper layers of the device and is absorbed as it travels through the structure (Figure 1). The absorption process generates electron-hole pairs, which then travel under the influence of the bias field to the device contacts, producing a photocurrent. The response of such devices depends on the time taken for the photo-induced carriers to reach the

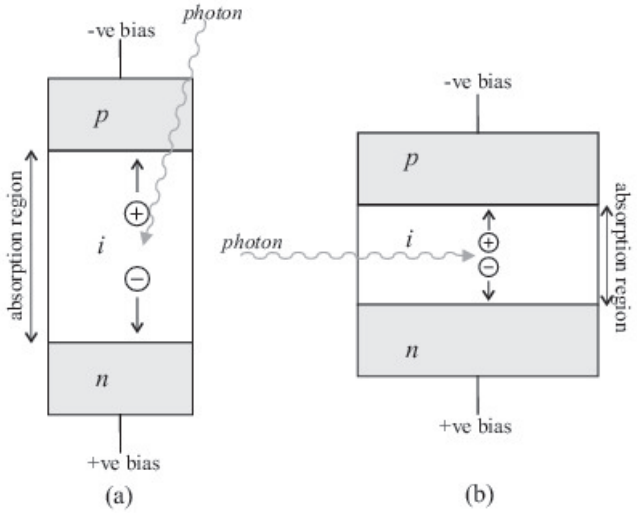

Figure 1. (a) A vertically illuminated photodetector. (b) An edge-coupled photodetector.

G. Rangel-Sharp, R. E. Miles, and S. Iezekiel are with the School of Electronic and Electrical Engineering, University of Leeds, Leeds, LS2 9JT, United Kingdom; Tel: +44 (0)113 343 2070; Fax: +44 (0)113 343 2032; E-mail: een7gdr@ieee.org (G. Rangel-Sharp); R.E.Miles@leeds.ac.uk; S.Iezekiel@leeds.ac.uk.

This is one of the invited *Reviews of Radio Science*, from Commission D.

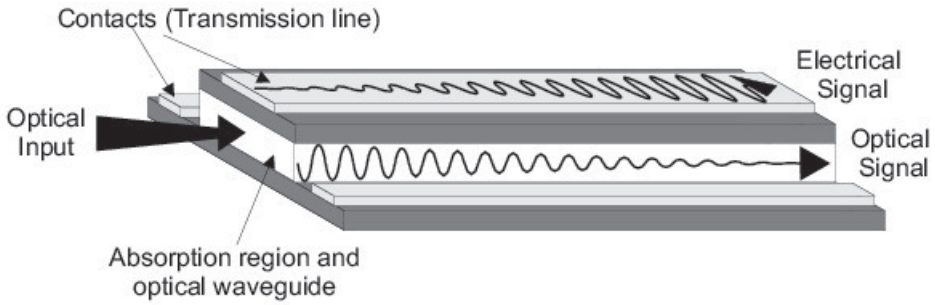

Figure 2. A traveling-wave photodetector.

contacts. This is termed the transit time, and is governed by the saturation velocity of the semiconductor material and the width of the active absorption region. The amount of light absorbed by the device is also dependent on the thickness of the active region and the absorption coefficient for that particular material. The amount of optical power absorbed is given by

$$P(d) = P_0\left[1 - e^{-\alpha_s(\lambda)d}\right], \qquad (1)$$

where $P(d)$ and P_0 are the total power absorbed in a distance d and the incident power, respectively. $\alpha(\lambda)$ is the optical absorption coefficient of the material in question. It follows that for improved efficiency, the device must be thick enough to absorb a large fraction of the incident power. This, however, contrasts with the requirement of a thin device to give high-speed/low-transit-time operation. The maximum bandwidth-efficiency product for typical single-pass VPDs (vertically illuminated photodetectors) has been found to be approximately 30 GHz [1].

Edge-coupled or waveguide-fed devices overcome this limitation by allowing the optical signal to enter through the edge of the device; hence, photo-induced carrier flow is orthogonal to the propagation of light. This allows the freedom to design long but narrow absorption regions, having both high efficiency and low transit times. However, device capacitance becomes significant due to the large-area narrow depletion region, leading to lumped-element *RC* limitations. Coupling and alignment problems also exist, since the light must be guided into an active region many times smaller than even the narrowest optical fiber, often less than 1 μm wide. Introduction of doped optical guiding layers around the absorption region can reduce this problem without adversely effecting transit times [2]. Typical bandwidth-efficiency limitations of edge-coupled devices are in the 55 GHz region [3].

With the introduction of EDFAs (erbium-doped fiber amplifiers) and higher power lasers, particularly in the 1550 nm window, optoelectronic devices must be able to handle high optical input powers and saturation currents, thus improving spurious free dynamic range, signal-to-noise ratios, and insertion loss [4]. Designs for high saturation currents require large absorption volumes, once again conflicting with bandwidth requirements.

The approaches listed above are considered to be lumped-element, since characteristics are dependent on the total device area and microwave impedance matching is often accomplished by additional resistive networks, rather than by device design. These lumped-element devices can no longer cope with the bandwidth-efficiency-power requirements of communications, today.

Distributed or traveling-wave photodetectors (TWPDs) were first proposed in the early 1990s, and are a development of the waveguide-fed photodetector, with contacts designed to support traveling waves. The photo absorption occurs in a distributed manner along the length of the device, such that it contributes to the overall electrical signal in the contact transmission line (Figure 2). In this manner, the device is no longer limited by the lumped *RC* time constants, but by velocity mismatch between the optical group velocity and the electrical phase velocity [2]. If the two waves travel coherently along the waveguides, the device is said to be velocity matched. This scheme allows the device to be much longer than standard edge-coupled devices, hence increasing absorption volume and therefore improving the saturation power [5].

Various traveling-wave photodetectors have been demonstrated using different device structures. These include p-i-n [3], MSM (metal-semiconductor-metal) [6], Schottky [7], and photo-transistor configurations [4], all showing excellent pulse response characteristics with transform bandwidths up to 570 GHz [6]. Figure 3 shows bandwidth-efficiency comparisons of the three main photodetector structures mentioned above.

2. TWPD Theory

Traveling-wave or distributed devices depend on the interaction of the co-propagating optical and electrical waves [14]. The device consists of a leaky optical waveguide core that permits an overlap of the optical-field profile into an active absorbing region. The effective absorption coefficient of the resulting structure is simply $\Gamma\alpha$, where Γ is the confinement factor of the waveguide, and α is the

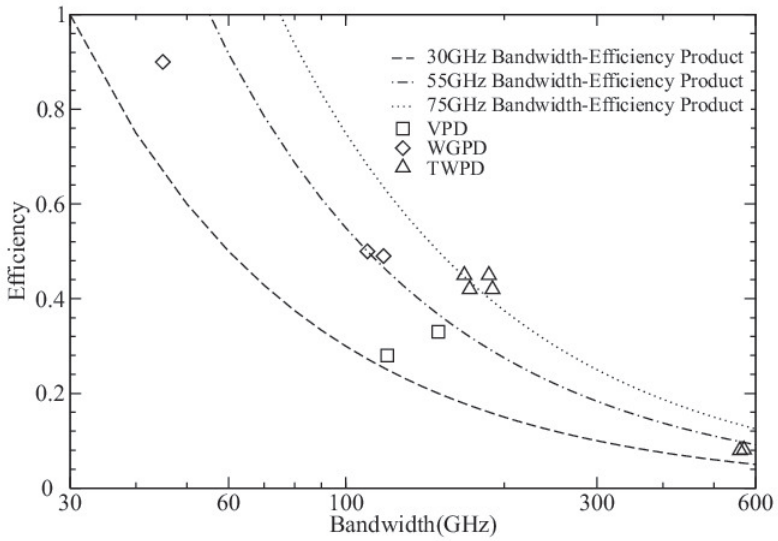

Figure 3. A comparison of bandwidth-efficiency products for VPD (vertically illuminated photodetector), WGPD (waveguide photodetector), and TWPD (traveling-wave photodetector) topologies [2-3, 8-13].

absorption coefficient of the active material. Hence, traveling-wave devices are generally much longer than their lumped-element equivalent devices, to ensure almost 100% absorption.

The extension of the device length allows the contacts to be designed to support the guiding of traveling electrical waves. Typically, the contact geometry approximates that of a coplanar transmission-line structure, and hence has been shown to support quasi-TEM mode propagation. In this manner, the device capacitance and the inductance of the contact strips characterize the transmission-line parameters, such as electrical phase velocity and characteristic impedance, rather than the lumped-element parasitic *RC* limitations[15].

The absorption of photons with energies above that of the material bandgap leads to a distributed generation of electron-hole pairs along the device. Under the influence of an applied bias field, this gives rise to a distributed current along the device that is then guided by the contact transmission-line structure to an output load. The current on the transmission line travels in both directions from its source: the forward-traveling wave in the direction of the optical signal, and the backwards wave traveling back towards the input of the device. If there is no matched electrical termination at the input end, the total received power will consist of the superposition of the forward wave and that reflected from the input. This leads to a general reduction in bandwidth, owing to the additional time lag of the reverse-traveling wave. If a matched termination is placed on the input, then the backwards wave is completely absorbed. However, 50% of the total power is lost in the termination.

Typically, at the frequencies of interest, the transmission-line structure on the photodetecting semiconductor layers causes what is known as slow-mode electrical propagation [16]. Essentially, the conductance of the doped semiconductor layers immediately below the transmission line, along with the capacitance caused by narrow depletion/intrinsic regions of the active device, cause electrical waves to travel much slower than if they were on a standard dielectric surface. Traditionally, rigorous analysis of this structure would require full-wave electromagnetic simulations. Giboney [15] applied a wave model to a parallel-plate p-i-n structure to evaluate field distributions in the device, and showed that the propagation was still, in fact, quasi-TEM in nature. As such, it can be satisfactorily represented by an equivalent-circuit transmission-line model (as used previously by many authors, e.g., [5, 15, 17, 18]), based on that of Hasegawa's [16].

An example of an equivalent-circuit representation of the traveling-wave structure is shown in Figure 4. The distributed photocurrent is shown as a longitudinal position-dependent current source, $I_{ph}(z)$, in parallel with a capacitance, *C*, representing the stored charge in the active intrinsic/depletion region. Z_{semi} is the impedance of the doped semiconductor layers outside the absorption region, and is normally modeled by a resistor and a capacitor in parallel [5]. The doping, however, is often high enough to allow the capacitance to be neglected. L_{cpw} is the inductance per unit length of the metal center strip, Z_{cpw} (which is normally assumed to be resistive) gives the conductor losses per unit length, and G_s is the parallel conductance of the semiconductor layers due to finite longitudinal drift currents. Following the usual analysis, the characteristic impedance (Z_0) and complex propagation coefficient (γ) of the transmission line can be found from

$$Z_0 = \sqrt{\frac{Z}{Y}} = \sqrt{\frac{\left(j\omega L + Z_{cpw}\right)\left(1 + j\omega C Z_{semi}\right)}{j\omega C\left[1 + G_s\left(j\omega L + Z_{cpw}\right)\right]}}, \quad (2)$$

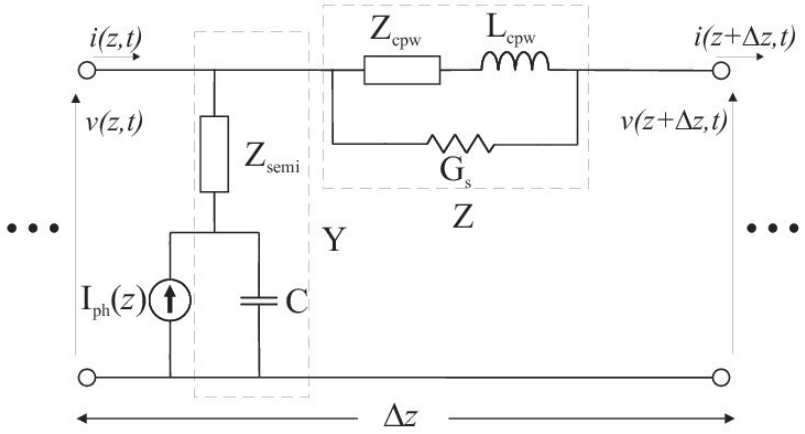

Figure 4. The equivalent circuit for a traveling-wave photodetector structure, assuming quasi-TEM-mode propagation.

$$\gamma = \sqrt{ZY} = \sqrt{\frac{j\omega C\left(j\omega L + Z_{cpw}\right)}{\left(1 + j\omega C Z_{semi}\right)\left[1 + G_s\left(j\omega L + Z_{cpw}\right)\right]}} \,. \quad (3)$$

If the elements attributed to loss (Z_{cpw} , Z_{semi} , and G_s) approach zero, Equations (2) and (3) reduce to the ideal lossless transmission-line form of $\sqrt{L/C}$ and $j\omega\sqrt{LC}$, respectively.

In most cases, the values for the equivalent-circuit components are assumed to be frequency independent, and only the conductor loss, Z_{cpw} , varies continuously with frequency, due to the skin effect. The values used for the simulation are typically determined either analytically from the device geometry, from RF measurements, or from full-wave EM analysis of structures. Depletion-layer capacitance is often approximated for diode structures by calculating the width (*d*) and the area (*a*) of the depletion layer, such that $C \approx \varepsilon_0 \varepsilon_r a/d$. For more complicated structures, this can be found from *C-V* measurements or physical device models [19]. The semiconductor impedance, Z_{semi} , can be found once layer doping is known. However, effects of the parallel semiconductor conductance must be simulated or extracted from *S*-parameter measurements, since the field penetration into this region is not easily found analytically. The stripline inductance can often be estimated from conductor dimensions and known material parameters; however, due to the multilayer non-perfect dielectric substrates, EM simulation or RF measurements often give more accurate values.

Once the passive device elements are known, the photocurrent must be included to complete the equivalent-circuit model. In the simplest case, the distributed-current source, I_{ph} , is proportional to the absorbed power at each point:

$$I_{ph}(z) = P_0 \frac{\eta q \lambda}{hc} \Gamma\alpha_0 e^{(j\beta_0 - \Gamma\alpha_0)z} \,, \quad (4)$$

where P_0 is the incident optical power at a wavelength λ , $\Gamma\alpha_0$ is the effective optical absorption coefficient, β_0 is the optical phase constant, and η is the quantum efficiency. This gives the photocurrent generated per unit length, assuming a fraction η of the absorbed optical power at a point *z* generates a current that appears immediately on the electrical transmission line. Such an approach is fairly easy to implement with a transmission-line model, although carrier transit-time effects are completely neglected. A more sophisticated approach was taken by Malcoci et al. [17, 20], in which they developed an analytical expression for the photocurrent based on simplified drift-diffusion carrier-transport equations. In this way, carrier generation and transit effects are included, as well as transport through the non-absorbing layers.

In order to model the device using the transmission-line method, the telegrapher's equations, arising from the equivalent circuit, must be solved for specified boundary and initial conditions. Boundary conditions for this model represent the type of termination at either end of the transmission line. Two possibilities in particular are most informative for the analysis of traveling-wave devices. The first is a matched termination at the output and an open-circuit termination at the input side, leading to reflection of the backwards-traveling wave to the output load. The second involves matched terminations at either end of the device, leading to complete absorption of the reverse traveling wave [21].

Even with the simplified approach taken with the equivalent-circuit modeling of traveling-wave devices, good correlation has been attained between measured and simulated results, as in Figure 5 and in [21], for example. The good agreement that has been seen between numerical and measured data is generally limited to the small-signal case. In large-signal operation, however, various sources of nonlinearity occur within the device. The electrical transmission-line characteristics are dependent on line capacitance and inductance. The major factor determining

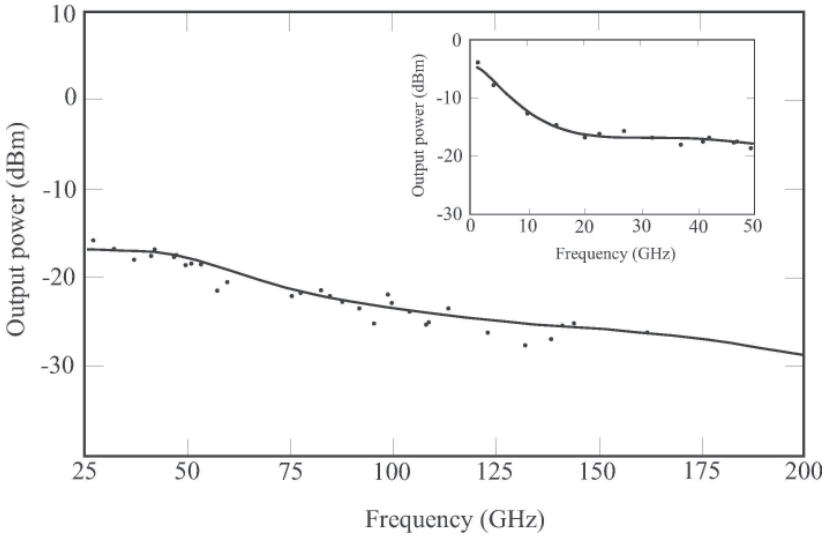

Figure 5. The experimental (circles) and numerical (solid line) broadband output power of a traveling-wave photodetector. The inset shows the low-frequency (<50 GHz) response (after Stöhr et al. [17]).

the line capacitance arises from the junction capacitance, *C*, in Figure 4. Under bias, this capacitance is a function of the depletion-region width and, hence, local voltage. This, in turn, is affected by the traveling electrical signal from the distributed photocurrent source. As a further complication, the carrier transit times and absorption rates are affected by the local electric field. Capelluti et al. [18] gave an excellent discussion of these effects from the point of view of traveling-wave electro-absorption modulators (TW-EAMs), and suggested a fully coupled device and electrical transmission-line model.

2.1. Velocity-Mismatch Bandwidth Limitations

It has already been said that in an ideal traveling-wave device, the bandwidth is not limited by lumped *RC* time constants, but rather by a mismatch between the electrical phase velocity and the optical group velocity. Giboney et al. derived an expression for the impulse current response of a traveling-wave photodetector, limited only by velocity mismatch [15]. Applying a Fourier transform to this leads to a normalized mismatch-limited frequency response described by

$$i_{vm}(\omega)=\frac{1}{2}\left(\frac{\omega_f}{\omega_f-j\omega}+\gamma(\omega)\frac{\omega_r}{\omega_r+j\omega}\right)e^{-j\omega\frac{l}{v_e}}, \quad (5)$$

where $i_{vm}(\omega)$ is the normalized output current at frequency ω, and γ is the reflection coefficient of the input termination ($\gamma=0$ for matched input, $\gamma=1$ for open-circuit input). ω_f and ω_r are the characteristic frequencies of the forward- and reverse-traveling waves, given by

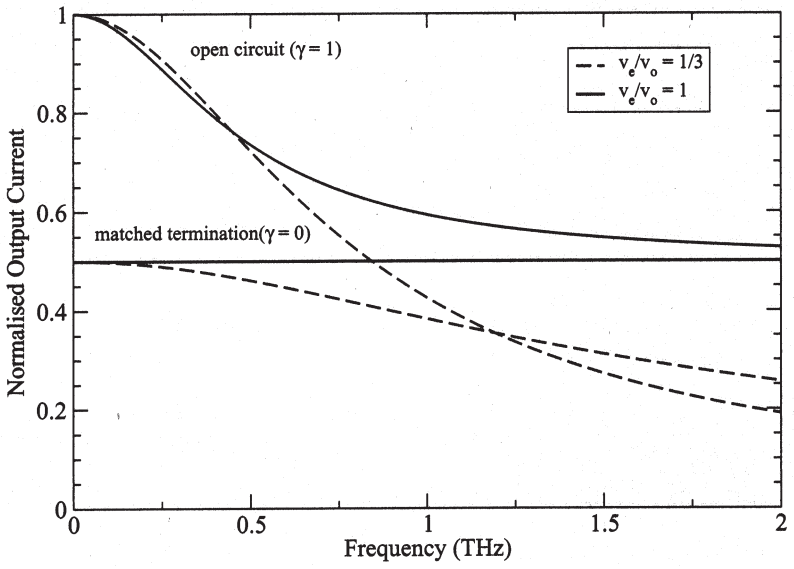

Figure 6. The normalized output current as a function of frequency for matched and open-circuit input termination for the velocity-matched case ($v_e/v_o=1$) and a velocity mismatched case ($v_e/v_o=1/3$). v_e was kept constant for all curves (after [15]).

$$\omega_f = \Gamma\alpha v_e / (1 - v_e/v_o), \quad (6)$$

$$\omega_r = \Gamma\alpha v_e / (1 + v_e/v_o). \quad (7)$$

Figure 6 shows the normalized output current as a function of frequency for a traveling-wave photodetector limited only by velocity mismatch using the above equations. It can be seen from Equation (5) in the $\gamma = 0$ case (matched input termination) that the reverse-traveling wave has no effect on the frequency response. For the velocity-matched case ($v_e = v_o$), there is no frequency dependence at all, i.e., infinite bandwidth. However, the termination does absorb half of the generated photocurrent, and so the maximum efficiency is reduced to 50%. Hence, in the open-circuit velocity-matched case, although there is a finite bandwidth, the output current is higher than in the $\gamma = 0$ case over the entire frequency range, the two responses converging only asymptotically.

For the velocity-mismatched condition, $v_e = v_o/3$, the $\gamma = 0$ response has less frequency dependence than the open-circuit ($\gamma = 1$) case. As such, the bandwidth of the open-circuit device is lower than the traveling-wave photodetector with a matched input load. However, the open-circuit device has a greater output current over the entire bandwidth range of the matched traveling-wave photodetector. Hence, devices with input terminations generally have worse bandwidth-efficiency performance than open-circuit devices [14], not to mention the difficulties involved in placing input terminations without affecting optical coupling efficiency.

Analysis of the single-pole, matched-input termination case of Equation (5) leads to a velocity-mismatch limited bandwidth given by [15]

$$B_{vm0} = \frac{\Gamma\alpha}{2\pi} \frac{v_e}{1 - v_e/v_o}. \quad (8)$$

Referring to Figure 6, the $\gamma = 1$ curves show little change in bandwidth due to velocity matching. In fact, over the range $0 \le v_e / v_o \le 1.47$, the bandwidth shows almost no variation with v_o, and is given approximately by [15]

$$B_{vm1} \approx \frac{\Gamma\alpha v_e}{3\pi}. \quad (9)$$

Hence, in the open-circuit configuration, the bandwidth is proportional to the electrical wave velocity rather than to the mismatch factor and, hence, the speed of the electrical wave should be maximized. According to this equation, the bandwidth can be increased even when the electrical velocity exceeds that of the optical group velocity. However, for $v_e > 1.47 v_o$ this equation is no longer valid, and the curve of bandwidth as a function of v_e saturates to a limit dependent on $\Gamma\alpha$, the effective absorption coefficient [5].

Murthy et al. [22] investigated a structure designed to cancel the backwards-reflected wave using a tapered impedance line and a periodic structure. Partial reflections of the forward traveling wave at each taper interface canceled out the induced reverse-traveling wave, rather than it being absorbed. In this manner, the bandwidth can be improved, as with the matched-input case, without sacrificing the power lost to the input load.

2.2. Microwave loss

Apart from the fundamental velocity-mismatch bandwidth limitation of traveling-wave devices, frequency-dependent electrical losses can be significant. The placement of metal coplanar transmission lines on doped semiconductor multilayer structures is far from an ideal dielectric structure. The loss mechanisms arise from the series layer impedance, Z_{semi}, in Figure 4; the parallel semiconductor conductance, G_s; and the frequency-dependent metal impedance, Z_{cpw}, due to the skin-effect nature of the propagation.

The microwave attenuation factor can be determined from the real part of the complex propagation coefficient given in Equation (3). Giboney et al. gave an approximation, ignoring the skin effect, which was proportional to the square of the frequency:

$$\alpha \approx \frac{\omega^2}{2v_e}\left(Z_{semi}C + G_s L_{cpw}\right). \quad (10)$$

The increase in resistance due to the skin effect is normally taken as being proportional to the square root of the frequency [17]. The other factors limiting bandwidth – velocity mismatch and transit times – only have an effect where photo-absorption takes place. Traveling-wave photodetectors much longer than the absorption region show a length dependence on measured bandwidth that must be due purely to microwave losses. Deconvolution of measured responses of long traveling-wave photodetectors can then be used to calculate the propagation coefficient more accurately [3]. Results from such a calculation show an initial ω^2 dependence on loss, as predicted above; however, as the frequency increases, it tends to a $\sqrt{\omega}$ dependence as the skin effect or quasi-TEM type propagation becomes more dominant [5].

2.3. Carrier Transit/Trapping Time

The temporal response of all photodetectors, lumped or distributed, is affected somewhat by carrier transit and trapping times. Devices such as vertically illuminated photodetectors, which typically have wide absorption areas, are the worst affected by carrier transit times. The pulse

response of a wide absorption region is determined by the time it takes for the photo-induced carriers to reach the contacts. This can have a wide spread of values, since the carriers can be generated anywhere in the absorption region. In EGPDs and traveling-wave photodetectors, the absorption width is much narrower than in vertically illuminated photodetectors, and so a well-designed device would be limited more by velocity mismatch/microwave loss than by transit-time limitations.

Photodetector frequency response is also dependent on the carrier lifetimes, determining the rate at which carriers can recombine. Clearly, long lifetimes lead to a slow detector response and, hence, should be minimized. Use of low-temperature-grown (LTG) materials, particularly GaAs, in photodetectors leads to very short carrier-trapping times, of the order of 300 fs [8].

Semiconductor currents are due to the motion of charged carriers, electrons, and holes. Often, hole transport is much slower than electron, and, hence, the limiting factor due to carrier transit/trapping is due to the slower hole current. This has lead to the introduction of UTC (Uni-traveling-Carrier) structures, in which the absorption layer is p-type and, as such, the generated holes are majority carriers. It is the minority electrons that are the dominant carriers, greatly increasing the bandwidth potential of the devices [23].

3. Periodic TWPDS (P-TWPDS)

Up to now, only fully-distributed traveling-wave devices have been discussed. It is possible, however, to design a traveling-wave structure by placing lumped photodetectors periodically on an electrical transmission line (Figure 7). This approach is generally used when attempting to increase the saturation power of a detector structure. As mentioned previously, lumped elements often have a speed/saturation power tradeoff, due to the downscaling of sizes for high-speed operation, leading to high power densities. Simply placing more devices in parallel increases the effective area of the device and, hence, increases power-handling capabilities. However, the device capacitances also add, leading to reduced *RC*-limited bandwidths. Parallel placement on an electrical transmission line – again, with suitable matching between optical and electrical wave velocities – prevents the summation of device capacitance in a similar manner to the fully distributed devices.

The use of a periodic structure generally gives increased design flexibility, allowing separate design of the CPW (coplanar waveguide) and individual detector elements. It is also apparent that since the active regions are now separate and, hence, non-continuous, the parallel conductance, G_S, associated with longitudinal current flow in the doped semiconductors has been eliminated, along with its associated attenuation [15]. In this manner, the transmission-line structure approaches that of an ideal coplanar-waveguide line; however, it is still periodically loaded. If the distance between the lumped elements is much shorter than the intended wavelengths, $d < \lambda/10$, then the capacitance per unit length of the loaded line can be considered to be an average of the coplanar waveguide and the individual detector elements [21]. In such a way, the characteristics of the line can be easily tailored for impedance and velocity matching by coplanar waveguide and photodetector design along with the choice of *d*, the distance between detector elements. Assuming lossless transmission lines,

$$v_e(\omega) = \frac{1}{\sqrt{\left[C_{cpw}(\omega) + C_{pd}/d\right] L_{cpw}(\omega)}}, \quad (11)$$

$$Z_0(\omega) = \sqrt{\frac{L_{cpw}(\omega)}{C_{cpw}(\omega) + C_{pd}/d}}. \quad (12)$$

The reduced capacitance of the periodic structure prevents slow-wave propagation; hence, the characteristic impedance and electrical wave velocities can be increased much higher than in the fully-distributed case. An important feature of the periodic structure is the ability to implement impedance tapering using different-sized lumped elements and stepped changes in the coplanar waveguide dimensions. A decreasing impedance towards the output load would reflect the reverse-traveling wave at each step change, leading to a cancellation of the backwards wave, and improving the velocity-mismatch bandwidth without sacrificing efficiency, as in the fully-distributed structure [24].

The high-frequency limitations of the periodic traveling-wave photodetector arise from the bandwidths of the individual lumped detectors, velocity mismatch, and microwave losses. However, in a well-designed structure, the microwave-loss limitations and velocity-mismatch bandwidths would be much higher than those of the individual devices. The major drawback of the periodic structures is the difficulty in fabricating the complex structure, compared to the uniformity of the fully distributed devices. Increased optical scattering and reflections caused by the complex structure can also degrade performance, especially due to imperfections in the fabrication process.

4. Recent TWPD Devices

4.1. Fully Distributed Devices

The first traveling-wave photodetectors to be fabricated were based on a GaAs-AlGaAs p-i-n structure, and showed the greatest bandwidth and bandwidth-efficiency products for a p-i-n structure without gain at that

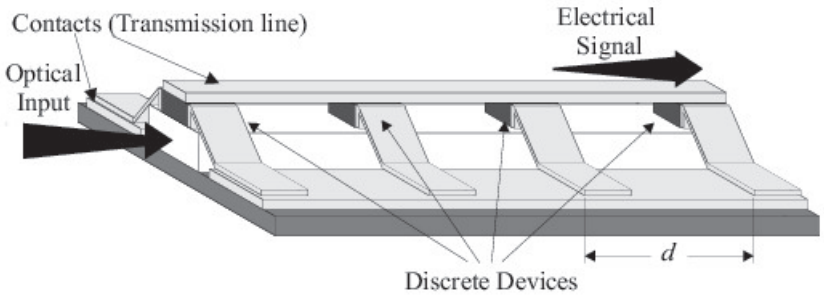

Figure 7. A schematic representation of a periodic traveling-wave photodetector (P-TWPD) structure.

time: 172 GHz and 76 GHz in 1995 [3]. This showed the enormous potential for traveling-wave devices in high-speed, high-efficiency applications. The co-planar contact structure was designed such that the 1 μm device had a characteristic impedance of 50 Ω, and had no termination at the input (open circuit). Other waveguide photodetectors (WGPDs) and vertically illuminated photodetectors were also fabricated on the same wafer to enable direct performance comparisons. Pulse responses for the different devices were measured to calculate bandwidth, whilst quantum efficiencies were found from simple dc measurements. Not only were the excellent results above found for the traveling-wave photodetector, the 2 × 9 μm^2 waveguide photodetector exhibited better performance than had been previously reported, with a 57 GHz bandwidth-efficiency product. However, the value for the traveling-wave photodetector structure was still 33% higher. Bandwidth measurements of the different device structures as a function of junction area were given, and showed that the traveling-wave photodetector devices were not affected by the same *RC* limitations of the lumped-element devices (Figure 8). The vertically illuminated photodetector and waveguide photodetector devices both showed an inverse-proportionality relationship between bandwidth and junction area, and thus capacitance. The traveling-wave photodetector bandwidth, however, had little variation initially with increasing area, up to approximately 20 μm^2. The limitations

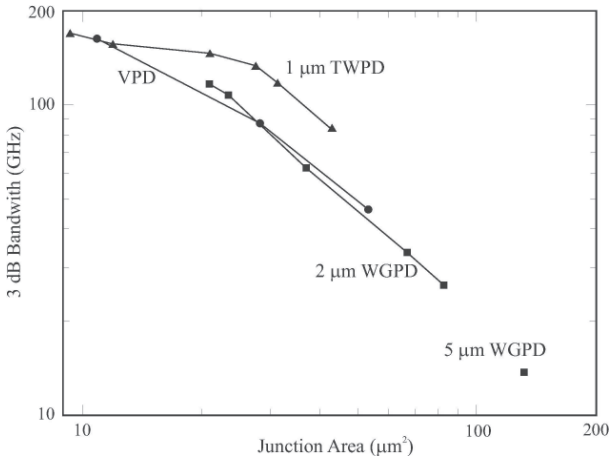

Figure 8. A comparison of the bandwidths of TWPDs (traveling-wave photodetectors, triangles), WGPDs (waveguide photodetectors, squares), and VPDs (vertically illuminated photodetectors, circles) as a function of the junction area (after [3]).

normally attributed to traveling-wave devices, such as velocity mismatch, have no effect once all the incident light has been absorbed. Hence, the decrease in bandwidth with increasing length after this point was due to the microwave loss of the contact transmission lines.

A further paper from the same author [9] calculated corrected bandwidth measurements, taking into account pulse widths and spreading of the input optical signal due to fiber coupling. This gave an improved bandwidth of 190 GHz and a bandwidth-efficiency product of 84 GHz.

A second group [21] also presented the fabrication and measurements of a similar traveling-wave photodetector in the same year; however, the primary design criteria was to optimize power handling while retaining high-bandwidth operation. As has been mentioned, high-power operation is often attributed to traveling-wave devices since they typically have a much larger absorption volume than lumped elements, whilst retaining high-bandwidth operation. This calls for a relatively low optical-confinement factor in the active detection region, such that a long device can be fabricated, in which the power is absorbed over an extended region and, hence, power density is reduced. Due to the exponential nature of optical absorption, it can be seen that the peak power absorption occurs at the input facet of the device ($x = 0$ in Equation (14)), and can be controlled by the choice of $\Gamma\alpha$ from the optical-waveguide design:

$$P(x) = P_0 \Gamma \alpha_s e^{-\Gamma \alpha_s x}, \tag{13}$$

$$P(0) = P_0 \Gamma \alpha_s \cdot \tag{14}$$

The power-handling considerations are expressed in terms of temperature rise, and it was shown that in principle, a traveling-wave photodetector can be designed to cope with an input power level up to that which causes catastrophic optical damage to the semiconductor facet (approximately 5 MW/cm^2) by the choice of these parameters. Preliminary measurements of the device, however, showed a low bandwidth of approximately 4.8 GHz, well below the predicted value of 14 GHz. The drawback with the high-power designs is that the device length needed to distribute the power absorption again leads to microwave losses in the microwave transmission line, which, for this design, can be excessive.

A novel progression from the previous traveling-wave photodetectors involves the use of a transistor photo-detection structure. The electrons generated by photo-absorption in the reverse-biased base-collector depletion region travel to the collector electrode, as in a simple p-i-n structure. The holes, however, travel towards and get trapped in the base, causing a change in the base potential. Normal transistor action then takes place, in which many electrons are injected from the emitter for every hole entering the base, dependant on the injection efficiency of the structure. In this manner, the efficiency of the device can be artificially increased beyond 100% and, hence, bandwidth-efficiency products can also be increased. The approach taken by Scott et al. [4] was to integrate a polyimide optical waveguide on top of the traveling-wave HPT (heterojunction phototransistor), rather than to build the optical guide in the layer structure, itself. In this manner, the transistor dimensions can be optimized separately to the optical guide, hence reducing overall design complexity. Results show a dc optical gain of 13.5 for a 200 μm device, and no compression was found with a dc photocurrent of up to 50 mA at 60 GHz.

Chiu et al. [8] reported a p-i-n traveling-wave photodetector based on LTG-GaAs that was used in the absorbing layer. The use of the low-temperature-grown material leads to reduced carrier lifetimes and, hence, improved high-frequency response. However, the reduced carrier lifetimes also lead to a reduction in efficiency, since a greater proportion of generated electron-hole pairs recombine before they reach the contacts. The dc efficiency of this device was limited to only 8%; however, optical pulse measurements gave a 530 fs FWHM output, corresponding to an exceptional bandwidth of approximately 560 GHz.

Alles et al. [7] fabricated a traveling-wave photodetector structure using a Schottky barrier active absorption region. The intended use of the device was in optical heterodyne photo-mixing for analog optical links; hence, the device was primarily intended to give a high power-conversion efficiency, rather than ultra-high-frequency performance. Nevertheless, measurements indicated that a high conversion efficiency of 0.3 A/W was attained at a respectable frequency of 60 GHz.

More recently, MQW (multi-quantum-well) p-i-n traveling-wave photodetector structures have also been used for optical heterodyne millimeter-wave generation [25]. Strain was applied to the MQW structure to reduce absorption sensitivity to optical field polarization. The detector exhibited a dc responsivity of 0.2 A/W, and showed millimeter-wave generation beyond 160 GHz for the first time.

4.2. Periodic Devices

One of the earliest periodic traveling-wave photodetectors was reported by Wu et al. [26]. It consisted of periodically spaced ultra-fast 200 GHz photodetectors on an input optical waveguide. The output electrical transmission line connected to each device, but wound around the optical guide to increase the electrical path length with respect to the optical path, which enabled phase matching, due to the faster electrical wave propagation. The total efficiency was a summation of the individual devices. Theoretical models predicted an efficiency of 92% and bandwidths over 100 GHz, limited more by electrical loss than either velocity mismatch or lumped-element parasitics. A high-power device, capable of producing 56 mA saturation current and an instrument-limited bandwidth at 49 GHz for a three-element detector was reported by the same group [27]. Increasing the number of elements was found to increase the output power and efficiency; however, the increase in device length led to low bandwidths, due to increased microwave losses.

Goldsmith et al. [28] described a periodic device that was novel in two respects. Firstly, the structure was the first to be reported using commercially available photodetectors, hence reducing fabrication costs. Secondly, the elements were placed periodically on an electrical waveguide, and the optical signals were coupled in parallel, rather than serially, as described previously. An optical splitter was used to distribute the input optical signal among a number of separate fibers, which each fed a single device. Velocity matching was performed by using varying lengths of input fiber for each device, corresponding to the difference in electrical time delay between each element. In this manner, each device received equal signal power, whereas for the serial feed the power handling is limited by the first element that receives the highest signal. A four-element detector exhibited a frequency response almost exactly the same as the individual detector responses; however, a 13 dB increase in RF output signal was possible. The measured responsivity, including fiber-splitter losses, was found to be 0.7 A/W. Results showed clearly that devices can be combined on a traveling-wave structure without substantially affecting the overall bandwidth, while considerably increasing power handling.

5. Conclusion

The operating principles of traveling-wave photodetectors, both fully distributed and periodic, have been discussed. In principle, the only high-speed limitation of fully distributed devices is due to velocity mismatch. However, in practice, transit times and microwave losses due to imperfect dielectric transmission lines often have a greater effect on device bandwidth. Periodically distributed devices are generally limited by the lumped elements of which they consist. However, saturation power and efficiency are improved dramatically over the single-element case. Periodic structures allow more degrees of freedom in the design, and allow more control over microwave velocities and impedance, than the fully distributed devices. However, the potential has been shown for traveling-wave structures, either periodic or continuous, to allow considerable

improvements in bandwidth, power handling, and efficiency over single lumped-element devices, characteristics that are required by the communications industry of today.

6. References

1. J. E. Bowers and C. A. Burrus, "Ultrawide-Band Long-Wavelength p-i-n Photodetectors," *Journal of Lightwave Technology*, **LT-5**, 10, 1987, pp. 1339-1350.

2. K. Kato, "Ultrawide-Band/High-Frequency Photodetectors," *IEEE Transactions on Microwave Theory and Techniques*, **MTT-47**, 7, 1999, pp. 1265-1281.

3. K. S. Giboney, R. L. Nagarajan, T. E. Reynolds, S. T. Allen, R. P. Mirin, M. J. W. Rodwell, and J. E. Bowers, "Travelling-wave Photodetectors with 172-GHz Bandwidth and 76-GHz Bandwidth-Efficiency Product," *IEEE Photonics Technology Letters*, **7**, 4, 1995, pp. 412-414.

4. D. C. Scott, D. P. Prakash, H. Erlig, M. A. Bhattacharya, H. R. Fetterman, and M. Matloubian, "High Power, High Frequency Traveling Wave Heterojunction Phototransistors with Integrated Polyimide Waveguide," *IEEE International Microwave Symposium Proceedings*, 1998, pp. 1237-1240.

5. J-W. Shi and C-K. Sun, "Design and Analysis of Long Absorption-Length Traveling-Wave Photodetectors," *Journal of Lightwave Technology*, **18**, 12, 2000, pp. 2176-2187.

6. J-W. Shi, K-G. Gan, Y-J. Chiu, Y-H. Chen, C-K. Sun, Y-J. Yang, and J. E. Bowers, "Metal-Semiconductor-Metal Traveling-Wave Photodetectors," *IEEE Photonics Technology Letters*, **16**, 6, 2001, pp. 623-625.

7. M. Alles, U. Auer, F-J. Tegude, and D. Jäger, "Distributed Velocity-Matched 1.55 µm InP Travelling-Wave Photodetector for Generation of High Millimeterwave Signal Power," *IEEE International Microwave Symposium Proceedings*, 1998, pp. 1233-1236.

8. Y-J. Chiu, S. B. Fleischer, and J. E. Bowers, "High-Speed Low-Temperature-Grown GaAs p-i-n Traveling-Wave Photodetector," *IEEE Photonics Technology Letters*, **10**, 7, 1998, pp. 1012-1014.

9. K. S. Giboney, M. J. W. Rodwell, and J. E. Bowers, "Traveling-wave Photodetector Design and Measurements," *Selected Topics in Quantum Electronics*, **2**, 3, 1996, pp. 622-629.

10. J-W. Shi, K-G. Gan, Y-J. Chiu, Y-H. Chen, C-K. Sun, Y-J. Yang, and J. E. Bowers, "Ultra-high Bandwidth (570 GHz) Metal-Semiconductor-Metal Traveling-Wave-Photodetectors," APMC2001, 2001, pp. 358-361.

11. G. Unterbörsch, D. Trommer, A. Umbach, and G. G. Mekonnen, "High-Bandwidth 1.55 ìm Waveguide Integrated Photodetector," Indium Phosphide and Related Materials, 1996, pp. 251-254.

12. E. Özbay, K. D. Li, and D. M. Bloom, "2.0 ps, 150 GHz GaAs Monolithic Photodiode and All-Electronic Sampler," *IEEE Photonics Technology Letters*, **3**, 6, 1991, pp. 570-572.

13. I-H. Tan, C-K. Sun, K. S. Giboney, J. E. Bowers, E. L. Hu, B. I. Miller and R. J. Capik, "120-GHz Long-Wavelength Low-Capacitance Photodetector with an Air-Bridged Coplanar Metal Waveguide," *IEEE Photonics Technology Letters*, **7**, 12, 1995, pp. 1477-1479.

14. K. S. Giboney, M. J. W. Rodwell, and J. E. Bowers, "Traveling-Wave Photodetectors," *IEEE Photonics Technology Letters*, **4**, 12, 1992, pp. 1363-1365.

15. K. S. Giboney, M. J. W. Rodwell, and J. E. Bowers, "Traveling Wave Photodetector Theory," *IEEE Transactions on Microwave Theory and Techniques*, **MTT-45**, 8, 1997, pp. 1310-1319.

16. H. Hasegawa, M. Furukawa, and H. Yanai, "Properties of Microstrip Line on Si-SiO_2 System," *IEEE Transactions on Microwave Theory and Techniques,* **MTT-19**, 11, 1971, pp. 869-881.

17. A. Stöhr, R. Heinzelmann, A. Malcoci, and D. Jäger, "Optical Heterodyne Millimeter-Wave Generation Using 1.55-µm Traveling-Wave Photodetectors," *IEEE Transactions on Microwave Theory and Techniques*, **MTT-49**, 10, 2001, pp. 1926-1933.

18. F. Cappelluti and G. Ghione, "Self-Consistent Time-Domain Large-Signal Model of High-Speed Traveling-Wave Electroabsorption Modulators," *IEEE Transactions on Microwave Theory and Techniques*, **MTT-51**, 4, 2003, pp. 1096-1104.

19. G. D. Rangel-Sharp, R. E. Miles, and S. Iezekiel, "Towards a Physical Model for the Study of Travelling Wave photo-HBTs," Nefertiti Workshop on Microwave Phototransistors, Budapest, Hungary, 2003, (available at HTTP://www.diamond-congress.hu/diamond/uploaded/ 11/full1/228_155_1.pdf).

20. A. Malcoci, A. Stöhr, R. Heinzelmann, K. Hagedorn, R. Güsten, H. Schäfer, H. Stüer, F. Siebe, P. van der Wal, V. Krozer, M. Feiginov, and D. Jäger, "Photonic (Sub)Millimeterwave Local Oscillators," *Proceedings of Microwaves, Radar and Wireless Communications, 2002, MIKON-2002*, **3**, pp. 722-734.

21. V. Hietala, G. A. Vawter, T. M. Brennam, and B. E. Hammons, "Traveling-Wave Photodetectors for High-Power, Large-Bandwidth Applications," *IEEE Transactions on Microwave Theory and Techniques*, **MTT-43**, 9, 1995, pp. 2291-2298.

22. S. Murthy, S-J. Kim, T. Jung, Z-Z. Wang, W. Hsin, T. Itoh, and M-C. Wu, "Backward-Wave Cancellation in Distributed Traveling-Wave Photodetectors," *IEEE Journal of Lightwave Technology*, **21**, 12, 2003, pp. 3071-3077.

23. Y. Hirota, E. Ishiwata, and H. Ito, "1.55-µm Wavelength Periodic Traveling-Wave Photodetector Fabricated using Unitraveling-Carrier Photodiode Structures," *Journal of Lightwave Technology*, **19**, 11, 2001, pp. 1751-1758.

24. J-W. Shi and C-K. Sun, "Theory and Design of a Tapered Line Distributed Photodetector," *Journal of Lightwave Technology*, **20**, 11, 2002, pp. 1942-1950.

25. A. Stöhr, R. Heinzelmann, A. Malcoci, and D. Jäger, "Ultra-broadband 160 GHz InGaAsP Photodetector for Photonic LO," *Proceedings of 27th European Conference on Optical Communications*, Amsterdam, 2001, pp. 562-563.

26. M. C. Wu and T. Itoh, "Ultrafast Photonic-to-Microwave Transformer (PMT)," LEOS 1993, 1993.

27. L. Y. Lin, M. C. Wu, T. Itoh, T. A. Vang, R. E. Muller, D. L. Sivco, and A. Y. Cho, "High-speed Photodetectors with High Saturation for High Performance Microwave Photonic Systems," *Proceedings of 1996 International Topical Meeting on Microwave Photonics*, 1996, pp. 313-316.

28. C. L. Goldsmith, G. A. Magel, and R. J. Baca, "Principles and Performance of Traveling-Wave Photodetector Arrays," *IEEE Transactions on Microwave Theory and Techniques*, **MTT-45**, 8, 1997, pp. 1342-1350.

Advances in Radiated EMC Measurement Techniques

Perry F. Wilson

Abstract

Recent research on radiated electromagnetic compatibility measurement techniques is reviewed. Our focus is on both widely used test methods (open-area test sites, anechoic chambers, TEM devices) and on emerging methods (reverberation chamber, near-field techniques). The challenges related to using these facilities for immunity and emissions tests are highlighted, particularly at higher frequencies, where test objects can have complicated radiation patterns.

1. Introduction

Electromagnetic compatibility (EMC) measurements seek to identify and reduce the effects of electromagnetic interference (EMI) on the performance of electronic equipment and systems. EMC standards specify tests to quantify the performance of a test object as either a victim (immunity) or source (emission) of EMI. More fundamental is research on basic electromagnetic coupling mechanisms, and on the design of electronics to mitigate EMI and to advance EMC. This article will focus on radiated fields for EMC measurements, specifically, the techniques used to characterize how electronic systems couple energy and create interference. These test methods originally had as a primary goal the prevention of interference to broadcast signals, such as television and radio. However, as digital and wireless devices have proliferated and as their operational frequencies have moved well away from the broadcast bands, the emerging goal is to avoid direct interference among digital and wireless devices, themselves. This article will highlight the EMC measurement challenges presented by the changing electronic landscape.

2. Radiated EMC Measurement Techniques

The simplest radiated test environment is an ideal free space with plane-wave coupling. Thus, EMC measurements typically are made in facilities that either approximate free space (a fully anechoic chamber), or approximate an ideal half-space (an open-area test site, or OATS, or a semi-anechoic chamber). Plane-wave coupling can also be approximated using the transverse electromagnetic (TEM) mode in a planar transmission line (striplines, TEM cells). Time-domain techniques that window out reflections can also be used to simulate an ideal free space or half space. An alternative to these well-controlled coupling environments is the reverberation chamber. In a reverberation chamber, a highly nonuniform electromagnetic field is varied multiple times such that on average it has plane-wave-like characteristics. All of the above techniques seek to produce plane-wave coupling and are inherently far-field methodologies. Recently, near-field techniques are also finding application to EMC tests.

This paper will briefly review advances in radiated EMC measurement techniques. In particular, current research on open-area test-site, anechoic-chamber, transmission-line, reverberation-chamber, and near-field measurement techniques for EMC testing will be highlighted. Immunity and emission testing will be discussed for each method, although this separation is at times artificial in reciprocal problems.

An important issue for the EMC engineer, when faced with characterizing a device, is which of the above test methods to select. Ideally, the methods are equivalent, in the sense that if pass/fail limits on radiated immunity or emissions exist, then a device that passes in one facility will pass in another, and a device that fails at one facility will fail at another. Thus, significant work has been done to correlate data among methods. Unfortunately, this is a difficult task for all but the simplest of test objects. Site imperfections, setup variability, cables, operator procedures, and other factors make correlation among methods challenging. When comparing data among EMC test methods, there is the unfortunate tendency to assume that one approach yields "correct" results, and that correlated data from other sites must match this "reference data" or be judged to be in "error." Differences may be caused more by each test method tending to accentuate differing aspects of the overall

Perry F. Wilson is with the National Institute of Standards and Technology, RF Fields Group, NIST 813.02, 325 Broadway, Boulder, CO 80305, USA; Tel: +1 (303) 497-3406; Fax: +1 (303) 497-6665; E-mail: pfw@boulder.nist.gov.

This is one of the invited *Reviews of Radio Science*, from Commission E.

Frequency (MHz)	k (1/m)	a	ka	N_s
30	0.63	0.25	0.16	12
100	2.09	0.25	0.52	12
200	4.19	0.25	1.05	13
500	10.47	0.25	2.62	48
1000	20.94	0.25	5.23	152
2000	41.89	0.25	10.47	522
5000	104.72	0.25	26.18	2951
10000	209.44	0.25	52.36	11385
20000	418.88	0.25	104.72	44703

Table 1. The number of independent samples required to determine the radiation pattern for a 50 cm diameter test object.

immunity and emissions of the test object. Fortunately, there is an emerging trend to develop independent standards for each test method. This allows the test engineer to choose the method most natural for the problem at hand. Correlation is most useful for establishing equivalent pass/fail limits. A good starting point is to develop analytical models of each method with simple dipoles used as the test objects. This review will not attempt to connect these methods, although correlation between facilities will be discussed, where appropriate. More important is to highlight the applications and challenges that are driving current research in each test method.

3. Electrically Large Test Objects

An emerging difficulty for radiated EMC test methods is the complicated radiation patterns that most test objects will possess at higher frequencies. We define an object as electrically small if $ka \le 1$ and electrically large if $ka > 1$, where k is the wavenumber ($= 2\pi/\lambda$, where λ is the wavelength), and a is the radius of the minimum sphere enclosing the object. Electrically small test objects will have simple, dipole-like radiation patterns. Electrically large objects can have complicated radiation patterns with multiple lobes. These complicated patterns make it difficult to find the orientation that yields maximum coupling when performing an EMC-type test.

In principle, the maximum or minimum of a radiation pattern can be found through sufficient sampling. The number of independent samples, N_s, necessary to determine the full three-dimensional radiation pattern is given by [1]

$$N_s = 12, \quad ka \le 1, \qquad (1)$$

$$N_s = 4(ka)^2 + 8ka, \quad ka > 1.$$

The interpretation for the electrically small case $N_s = 12$ is that the test object will behave like six independent dipoles (three electric and three magnetic), each with a real and a complex part (or, equivalently, an amplitude and phase). For electrically large test objects, the sample number grows as the square of the electrical size. Thus, even objects of modest size will require dense sampling at higher frequencies. Table 1 gives the number of independent samples required to determine the radiation pattern for a test object of diameter 50 cm ($a = 25$ cm) for frequencies covering the range from 30 MHz to 20 GHz. Thus, for a test object of 50 cm diameter, we need 12 independent orientations at 30 MHz, increasing to 152 independent orientations at 1000 MHz, to determine the full radiation pattern and direction of maximum reception. At 10 GHz, this number exceeds ten thousand independent samples.

The number of independent samples given in Table 1 fully determines the radiation pattern, and thus allows the true maximum coupling to be found. If a reduced sample size is used, then the probability of finding the orientation yielding maximum coupling will be less than unity. Alternately stated, the fewer the number of independent directions tested, the lower the likelihood that minimum immunity or maximum emission will be found.

One way to quantify the effect of a reduced sample size is to examine the expected value for the maximum directivity (maximized over the radiation pattern) as a function of the sample size. The maximum directivity, D_{max}, determines both the maximum received power, P_{max}, and the maximum radiated electric field, E_{max}, via simple antenna equations:

$$\frac{\eta P_{max}}{\lambda^2 E_0^2} = \frac{D_{max}}{4\pi}, \text{ (immunity test)}, \qquad (2)$$

$$\frac{r^2 E_{max}^2}{\eta P_0} = \frac{D_{max}}{4\pi}, \text{ (emission test)},$$

where far-field coupling is assumed, η is the free-space wave impedance ($= 120\pi$), and r is the distance from the source. In the receiving case (immunity), an incident power density of E_0^2/η is assumed, and in the transmitting case

(emission), a total radiated power P_0 is assumed. If a reduced sample size is used, then the orientation that yields maximum coupling for the reduced sample set will give an estimate, $D_{max,est}$ for the true maximum directivity. Thus, the ratio

$$\frac{D_{max}}{D_{max,est}} \tag{3}$$

is a metric for quantifying the effect of a reduced sample size.

For unintentional emitters (most EMC test objects are not intentionally designed to have highly directive radiation patterns), a good estimate for the maximum directivity can be derived by evaluating the far-field form of the spherical-mode expansion of the emitter, under the assumption that the expansion coefficients are independent random variables. The general form for the far-field pattern, which may be found in various texts (e.g., Chapter 2 in [1]) is

$$\bar{E}(\theta,\varphi,r) = \frac{k}{\sqrt{\eta}}\frac{1}{\sqrt{4\pi}}\frac{e^{jkr}}{kr}\sum_{smn} Q_{smn}^{(3)}\bar{K}_{smn}(\theta,\varphi), \tag{4}$$

where the spherical coordinate system (θ,φ,r) is defined in the usual manner.

$$\sum_{snm} = \sum_{s=1}^{2}\sum_{n=1}^{N}\sum_{m=-n}^{n}$$

represents a summation over only the propagating spherical modes (the far-field approximation), where $N \approx ka$ (it is assumed that the spherical coordinate system is centered in this sphere enclosing the emitter), $Q_{smn}^{(3)}$ are the wave coefficients, and $\bar{K}_{smn}(\theta,\varphi)$ are the far-field (large-argument) forms of the (dimensionless) power-normalized spherical wave functions. This convention yields the simple expression

$$P_{rad} = \frac{1}{2}\sum_{snm}\left|Q_{snm}^{(3)}\right|^2 \tag{5}$$

for the total radiated power, P_{rad}, from the emitter. In general, the summation over *n* goes to infinity; however, as noted above, spherical wave functions with indices $n > ka$ are cut off in the far field of the source, and the series can be truncated. The total number of modes, N_m, for the truncated series is

$$N_m = 2\sum_{n=1}^{N}(2n+1) = 2\left(N^2+2N\right). \tag{6}$$

The number of samples, N_s, required to determine the wave coefficients is twice N_m, since each coefficient has independent real and imaginary parts.

The directivity, *D*, is the sum of the co- and cross-polarized terms:

$$D = D_{co} + D_{cross}. \tag{7}$$

For unintentional emitters, the mean values of the co- and cross-polarized terms will be equal, and since the mean value of *D* is unity, we have

$$\langle D_{co}\rangle = \langle D_{cross}\rangle = \frac{1}{2}. \tag{8}$$

Returning to Equation (4), the field components can be written as follows:

$$\left|\bar{E}_\theta(\theta,\varphi,r)\right|^2 = \frac{1}{\eta}\frac{1}{4\pi r^2}\left|\sum_{smn} Q_{smn}^{(3)}\bar{K}_{smn}(\theta,\varphi)\cdot\bar{a}_\theta\right|^2 \tag{9}$$

$$\left|\bar{E}_\varphi(\theta,\varphi,r)\right|^2 = \frac{1}{\eta}\frac{1}{4\pi r^2}\left|\sum_{smn} Q_{smn}^{(3)}\bar{K}_{smn}(\theta,\varphi)\cdot\bar{a}_\varphi\right|^2.$$

For an unintentional emitter, we will assume that the real and imaginary parts of $Q_{smn}^{(3)}$ are independent and Gaussian distributed with zero mean. Under this assumption, the field components will be chi-square distributed with two degrees of freedom. The directivities, D_{co} and D_{cross}, will be similarly distributed. The expected value for the maximum over N_s samples of a chi-square-with-two-degrees-of-freedom distribution (using D_{co} as an example) is

$$\langle D_{co,max}\rangle = \langle D_{co}\rangle\sum_{n=1}^{N_s}\frac{1}{n}. \tag{10}$$

The summation in Equation (10) can be approximated (e.g., [2], Equation (0.131)), and the substitution of the expected value of D_{co} from Equation (8) into the approximation then yields

$$\langle D_{co,max}\rangle \approx \frac{1}{2}\left[0.577 + \ln(N_s) + \frac{1}{2N_s}\right]. \tag{11}$$

This is the result for $ka > 1$, noting that $N_s = 2N_m$ and $N = ka$ in Equation (6). For $ka = 1$ ($N_s = 12$), Equation (11) yields $\langle D_{co,max}\rangle \approx 1.55$. This is nearly identical to the directivity of a short dipole ($D = 1.5$). Thus, using 1.55 for electrically small emitters results in a continuous function for $\langle D_{co,max}\rangle$ as a function of *ka* and should give good results. The estimate for D_{max} will be double that for each polarization, based on Equation (8).

The above model is idealized, in that it assumes that the distribution function for the field statistics is independent of orientation. It is more likely that some global pattern will be imposed on the distribution, such as that due to apertures

on only one side of a box. This will result in a local mean that is different as the box is rotated. However, the basic results regarding variations due to reduced sampling should be similar.

For the electrically large case, the ratio of the expected values for the maximum directivity for the full sample size, N_s, and the reduced sample (subscript *rs*) size, N_{est} ($N_{est} < N_s$) is given by

$$\Delta_{rs} \equiv \frac{\langle D_{max} \rangle}{\langle D_{max,est} \rangle} \approx \frac{0.577 + \ln(N_s) + \frac{1}{2N_s}}{0.577 + \ln(N_{est}) + \frac{1}{2N_{est}}} . \quad (12)$$

This can be converted to dB units to give an estimate for the difference in dB units resulting from the smaller sample size. This ratio quantifies the expected offset between the true maximum received or emitted power and the estimated maximum received or emitted power based on the reduced sample size.

Consider the effect of testing only the four "faces" of a test object (rotation about the vertical axis), as is presently recommended for some test methods. Using the same 50 cm diameter test object as in Table 1, Equation (12) yields the Δ_{rs} values given in Table 2. Table 2 suggests that testing only four orientations underestimates coupling by approximately 3 dB at 500 MHz and by 4 dB at 1000 MHz. If the four-faces approach were to be extended to 5 GHz, the difference would be approximately 6 dB. At 20 GHz, this increases to 7.3 dB. These results are for a test object of 50 cm diameter. Larger test objects would have larger differences.

The above discussion highlights problems with current EMC test methods if applied to higher frequencies, where most test objects will be electrically large. Clearly, the sample sizes that result from Equation (1) along with the test-object manipulations required to sample over a sphere are prohibitive (too costly) for most EMC test purposes. Thus, the challenge for better EMC test methods will be to find a compromise between test time (sampling density) and estimating maximum coupling. This will be a key issue in developing and improving EMC test methods in the near future, and will be highlighted, where appropriate, in the discussion of EMC measurement techniques that follows.

4. Open-Area Test Sites

An open-area test site (OATS) is the most basic EMC test facility. Prior to the development of open-area test site-usage standards, an open-area test site was simply any flat, open outdoor area where radiated field measurements could be made. Prime considerations are the absence of nearby scattering objects (buildings, fences, etc.) and a low level of ambient noise. Thus, open-area test sites are often located at remote sites away from population centers, although rooftop sites and other urban locations are also used. Initially, measurements at different open-area test sites were difficult to compare, as the ground effect could be very different, site-to-site. Some sites used parking lots (pavement), while other sites used fields, where soil might be dry or wet depending on location or season. Standardization efforts led to the use of large, flat, metallic ground screens to ensure that sites had very similar characteristics.

Site attenuation is the basic open-area-test-site evaluation method. The site attenuation method consists of transmitting and receiving antennas placed over the open-area test site in a specified geometry (e.g., 3 m horizontal separation, 1 m transmitting antenna height). The receiving antenna is moved vertically over some specified range, and the maximum received power over the vertical sweep is used to determine the site attenuation at each frequency. These data can then be compared to theoretical values. Standards typically require that the measured values be within ± 4 dB of the theoretical values for a site to be acceptable.

Frequency (MHz)	*k* **(1/m)**	*a* **(m)**	*ka*	N_s	N_{est}	Δ_{rs} **(dB)**
30	0.63	0.25	0.16	12	4	1.7
100	2.09	0.25	0.52	12	4	1.7
200	4.19	0.25	1.05	13	4	1.8
500	10.47	0.25	2.62	48	4	3.3
1000	20.94	0.25	5.23	152	4	4.3
2000	41.89	0.25	10.47	522	4	5.1
5000	104.72	0.25	26.18	2951	4	6.1
10000	209.44	0.25	52.36	11385	4	6.8
20000	418.88	0.25	104.72	44703	4	7.3

Table 2. The difference in the maximum directivity for four versus N_s independent samples for a test object of 50 cm diameter.

Meeting site-attenuation requirements involves both a good open-area test site and careful measurement practice [3, 4]. Theoretical site attenuation can be readily calculated for short dipoles. The antenna factors for the dipoles can be factored out, giving normalized site attenuation. Normalized site attenuation can be measured using any pair of arbitrary antennas by again factoring out antenna factors [5]. A specific challenge in the above procedure is that antenna characteristics (gain, pattern) are affected by the proximity to the ground plane [6]. An active area of investigation is to correct for these proximity effects and to improve the agreement between measured and theoretical values of normalized site attenuation. Resonant-dipole, spherical-dipole, biconical, log-periodic, and hybrid biconical-log-periodic (bilog) antennas all can be modeled over an open-area test site using numerical simulations. Their antenna factors as a function of the height above an ideal ground plane can then be determined [7-11]. The phase center of an antenna also needs to be accurately known when determining normalized site attenuation, particularly for log-periodic antennas [12]. Proximity effects also make it difficult to use open-area test sites to measure free-space antenna factors. Antennas can be positioned high above the open-area test site and vertically polarized to minimize the contribution from the image source, but this is often not practical, particularly at frequencies near 30 MHz. The use of radio-frequency (RF) absorber to mitigate the proximity effect has been examined [13]. Higher frequencies (>1 GHz) and directive antennas present a challenge to current methods of measuring site attenuation. This topic is briefly discussed in the section on anechoic chambers.

Weather can limit the use of an open-area test site. Thus, "low-reflecting" structures are often used to protect equipment and the test object. These can be equipment sheds or complete open-area test site covers. The effect of these structures on measurement accuracy needs to be examined. Time-domain techniques have been used to separate out the contribution of the weather structure [14]. Measurements on a fiberglass structure showed that emissions testing can be significantly affected above 100 MHz. The effect of peripheral equipment (shelters, tables, supports) on measurement uncertainty is also being actively investigated [15-17].

4.1 Immunity

Open-area test sites are not well suited for immunity tests, since the radiated power needed to establish a test field over broad bands usually exceeds allowable broadcast limits, and could cause interference with other users and services. Sufficiently remote sites may avoid restrictions. Thus, immunity tests are usually performed in enclosed, shielded facilities.

4.2 Emission

The challenges in making good measurements of emissions from a test object are similar to those associated with site-attenuation measurements, particularly in correcting for proximity effects on antennas.

5. Anechoic Chambers

Anechoic chambers are shielded enclosures lined with RF absorber, either on all walls (fully anechoic) or on the walls above a metal floor (a semi-anechoic chamber). A fully anechoic chamber approximates ideal free space and is well suited for antenna calibrations. A semi-anechoic chamber approximates an ideal open-area test site and is well suited for EMC immunity and emission tests. In both cases, the performance of the anechoic chamber depends on the ability of the absorber to reduce reflections; thus, considerable work has focused on absorber design and verification. A good review of absorber design is given in [18].

A variety of RF absorber types have been developed. The most common absorber used in anechoic chambers is carbon-loaded foam, shaped into either a cone or a wedge. Shaped absorber performs well when its depth is comparable to a wavelength or larger. The performance degrades as the absorber depth becomes small compared to the wavelength. This is a fundamental problem for EMC anechoic chambers that are intended for use down to 30 MHz (10 m wavelength). A very large absorber is prohibitively expensive, consumes large amounts of space, and is mechanically difficult to install and maintain. Thus, much recent research has focused on methods of improving low-frequency performance while keeping the absorber relatively compact. The performance of shaped absorber at lower frequencies can be analytically simulated using homogenization [19, 20]. This technique models the air and absorber array as a single anisotropic media, with effective electrical parameters derived from weighting the two materials according to the percentage of volume they each fill [21]. Analytical models of absorber can then be used to simulate the performance of anechoic chambers and to optimize their design [22]. The low-frequency performance of cone absorber can be further improved by layering the carbon loading within the cone [23, 24]. An alternative to shaped-foam absorber is to use ferrite tiles, which provide very good absorption, but only over a narrow frequency band. Multiple ferrite layers can be used to broaden the performance bandwidth [25], as can the use of dielectromagnetic materials [26]. Ferrite tiles, tuned to the low-frequency end of the chamber's use, can be combined with short high-frequency cone absorber to achieve good broadband performance [27]. Numerical techniques may be used to optimize combinations of absorber layers for given performance specifications [28, 29]. A possible area of future research is active absorbers, which tune reflective properties according to the incident wave type and frequency [30].

Various measurement methods have been developed to verify absorber performance. Large waveguides and coaxial lines are used to test cone-type absorber [31, 32]; however, these are inherently band limited. An alternative

is to use time-domain techniques to measure absorber walls in-situ [33-35]. The time-domain approach is very useful in performing diagnostics in chambers because individual locations (e.g., walls, corners, peripherals) can be isolated in the time record and measured. Another diagnostic approach is to use the pencil-matrix method to identify the relative strength of direct and reflected-path signals [36, 37].

5.1 Immunity

Fully anechoic chambers are regularly used for immunity tests where a uniform field over some specified area is required. Semi-anechoic chambers are more problematic for immunity tests because of the ground-plane reflection. In particular, it is difficult to establish a uniform horizontal electric field near the ground plane, where the tangential electric field goes to zero. A simple solution is to place RF absorber on the ground plane in the path of the reflected wave [38]. Some chambers are designed with a removable floor, so that they can be converted between fully and semi-anechoic. Immunity tests require that the test object be rotated to determine the direction of maximum coupling. A different approach is to electronically rotate the field, with the intent of reducing measurement time [39].

5.2 Emission

Semi-anechoic chambers are used for emission testing in a manner similar to that for an open-area test site. Fully anechoic chambers are also used for emission testing [40]. Semi-anechoic chambers are qualified by the use of site-attenuation measurement methods similar to those used for an open-area test site. Site-attenuation tests are intended to determine whether unacceptable reflections occur at walls and ceilings. Implicit in a site-attenuation test is that the antennas used are omni-directional, so that both the reflected (absorber walls) and direct (line-of-sight) coupling paths are excited. Below 1 GHz, various antennas have broad, omni-directional patterns (e.g., dipole, biconical). However, as EMC testing moves to frequencies above 1 GHz, typical antennas (horns) become very directional, and to excite all directions simultaneously becomes problematic. Thus, site-attenuation qualification methods may need to be modified. One approach under study is to use directional antennas, but to then rotate one of the antennas and compare coupling data to reference data from a site with no reflections [41]. An alternative to physically rotating directive antennas is to create a source that self-rotates the field. A pseudo-isotropic source can be realized using a small reverberation chamber that radiates via apertures located over the surface [42]. The average fields from such a source are similar in all directions, and good isotropy should be possible.

6. Transmission Lines

The fundamental transverse-electromagnetic (TEM) mode of a transmission line can be used to simulate an ideal plane wave. A variety of striplines, TEM cells (an expanded section of rectangular coaxial line, tapered at each end), and multiconductor coaxial lines have been developed for EMC test purposes. Initial research on transmission lines focused on investigating the field distribution of the TEM mode and the characteristic impedance of the line, particularly for lines with rectangular cross sections [43, 44]; the cutoff frequencies and field distributions of higher-order modes [45-48]; cell resonances [49]; test-object loading [50]; and emissions for simple sources [51, 52]. Good reviews of this work have been published [53, 54]. More recent research has considered methods of extending the use of transmission lines to higher frequencies (broadband cells), correlation with other test facilities, and emissions from electrically large test objects. The recent publication of IEC 61000-4-20 [55], an independent standard on EMC tests using TEM devices, should further increase interest.

6.1 Immunity

IEC 61000-4-20 gives a procedure for establishing the uniform area that can be used for immunity testing. TEM devices operating well below higher-order-mode cutoff have very well defined fields usable for probe calibrations [43, 56] and immunity tests [57, 58]. In addition, a transmission line may be terminated with unmatched loads (open, short) to create standing waves, with resulting low-impedance and high-impedance fields for probe calibrations [59]. Above cutoff, higher-order modes must be suppressed with respect to the TEM mode if usable field uniformity is to be maintained. A number of broadband TEM-device designs have been developed [60-64]. These designs use a combination of a matched ohmic load at low frequencies, and RF absorber at high frequencies, to create a broadband termination that minimizes reflections and higher-order mode excitation.

6.2 Emission

A TEM device acts as its own transducer for emission measurements; thus, emission measurements in a TEM device do not require an additional antenna. Ideally, emission pass/fail limits would be expressed in terms of the signals measured at the TEM-device output [65]; however, correlation to established methods (e.g., an open-area test site) is of interest in order to establish the equivalence of emission data. The simplest correlation algorithm determines the total radiated power from the test object (modeled as a set of dipoles) using emission data from three orthogonal orientations [66]. The total radiated power is then used to simulate emissions either in free space or over an ideal ground plane. Additional test-object orientations can be used to refine the dipole model to include phase effects [51, 67], higher-order multipole moments [43], and to model near-field emissions [68]. TEM devices that themselves rotate, or that have multiple field polarizations such that the test object need not be rotated, have also been developed [69, 70]. As in the immunity case, TEM devices are well

suited to testing emissions from small devices and components [71].

An alternative to modeling the test object in order to develop a correlation algorithm is to treat the TEM device as an antenna, and to develop an equivalent antenna factor [72, 73]. The equivalent antenna factor can be used in simple transmission formulas to simulate emission measurements made with other EMC test facilities. The antenna-factor approach is not limited to electrically small test objects, as is the case for dipole models, and can be applied to general emission tests in broadband TEM devices. The use of TEM devices at higher frequencies (>1 GHz) and for electrically large test objects is an ongoing area of investigation.

7. Reverberation Chambers

The EMC measurement methods discussed in the above sections have as a goal the generation of coupling interactions based on a single, well-defined plane-wave-like field. A reverberation chamber takes a different approach. A reverberation chamber is a highly resonant cavity that uses a variable scatterer, or variable excitation, to generate multi-mode fields that have statistical quantities, such as mean field magnitude, that approach plane-wave-like values uniformly throughout much of the cavity volume. Advantages of the reverberation-chamber approach include a large test volume, a field that effectively rotates around the test object, very high field levels, and excellent high-frequency performance. Limitations include a loss of directional-coupling information and poor lower-frequency performance as the mode density decreases.

Much of the early research on reverberation chambers for EMC applications focused on chamber design, on verifying the uniformity of the field statistics in the test volume, and on establishing the connection between mode density in the chamber and the lower-frequency limit of operation. The primary application was generating high field levels for immunity testing, as is required in certain defense and aerospace immunity tests. Good reviews of this work may be found in [74-76]. As reverberation chambers have become more accepted and applied to a wider range of EMC tests, areas of research have also broadened. Topics now being investigated include theoretical descriptions of the field statistics, numerical simulations, variable-boundary-condition performance (paddle mixing, vibrating walls), electronic stirring, and equipment-under-test directivity. Applications of reverberation chambers have moved beyond immunity tests to include emissions tests (total radiated power), measurements of the shielding effectiveness of cables and connectors, measuring the performance of wireless handsets, studying the effects on animals due to exposure to RF fields, and investigating MIMO (multiple-input multiple-output) systems. The recent publication of IEC 61000-4-21 [77], an independent standard on using reverberation chambers for EMC tests, should further increase interest.

7.1 Immunity

Immunity tests in a reverberation chamber require that the uniformity of the test field be established. Initial work on field uniformity was largely experimental [78]. More recent work has investigated theoretical and numerical models of reverberation-chamber fields. A good theoretical description of the fields in a reverberation chamber has been given by Hill [75]. He formulated the fields in terms of a plane-wave representation such that Maxwell's equations are satisfied [79]. He assumed that, at each point in the test volume, the real and imaginary parts of each field component were Gaussian distributed with zero mean. This description led to chi-square distributions for the magnitudes of various field quantities (two degrees of freedom for field components and six degrees of freedom for the total field), and agreed with earlier work [80]. Hill also showed that the correlation function between two points has its first zero at a separation of $\lambda/2$ [81]; thus, a separation of $\lambda/2$ or greater is recommended if test objects are to be decoupled. More recent work has considered how close the test volume should approach the chamber walls. IEC 61000-4-21 recommended an offset of $\lambda/4$. Hill has used the spectral representation [75] to develop correlation functions for walls and corners [82]. The above representation is a good model for a highly-moded reverberation chamber. Near the lower-frequency limit of operation, the assumptions that lead to the chi-square distributions may no longer be justified. To address this problem, a compound distribution, based on the decomposition of partially polarized fields into polarized and un-polarized components, was proposed [83]. The compound distribution accurately predicts the performance of basic reverberation-chamber quantities (e.g., mean field value, cumulative distribution function), and their deviation from ideal as the frequency is lowered.

Numerical simulations of the performance of reverberation chambers are difficult. The volume to be simulated is electrically very large, making the problem size challenging. Effective mode stirrers have complicated geometries and require complex meshing. Complex geometries mean that reductions due to symmetry are usually not possible. Reverberation chambers are wideband. This means frequency-domain techniques (e.g., the Method of Moments) require numerous steps to describe performance. Chambers are highly resonant, and time-domain techniques (e.g., the Finite-Difference Time-Domain technique) require long simulation duration and fine time steps [84]. Finally, reverberation chambers are very sensitive to loss mechanisms, such as the finite conductivity of the walls, objects within the chamber, aperture leakage, and receiving antennas [85]. These loss mechanisms also present difficult modeling challenges. Two-dimensional (2D) simulations can be used to significantly reduce problem size while still demonstrating fundamental properties. For example, a two-dimensional finite-element model was used to investigate stirrer efficiency [86] and coupling to a box with an aperture [87]. Three-dimensional (3D) models have also been developed. The Method of Moments has been

used to simulate a medium-sized reverberation chamber [88]. The simulations demonstrate that results are indeed sensitive to a variety of parameters, including source type and location, and to door leakage. Because these parameters are difficult to quantify for actual reverberation chambers, achieving reliable agreement between simulations and measured data remains a challenge.

Reverberation chambers require a mechanism to broadly change the modal excitation to achieve meaningful statistical quantities. The usual method is the use of an electrically large, rotating paddle. The paddle may be turned in discrete steps (mode-tuned) or continuously (mode-stirred). With the mode-tuned method, the parameters of interest (e.g., net input power, test-object response) are measured between steps, and can be corrected as a function of VSWR. In the mode-stirred case, paddles are turned continuously, and the field is sampled at a rate much higher than the rotational frequency. While the mode-stirred method allows data to be acquired rapidly, effects may be missed if the test-object response time is large compared to the dwell time determined by the rate of change of the field. The advantages and disadvantages of the two approaches are areas of active discussion [89]. While most reverberation chambers feature a single paddle, multiple paddles may further improve performance. A rotating paddle is simple to realize; however, other methods to change the field have been investigated. Tent-like structures with vibrating walls allow for in-situ testing of fixed test objects [90]. Moving walls have also been considered [91, 92]. An alternative to mechanical variations is to use electronic stirring. Varying the bandwidth of the input signal to increase the number of modes has been investigated [93]. The use of multiple wires in a chamber that are given random amplitude and phase excitation has been proposed [94]. The wires support TEM modes; thus, the field distribution in the chamber may be varied even at low frequencies, and the method is not as dependent on a sufficient level of mode density as are mechanical methods.

The high field levels that can be generated in a reverberation chamber can be applied to the testing of the shielding effectiveness of cables, connectors, and gaskets [95, 96]. Gaskets are often measured using nested reverberation chambers. A small cavity with an internal paddle is placed inside a larger reverberation chamber. Coupling then occurs primarily through a large aperture that can be covered with a gasketed plate or a test material [97]. An alternative under consideration is to use two large reverberation chambers placed side by side with a large coupling aperture. This would allow for the testing of very large gasketed openings, such as doors and large access panels.

Most immunity tests involve electronic devices; however, the large test volume of a reverberation chamber may also be applied to the exposure of animals to well-controlled electromagnetic fields. An example is a proposed study by the National Institutes of Health to investigate potential human health effects associated with exposure to RF fields, such as those produced by cellular telephones [98]. A large number of animals in a reverberation chamber constitutes a large, lossy load, and thus affects the performance of the chamber. Experiments using phantoms filled with a tissue-simulating liquid showed that, at frequencies used by cellular telephones (900 MHz and 1900 MHz), reverberation-chamber efficiency approached 85% (the percentage of power coupled to the phantoms) for a heavily-loaded chamber (greater than 100 kg of lossy material), and that the variation in the average specific absorption rate (averaged over the whole of the phantom) was less than 1 dB for phantoms placed throughout the test volume of the chamber [99]. These results suggest that the reverberation chamber is well suited to studies of a large population of small animals.

7.2 Emission

The reverberation chamber is a reciprocal device, and may be applied to emission testing as well as immunity testing [100]. Because directivity information is lost in the statistical data output from a reverberation-chamber measurement, only total radiated power may be measured. Total radiated power may be determined directly from the average power (averaged over multiple modal distributions) received by a matched, lossless reference antenna, if the quality factor (Q) of the chamber is known [75]. However, the Q is generally not well characterized, and antenna loss effects can be difficult to correct. To avoid these parameters, the more usual method of determining total radiated power in a reverberation chamber is to make a comparative measurement with a reference source of known power. Total radiated power is a natural quantity for reverberation-chamber emission limits [101].

Total radiated power may be used to determine the maximum emissions from a test object if the directivity (D) of the test object is known. Maximum emission results may then be correlated with data from other EMC facilities. In general, D is not known. IEC 61000-4-21 recommends the use of $D = 1.7$ (the value for a half-wave dipole) for uncharacterized test objects. However, this is clearly not an accurate choice for electrically large, complex emitters. D may be bounded based on its electrical size, ka; however, this upper bound grows as $(ka)^2$, and rapidly gives values of little practical use. A more useful estimate for D, applicable to unintentional emitters (Equation (11)) was outlined in Section 3. Experimental data on a source configured to simulate an unintentional emitter showed that this estimate accurately predicts actual directivity [102]. Estimates of directivity combined, with simple measurements of total radiated power in a reverberation chamber, are a straightforward method for quantifying emissions for electrically-large test objects at high frequencies.

Another recent emission application in reverberation chambers is the measurement of the radiated efficiency from cellular handsets in compact reverberation chambers [103]. The reverberation chamber is well suited to wireless

applications, as it simulates a multipath environment for transmitting and receiving tests. As discussed above, a reverberation chamber simulates plane waves incident from multiple angles and polarizations. This is effective in evaluating mobile-phone antennas [104]. The multipath environment in a reverberation chamber can be used to test the effectiveness of MIMO systems [105]. In principle, the antenna placement can be used to control the level of direct coupling and to simulate various types of Rayleigh and Ricean channels. With wireless devices expected to proliferate, the application of reverberation chambers to the testing of wireless devices is a promising area of research.

8. Near-Field Methods

Near-field techniques have been developed to accurately determine the radiation patterns of electrically large antennas, such as phased arrays, where direct, far-field measurements are not practical [1, 106, 107]. Measurements of the complex field are made on a grid (planar, cylindrical, and spherical) in the near field of the antenna. These data then undergo mathematical transformations to generate detailed far-field patterns (main beam, lobes). All near-field data points contribute to each far-field pattern direction. Thus, considerable effort is involved in accurately positioning the near-field probe on the desired measurement grid, correcting for the probe pattern, and correcting for probe-to-antenna interactions.

8.1 Emission

Near-field techniques to detect currents and "hot spots" on printed circuit boards are already widely used for EMC diagnostics [108, 109]. These local tests do not provide direct information as do far-field emissions, however. The detailed radiation patterns that result from near-field antenna measurements would be very useful for EMC applications. Unfortunately, there are problems in directly applying near-field methods to EMC test objects. A basic difficulty is that unintentional emitters, such as digital devices, often have strongly time-dependent signals, whereas near-field transformations assume a CW signal. The relatively low frequencies (down to 30 MHz) required by EMC emission standards are outside the capability of most near-field ranges. EMC test objects often have cables and other peripherals that make it difficult to enclose them in a well-defined volume. Finally, the effort and cost associated with near-field ranges and measurements are significant, and are not practical for most EMC test budgets. Nonetheless, as EMC emission measurements move to higher frequencies, where most test objects have complicated radiation patterns, the possible use of near-field techniques for EMC purposes merits consideration [110].

One approach to adapting near-field techniques to EMC emission testing is to reduce the amount of measurement data needed to perform the far-field transformation. Various approaches are being investigated. A spatial-coherence-function model has been proposed to handle the random emissions associated with EMC test objects [111, 112]. The transformation problem can be significantly reduced if the test object is known or can be modeled. Models using equivalent dipoles [113] and equivalent circuits [114] have been proposed. Another method to reduce measurement complexity is to use phase-less data, as is typically done in measurements of EMC emissions. A general approach based on the use of two scanning surfaces has been investigated [115]. A source model using an equivalent magnetic-current density can also be used to predict emissions from amplitude-only data [116].

8.2 Immunity

Near-field techniques are primarily applied to test-object emissions. However, there is also interest in using near-field techniques for immunity tests. Antenna arrays may be used to synthesize a plane wave in the near field of the array. This approach allows the angle of incidence to be scanned electronically, and allows for relatively high field levels when compared to the far field of the same antenna. Least-squares techniques have been applied to the synthesis problem [117-119], and, more recently, genetic algorithms have been used [120].

9. Summary

The difficulties and challenges related to using various EMC measurement techniques for radiated immunity and emissions tests have been summarized. The higher frequencies of operation of high-speed digital and wireless devices mean that both existing and emerging EMC measurement methods will need to be effective at ever-higher frequencies. Test methods also need to remain cost effective to gain wide acceptance. Future research in this area will be needed to meet these goals.

10. References

1. J. Hansen (ed.), *Spherical Near-Field Antenna Measurements*, London, UK, Peter Peregrinus, 1988.

2. I. Gradshteyn and I. Ryzhik, *Table of Integrals, Series, and Products*, San Diego, CA, Academic Press, 1980.

3. R. Fitzgerrel, "Site Attenuation," *IEEE Transactions on Electromagnetic Compatibility*, **EMC-28**, 1, 1986, pp. 38-40.

4. M. Salter and M. Alexander, "EMC Antenna Calibration and the Design of An Open-Field Site", *Journal of Physics E: Measurement Science Technology*, 1991, pp. 510-519.

5. A Smith, R. German, and J. Pate, "Calculation of Site Attenuation from Antenna Factors," *IEEE Transactions on Electromagnetic Compatibility*, **EMC-24,** 3, 1982, pp. 301-316.

6. A. Suguira, T. Shinokuka, and A. Nishikata, "Correction Factors for the Normalized Site Attenuation," *IEEE Transactions on Electromagnetic Compatibility*, **EMC-34,** 4, 1992, pp. 461-470.

7. N. van Dijk, "Numerical Tools for Simulation of Radiated Emission Testing and its Application in Uncertainty Studies," *IEEE Transactions on Electromagnetic Compatibility*, **EMC-44,** 3, 2002, pp. 466-470.

8. A. Kitani, N. Kuwabara, and F. Amemiya, "Analysis of Site Attenuation for Spherical Dipole Antenna and its Application," *Proceedings 2003 IEEE International Symposium on Electromagnetic Compatibility*, (Boston, MA), 2003, pp. 680-685.

9. Z. Chen and M. Foegelle, "A Numerical Investigation of Ground Plane Effects on Biconical Antenna Factor," *Proceedings 1998 IEEE International Symposium on Electromagnetic Compatibility*, (Denver, CO), 1998, pp. 802-806.

10. Z. Chen, M. Foegelle, and T. Harrington, "Analysis of Log Periodic Dipole Array Antennas for Site Validation and Radiated Emission Testing," *Proceedings 1999 IEEE International Symposium on Electromagnetic Compatibility*, (Seattle, WA), 1999, pp. 618-623.

11. H.-F. Chen, "A Numerical Analysis of Antenna Factor of Bilog Antennas for Normalized Site Attenuation and EMC Measurement," *Proceedings 2003 IEEE International Symposium on Electromagnetic Compatibility*, (Boston, MA), 2003, pp. 817-821.

12. Z. Chen and M. Foegelle, "Complex Fit Normalized Site Attenuation for Antennas with Complex Radiation Patterns," *Proceedings 2003 IEEE International Symposium on Electromagnetic Compatibility*, (Boston, MA), 2003, pp. 822-827.

13. Y. Matsumoto, T. Umeda, A. Nishikata, K. Fujii, Y. Yamanaka, and A. Sugiura, "EMI Antenna Calibration on an Absorber-Lined Ground Plane to Determine Free-Space Antenna Factor," *IEEE Transactions on Electromagnetic Compatibility*, **EMC-45,** 4, 2003, pp. 656-660.

14. R. Johnk, D. Novotny, C. Weil, and H. Medley, "Assessing the Effects of an OATS Shelter: is ANSI C63.7 Enough?" *Proceedings 2000 IEEE International Symposium on Electromagnetic Compatibility*, (Washington, DC), 2000, pp. 523-528.

15. C. Zombolas, "The Effects of Table Material on Radiated Field Strength Measurement Reproducibility at Open Area Test Sites," *Proceedings 2001 IEEE International Symposium on Electromagnetic Compatibility*, (Montreal, Canada), 2001, pp. 260-264.

16. P. Beeckman, "The Influence of Positioning Tables on the Results of Radiated EMC Measurements," *Proceedings 2001 IEEE International Symposium on Electromagnetic Compatibility*, (Montreal, Canada), 2001, pp. 280-285.

17. E. Blankenship and D. Arnett, "Field Perturbations due to Accessories used in Radiated Emission Tests," *Proceedings 2001 IEEE International Symposium on Electromagnetic Compatibility*, (Montreal, Canada), 2001, pp. 292-297.

18. C. Holloway, R. DeLyser, R. German, P. McKenna, and M. Kanda, "**Comparison of Electromagnetic Absorber used in Anechoic and Semi-Anechoic Chambers for Emissions and Immunity Testing of Digital Devices,"** *IEEE Transactions on Electromagnetic Compatibility*, **EMC-39**, 1, 1997, pp. 33-47.

19. E. Kuester and C. Holloway, "**A Low-Frequency Model for Wedge or Pyramid Absorber Arrays-I: Theory,"** *IEEE Transactions on Electromagnetic Compatibility*, **EMC-36**, 4, November 1994, pp. 300-306.

20. C. Holloway and E. Kuester, "**A Low-Frequency Model for Wedge or Pyramid Absorber Arrays-II: Computed and Measured Results,"** *IEEE Transactions on Electromagnetic Compatibility*, **EMC-36**, 4, 1994, pp. 307-313.

21. E. Kuester and C. Holloway, "Comparison of Approximations for Effective Parameters of Artificial Dielectrics," *IEEE Transactions on Microwave Theory and Techniques*, **MTT-38**, 11, 1990, pp. 1752-1755.

22. C. Holloway and E. Kuester, "Modeling Semi-Anechoic Electromagnetic Measurement Chambers," *IEEE Transactions on Electromagnetic Compatibility*, **EMC-38**, 1, 1996, pp. 79-84.

23. T. Ellam, "An Update on the Design and Synthesis of Compact Absorber for EMC Chamber Applications," *Proceedings 1994 IEEE International Symposium on Electromagnetic Compatibility*, (Chicago, IL), 1994, pp. 408-412.

24. K. Ishino, T. Morikawa, T. Saito, Y. Hashimoto, and Y. Shimzu, "Realization of Compact Semi- and Fully Anechoic Chambers using a New Developed Composite Absorber," *Proceedings 1994 IEEE International Symposium on Electromagnetic Compatibility*, (Chicago, IL), 1994, pp. 413-418.

25. H. Komori and Y. Konishi, "Wide Band Electromagnetic Wave Absorber with Thin Magnetic Layers," *IEEE Transactions on Broadcasting*, **BT-40**, 4, 1994, pp. 219-222.

26. F. Mayer and J.-P. Chaumat, "Dielectromagnetic Materials for Absorber-Lined Chambers (ALC)," *Proceedings 9th International Zurich Symposium on Electromagnetic Compatibility*, (Zurich, Switzerland), 1991, pp. 569-572, (available from the Symposium Secretariat, c/o ETHZ Zentrum, Gloriastrasse 35, CH-8092 Zurich, Switzerland).

27. C. Holloway, P. McKenna, R. Dalke, A. Perala, and C. Devor, "Time-Domain Modeling, Characterization, and Measurements of Anechoic and Semi-Anechoic Electromagnetic Test Chambers," *IEEE Transactions on Electromagnetic Compatibility*, **EMC-44**, 1, 2002, pp. 102-118.

28. J. Perini and L. Cohen, "**Design of Broad-Band Radar-Absorbing Materials for Large Angles of Incidence,"** *IEEE Transactions on Electromagnetic Compatibility*, **EMC-35**, 2, 1993, pp. 223-230.

29. F. Teixeira, "On Aspects of the Physical Realizability of Perfectly Matched Absorbers for Electromagnetic Waves," *Radio Science*, **38**, 2, 2003, pp. VIC15:1-10.

30. L. Arnaut, "Adaptive Control and Optimization of Electromagnetic Radiation, Attenuation and Scattering using Self-Adaptive Material Systems," *IEEE Transactions on Antennas and Propagation*, **AP-51**, 7, 2003, pp 1530-1548.

31. S. Takeya and K. Shimada, "New Measurement Method of RF Absorber by Large Square Coaxial Line," *in Proceedings 1993 IEEE International Symposium on Electromagnetic Compatibility*, (Dallas, TX), pp. 9-13.

32.P. Pues, "Electromagnetic Wave Absorber Measurement in a Large Coax," *Proceedings 9th International Zurich Symposium on Electromagnetic Compatibility*, (Zurich, Switzerland), 1991, pp. 541-546, (available from the Symposium Secretariat, c/o ETHZ Zentrum, Gloriastrasse 35, CH-8092 Zurich, Switzerland).

33.S. Tofani, A. Ondrejka, and M. Kanda, "Time Domain Method for Characterizing the Reflectivity of Absorbing Materials from 30 to 1000 MHz," *IEEE Transactions on Electromagnetic Compatibility*, **EMC-33**, 3, 1991, pp. 234-240.

34.S. Tofani, A. Ondrejka, M. Kanda, and D. Hill, "Bistatic Scattering of Absorbing Materials from 30-1000 MHz," *IEEE Transactions on Electromagnetic Compatibility*, **EMC-34**, 3, 1992, pp. 304-307.

35.R. Johnk, A. Ondrejka, S. Tofani, and M. Kanda, "Time-Domain Measurements of the Electromagnetic Backscatter of Pyramidal Absorbers and Metallic Plates," *IEEE Transactions on Electromagnetic Compatibility*, **EMC-35**, 4, 1993, pp. 429-433.

36.B. Fourestie, Z. Altman, and M. Kanda, "**Anechoic Chamber Evaluation using the Matrix Pencil Method,"** *IEEE Transactions on Electromagnetic Compatibility*, **EMC-41**, 3, 1999, pp. 169-174.

37.B. Fourestie, Z. Altman, and M. Kanda, "**Efficient Detection of Resonances in Anechoic Chambers using the Matrix Pencil Method,"** *IEEE Transactions on Electromagnetic Compatibility*, **EMC-42**, 1, 2000, pp. 1-5.

38.M. Windler and S. Urbanski, "**A Radiated Immunity Uniform Field Over a Ground Plane,"** *Proceedings 2003 IEEE International Symposium on Electromagnetic Compatibility*, (Boston, MA), 2003, **pp. 669-673.**

39.K. Murano and Y. Kami, "A New Immunity Test Method," *IEEE Transactions on Electromagnetic Compatibility*, **EMC-44**, 1, 2002, pp. 119-124.

40.M. Alexander, "Development of New Measurement Methods of the EMC Characteristics in Smaller Relatively Inexpensive Fully Anechoic Rooms," *Proceedings 13th International Zurich Symposium on Electromagnetic Compatibility*, (Zurich, Switzerland), 1999, pp 267-272, (available from the Symposium Secretariat, c/o ETHZ Zentrum, Gloriastrasse 35, CH-8092 Zurich, Switzerland).

41.M. Windler and D. Camell, "Research on Site Qualifications Above 1 GHz," *Proceedings 15th International Zurich Symposium on Electromagnetic Compatibility*, (Zurich, Switzerland), 2003, pp. 333-336, (available from the Symposium Secretariat, c/o ETHZ Zentrum, Gloriastrasse 35, CH-8092 Zurich, Switzerland).

42.P. Wilson, "Pseudo-Isotropic Source for Anechoic Chamber Qualification," *Proceedings 2002 IEEE International Symposium on Electromagnetic Compatibility*, (Minneapolis, MN), 2002, pp. 39-42.

43.M. Crawford, "Generation of Standard Fields using TEM Transmission Cells," *IEEE Transactions on Electromagnetic Compatibility*, **EMC-16**, 4, 1974, pp. 189-195.

44.J. Tippet **and D. Chang, "Characteristic Impedance of a Rectangular Coaxial Line with Offset Inner Conductor,"** *IEEE Transactions on Microwave Theory and Techniques*, **MTT-26**, 11, 1978, pp. 876-883.

45.J. Tippet and D. Chang, "Higher Order Modes in Rectangular Coaxial Line with Infinitely Thin Inner Conductor," National Bureau of Standards Internal Report 78-873, 1978, (available from National Institute of Standards and Technology, 325 Broadway, Boulder, CO, 80305).

46.C. Weil and L. Gruner, "Higher Order Mode Cutoff in Rectangular Striplines," *IEEE Transactions on Microwave Theory and Techniques*, **MTT-32**, 6, 1983, pp. 638-641.

47.P. Wilson and M. Ma, "Simple Approximate Expressions for Higher Order Mode Cutoff and Resonant Frequencies in TEM Cells," *IEEE Transactions on Electromagnetic Compatibility*, **EMC-28**, 3, 1986, pp. 125-130.

48.P. Wilson, "Higher-Order Mode Field Distribution in Asymmetric Transverse Electromagnetic Cells," *Radio Science*, **26**, 2, 1991, pp. 551-557.

49.D. Hill, "Bandwidth Limitations of TEM Cells due to Resonances," *Journal of Microwave Power*, **18**, 1983, pp. 181-195.

50.M. Kanda, "Electromagnetic-Field Distortion due to a Conducting Cylinder in a Transverse Electromagnetic Cell," *IEEE Transactions on Electromagnetic Compatibility*, **EMC-24**, 3, 1982, pp. 294-301.

51.J. Tippet and D. Chang, "Radiation Characteristics of Electrically Small Devices in a TEM Transmission Cell," *IEEE Transactions on Electromagnetic Compatibility*, **EMC-18**, 4, 1976, pp. 134-140.

52.I. Sreenivasiah, D. Chang, and M. Ma, "Emission Characteristics of Electrically Small Radiating Sources from Tests inside a TEM cell," *IEEE Transactions on Electromagnetic Compatibility*, **EMC-23**, 3, 1981, pp. 113-121.

53.M. Kanda and R. Orr, "Generation of Standard Electromagnetic Fields in a TEM Cell," National Bureau of Standards Technical Note 1319, 1988, (available from National Institute of Standards and Technology, 325 Broadway, Boulder, CO, 80305).

54.P. Wilson, "A Review of TEM Cell Development", *Proceedings 12th International Wroclaw Symposium on Electromagnetic Compatibility*, (Wroclaw, Poland), 1988, pp. 117-120, (available from the Secretariat, c/o Wroclaw University of Technology, Box 2241, 51-519 Wroclaw 22, Poland).

55.IEC 61000-4-20: Electromagnetic Compatibility (EMC) Part 4: Testing and Measurement Techniques Section 20: Emission and Immunity Testing in Transverse Electromagnetic (TEM) Waveguides, International Electrotechnical Commission, 2003 (available from the IEC, http://www.iec.ch).

56.J. Kärst, C. Groh, and H. Garbe, "Calculable Field Generation using TEM Cells Applied to the Calibration of a Novel E Field Probe," *IEEE Transactions on Electromagnetic Compatibility*, **EMC-44**, 1, 2002, pp. 59-71.

57.F. Fiori and F. Musolino, "Investigation on the Effectiveness of the IC Susceptibility TEM Cell Method," *IEEE Transactions on Electromagnetic Compatibility*, **EMC-46**, 1, 2004, pp. 110-115.

58.J. Yun, H. Lee, and H. Hwang, "Straight Coupled Transmission-Line Cell for Generating Standard Electromagnetic Fields," *IEEE Transactions on Electromagnetic Compatibility*, **EMC-44**, 4, 2002, pp. 515-521.

59.M. Ma, E. Larson, and M. Crawford, "Electromagnetic Fields with Arbitrary Wave Impedances Generated inside a TEM Cell," *IEEE Transactions on Electromagnetic Compatibility*, **EMC-33**, 4, 1991, pp. 358-362.

60.M. Crawford, J. Workman, and C. Thomas, "Generation of EM Susceptibility Test Fields using Large Absorber-Loaded TEM Cell," *IEEE Transactions on Instrumentation and Measurement*, **IM-26**, 3, 1977, pp. 336-343.

61.M. Crawford, J. Workman, and C. Thomas, "Expanding the Bandwidth of TEM Cells for EMC Measurements," *IEEE Transactions on Electromagnetic Compatibility*, **EMC-20**, 3, 1978, pp. 368-375.

62.D. Koenigstein and D. Hansen, "A New Family of TEM-Cells with Enlarged Bandwidth and Optimized Working Volume," *Proceedings 7th International Zurich Symposium on Electromagnetic Compatibility*, (Zurich, Switzerland), 1987, pp. 127-132, (available from the Symposium Secretariat, c/o ETHZ Zentrum, Gloriastrasse 35, CH-8092 Zurich, Switzerland).

63.L. Jendernalik and D. Peier, "Expanding the Bandwidth of a TEM Cell with a Planar Terminator," *Proceedings 10th International Zurich Symposium on Electromagnetic Compatibility (Zurich, Switzerland)*, 1993, pp. 579-582, (available from the Symposium Secretariat, c/o ETHZ Zentrum, Gloriastrasse 35, CH-8092 Zurich, Switzerland).

64.A. Nothofer, M. Alexander, D. Bozec, D. Welsh, L. Dawson, L. McCormack, and A. Marvin, "A GTEM Best Practice Guide – Applying IEC 61000-4-20 to the Use of GTEM Cells," *Proceedings 15th International Zurich Symposium on Electromagnetic Compatibility*, (Zurich, Switzerland), 2003, pp. 207-212, (available from the Symposium Secretariat, c/o ETHZ Zentrum, Gloriastrasse 35, CH-8092 Zurich, Switzerland).

65.P. Wilson, H. Garbe, and E. Steinke, "An Equivalent "Radiated Emission" Voltage Measurement Standard for TEM Cells," *Proceedings 11th International Wroclaw Symposium on Electromagnetic Compatibility*, (Wroclaw, Poland), 1992, pp. 301-304, (available from the Secretariat, c/o Wroclaw University of Technology, Box 2241, 51-519 Wroclaw 22, Poland).

66.P. Wilson, D. Hansen, and D. Koenigstein, "Simulating Open Area Test Site Emission Measurements Based on Data Obtained in a Novel Broadband TEM Cell," *Proceedings 1989 IEEE National Symposium on Electromagnetic Compatibility*, (Denver, CO), 1989, pp. 171-177.

67.L. Turnbull and M. Marvin, "A Treatment of the Phase Properties of GTEM to Open-Area-Test-Site Correlation Techniques," *IEEE Transactions on Electromagnetic Compatibility*, **EMC-40**, 1, 1998, pp. 62-68.

68.P. Wilson, "On Correlating TEM Cell and OATS Emission Measurements," *IEEE Transactions on Electromagnetic Compatibility*, **EMC-37**, 1, 1995, pp. 1-16.

69.F. Leferink, "A Triple TEM Cell: Three Polarizations in One Setup," *Proceedings 10th International Zurich Symposium on Electromagnetic Compatibility*, (Zurich, Switzerland), 1993, pp. 573-578, (available from the Symposium Secretariat, c/o ETHZ Zentrum, Gloriastrasse 35, CH-8092 Zurich, Switzerland).

70.M. Klingler, S. Egot, J.-P. Ghys, and J. Rioult, "On the Use of 3-D Cells for Total Radiated Power Measurements," *IEEE Transactions on Electromagnetic Compatibility*, **EMC-44**, 2, 2002, pp. 364-372.

71.K. Slattery, J. Muccioli, and T. North, "Measuring the Radiated Emissions from a Family of Microprocessors using a 1-GHz TEM Cell," *IEEE Transactions on Electromagnetic Compatibility*, **EMC-41**, 2, 1999, pp. 146-151.

72.S. Clay, "Improving the Correlation Between OATS, RF Anechoic Room and GTEM Radiated Emission Measurements for Directional Radiators at Frequencies Between Approximately 150 MHz and 10 GHz," *Proceedings 1998 IEEE International Symposium on Electromagnetic Compatibility*, (Denver, CO), 1998, pp. 1119-1124.

73.P. Wilson, "Antenna Gain Equivalent for TEM Cells," *IEEE Transactions on Electromagnetic Compatibility*, 2004 (submitted).

74.M. Ma, "Understanding Reverberating Chambers as an Alternative Facility for EMC Testing," *Journal of Electromagnetic Waves and Applications*, **2**, 1988, pp. 339-351.

75.D. Hill, "Electromagnetic Theory of Reverberation Chambers," National Institute of Standards and Technology Technical Note 1506, 1998, (available from National Institute of Standards and Technology, 325 Broadway, Boulder, CO, 80305).

76.M. Bäckström, K. Lövstrand, and B. Nordström, "The Swedish Microwave Test Facility: Technical Features and Experience from System Testing," *Proceedings XXVIIth General Assembly of the International Union of Radio Science*, (Maastricht, Netherlands), 2002, p. 123 (available from the URSI Secretariat, c/o Eindhoven University of Technology, P.O. Box 513, NL-5600 MB Eindhoven, The Netherlands).

77. IEC 61000-4-21, Electromagnetic Compatibility (EMC) Part 4-21: Testing and Measurement Techniques Section 21: Reverberation Chamber Test Methods, *International Electrotechnical Commission*, 2003, (available from the IEC, http://www.iec.ch).

78.M. Crawford, "Evaluation of a Reverberation Chamber Facility for Performing EM Radiated Fields Susceptibility Measurements," National Bureau of Standards Internal Report 81-1638, 1981, (available from National Institute of Standards and Technology, 325 Broadway, Boulder, CO, 80305).

79.D. Hill, "Plane Wave Integral Representation for Fields in Reverberation Chambers," *IEEE Transactions on Electromagnetic Compatibility*, **EMC-40**, 3, 1998, pp. 209-217.

80. J. Kostas and B. Boverie, "Statistical Model for a Mode-Stirred Chamber," *IEEE Transactions on Electromagnetic Compatibility*, **EMC-33**, 4, 1991, pp. 366-370.

81.D. Hill and J. Ladbury, "Spatial Correlation Function for Fields in Reverberation Chambers," *IEEE Transactions on Electromagnetic Compatibility*, **EMC-44**, 1, 2002, pp. 95-101.

82.D. Hill, "Boundary Fields in Reverberation Chambers," *IEEE Transactions on Electromagnetic Compatibility*, 2004 (submitted).

83.L. Arnaut, "Compound Exponential Distributions for Undermoded Reverberation Chambers," *IEEE Transactions on Electromagnetic Compatibility*, **EMC-44**, 3, 2002, pp. 442-457.

84.F. Moglie, "Finite Difference, Time Domain Analysis Convergence of Reverberation Chambers," *Proceedings 15th International Zurich Symposium on Electromagnetic Compatibil-*

ity, (Zurich, Switzerland), 2003, pp. 223-228, (available from the Symposium Secretariat, c/o ETHZ Zentrum, Gloriastrasse 35, CH-8092 Zurich, Switzerland).

85. D. Hill, M. Ma, A. Ondrejka, B. Riddle, M. Crawford, and R. Johnk, "Aperture Excitation of Electrically Large, Lossy Cavities," *IEEE Transactions on Electromagnetic Compatibility*, **EMC-36**, 3, 1994, pp. 169-178.

86. C. Bunting, "Statistical Characterization and the Simulation of a Reverberation Chamber Using Finite-Element Techniques," *IEEE Transactions on Electromagnetic Compatibility*, **EMC-44**, 1, 2002, pp. 214-221.

87. C. Bunting, "Shielding Effectiveness in a Two-Dimensional Reverberation Chamber Using Finite-Element Techniques," *IEEE Transactions on Electromagnetic Compatibility*, **EMC-45**, 3, 2003, pp. 548-552.

88. P. Leuchtmann, C. Bruns, and R. Vahldeck, "Broadband Method of Moment Simulation and Measurement of a Medium-Sized Reverberation Chamber," *Proceedings 2003 IEEE International Symposium on Electromagnetic Compatibility*, (Boston, MA), 2003, pp. 844-849.

89. J. Ladbury, "Stirring Up Trouble: Stirring vs. Tuning in Reverberation Chamber Testing," *Workshops and Tutorials 2002 IEEE International Symposium on Electromagnetic Compatibility*, (Minneapolis, MN), 2002, pp. 235-239.

90. F. Leferink, J. Boudenot, and W. van Etten, "Experimental Results Obtained in the Vibrating Intrinsic Reverberation Chamber," *Proceedings 2000 IEEE International Symposium on Electromagnetic Compatibility*, (Washington, DC), 2000, pp. 639-644.

91. Y. Huang and D. Edwards, "An Investigation of the Electromagnetic Field Inside a Moving Wall Reverberation Chamber," *Proceedings 8th IEE International Conference on Electromagnetic Compatibility*, (Edinburgh, UK), 1992, pp. 115-119.

92. N. Kouveliotis, P. Trakadas, and C. Capsalis, "Theoretical Investigation of the Field Conditions in a Vibrating Reverberation Chamber with Unstirred Component," *IEEE Transactions on Electromagnetic Compatibility*, **EMC-45**, 1, 2003, pp. 77-81.

93. D. Hill, "Electronic Mode Stirring for Reverberation Chambers," *IEEE Transactions on Electromagnetic Compatibility*, **EMC-36**, 4, 1994, pp. 294-299.

94. J. Perini and L. Cohen, "An Alternative Way to Stir the Fields in a Mode Stirred Chamber," *Proceedings 2000 IEEE International Symposium on Electromagnetic Compatibility*, (Washington, DC), 2000, pp. 633-637.

95. R. Jesch, "Measurement of Shielding Effectiveness of Different Cable and Shielding Configurations by Mode-Stirred Techniques," *IEEE Transactions on Electromagnetic Compatibility*, **EMC-30**, 3, 1988, pp. 222-228.

96. J. Adams, "Electromagnetic Shielding of RF Gaskets Measured by Two Methods," *Proceedings 1992 IEEE International Symposium on Electromagnetic Compatibility*, (Anaheim, CA), 1992, pp. 154-157.

97. C. Holloway, D. Hill, J. Ladbury, G. Koepke, and R. Garzia, "Shielding Effectiveness Measurements of Materials Using Nested Reverberation Chambers," *IEEE Transactions on Electromagnetic Compatibility*, **EMC-45**, 2, 2003, pp. 350-356.

98. R. Melnick, J. Bucher, J. Roycroft, C. Portier, and P. Wilson, "Health Effects of Cell Phone Radio Frequency Radiation: National Toxicology Program's Carcinogenicity Studies in Rats and Mice," *Proceedings 25th Bioelectromagnetics Society Annual Meeting*, (Maui, HI), 2003, p. 157.

99. J. Ladbury, P. Wilson, G. Koepke, and T. Lammers, "Reverberation Chamber: Evaluation for Possible Use as a RF Exposure System in Animal Studies," *Proceedings 25th Bioelectromagnetics Society Annual Meeting*, (Maui, HI), 2003, pp. 150-151, (available from BEMS, http://www.bioelectromagnetics.org).

100. D. Hill, "Reciprocity in Reverberation Chamber Measurements," *IEEE Transactions on Electromagnetic Compatibility*, **EMC-45**, 1, 2003, pp. 117-119.

101. C. Holloway, P. Wilson, G. Koepke, and M. Candidi, "Total Radiated Power Limits for Emissions Measurements in a Reverberation Chamber," *Proceedings 2003 IEEE International Symposium on Electromagnetic Compatibility*, (Boston, MA), 2003, pp. 838-843.

102. P. Wilson, D. Hill, and C. Holloway, "On Determining the Maximum Emissions from Electrically Large Sources," *IEEE Transactions on Electromagnetic Compatibility*, **EMC-44**, 1, 2002, pp. 79-86.

103. K. Rosengren, P.-S. Kildal, C. Carlsson, and J. Carlsson, "**Characterization of Antennas for Mobile and Wireless Terminals by Using Reverberation Chambers: Improved Accuracy by Platform Stirring," IEEE International Symposium on** Antennas and Propagation *Digest*, (Boston, MA), 2001, pp. 350-353.

104. K. Rosengren and P.-S. Kildal, "Theoretical Study of the Angular Distribution of Plane Waves in a Small Reverberation Chamber for Simulating Multipath Environment and Testing Mobile Phones," **IEEE International Symposium on** Antennas and Propagation *Digest*, (Boston, MA), 2001, pp. 358-361.

105. M. Liénard, P. Degauque, and P. Laly, "Mode Stirred Chambers for Simulating MIMO Channels," COST 273, TD (04) 024, 2004, (available from COST 273, http://www.lx.it.pt/cost273).

106. A. Yaghjian, "An Overview of Near-Field Antenna Measurements," *IEEE Transactions on Antennas and Propagation*, **AP-36**, 1, 1986, pp. 30-45.

107. E. Gillespie (ed.), "Special Issue on Near-Field Scanning Techniques," *IEEE Transactions on Antennas and Propagation*, **AP-38**, 6, 1988.

108. B. Yordanov, K. Doughty, and R. Yordanov, "Near-Field Probes for EMC Applications," *EMC Test and Design*, 1994, pp. 18-26.

109. J.-J. Laurin, Z. Ouardhiri, and J. Colinas, "Near-Field Imaging of Radiated Emission Sources on Printed-Circuit Boards," *Proceedings 2001 IEEE International Symposium on Electromagnetic Compatibility*, (Montreal, Canada), 2001, pp. 368-373.

110. J.-C. Bolomey, "Introduction to Near-Field Techniques for EMC Applications: State of the Art and Perspectives," *Proceedings 2001 IEEE International Symposium on Electromagnetic Compatibility*, (Montreal, Canada), 2001, p. 356.

111. B. Fourestie, Z. Altman, J.-C. Bolomey, J. Wiart, and F. Brouaye, "Statistical Modal Analysis Applied to Near-Field Measurements of Random Emissions," *IEEE Transactions on Antennas and Propagation*, AP-50, 12, 2002, 1803-1812.

112.**B. Fourestie, Z. Altman, J. Wiart, J.-C. Bolomey, and F. Brouaye, "A Novel Near-Field Measurement Facility for Random Emissions,"** *Proceedings 2001 IEEE International Symposium on Electromagnetic Compatibility*, (Montreal, Canada), 2001, pp. 378-382.

113. J, Perez and J. Basterechea, "Prediction of DUT Radiation from Near-Field Measurements in a Screened Room using GAs," *Proceedings 2001 IEEE International Symposium on Electromagnetic Compatibility*, (Montreal, Canada), 2001, pp. 383-388.

114. T. Sarkar and F. Las-Heras, "An Iterative Spherical Near-Field to Far-Field Emissions and Source Reconstruction Using the Equivalent Circuit Approach," *Proceedings 2001 IEEE International Symposium on Electromagnetic Compatibility*, (Montreal, Canada), 2001, pp. 395-398.

115.O. Bucci, G. Elia, M. Migliori, and R. Pierri, "Phaseless Near-Field Measurements," *Proceedings 2001 IEEE International Symposium on Electromagnetic Compatibility*, (Montreal, Canada), 2001, pp. 389-394.

116.T. Sarkar and F. Las-Heras, "A Direct Optimization Approach for Source Reconstruction NF-FF Using Amplitude Only Data," *Proceedings 2001 IEEE International Symposium on Electromagnetic Compatibility*, (Montreal, Canada), 2001, pp. 399-402.

117.D. Hill, "A Numerical Method for Near-Field Array Synthesis," *IEEE Transactions on Electromagnetic Compatibility*, **EMC-27**, 4, 1985, pp. 201-211.

118.D. Hill, "A Near-Field Array of Yagi-Uda Antennas for Electromagnetic Susceptibility Testing," *IEEE Transactions on Electromagnetic Compatibility*, **EMC-28**, 3, 1986, pp. 170-178.

119.D. Hill, "A Circular Array for Plane-Wave Synthesis," *IEEE Transactions on Electromagnetic Compatibility*, **EMC-30**, 1, 1988, pp. 3-8.

120. R. Haupt, "Generating a Plane Wave in the Near-Field with a Planar Array Antenna," *Microwave Journal*, 2003, pp. 152-166.

New Techniques and Results from Incoherent Scatter Radars

R. Robinson

Abstract

The incoherent scatter technique has been used for more than four decades to remotely detect properties of the upper atmosphere and ionosphere. Nevertheless, the global network of incoherent scatter radars (ISRs) continues to provide measurements leading to ever-improving knowledge of the upper atmosphere and ionosphere. Each of the ISRs is unique, and each takes advantage of its distinct design and location in the way the radar is operated and the type of scientific research supported. The continuing contributions the ISRs have made to upper-atmospheric science are a result of new and innovative methodologies for performing experiments. These methodologies include the use of high-speed digital signal processing, application of advanced transmitter waveform techniques, implementation of innovative antenna modes, better coordination of observations with measurements provided by collocated instrumentation, the operation of ISRs as coherent radars, and the scheduling of long-duration experiments. The improvements achieved in using new techniques with existing radars have inspired creative ideas relating to the specification and design of the next generation of incoherent scatter radars. The Advanced Modular Incoherent Scatter Radar (AMISR), currently under development, will be able to exploit all of these strategies, but will have the additional advantage of being fully re-locatable. Successful use of the ISRs will increasingly demand better coordination and planning, more standardization in data-acquisition systems, and more aggressive educational programs to ensure a broad user base for the radars. The future will see the ISRs continue to be an integral part of all space science research programs.

1. Introduction

Incoherent scatter radars (ISRs) have been used for more than four decades to remotely detect properties of the upper atmosphere and ionosphere, and they continue to provide measurements leading to new scientific breakthroughs and understanding. The continuing contributions the ISRs have made are the result of the development of innovative methodologies for performing experiments. The basic incoherent scatter technique has not changed significantly in the last forty years, yet original science is still being performed by virtue of these new methodologies. The goal of this paper is to illustrate the new strategies that are being applied in conducting ISR observations, and to demonstrate the broad range of science topics that can be addressed with the global ISR network.

The paper begins with a brief description of the world's incoherent scatter radars, noting in particular their unique attributes and the upgrades that have been implemented over the past ten years. Section 3 describes the new methodologies that have been most important in recent scientific research enabled by the radars. The advancements achieved in using new techniques with existing radars have inspired creative ideas relating to the specification and design of the next generation of incoherent scatter radars. Section 4 describes the Advanced Modular Incoherent Scatter Radar, which is currently under development. The concluding section identifies some of the challenges that ISR users will face over the next decade. Despite these challenges, the future will see ISRs continue to be an integral part of virtually all space science programs.

2. Unique Aspects of the Incoherent Scatter Radar Observatories

The incoherent scatter radar (ISR) technique has been described in detail in a number of sources [1-3]. Incoherent scatter radar returns are analyzed to yield the basic properties of the ionosphere, including electron density, ion velocity, ion and electron temperatures, ion composition, and collision frequencies. These basic properties can be used with models or ancillary observations to derive other important atmospheric parameters, such as electrical conductance, neutral wind velocity, and exospheric temperature. Of course, because of ionospheric conditions and the limited sensitivity of the radars, all of these

Robert Robinson is with the National Science Foundation, 4201 Wilson Blvd., Arlington, VA 22230, USA ; Tel : +1 (703) 292-8529; Fax : +1 (703) 292-9023 ; E-mail: rmrobins@nsf.gov.

This is one of the invited *Reviews of Radio Science*, from Commission G.

Observatory	Initial Year of Operation	Location	Latitude	Longitude	Magnetic Latitude	Frequency (MHz)	Antenna Type	Antenna Size	Peak Power (MW)	Maximum Duty Cycle %
EISCAT UHF	1981	Tromsø, Norway	69.58	19.22	66.60	928	Steerable parabolic dish	32 m diameter	2	12.5
EISCAT VHF	1986	Tromsø, Norway	69.58	19.22	66.60	224	Offset parabolic cylinder	120 m × 40 m	3	12.5
EISCAT Svalbard Radar	1996	Longyearbyen, Norway	78.15	16.03	75.30	500	One fixed and one steerable parabolic dish	32 m steerable; 42 m fixed	1	25
Sondrestrom Radar Facility	1983	Kangerlussuaq, Greenland	66.99	309.05	72.80	1290	Steerable parabolic dish	32 m	3.5	3
Jicamarca Radio Observatory	1961	Jicamarca, Peru	-11.95	283.13		50	Square phased array	290 m × 290 m	3	6
Millstone Hill Observatory	1960	Westford, Massachusetts	42.62	288.51	52.45	440	One fixed and one steerable parabolic dish	46 m steerable; 68 m fixed	2.5	6
Arecibo Observatory	1962	Arecibo, Puerto Rico	18.35	293.24	27.60	430	Spherical dish	305 m	2.5	6
Middle and Upper Atmosphere (MU) Radar	1985	Shigaraki, Japan	34.85	136.1	28.15	46.5	Circular phased array	103 m diameter	1	4
Kharkov Radar		Kharkov, Ukraine	50.00	36.23	45.74	150	One fixed parabolic dish	100 m diameter	2-3	

Table 1. Characteristics of incoherent scatter radars.

measurements are not always possible. However, tremendous progress has been made in developing radar techniques to optimize measurement capabilities.

Table 1 lists properties of ISRs currently operating for scientific research. Most of the radars were constructed in the early 1960s. The newest ISR is the EISCAT Svalbard system, which began operations in 1996. Each ISR is unique, and each takes advantage of its distinct design and location in the way the radar is operated and the type of scientific research supported. In terms of geomagnetic location, the global ISR network spans the northern hemisphere from the magnetic equator to the edge of the polar cap. The antennas range in size from the 32 m parabolic reflector at Sondrestrom, Greenland, to the 300 m spherical dish at Arecibo, Puerto Rico. Most of the ISRs employ parabolic or spherical reflectors, while the Jicamarca Radar in Peru and the MU Radar in Japan use arrays of dipole antennas. The Jicamarca and MU Radars are also distinct in that they operate at frequencies of about 50 MHz, while most of the remaining ISRs operate at frequencies of a few hundred MHz. The Sondrestrom Radar operates at 1290 MHz. Here, we briefly summarize the distinctive aspects of the ISRs, and describe recent modifications that have been implemented.

The uniqueness of the Sondrestrom facility resides in its strategic location at the equator-ward edge of the polar cap, and the ability to steer its antenna, which offers many options in designing experimental configurations. The relatively small dish antenna can slew rapidly in azimuth and elevation, making it ideal for observing the spatially and temporally dynamic conditions characteristic of the high-latitude ionosphere. At a magnetic latitude of 72.8º, the Sondrestrom radar is able to observe the polar cusp near local noon and the northern portions of the auroral oval at other local times. Often, the auroral oval is far to the south of Sondrestrom and the radar is able to view sun-aligned arcs and ionization patches in the polar cap. This strategic location has made the facility highly desirable as a site for deploying other atmospheric observing instrumentation. These clustered observations have been used in many coordinated experimental campaigns using the Sondrestrom ISR.

The European Incoherent Scatter (EISCAT) radars include several different systems. The UHF system consists of a tristatic array with its transmitter at Tromsø, Norway, and receiving sites at Kiruna, Sweden, and Sodankyla, Finland. The antennas at each location are fully steerable, providing the coverage necessary to fully exploit the tristatic configuration. Tromsø also has a VHF system with an antenna comprised of four cylindrical parabolic sections, able to steer in elevation in the magnetic meridian. The EISCAT system also includes the EISCAT Svalbard Radar (ESR), which is at about the same magnetic latitude as Sondrestrom. ESR was originally constructed with one steerable parabolic antenna, but in 1999 a second, fixed, 42 m parabolic antenna was added to make measurements in the magnetic zenith simultaneously with the steerable antenna. With the ancillary instrumentation present in the Scandinavian countries, the EISCAT system provides measurement capabilities for a full range of ionospheric and atmospheric properties throughout the auroral zone. In addition, a high-frequency heating facility at Tromsø is used to conduct active experiments of artificially-modified ionospheric plasmas. A second heater – called SPEAR, for Space Plasma Exploration by Active Radar – is under construction at the ESR site on Svalbard [4].

The Millstone Hill ISR is part of the Haystack Observatory, which conducts research in both ionospheric and thermospheric physics, as well as radio astronomy. The Millstone Hill ISR uses two antennas, one a steerable dish

of 42.6 m diameter, the other a fixed zenith-pointing dish with a diameter of 68 m. The steerable antenna is able to scan to very large zenith angles, and with suitable integration times, the radar can make measurements in the F region typically over about 20° of latitude. The ISR at Kharkov, Ukraine, is similar in layout to the Millstone Hill Observatory, but operates only with a fixed, zenith-directed antenna at 150 MHz.

The uniqueness of the Arecibo ISR is its 300-meter dish, which makes it the most sensitive ISR in the world. Though limited in steering ability, the recent addition of Gregorian optics (driven primarily by radio-astronomy requirements) has made it possible to point in two directions simultaneously. The original line feed, used for 430 MHz observations, shares the same elevation track as the Gregorian dome, and a recently installed divider in the waveguide allows transmitter power to be shifted rapidly between the two positions or split between the two positions. Because of its sensitivity, Arecibo can be used to detect the subtle changes in the ISR spectrum produced by different ionic constituents and non-thermodynamic equilibrium. Additionally, Arecibo can effectively use short pulse lengths to observe highly structured electron-density profiles.

The Jicamarca Radar is the only ISR used for scientific research located at the magnetic equator. Because of its location, the antenna beam can be directed perpendicular to the magnetic field over a broad range of altitudes. For this geometry, the incoherent scatter radar spectrum becomes extremely narrow, allowing very precise determination of the Doppler shift. However, in this operating mode, the incoherent scatter spectrum cannot be fit for other parameters, such as electron densities and ion and electron temperatures. For these measurements, the antenna beam must be redirected to an off-perpendicular position by manually changing cable lengths feeding the dipole array. Even this configuration presents difficulty in the spectral fitting to extract ionospheric parameters. Only recently have electron and ion temperatures been possible, owing to reformulation of the ISR theory for the situation when the radar line of sight is nearly perpendicular to the magnetic field [5, 6]. Jicamarca's lower operating frequency also allows electron-density measurements to be made using the Faraday-rotation method. This has been done routinely in the F region, but more recently it has been accomplished in the E region as well, using a bistatic configuration [7]. Another important aspect of the Jicamarca frequency is that it enables the detection of irregularities through coherent scattering. These reflections are strong enough that the radar has been configured in a low-power mode in which it can be continuously operated. Called JULIA, for Jicamarca Unattended Long-term Investigations of the Ionosphere and Atmosphere, the system uses a separate pair of 30-kW-peak-power pulsed transmitters [8]. JULIA has been routinely used to make lower thermosphere/mesosphere observations at Jicamarca since 1996. Recently, the SOUSY radar [9] has been relocated to Jicamarca, where it can be used in conjunction with the main antenna to measure F-region line-of-sight drift velocities simultaneously in two directions.

The MU Radar in Japan is the only ISR based on solid-state technology. Operating at a frequency of 46.5 MHz, it is primarily used for mesospheric, stratospheric, and tropospheric studies. However, it has also been used as an incoherent scatter radar to study low-latitude ionospheric processes.

3. Continuously Improving ISR Methodologies

ISRs continue to provide essential measurement capabilities for a broad range of space-science research. Part of this is due to their ability to measure the most basic properties of the ionospheric plasma. In addition, however, new strategies in the way ISR experiments are conducted have led to better understanding of the ionosphere and thermosphere, and their coupling to the solar-terrestrial system. This section highlights some of the methodologies that have kept the ISRs at the forefront of upper-atmospheric research.

3.1 High-Speed Digital Signal Processing

Virtually all of the incoherent scatter radars have implemented new data-acquisition systems, which take advantage of currently available high-speed data processors. In fact, one of the most important technological developments benefiting incoherent scatter radar experiments is the availability of high-speed computers. Recovery of all information from backscattered incoherent scatter radar signals requires the ability to sample and store large quantities of data. Without the ability to digitally sample at high frequencies and to record to a physical medium that can accommodate the volume of large data, it has been necessary to calculate spectra (or, equivalently, the autocorrelation function) from the received signal in real time. This limits the amount of online processing that can be performed before data are recorded. With limited computer capability, difficult tradeoffs have to be made in the way the data stream is sampled, as there is no way to later recover the information in the original signal.

For many ISR experiments, it is desirable to acquire measurements with good spatial resolution along the entire line of sight through the ionosphere. A simple analysis shows how this requirement is related to computing speed. If the total range along the line of sight is R and the desired range resolution is ΔR, then $R/\Delta R$ is the number of independent measurements required. ISR data are derived from the measured spectrum, which is the Fourier transform of the autocorrelation function (ACF). An autocorrelation function is calculated using a time sequence of data of

length T, sampled at a time interval of ΔT, where ΔT is related to ΔR according to $\Delta T = \Delta R\, 2/c$, with c being the speed of light. The number of floating-point operations required to calculate an autocorrelation function is roughly proportional to $T/\Delta T$. For the entire range to be sampled, the total number of floating-point operations is proportional to $(T/\Delta T)(R/\Delta R)$, or $TR/\Delta R^2$. Thus, the number of floating-point operations to be performed during any given inter-pulse period is inversely proportional to the square of the desired range resolution, which places difficult demands on ISR data-acquisition systems.

Some reduction in the number of floating-point operations can be achieved by reducing the quantities T and R. However, T is dictated by the correlation properties of the medium. At the lower altitudes, the ISR spectrum is narrower, owing to the high ion-neutral collision frequency and the lower temperature of the plasma. The narrower spectra correspond to long correlation times, such that the autocorrelation function from a single pulse will have no zero crossing. In many applications, T cannot be reduced without sacrificing the information content of the autocorrelation function. The alternative is to calculate the autocorrelation function by correlating the time series of the received signal from consecutive pulses originating from the same volume of space. In either case, the number of floating-point operations is the same. The total range, R, can be reduced to minimize computational demands, but then useful data at other ranges would be lost. Alternatively, the number of ranges at which autocorrelation functions are obtained can be reduced. This retains the total range over which measurements are made, but leaves gaps between adjacent measurements.

Fortunately, improvement in computer processing speed has more than compensated for the inverse-square dependence on range resolution. Using Moore's Law [10] as a rough indicator of the improvement in computer speed, the number of floating-point operations that can be performed has doubled every two years. Assuming processor speed has increased 2^5 in the last ten years, a corresponding improvement in range resolution of more than a factor of five is possible without sacrificing spectral quality or range sampling. If Moore's Law holds during the current decade, another five-fold improvement in range resolution for incoherent scatter experiments is conceivable. Of course, the shorter pulse lengths will spread the signal over a broader bandwidth, thus increasing noise and reducing sensitivity. This will eventually impose a practical limit to the improvement that can be achieved as a result of raw computing power.

As mentioned above, the requirement for high-speed, real-time processing of radar autocorrelation functions is alleviated if all data can be conveniently recorded in real time. Emerging mass-storage technologies are making this possible, and have already been used in experiments of limited duration. The future will undoubtedly see this capability improve to the point that many hours of ISR data can be recorded and used for post-processing, no longer limited by *a priori* selections of the parameters used for real-time lag-product calculations.

One challenge in the implementation of new data-acquisition systems at the ISRs is that they have been accomplished largely independently at each of the sites. Little attempt has been made to enforce any standardized approach that would make it easier for users to interchangeably configure experiments at any of the radar installations. This independent development has been beneficial, in that a variety of approaches have been explored, each with unique advantages and disadvantages. The MIDAS-W system, developed at Millstone Hill, offers a software system that is easily transportable to different ISRs [11, 12]. However, standardization may prove difficult because of the differences between the radar systems, as well as the different scientific objectives being addressed at each location. Nevertheless, better coordination in the development of data-acquisition systems in the future will eliminate the hurdles experienced by users wishing to perform experiments at multiple ISRs, in the same way that using processed data from different sites has been facilitated by the widespread use of the NCAR CEDAR database format.

3.2 Improved Transmitter Waveform Techniques

Another improvement enabled by high-speed computer processing has been the ability to take advantage of complex transmitter waveforms. Many ISR experiments require short effective pulse lengths in the D and E regions, to resolve the small-scale structures characteristic of lower altitudes, while longer pulses are necessary to sample the F region, to ensure sufficiently strong signals out to altitudes of several hundred kilometers. The ability to make measurements of ionospheric parameters with a given range resolution is a complex function of transmitter frequency, transmitter duty cycle, receiver bandwidth, and the correlation properties of the medium. Incoherent scatter techniques for optimizing measurements continue to evolve as computing capabilities improve.

Multi-pulse techniques were developed by Farley [13, 14] to provide the means to improve spectral resolution without significant loss in overall sensitivity. The early multi-pulse schemes had a limited number of lag samples per pulse-repetition frequency (PRF), so that sensitivity was compromised unless the PRF could be increased. However, too high a PRF meant that signals might be aliased with reflections from previous pulses returned from backscatter at higher altitudes. Therefore, multiple pulses are sometimes used in conjunction with phase coding so that the returns from one pulse can be separated from the returns from another at a different altitude. Alternating codes, introduced by Lehtinen [15], Lehtinen and Haggstrom [16], and Sulzer [17], make better use of the transmitter duty

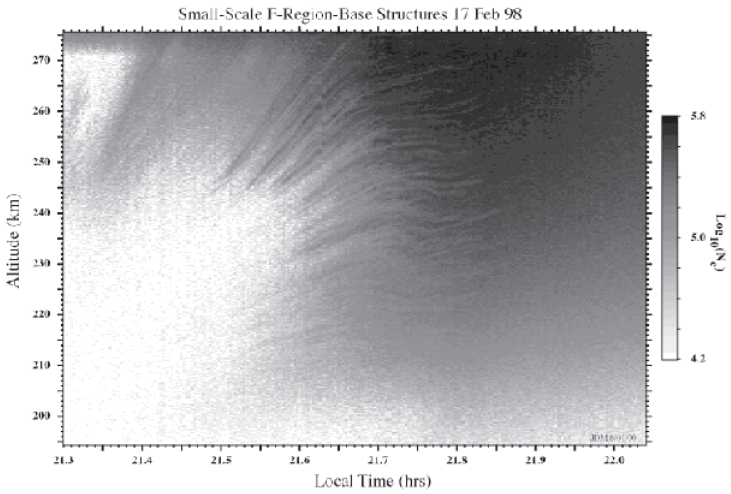

Figure 1. A display of F-region electron densities measured at Arecibo with a resolution of 150 meters. The small-scale structures are believed to be due to Perkins-like instabilities [20].

cycle and achieve high spatial resolution throughout a wide altitude range (i.e., a wide range of correlation times). Pulse coding similar to that used at EISCAT has now been implemented at all the US radars, most recently at Jicamarca [18], where the low transmitter frequency requires autocorrelation functions to be constructed from consecutive pulses.

An example of high-range-resolution electron-density measurements from Arecibo, using 1 μs/baud phase coding, is shown in Figure 1 [19]. The intrinsic range resolution was 150 m, and the integration time for each sample was 10.3 s. The electron density is shown in gray shades as a function of altitude and local time. The large-scale F-region ionization was descending from 270 km altitude at a local time of 21.3 hours to 220 km, only a half-hour later. Embedded within the large-scale F-region plasma were small-scale structures that appeared to be moving upward with time. Kelley and Miller [20] have interpreted these as field-aligned structures produced by instabilities associated with large-scale plasma gradients [21, 22]. One possibility for seeding these instabilities is large-scale acoustic gravity waves. The resulting irregularities are a source of scintillations, as reported by Basu et al. [23]. Thus the ability to directly observe these small-scale ionization features may prove to be an important diagnostic for studying space-weather effects at mid- and low latitudes.

Pulse coding has also enabled D-region measurements, where high range resolution is particularly important. Measurements of Doppler velocities in the D region are extremely difficult, owing to the small radar cross sections at the high frequencies used by incoherent scatter radars. For example, more than two decades ago at Arecibo, Ganguly [24] had to use a 45-minute integration time to measure vertical velocities in the D region. More recently, Zhou [25] has used a 13-baud Barker-coded pulse scheme to measure D-region velocities with an integration time of less than one minute. The Barker codes were well suited for sampling autocorrelation functions with relatively long correlation times. The incoherent scatter spectra are calculated by the pulse-to-pulse fast Fourier Transform technique described by Mathews [26]. The inter-pulse period used for these measurements was a compromise between two competing factors. Short inter-pulse periods of 1 ms yield better D-region measurements, because they allow pulse-to-pulse construction of spectral characteristics in the presence of long correlation times. However, this can only be used at altitudes where the spectral width is sufficiently narrow that the aliasing from much broader F-region echoes can be neglected. Zhou [25] found that an inter-pulse period of 4 ms actually improved the measurement statistics because, in spite of the fact that only one-quarter of the number of measurements were made in a given time, the F-region "noise" from previous inter-pulse period did not overlap with the D-region measurements. The tradeoff was that the longer inter-pulse periods did not allow measurements to as high an altitude as the 1 ms inter-pulse periods because of the correlation-time limitation. Figure 2 shows vertical wind measurements at Arecibo obtained using this technique. Of particular interest are the periodic variations in velocity originating from the passage of gravity waves through the middle atmosphere. Thus, this technique provides a new means to routinely study gravity-wave propagation in the mesosphere.

D-region measurements have also been made at EISCAT by Turunen et al. [27], using a pulse-coding scheme that combines in-pulse correlations for E-region measurements with pulse-to-pulse correlations for D-region measurements. This minimizes the effects of clutter from distant pulses, while at the same time maximizes the sensitivity and resolution in the D region.

Alternating-code techniques used at Sondrestrom have enabled measurements with an altitude resolution of 3 km. An example of this technique was described by Thayer [28], who combined an alternating-code scheme with a long pulse to simultaneously measure E- and F-region parameters, by which the height-resolved contribution of neutral winds to Joule heating rates could be determined. As in earlier studies, the electric field is determined from F-region ion-

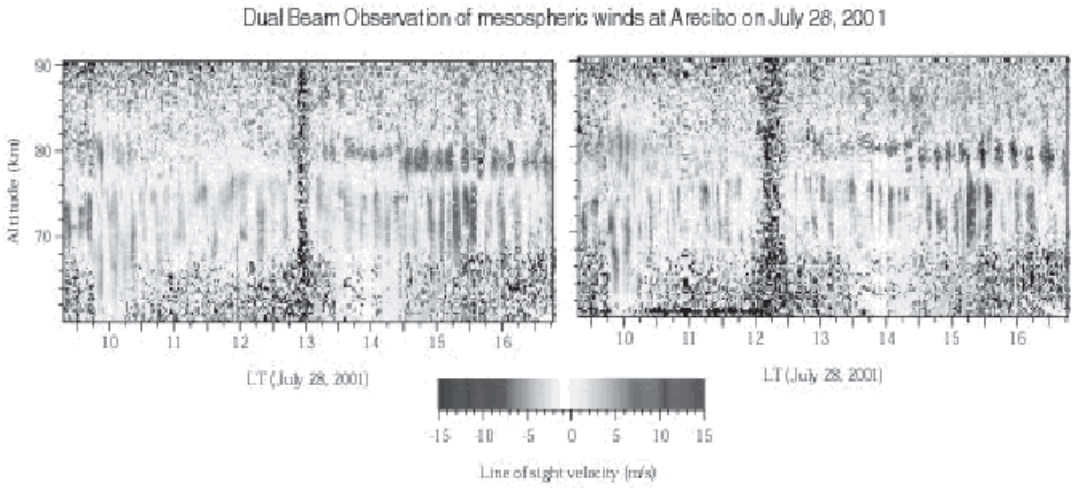

Figure 2. Measurements of vertical velocity in the D region made by the Arecibo ISR. The periodic structures are signatures of gravity-wave perturbations in the mesosphere.

velocity measurements where collisions are negligible. The electric field maps into the E region, where the ion velocity is also affected by the neutral wind. By measuring the E-region ion velocity directly using the incoherent scatter radar, the neutral wind can be determined. However, this technique is inaccurate if the measured ion velocity is not sufficiently height resolved. This limitation is removed by using the alternating-code technique, and a complete determination of electric fields, neutral winds, and Joule heating rates can be obtained. With the improved altitude resolution, Thayer [28] measured neutral winds of more than 400 m/s at an altitude of 120 km. Wind speeds of this magnitude can have a tremendous impact on electrical currents and Joule heating rates.

3.3 Innovative Antenna Modes

Other scientific accomplishments using incoherent scatter have been achieved using innovative antenna modes. An example is the technique used by Doe et al. [29] to observe the ionospheric signature of the polar cusp using the Sondrestrom incoherent scatter radar. In this operating mode, the antenna is successively scanned in azimuth and elevation, with the elevation scan fixed in the magnetic meridian plane. The azimuth scans are designed to overlap such that the magnetic local time may be sampled two or more times, depending on the altitude of the measurement. By binning the data from azimuth scans according to magnetic local time and latitude, Doe et al. [29] were able to produce maps of the horizontal distribution of electron density at any altitude. A feature such as the enhanced ionization produced by cusp precipitation is fixed in local time. By combining the overlapping measurements obtained at different universal times, any such feature will appear prominently in the resulting data. Figure 3 shows a map of electron density between 260 and 320 km altitude derived using this method. This map was produced using data from the west-looking portion of the azimuth scan. By comparing to a similar map produced from the east-looking portion of the scan, Doe et al. [29] were also able to determine any temporal variability in the electron-density features.

A more complex antenna mode was used by Pedersen et al. [30] to "image" ionization patches in the polar cap. Strong radio scintillation is typically associated with the edges of these patches, and the ability to observe their behavior by ISR techniques has helped in studying patch origin and evolution. Carlson et al. [31] operated the EISCAT

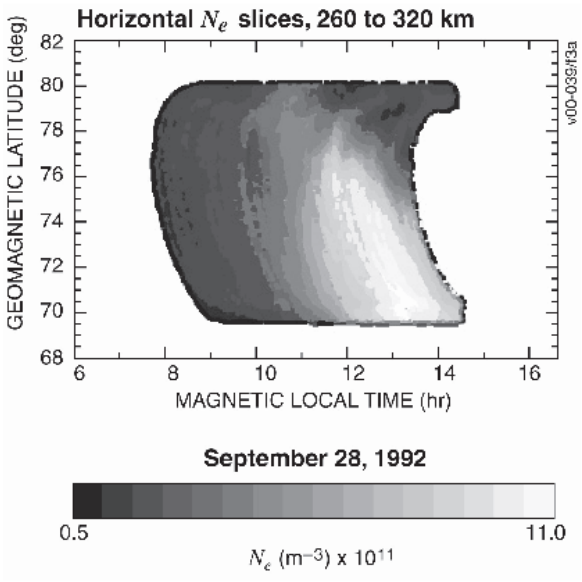

Figure 3. A map of the horizontal distribution of electron density between 260 and 320 km altitude over Sondrestrom. The map was produced by combining data from the west-looking segments of successive azimuth scans. The region of enhanced density is a signature of the tongue of ionization that extends poleward from the dayside ionosphere [29].

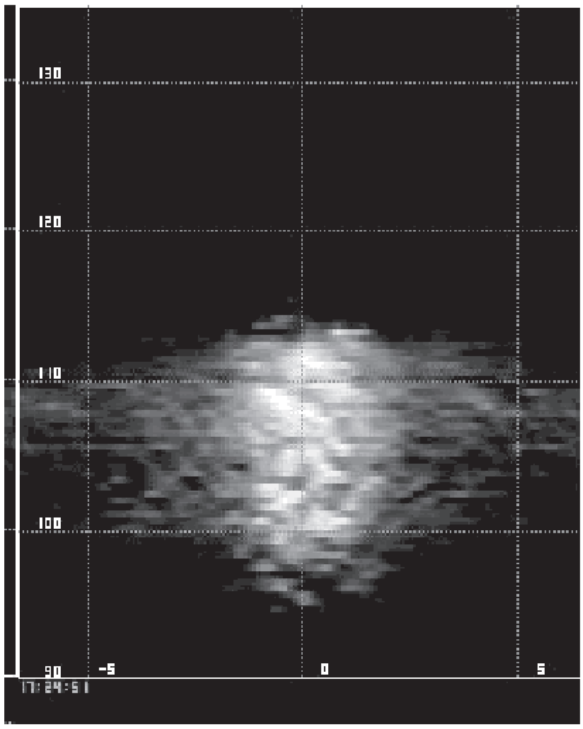

Figure 4. A single image of ionospheric irregularities observed at Jicamarca using interferometric techniques. A sequence of such images reveals complex motions of the irregularities that can be used to study their origin and evolution [32].

Svalbard Radar to observe polar-cap patches using a low-elevation-angle azimuth scan in a windshield-wiper mode, with a repeat time of about two minutes. The rapid scans demonstrated the need for fast temporal sequencing to identify formation mechanisms for polar-cap patches.

An innovative augmentation of the Jicamarca antenna array has allowed the use of interferometric methods to image large-scale plasma waves at the magnetic equator [32, 33]. The single transmitted beam from the large dipole array has been used in the past to detect coherent backscatter from irregularities at the magnetic equator. The resulting range-time-intensity plots indicated how the irregularities appeared to change within the radar beam, but there was no information by which to separate temporal and spatial effects. By adding additional antenna elements outside the main array, Hysell and Chau [33] were able to create six nearly collinear antenna modules for independent reception of reflected signals. The six modules were spaced to give 15 non-redundant interferometry baselines from which 15 cross-correlation functions could be computed. At each range gate, the functions were Fourier transformed to yield the brightness distribution as a function of horizontal displacement. The inversion of the data must be done using regularization techniques and statistical inverse theory, as described by Hysell and Woodman [34]. Figure 4 is an example of a single image of ionospheric structure observed at Jicamarca. The true power of the technique is captured when such images are viewed in sequence, as movies. In this way, motion of the structures in time becomes apparent, and extensive information about the behavior of the plasma waves can be extracted. As the database of such observations grows, patterns of irregularity growth, motion, and decay will undoubtedly be discerned, and the observations will prove extremely valuable for theoreticians wishing to test competing theories on wave-growth mechanisms.

Another example of using external antenna arrays at Jicamarca was demonstrated by the E-region electron-density measurements recently made using Faraday rotation. Because of its location at the magnetic equator, Jicamarca sees only radar clutter at E-region altitudes produced by plasma irregularities in the equatorial electrojet. This prevents the use of incoherent scatter to measure ambient electron densities. Although the Jicamarca antenna beam can be tilted a few degrees off vertical, the strong coherent backscatter from transmitted power in the antenna sidelobes prevents accurate determination of the incoherent scatter signal. Faraday-rotation measurements of electron densities in the F region over Jicamarca are possible because of the thickness of the layer resulting in measurable rotation of the wave vector. With the low density and narrowness of the E region, combined with the reduced rotation when the wave vector is perpendicular to B, Faraday rotation methods do not work at E-region altitudes. The method described by Hysell and Chau [7] uses a bistatic approach, with the transmitting station located at Paracas, Peru. The bistatic geometry attempts to maximize the Faraday rotation of a radar signal by avoiding the condition where the wave vector is perpendicular to the magnetic field. The scattering angle from the transmitter site to the receiver site is nearly 90º, so the radar signal becomes horizontally polarized. Most of the Faraday rotation occurs when the horizontally polarized signal passes down through the layer to the observing station. Although reconstructing the E-region electron density from such measurements is complicated, the technique yields reasonable values in the altitude range between 90 and 110 km. When validated, this capability will be used extensively to provide the necessary E-region boundary conditions for studies of the equatorial electrojet and ionospheric irregularities.

Interferometric measurements have also been made using the EISCAT Svalbard radar [12, 35, 36]. Figure 5 shows power spectra and coherence measured during the Svalbard experiments, illustrating the localized nature of the scattering source region. In contrast to the interferometric methods used at Jicamarca, where subsets of the main antenna could be used because of the strong signals characteristic of coherent backscatter, the Svalbard experiments were performed using the full aperture of the steerable and fixed antennas. The Svalbard observations confirmed the existence of small-scale structures oriented along magnetic field lines produced by plasma instabilities in the auroral ionosphere.

Although interferometric techniques work best for localized source regions, there are a number of natural targets that make these types of observations extremely

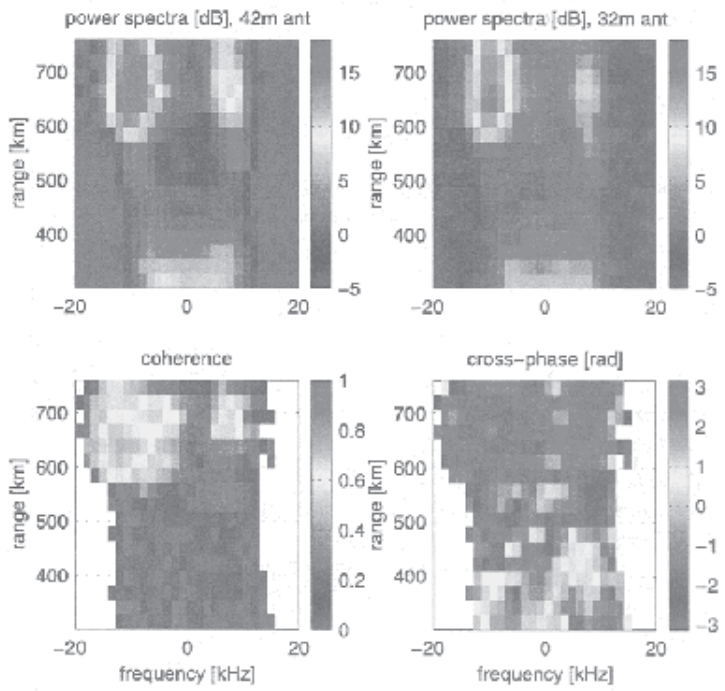

Figure 5. The power spectra of coherent echoes observed using the two antennas of the EISCAT Svalbard Radar. The observations confirmed the existence of filamentary structures on auroral field lines produced by field-aligned plasma instabilities [35].

useful for ionospheric remote sensing. Such experiments help relate micro-scale plasma processes to the characteristics of the basic ISR thermal scattering. The flexibility of the modern systems permits useful measurements of such non-thermal phenomena. This reveals details of the coupling among plasma scales and regimes.

3.4 Coherent Radar Experiments using ISRs

The sensitivity and characteristics of the ISR systems permit using them to probe aspects of the coherent scattering mechanism that cannot be addressed with the smaller radar systems usually used in such studies. The observations of Hysell and Chau [33] described above, using the Jicamarca Radar to image irregularities through interferometry, are possible because of the strong backscatter from structures in the ionosphere at the radar wavelength. Coherent scatter experiments are performed using ISRs at higher frequencies, as well. The EISCAT 224 MHz radar was used to simultaneously detect ion and plasma lines in coherent echoes associated with HF-induced plasma turbulence and an auroral arc [37]. Like the interferometric measurements of Grydeland et al. [35, 36] described above, the source of the auroral arc echoes is believed to be plasma instabilities produced by ion acoustic waves on auroral field lines. Chilson et al. [38] used the EISCAT VHF transmitter at 224.0 and 224.6 MHz to perform frequency-domain interferometric measurements of coherence in polar mesosphere summer echoes (PMSE). The observations were consistent with steepening of upward-propagating gravity waves in the summer mesosphere.

Coherent scatter at 430 MHz has been used at Millstone Hill to measure zonal plasma drifts associated with the high electric fields occurring at mid-latitudes during major magnetic storms [39]. The measurements are made using sidelobe transmissions from the main antenna beam of the Millstone steerable dish. When the sidelobe transmission is oriented appropriately, coherent echoes are seen at a low elevation to the northwest of Millstone, where the sidelobe beam is perpendicular to the magnetic field at E-region altitudes. At the same time, the main beam is used to measure the electric field in the F region from incoherent scatter returns. The results are shown in Figure 6. Using this technique, Foster and Erickson [39] experimentally established a relation between coherent echo power and both the phase velocity of irregularities and the magnitude of the electric field.

Another example of ISRs being used successfully in modes other than classical incoherent scatter is in the detection of meteors. Radar returns from meteors are complicated because in varying degrees they include the echoes from the meteor head itself, the hot plasma of the meteor trail, and the residual plasma that remains after the meteor has ablated. The type of scatter is different in each case, and new theoretical approaches are necessary to interpret the observations. Meteor observations have been made using almost all of the ISRs. Chapin and Kudeki [40, 41] used radar interferometric techniques to study meteor trails at Jicamarca. Zhou et al. [42] described meteor observations made at Arecibo at both VHF and UHF frequencies. A review of more recent meteor studies at Arecibo was presented by Mathews et al. [43]. EISCAT observations of meteors have been made routinely since the first experiments reported by Pellinen-Wannberg and

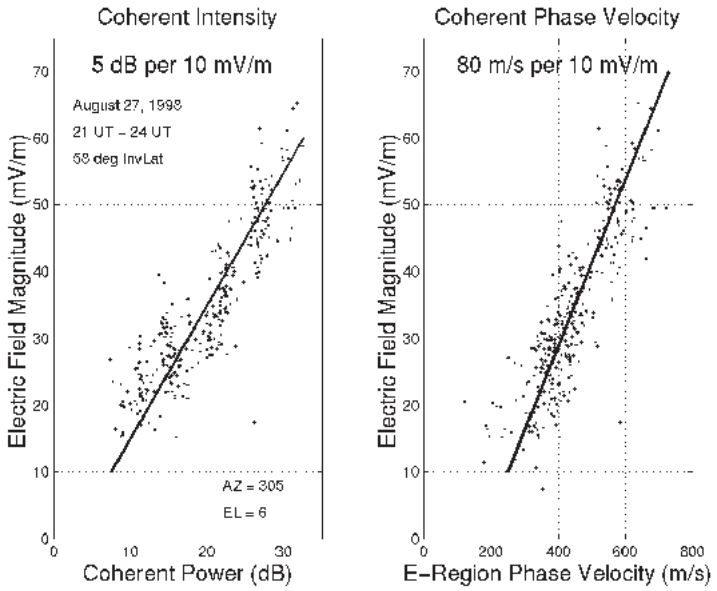

Figure 6. The correlation between coherent echo characteristics and electric field measured simultaneously using coherent and incoherent scatter returns at Millstone. The electric field was well correlated with both the coherent power and the E-region phase velocity [39].

Wannberg [44]. Janches [45] used the tristatic configuration of the EISCAT UHF system to determine the orbital parameters of meteors from vector velocity measurements. Other meteor observations have been made using the MU Radar [46] and the Department of Defense radar ALTAIR (Advanced Research Projects Agency Long-Range Tracking and Instrumentation Radar) [47]. Although not particularly well-suited for conducting synoptic meteor observations, owing to their relatively small fields of view, the ISRs still provide a wealth of new information on the frequency dependence of meteor echoes. The frequency dependence of meteor echoes may help sort out the various processes producing the backscatter during the meteor's passage through the Earth's atmosphere.

3.5 Coordinated Observations

Coordinated measurements made in conjunction with incoherent scatter radar observations have proven to be an excellent methodology for studying complex ionospheric processes. The literature is filled with excellent examples of the way in which ISR observations have been used with other data obtained from both ground-based and space-based instrumentation. Recent years have seen particular emphasis on performing ISR observations simultaneously with the operation of collocated instrumentation, as well. This facilitates coordinated experiments and guarantees simultaneity in space and time, which otherwise would depend on fortuitous conjunctions.

Coordinated measurements open up regions of the atmosphere to study that were previously difficult to investigate using ISR observations alone. An excellent example is in the mesosphere, where chemical and dynamical effects occur in association with meteoric input and gravity-wave forcing. Observations of these processes using lidars and passive optical techniques in conjunction with ISR measurements have provided important new insight into the chemistry of sporadic sodium layers. For example, Figure 7 shows sodium-density concentrations and plasma frequency in the altitude range 75 to 110 km, using a sodium lidar collocated with the Sondrestrom incoherent scatter radar [48, 49]). In this case, an attempt was made to identify the potential auroral contribution to sodium-layer chemistry. By modeling the expected relationship between ionization produced by auroral precipitation and sodium-layer concentrations, Heinselman [49] showed that aurorally produced ionization can change the sodium column content by 50% over tens of minutes. The sodium response to auroral precipitation is due to the production of molecular ions produced by the incoming electrons. The presence of molecular ions modifies the gas-phase chemistry of sodium, thus changing the steady-state concentrations. Recognition of this association is important in that it implies that auroral precipitation simulates an active experiment, where the response to a transient input in atmospheric parameters can be studied to test understanding of the chemical processes.

Simultaneous lidar and radar measurements can also be used to study the effects of tidal motion on sodium distribution. Friedman et al. [50] measured sodium density concentrations and plasma frequency in the altitude range of 75 to 110 km on three nights, using a sodium lidar and the 430 MHz radar at Arecibo. The sporadic E layer observed by the radar is generally situated above the sodium layer observed with the lidar. In some cases, the strong enhancements in sodium concentrations are coincident with increases in ion-layer densities. The downward tidal motion in these layers is believed to be the mechanism creating sporadic-E layers at lower altitudes. The spatial and temporal behavior of the sodium layers and ionization layers will enable atmospheric chemical and dynamical models to be tested.

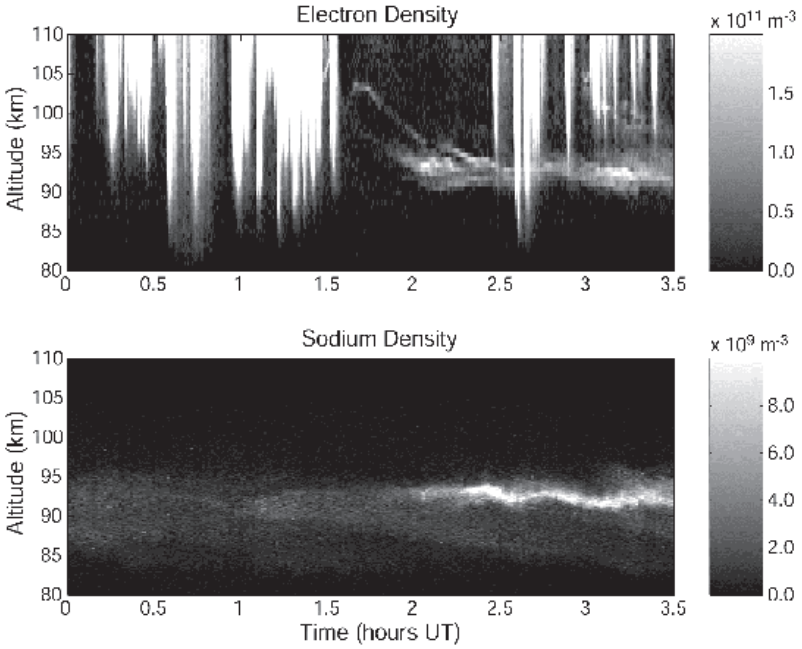

Figure 7. Simultaneous electron density and sodium density in the mesosphere over Sondrestrom measured with the incoherent scatter radar and Rayleigh lidar, respectively. The electron-density display shows the discrete ionization associated with auroral precipitation and the more diffuse regions of sporadic E [48].

The power of multi-instrument observations is also exemplified in recent studies of plasmaspheric plumes and their ionospheric signatures [51]. In this case, Millstone Hill Radar observations were combined with measurements of total electron content (TEC) made by a network of Global Positioning System (GPS) satellite receivers. The left-hand panel of Figure 8 shows a TEC map of North America, determined from the time delay in transionospheric GPS signal propagation. The narrow region of enhanced electron density extending northwestward from the eastern United States coincides with high-speed westward convecting plasma measured by the radar, as shown in the right-hand panel of the figure. When mapped into the equatorial plane of the magnetosphere, the jet of plasma is seen to extend sunward from the plasmasphere in a feature that is commonly seen in extreme ultraviolet images of Earth, obtained by NASA's IMAGE satellite. This sub-auroral polarization stream (SAPS) has been characterized in a number of studies using Millstone Hill radar data and other ground- and space-based instrumentation [52, 53].

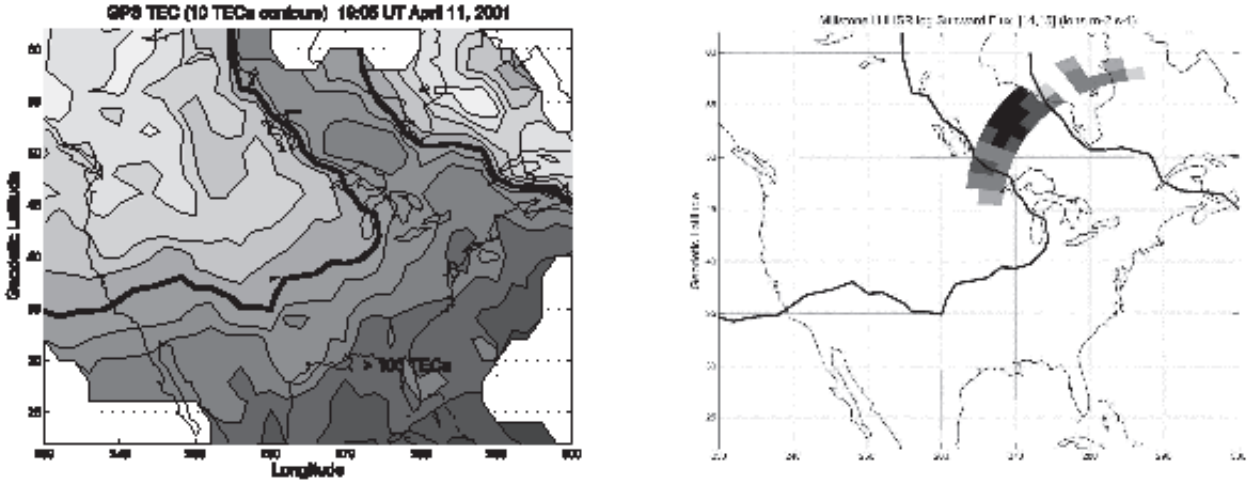

Figure 8. Observations of a sub-auroral plasma stream (SAPS) during a large magnetic storm. The left panel shows a jet of enhanced total electron content derived from GPS measurements. The right panel shows the sunward flux of plasma derived from Millstone Hill ISR measurements of ion velocity and electron density. The plasma stream is spatially collocated with the region of high sunward flux, which maps to a plasmaspheric plume in the magnetosphere [51].

Coordinated observations with sensitive optical instruments allow study of fine-scale structures produced by auroral precipitation. There has been much recent work in determining the physical processes associated with auroral rays. Semeter [54] combined multi-spectral optical observations and Sondrestrom incoherent scatter radar measurements to understand the distribution of auroral emissions in rays. Grydeland et al. [36] and Blixt et al. [55] studied auroral ray structure using a high-resolution, narrow-field-of-view imager and the EISCAT Svalbard Radar. The radar observations confirmed the existence of naturally enhanced ion-acoustic echoes along the magnetic field lines coincident with the rays. These studies underscore the importance of using optical observations to establish a geophysical context to interpret radar measurements of small-scale, dynamic structures, as well as the importance of radar measurements in understanding the microphysics of optical structures in the ionosphere.

Making use of all available data in the interpretation of radar measurements is also essential in studying the coupling between the magnetosphere and the ionosphere. Huang et al. [56-58] and Huang and Foster [59] combined Millstone Hill data with interplanetary magnetic-field measurements to show how the mid-latitude ionosphere responds directly to variations in the solar wind. These observations demonstrated that penetrating westward electric fields driven by the solar wind produce uplifting of the mid-latitude F region. The change in recombination rates with altitude result in a corresponding prompt response of the F-region plasma density.

The trend toward operating ISRs in conjunction with other instruments, particularly those collocated with the radars, will continue. An excellent example is the Coordinated Ionosphere Campaigns, which brought together many observational assets in conjunction with ISR measurements from Arecibo and Jicamarca [60-62]. Obviously, such coordinated observations require more advanced planning than when performing standalone ISR observations. Thus, more active coordination among experimenters is highly desirable, and the ISRs should provide the cohesive force in bringing together scientists applying different observing techniques to upper atmospheric research.

3.6 Long-Duration Experiments

Coordinated observations by the global network of incoherent scatter radars have been made over the last two decades during World Day campaigns. World Day campaigns are scheduled through the URSI Incoherent Scatter Working Group. Initiated as 24-hour experiments, the World Days have been growing in length, in part to respond to the demands of modelers needing extended-quiet-time baseline observations to initiate computer models of ionospheric storms and other transient events. Extended observations, of course, also maximize the likelihood that a given World Day experiment will include the kinds of dynamic conditions necessary to study ionospheric effects due to geomagnetic storms.

The increase in experiment duration for World Days led to a ten-day run conducted in 1993. The prolonged operations enabled a number of important scientific breakthroughs, which inspired demands for more such experiments. In 1999, several of the incoherent scatter radars were operated continuously for five days during a dedicated campaign coordinated by COSPAR, referred to as Space Weather Month [63, 64]. In 2002, the EISCAT radar was operated for 18 consecutive days. The success of this experiment led to a campaign in 2003 where the EISCAT Svalbard Radar and the Millstone Hill Radar ran continuously for 30 days [65]. This has produced a tremendous database for modelers to test the ability to specify ionospheric conditions on a continuous basis.

As beneficial as these long experiments have been, the incoherent scatter radars are limited in their ability to conduct long-duration observations on a routine basis. These limitations include the cost of fuel and the availability of personnel necessary to support continuous measurements for many days. In addition, many of the radars are still using klystron-based transmitters with finite lifetimes. Extended operation means less time between klystron failures. The Arecibo Observatory faces an additional challenge, in that the ionospheric observations must compete for time on the system with radio astronomy. World Days are scheduled a year in advance, and there is little flexibility to modify the dates of an experiment based on geomagnetic activity. Recently, the incoherent scatter radars have implemented an alert system, whereby all the observatories are notified when there is a strong likelihood of a geomagnetic storm within the next several days. The predictions are based on observations of the sun, where a solar flare or coronal-mass ejection may signal the advent of geomagnetic activity two or three days in advance. This method has successfully enabled the radars to operate during major geomagnetic storms.

4. The Future

The success of the incoherent scatter radars in enabling new understanding of the upper atmosphere is attributable to the creative ways the systems have been used. Somewhat contrary to the paradigm that new understanding depends on completely new observational capabilities, the results described above have been achieved through innovative application of a basic technique that has not changed in more than forty years.

Extrapolating such trends into the future is risky, but it is reasonable to assume that the current momentum in the areas identified above will continue in the short term. Thus, it is likely that the existing ISRs will continue to inspire excellent scientific productivity over the next decade. Ironically, it is perhaps the versatility of the radars that has

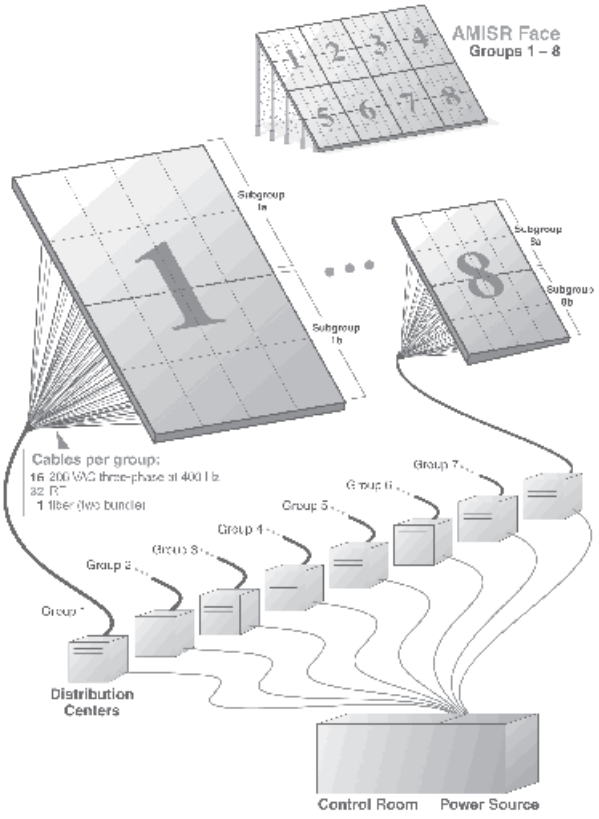

Figure 9. The conceptual design for a single face of the Advanced Modular Incoherent Scatter Radar. The 128 panels that make up a face can be operated as eight independent groups of 16 panels each. This allows for interferometric capabilities by combining signals returned from different groups of dipole elements.

prevented proliferation of these systems. Unlike, for example, optical telescopes, which reach the limits of their capabilities and must be replaced with improved instruments, the continued improvement of ISR techniques has thus far seen no such barriers. Nevertheless, the United States National Science Foundation has recently approved funding for a new project named the Advanced Modular Incoherent Scatter Radar (AMISR). The AMISR design allows tremendous versatility in all the areas described above, but with one important advantage. The radar will be able to be easily disassembled and relocated to provide observing capabilities in different locations driven by scientific needs or missions of opportunity.

Figure 9 shows the design concept. The basic design element is a single dipole antenna, attached to a transmitter/receiver unit with a 500 watt solid-state power amplifier. The transmitters can be operated in the frequency range from 430 to 460 MHz. Thirty-two of these antenna-element units are mounted on a single panel of dimensions 2.1 m by 3.7 m. Current plans call for assembling 384 of these panels into three arrays of dipoles, with dimensions of approximately 30 m by 30 m each. The first array, or face, is scheduled to be deployed at Poker Flat, Alaska, early in 2005, while the second and third faces will be deployed within two years thereafter at Resolute Bay, Canada, within the polar cap. Other antenna configurations are possible, as the cabling to the antenna panels allows for groups of 16 panels to be operated independently. This will allow interferometer modes using received signals from the eight 16-panel modules that comprise a face.

AMISR features pulse-to-pulse electronic steering capabilities within 30º of the bore-sight direction. The single face at Poker Flat will be canted northward, to provide better coverage of flight paths of rockets launched from Poker Flat. The two faces at Resolute Bay will be arranged to provide the extended coverage necessary for polar-cap science. Given the modularity of the design, many other antenna configurations are possible, and these can be optimized according to the location of the radar and the specific science objectives. Disassembling and relocating an AMISR face will take about six months, so decisions on future relocations will have to be considered carefully, and well in advance of the desired time of deployment.

The AMISR is able to take advantage of all the qualities that have made existing incoherent scatter radars timeless instruments. In addition to the flexibility of the antenna configuration, the instantaneous pointing capability allows image reconstruction of the ionospheric plasma, thus enabling better separation of spatial and temporal variations. The transmitted waveforms will provide for pulse coding to push the limits of possible range resolution. As with existing ISR facilities, the locations at which AMISR is deployed will become ideal sites for clustered instrumentation, thus providing ample opportunities for more of the kind of coordinated measurements described

above. The solid-state technology allows the radar to be operated continuously for long periods of time, limited only by the cost of power. The ease with which the radar can be operated also permits remote commanding with a minimum of onsite support staff. Scientific requirements increasingly call for long-duration, global ISR experimental campaigns. As these long experiments become more feasible and cost-effective, it is likely that the current World Day campaigns will evolve into World Week or World Month campaigns. Furthermore, Web-based technology will make the data widely accessible in near real time. Real-time commanding of radar operating modes will be possible so that scientists can reconfigure the radar in response to changing geophysical conditions. These same capabilities will make AMISR not only an asset to the global science community, but also to students and the general public.

The future will also see more frequent use of the incoherent scatter radars as chains and clusters. Examples given above illustrate the effective use of clustered instrumentation in the interpretation and analysis of radar data. Similarly, effective use of the global network of radars will become increasingly popular as standardized data-taking schemes are implemented, and data access is facilitated through Web-based data-archiving infrastructure. Ease in access to archived ISR data will also inspire more statistical studies to identify common properties and long-term trends in the ionosphere, as well as to build empirical models [66, 67].

The use of the incoherent scatter radars to support space-weather objectives will also increase. The EISCAT system has been used in a non-radar mode to observe interplanetary scintillations [68-70]. The interplanetary scintillation measurements are important in that they could potentially provide useful information about solar-wind structures. Thus, the technique can be developed into a valuable space-weather forecasting tool. Recent experiments have explored the possibility of using the Jicamarca Radar to directly measure properties of the solar corona. ISR observations can also be used to understand the processes leading to steep ionospheric-density gradients that impede the use of GPS navigation signals [71].

The completion of all three AMISR faces in 2007 coincides with the International Polar Year. Carefully planned experimental campaigns, featuring the global array of incoherent scatter radars, would highlight the tremendous improvements in observational campaigns that have been achieved in the last fifty years. This represents an excellent opportunity to take advantage of the radars and other ground-based instruments in addressing outstanding problems in upper atmospheric research, including radio science, plasma physics, space weather, and global change.

5. Conclusion

Incoherent scatter radars continue to provide the space-science community with the means to routinely observe the basic properties of the upper atmosphere and ionosphere at scientifically strategic locations over the globe. It is difficult to imagine a research project in space physics that would not benefit from incoherent scatter observations. The examples shown above demonstrate that incoherent scatter radars go far beyond the measurement of basic ionospheric parameters in support of scientific research. When used in innovative ways, making use of developing technologies and improved signal-processing capabilities, incoherent scatter radars also provide the means to discover new phenomena, inspiring research at the frontiers of knowledge.

Effective use of ISRs will not happen by chance, however. The increasing complexity of ISR experiments will require careful planning, far in advance. All possible coordinated observations, both from the ground and in space, must be taken into consideration and optimized to fit the particular science objectives. Future experiments will undoubtedly see increased use of simulated radar experiments, where ionospheric conditions are fed into a virtual radar system that will accurately recreate the possible results of the actual experiment. This can be used to optimize the antenna configurations, pulse-coding schemes, and data-acquisition system prior to the actual experiment. As discussed above, a standardized data-acquisition system will help to make the design of ISR experiments straightforward and easily transported from one radar to another.

All of this will require knowledgeable ISR users to effectively plan experiments and make use of the data. ISR techniques are not typically taught as part of standard graduate curricula in space-science-related fields. This has probably been the primary obstacle to more widespread use of the radars in graduate-student research. Although it will always require experts to understand the subtleties that may enter into designing ISR experiments, a more knowledgeable user base will ensure that these complexities do not inhibit the use of ISR observations.

Finally, most of the world's incoherent scatter radars still use outdated transmitters, involving high-power klystrons that are difficult to repair or replace. The recent acquisition of more than twenty 430 MHz klystrons from the Clear Air Force Station in Alaska will provide both Arecibo and Millstone Hill enough klystrons to last through the decade. Recent upgrades to the Sondrestrom Radar have made it possible for the ISR to use commercially available klystrons at a reasonable cost. The EISCAT Svalbard Radar has successfully made use of TV-type transmitters with lower-power klystrons, achieving high reliability and safety at operating powers of 65 kW/tube. Nevertheless, it is not too early to begin to consider how the current radars will be replaced in the future. The solid-state technology planned for the AMISR system has many advantages, but combining the output from small, low-power transmitters for use with single-dish antennas remains a technical challenge. Transitioning the existing ISRs to new technologies will require a significant investment of funds, but there is no

doubt that the ISRs will continue to enable high-quality atmospheric research far into the future.

6. Acknowledgement

The author benefited from valuable discussions with Craig Heinselman, John Kelly, and Richard Doe of SRI International, Sixto Gonzalez of the Arecibo Observatory, and Wes Swartz of Cornell University.

7. References

1. D. T. Farley, J. P. Dougherty, and D. W. Barron, "A Theory of Incoherent Scattering of Radio Waves by a Plasma, II. Scattering in a Magnetic Field," *Proceedings of the Royal Society A*, **263**, 1961, pp. 238-258.

2. J. V. Evans, "Theory and Practice of Ionosphere Study by Thomson Scatter Radar," *Proceedings of the IEEE*, **57**, 4, 1969, pp. 496-530.

3. A. Brekke (ed.), *Radar Probing of the Auroral Plasma*, Scandinavian University Books, 1977.

4. D. M. Wright, J. A. Davies, T. R. Robinson, P. J. Chapman, T. K. Yeoman, E. C. Thomas, M. Lester, S. W. H. Cowley, A. J. Stocker, R. B. Horne, and F. Honary, "Space Plasma Exploration by Active Radar (SPEAR): An Overview of a Future Radar Facility," *Annales Geophysicae*, **18**, 2000, pp. 1248-1255.

5. M. P. Sulzer, and S. Gonzalez, "The Effect of Electron Coulomb Collisions on the Incoherent Scatter Spectrum in the F Region at Jicamarca," *Journal of Geophysical Research*, **104**, 1999, pp. 22535-22552.

6. N. Aponte, M. P. Sulzer, and S. A. Gonzalez, "Correction of the Jicamarca Electron-Ion Temperature Ratio Problem: Verifying the Effect of Electron Coulomb Collisions on the Incoherent Scatter Spectrum," *Journal of Geophysical Research*, **106**, 2001, pp. 24785-24794.

7. D. L. Hysell, and J. L. Chau, "Inferring E Region Electron Density Profiles at Jicamarca from Faraday Rotation of Coherent Scatter," *Journal of Geophysical Research*, **106,** A12, 2001, pp. 30371-30380.

8. J. Burcham, *First Results of the JULIA Radar*, MS thesis, Clemson University, Clemson, SC, 1997.

9. P. Czechowsky, G. Schmidt, and R. Rüster, "The Mobile SOUSY Doppler Radar: Technical Design and First Results," *Radio Science*, **19**, 1984, pp. 441-450.

10. G. E. Moore, "Cramming More Components onto Integrated Circuits," *Electronics*, **38**, 8, 1965.

11. J. M. Holt, P. J. Erickson, A. M. Gorczyca, and T. Grydeland, "MIDAS-W: A Workstation-Based Incoherent Scatter Radar Data Acquisition System," *Annales Geophysicae*, **18**, 2000, pp. 1231-1241.

12. T. Grydeland, F. D. Lind, P. J. Erickson, and J. M. Holt, "Software Radar Signal Processing," *Annales Geophysicae*, 2004, in review.

13. D. T. Farley, "Incoherent Scatter Correlation Function Measurements," *Radio Science*, **4**, 10, 1969, pp. 935-953.

14. D. T. Farley, "Multiple-Pulse Incoherent Scatter Correlation Function Measurements," *Radio Science*, **7**, 6, 1972, pp. 661-666.

15. M. S. Lehtinen, *Statistical Theory of Incoherent Scatter Measurements*, PhD thesis, University of Helsinki, Finland, 1986.

16. M. S. Lehtinen, and I. Häggström, "A New Modulation Principle for Incoherent Scatter Measurements," *Radio Science*, **22,** 4, 1987, pp. 625-634.

17. M. P. Sulzer, "Recent Incoherent Scatter Techniques," *Advances in Space Research*, **9,** 5, 1989, pp. 153-162.

18. D. Hysell, "Incoherent Scatter Experiments at Jicamarca Using Alternating Codes," *Radio Science*, **35**, 6, 2000, pp. 1425-1435.

19. J. D. Mathews, S. Gonzalez, M. P. Sulzer, Q. –H. Zhou, J. Urbina, E. Kudeki, and S. Franke, "Kilometer-Scale Layered Structures Inside Spread-F," *Geophysical Research Letters*, **28**, 2001, pp. 4167-4170.

20. M. C. Kelley and C. A. Miller, "Electrodynamics of Midlatitude Spread F, 3. Electrodynamic Waves: A New Look at the Role of Electric fields in Thermospheric Wave Dynamics," *Journal of Geophysical Research*, **102**, 1997, pp. 11539-11547.

21. F. W. Perkins, "Spread F and Ionospheric Currents," *Journal of Geophysical Research*, **78,** 1973, pp. 218-226.

22. A. M. Hamza, "Perkins Instability Revisited," *Journal of Geophysical Research*, **104**, 1999, pp. 22567-22575.

23. S. Basu, S. Basu, S. Ganguly, and J. A. Klobuchar, "Generation of Kilometer Scale Irregularities during the Midnight Collapse at Arecibo," *Journal of Geophysical Research*, **86**, 1981, pp. 7607-7616.

24. S. Ganguly, "Incoherent Scatter Radar Observations of Mesospheric Dynamics at Arecibo," *Geophysical Research Letters*, **7**, 1980, pp. 369-372.

25. Q. Zhou, "Incoherent Scatter Radar Measurement of Vertical Winds in the Mesosphere," *Geophysical Research Letters*, **27**, 2000, pp. 1803-1806.

26. J. D. Mathews, "Incoherent Scatter Radar Probing of the 60-100 km Atmosphere and Ionosphere," *IEEE Transactions Geoscience Remote Sensing*, **GE-24**, 1986, pp. 765-776.

27. T. Turunen, A. Westman, I. Häggström, and G. Wannberg, "High Resolution General Purpose D-layer Experiment for EISCAT Incoherent Scatter Radars Using Selected Set of Random Codes," *Annales Geophysicae*, **20**, 2002, pp. 1469-1477.

28. J. P. Thayer, "Height-Resolved Joule Heating Rates in the High-Latitude E Region and the Influence of Neutral Winds," *Journal of Geophysical Research*, **103**, 1998, pp. 471-487.

29. R. A. Doe, J. D. Kelly, and E. R. Sanchez, "Observations of Persistent Dayside F Region Electron Temperature Enhancements Associated with Soft Magnetosheathlike Precipitation," *Journal of Geophysical Research*, **106**, 2001, pp. 3615-3630.

30. T. R. Pedersen, B. G. Fejer, R. A. Doe, and E. J. Weber, "An Incoherent Scatter Radar Technique for Determining Two-

Dimensional Horizontal Ionization Structure in Polar Cap F Region Patches," *Journal of Geophysical Research*, **105**, 2000, pp. 10637-10655.

31. H. C. Carlson, K. Oksavik, J. Moen, A. P. van Eyken, and P. Guio, "ESR Mapping of Polar-Cap Patches in the Dark Cusp," *Geophysical Research Letters*, **29**, 10, 2002, pp. 1386-1389.

32. D. L. Hysell, "Radar Imaging of Equatorial F-Region Irregularities with Maximum Entropy Interferometry," *Radio Science*, **31**, 1996, pp. 1567-1578.

33. D. L Hysell, and J. L. Chau, "Imaging Radar Observations and Nonlocal Theory of Large-scale Plasma Waves in the Equatorial Electrojet," *Annales Geophysicae*, **20**, 8, 2002, pp. 1167-1179.

34. D. L. Hysell, and R. F. Woodman, "Imaging Coherent Backscatter Radar Observations of Topside Equatorial Spread F," *Radio Science*, **32**, 1997, pp. 2309-2320.

35. T. Grydeland, C. La Hoz, T. Hagfors, E. M. Blixt, S. Saito, A. Strømme, and A. Brekke, "Interferometric Observations of Filamentary Structures Associated with Plasma Instability in the Auroral Ionosphere," *Geophysical Research Letters*, **30**, 6, 2003, pp. 1338-1341, DOI: 10.1029/2002GL016362.

36. T. Grydeland, E. M. Blixt, U. P. Løvhaug, T. Hagfors, C. LaHoz, and T. S. Turunen, "Interferometric Radar Observations of Filamented Structures due to Plasma Instabilities and Their Relation to Dynamic Auroral Rays," *Annales Geophysicae*, 22, 2004, pp. 1-18.

37. M. T. Rietveld, B. Isham, T. Grydeland, C. LaHoz, T. B. Leyser, F. Honary, H. Ueda, M. Kosch, and T. Hagfors, "HF-Pump-induced Parametric Instabilities in the Auroral E-region," *Advances in Space Research*, **29**, 9, 2002, pp. 1363-1368.

38. P. B. Chilson, S. Kirkwood, and I. Häggström, "Frequency Domain Interferometry Mode Observations of PMSE Using the EISCAT VHF Radar," *Annales Geophysicae*, **18**, 2001, pp. 1599-1612.

39. J. C. Foster, and P. J. Erickson, "Simultaneous Observations of E-region Coherent Backscatter and Electric Field Amplitude at F-Region Heights with the Millstone Hill UHF Radar," *Geophysical Research Letters*, **27**, 2000, pp. 3177-3180.

40. E. Chapin and E. Kudeki, "Radar Interferometric Imaging Studies of Long-Duration Meteor Echoes Observed at Jicamarca," *Journal of Geophysical Research*, **99**, 1994, pp. 8937-8949.

41. E. Chapin and E. Kudeki, "Plasma Wave Excitation on Meteor Trails in the Equatorial Electrojet," *Geophysical Research Letters*, **21**, 1994, pp. 2433-2436.

42. Q. H. Zhou P. Perillat, J. Y. N. Cho, and J. D. Mathews, "Simultaneous Meteor Echo Observations by Large-Aperture VHF and UHF Radars," *Radio Science*, **33**, 6, 1998, pp. 1641-1654.

43. J. D. Mathews, J. Doherty, C. –H. Wen, D. Janches, and D. D. Meisel, "An Update on UHF Radar Meteor Observations and Associated Signal Processing Techniques at Arecibo Observatory," *Journal of Atmospheric and Solar Terrestrial Physics*, **65**, 2003, pp. 1139-1149.

44. A. Pellinen-Wannberg and G. Wannberg, "Meteor Observations with the European Incoherent Scatter UHF Radar," *Journal of Geophysical Research*, **99**, 1997, pp. 11379-11390.

45. D. Janches, A. Pellinen-Wannberg, G. Wannberg, A. Westman, I. Haggstrom, and D. Meisel, "Tristatic Observations of Meteors Using the 930 MHz European Incoherent Scatter Radar System," *Journal of Geophysical Research*, 107, 2002, DOI 10.1029/2001JA009205.

46. T. Nakamura, T. Tsuda, and M. Tsutsumi, "Development of an External Interferometer for Meteor Wind Observation Attached to the MU Radar," *Radio Science*, **32**, 1997, pp. 1203-1214.

47. S. Close, S. M. Hunt, M. J. Minardi, and F. M. McKeen, "Analysis of Perseid Meteor Head Echo Data Collected Using the Advance Research Projects Agency Long-Range Tracking and Instrumentation Radar (ALTAIR)," *Radio Science*, **35**, 2000, pp. 1233-1240.

48. C. J. Heinselman, J. P. Thayer and B. J. Watkins, "A High Latitude Observation of Sporadic Sodium and Sporadic E-Layer Formation," *Geophysical Research Letters*, **25**, 1998, pp. 3059-3062.

49. C. J. Heinselman, "Auroral Effects on the Gas Phase Chemistry of Meteoric Sodium," *Journal of Geophysical Research*, **105**, 2000, pp. 12181-12192.

50. J. S. Friedman, S. A. Gonzalez, C. A. Tepley, Q., Zhou, M. P. Sulzer, S. C. Collins, and B. W. Grime, "Simultaneous Atomic and Ion Layer Enhancements Observed in the Mesopause Region over Arecibo During the Coqui II Sounding Rocket Campaign," *Geophysical Research Letters*, **27**, 2000, pp. 449-452.

51. J. C. Foster, P. J. Erickson, A. J. Coster, J. Goldstein, and F. J. Rich, "Ionospheric Signatures of Plasmaspheric Tails," *Geophysical Research Letters*, **29**, 13, 2002, 10.1029/2002GL015067.

52. J. C. Foster, and W. J. Burke, "SAPS: A New Categorization for Sub-Auroral Electric Fields," *EOS Transactions*, **83**, 2002, pp. 393-394.

53. J. C. Foster, and H. B. Vo, "Average Characteristics and Activity Dependence of the Subauroral Polarization Stream," *Journal of Geophysical Research*, **107**, A12, 2002, 10.1029/2002JA009409.

54. J. Semeter, "Critical Comparison of OII(732-733 nm), OI (630 nm), and N2(1PG) Emissions in Auroral Rays," *Geophysical Research Letters*, **30**, 2003, pp. 1225-1228.

55. E. M. Blixt, T. Grydeland, N. Ivchenko, T. Hagfors, C. LaHoz, B. S. Lanchester, U. P. Løvhaug, and T. S. Trondsen, "Dynamic Rayed Aurora and Enhanced Ion-Acoustic Radar Echoes," *Annales Geophysicae*, **22**, 2004, pp. 101-108.

56. C. S. Huang, J. C. Foster, and P. J. Erickson, "Effect of Solar Wind Variations on the Midlatitude Ionosphere," *Journal of Geophysical Research*", **107**, 2002, DOI: 10.1029/2001JA009025.

57. C. S. Huang, J. C. Foster, and J. M. Holt, "Westward Plasma Drift in the Midlatitude Ionospheric F Region in the Midnight-Dawn Sector," *Journal of Geophysical Research*, **106**, 2001, p. 30349.

58. C. S. Huang, J. C. Foster, G. D. Reeves, J. Watermann, J. H. Sastri, K. Yumoto, and P. Song, "Global Magnetospheric-Ionospheric Oscillations Initiated by a Solar Wind Pressure

Impulse," *Journal of Geophysical Research*, **108**, A6, 2003, DOI: 10.1029/2002JA009608.

59. C. S. Huang and J. C. Foster, "Variations of Midlatitude Ionospheric Plasma Density in Response to an Interplanetary Shock," *Geophysical Research Letters*, **28**, 2001, pp. 4425-4428.

60. M. C. Kelley, J. J. Makela, W. E. Swartz, S. C. Collins, S. Thonnard, N. Aponte, C. A. Tepley, "Caribbean Ionosphere Campaign, Year One: Airglow and Plasma Observations During Two Intense Mid-latitude Spread-F Event," *Geophysical Research Letters*, **27**, 18, 2000, pp. 2825-2828.

61. J. J. Makela, S. A. Gonzalez, B. MacPherson, X. Pi, M. C. Kelley, and P. J. Sultan, "Intercomparisons of Total Electron Content Measurements Using the Arecibo Incoherent Scatter Radar and GPS," *Geophysical Research Letters*, **27**, 18, 2000, pp. 2841-2844.

62. W. E. Swartz, M. C. Kelley, J. J. Makela, S. C. Collins, E. Kudeki, S. Franke, J. Urbina, N. Aponte, M. P. Sulzer, "Coherent and Incoherent Scatter Radar Observations During Intense Mid-latitude Spread F," *Geophysical Research Letters*, **27**, 18, 2000, pp. 2829-2832.

63. M. C. Kelley, J. J. Makela, M. N. Vlasov, and A. Sur, "Further Studies of the Perkins Stability During Space Weather Month," *Journal of Atmospheric and Solar-Terrestrial Physics*, **65**, 10 , 2003, pp. 1071-1075.

64. J. J. Makela, M. C. Kelley, S. A. Gonzalez, N. Aponte, and J. J. Sojka, "Mid-Latitude Plasma and Electric Field Measurements During Space Weather Month, September 1999," *Journal of Atmospheric and Solar-Terrestrial Physics,* **65**, 10, 2003, pp. 1077-1085.

65. S.-R. Zhang, J. M. Holt, P. J. Erickson, F. D. Lind, J. C. Foster, T. van Eyken, Y. Zhang, L. J. Paxton, W. C. Rideout, L. P. Goncharenko, G. R. Campbell, "October 2002 30-Day Incoherent Scatter Radar Experiments at Millstone Hill and Svalbard and Simultaneous GUVI/TIMED Observations," 2004, submitted to *Geophysical Research Letters*.

66. S. –R. Zhang and J. M. Holt, "Ionospheric Temperature Variations During 1976-2001 over Millstone Hill," *Advances in Space Research*, **33**, 2004, pp. 963-969.

67. S. –R. Zhang and J. M. Holt, "Plasma Temperature Data, Climatology, and Empirical Models Based on Millstone Hill Incoherent Scatter Observations," *URSI/COSPAR International Reference Ionosphere News*, **9**, 4, December 2002, pp. 1-4.

68. A. Canals, A. R. Breen, L. Ofman, P. J. Moran, and R. A. Fallows, "Estimating Random Transverse Velocities in the Fast Solar Wind from EISCAT Interplanetary Scintillation Measurements," *Annales Geophysicae*, **20**, 2002, pp. 1265-1277.

69. R. A. Fallows, P. J. S. Williams, and A. R. Breen, "EISCAT Measurements of Solar Wind Velocity and the Associated Level of Interplanetary Scintillation," *Annales Geophysicae*, **20**, 2002, pp. 1279-1289.

70. A. R. Breen, P. Riley, A. J. Lazarus, A. Canals, R. A. Fallows, J. Linker, and Z. Mikic, "The Solar Wind at Solar Maximum: Comparisons of EISCAT IPS and in situ Observations," *Annales Geophysicae*, **20**, 2002, pp. 1291-1309.

71. Vo, H. B, and J. C. Foster, "Quantitative investigation of ionospheric density gradients at mid latitudes," *Journal of Geophysical Research*, **106**, 2001, 21555-21563.

Physical Mechanisms of Non-Thermal Extremely-Low-Frequency Magnetic-Field Effects

S. Engström

1. Introduction

This review examines some candidates proposed to explain the still unresolved problem of how magnetic fields are able to influence biological systems. As the title suggests, the scope is limited to extremely-low-frequency (ELF; for the purpose of this paper, < 300 Hz), non-thermal magnetic fields. Non-thermal needs to be defined here, for it is used – sometimes rather casually – with different definitions. Some basic principles and resultant physical mechanisms are discussed, along with some theoretical models with relatively recent exposure in the literature.

1.1 Other Recent Theoretical Reviews

A large body of literature exists for the influence of extremely-low-frequency (ELF) magnetic fields (MF) on biological systems. The theoretical side of this field is not very well developed, but a few reviews capture some alternative views of the state of the field:

- Binhi and Savin [1]: A didactic review aimed at a physics audience. See also Binhi [2], which provides an in-depth discussion of the topics covered in the review.
- Zhadin [3]: A review of Russian literature on biological effects of weak static and low-frequency fields, starting with geomagnetic field disturbances and providing an overview of Russian theoretical work.
- Adair [4]: A mechanism review of low-frequency and static magnetic fields. It provides a critical evaluation of suggested mechanisms, with practical numerical examples.
- Matthes et al. [5]: A comprehensive review of health effects of magnetic and electric fields at frequencies below 100 kHz.

1.2 Non-Thermal Exposures

One incorrect use of "non-thermal" is to equate it with "non-ionizing," the complement of ionizing radiation: all electromagnetic fields with energies below ultraviolet for which single quanta are unable to break chemical bonds and dissociate electrons from molecules. A definition commonly used in connection with exposure to radio-frequency fields uses the literal meaning of heating: that a non-thermal exposure does not contain enough energy to overcome diffusion and thermoregulation and significantly heat some specified volume of tissue.

In the extremely-low-frequency spectrum (< 300 Hz), "non-thermal" is commonly used to convey the idea that the energy involved in the primary physical detection of the exposure is small compared to the thermal energy of a system, the bulk of which usually resides in the form of thermal motion of water molecules in the amount of $\frac{1}{2}kT$ per degree of freedom at equilibrium (k is Boltzmann's constant, and T is the absolute temperature in kelvin). If a magnetic field is to have a biological effect, it must make an energetic difference, or, equivalently, have a point of physical interaction with the system. For direct magnetic-field detection, this demands the presence of a magnetic dipole (or higher-order multipole). Various ways to accomplish this are discussed below, and here the kT threshold can be meaningfully applied, but the extent to which it is valid in non-equilibrium systems will be an issue. The competition with the thermal noise of the system now becomes that of systematic influences of the field vis-à-vis random displacements due to mechanical, electrical, and magnetic forces imparted by molecules and charges in motion.

Fields that vary in time induce electric fields, and this opens up a natural way to interact with biological systems. Biological systems are, in many important ways, electrical

Stefan Engström is with the Department of Neurology, Vanderbilt University, Stallworth Rehabilitation Hospital, 2201 Childrens Way, Nashville, TN 37212, USA.; Tel: +1 (615) 936-1522; Fax: +1 (615) 321-5247; E-mail: stefan.engstrom@vanderbilt.edu.

This is one of the invited *Reviews of Radio Science*, from Commission K.

in nature, as evidenced in the study of voltage-gated ion channels [6], cell motility [7], and neuronal sensitivity to electric fields [8], just to mention a few examples. More ways to interact with biological systems become apparent for electric fields, but the rate of change of the field in the ELF region is quite small (< 300 Hz). For many practical situations, induced electric fields are small compared to those induced by nearby charges set in motion by thermal vibrations.

Even if the first step of the physical interaction is understood and physically plausible, subsequent steps are also vulnerable to thermal perturbations. The average thermal energy (kT) is strongly descriptive of the statistical state only for systems in equilibrium, and this is most often not the case for many critical steps in the physical chemistry that defines living things. This does not let us off the hook in terms of worrying about its presence, but it does not provide a generally applicable exclusion criterion. Complex dynamical systems can be sensitive to specific subtle influences, especially if the influence is a global property, like the magnetic field.

With this preamble, it is hopefully clear that the much-used notion of "non-thermal" is not generally well defined. For the purpose of this paper, we will stick with the idea that "non-thermal" implies an interaction that relies on a first physical interaction step that has a characteristic energy associated with the field interaction comparable to, or less than kT .

2. Physical Mechanisms

2.1 Magnetic Induction of Electric Fields and Currents

Performing a Lorentz transformation of electric ($\vec{E}$) and magnetic ($\vec{B}$) fields between two frames of reference with relative velocity $\vec{v}$ (e.g., [9]) demonstrates how motion in a magnetic field induces an electric field perpendicular to both the velocity and the field. Another common form used to calculate induced electric fields is the integral from of Faraday's law:

$$\oint_C \vec{E} \bullet d\vec{l} = -\frac{d}{dt}\int_S \vec{B} \bullet dA \,, \qquad (1)$$

where the left-hand side is a line integral over a closed loop, C , and the right-hand side is the time derivative of a surface integral of the normal component of the magnetic flux through the area, S , enclosed by C . Equation (1) only relates the *average* electric field over the loop C to the rate of change of the enclosed magnetic flux, but it is often the only measure available to us when the actual local field in a complex system only can be estimated with numerical methods that require very detailed knowledge about the fields on the system boundary and its material properties. If we assume that the bulk conductivity of the material is relatively homogeneous, we can also infer the average induced current by Ohm's law.

Equation (1) estimates an average electric field when the integral on the right-hand side changes with time. If we consider the loop to be of fixed dimensions, this can happen in several different ways:

1. The magnetic field itself varies with time.

2. By motion in a field that has spatial variation.

3. The relative orientation between the loop and the field vector is changed.

A very detailed analysis of these possibilities is available in Ptisyna et al. [10]. The rate of change directly determines the induced field, so the frequency of the field application, the speed of the motion in a gradient, and the rotation frequency enter directly into the value of the induced fields.

Induced electric fields and currents can play a direct role in changing the behavior of biological systems, since living things rely heavily on electric signaling and charge transport. This mechanism becomes straightforward only for relatively large field amplitudes required for inducing fields that can compete directly with known electrical processes. One example is transcranial magnetic stimulation (TMS), which applies sharply pulsed tesla-level fields to induce electric fields capable of directly exciting motor cortex neurons. At the other end of the amplitude spectrum, one can consider how the transition probabilities of Brownian motion are affected by a magnetic field through the Lorentz force. The effects depend on the relation between the Larmor frequency and dynamical friction, as recently calculated in detail [11]. However, for biologically relevant temperatures and densities, this effect becomes very slight.

In order for fields and currents induced by low-level fields to have biological effects, elaborate and possibly dedicated sensory systems may be required to solve the issues of overcoming the disruptive random fluctuations of thermalized ions.

2.1.1 Magnetomechanical: Torque on Magnetic Dipole Moment

A magnetic dipole with moment $\vec{m}$ in an external magnetic field $\vec{B}$ experiences a torque $\vec{N} = \vec{m} \times \vec{B}$, and the potential energy associated with the system is $U = -\vec{m} \bullet \vec{B}$. We understand from these relations that the effect of the field is a tendency to rotate the dipole, and that the statistical preference of the dipole is alignment with the field. Note that this does not apply to magnetic dipoles that are formed in isotropic dia- or paramagnetic materials in response to an applied magnetic field, since their magnetic moments are

aligned parallel (or anti-parallel) with the local field. If we have a material with intrinsic magnetization or with anisotropic susceptibility, there is a foothold for a physical mechanism along these lines (see the section on "Anisotropic Diamagnetism," below).

In living systems, the effect of thermal noise will tend to randomize the dipole's orientation. The energy, U, has to be compared to kT for typical temperatures of living systems ($T \approx 310$ K). For protons with a Bohr magneton magnetic moment ($\mu_B = e\hbar/2m_e$), the comparison leaves a very slight alignment, even at high (> 1 T) fields, although it is large enough to be technologically useful for magnetic resonance imaging (MRI). With larger permanent magnetic moments, as found in single-domain magnetite particles, the interaction energy compares more favorably with kT. This provides a plausible physical transduction mechanism for fields down to μT for static fields [12].

Another example of systems that overcome the thermal drive to isotropy is a magnetic moment created by diamagnetic anisotropy in relatively large structures (e.g., 5 ìm microtubules) in tesla-level fields [13].

2.1.2 Magnetophoresis: Force on Magnetic Dipole Moment

A magnetic dipole ($\vec{m}$) in a static gradient magnetic field experiences a (lowest-order) force of

$$F = (\vec{m} \bullet \nabla)B \cdot \qquad (2)$$

The magnetic dipole can be a permanent dipole or it can be magnetization induced by the field itself. An example of the latter is diamagnetic levitation, in which the force is sufficiently large to oppose the gravitational pull [14, 15]. The magnetic moment of an object of volume V and magnetic susceptibility χ in a field B is $m = \chi VB/\mu_0$, where μ_0 is the permeability of free space, $4\pi \times 10^{-7}$ Vs/Am. As an example of the fields involved in balancing gravity ($g\rho V$), we need $B|\nabla B| > 1000$ T2/m for typical tissue parameters. This effect is a valid concern for ferromagnetic materials in high gradients, such as those encountered in magnetic resonance imaging (MRI). A realistic example [16] shows how typical MRI conditions can accelerate a steel wrench in excess of 40 m/s2!

Some therapeutic applications of magnets claim that strong gradients are required for efficacy [17], with a threshold gradient observed somewhere in the region of 1 T/m [18]. The corresponding threshold force on a Bohr magneton is approximately 10^{-23} N. As a comparison, the electric field required to apply this force on a unit charge is $E = 1.7 \times 10^{-4}$ V/m. This is a very small field, but it is near the level of another threshold ($E = 4 \times 10^{-4}$ V/m) suggested by other experimental studies [19, 20]. The mechanism of magnetophoresis of diamagnetic materials is the only proposed mechanism for gradient-specific effects, but it does require relatively large fields (to set up magnetic dipoles) and gradients to become a competitive force. Experiments on the rate of myosin phosphorylation in a gradient magnetic field [21] suggested that a combination of field and gradient are required to explain the mechanism producing the effect on this enzyme system. This experimental system is purely biochemical, so effects here do not rely on any aspects of cell structure, such as phospholipid bilayers or ion channels embedded in the membrane.

2.2 Anisotropic Diamagnetism

If a material has anisotropic diamagnetic susceptibility, a static magnetic field will apply a torque on the system, since the orientations parallel and perpendicular become differentially magnetized. Orientation with respect to the field becomes energetically differentiated and we have the basis for a physical transduction mechanism [22]. The energy of a cylindrical molecule with magnetic susceptibility χ_p and χ_q, parallel and perpendicular to the cylinder axis, respectively, is:

$$E = -VB^2(\chi_p - \chi_q)/2\mu_0 , \qquad (3)$$

where V is the molecular volume and μ_0 is the magnetic permeability of vacuum.

Substantial fields are typically needed to take advantage of this mechanism, and large, elongated, structured molecules do better in the competition with thermal noise. For example, a 5 μ m long microtubule is estimated to be completely aligned by a magnetic field in the 10 T range [13]. When material is organized so that the diamagnetic anisotropies align over some volume, we can achieve larger induced magnetic moments: this effect is sometimes called superdiamagnetism [23]. This mechanism is the basis for some detailed models of effects in lipid bilayers [24-26], subsequent effects on calcium liberation [27, 28], and an explanation of how mitotic structures may be affected by large fields [29, 30], resulting in abnormal embryonic development.

2.3 Biogenic Magnetite

Biogenic magnetite provides the foundation for a well-documented mechanism that explains how some bacteria can use the Earth's magnetic field to an evolutionary advantage [31]. A chain of magnetosomes provide a large-enough magnetic moment that the whole organism orients and swims along geomagnetic flux lines (magnetotaxis), providing a reliable source of direction for swimming up or down as this bacterium's circumstances require.

The large magnetic moment associated with a magnetite grain is an attractive possibility for solving the thermal noise problem, as the potential energy involved in rotation in magnetic fields of magnitudes found in nature compares favorably with kT at biological temperatures, the energy associated with natural thermal fluctuations so damning for many other proposed mechanisms of interaction.

Kirschvink et al. [12] reviewed the development of magnetite-based magnetoreception, and argued that we should expect a highly evolved sensory system capable of explaining the observed sensitivities to very small variations in the geomagnetic field [32, 33]. An interesting requirement for high-resolution observation of the magnetic vector orientation is an equally sensitive measurement of the gravitational vector, as well as integration/comparison of these two senses.

Magnetite-based mechanisms are mature models in bioelectromagnetic research in that there exist both credible mechanisms for observed effects [34-36], as well as physiological data that supports the presence and function in several different animal models [37-43].

2.3.1 Single-Domain Crystals

Single-domain magnetite crystals can only be magnetized along one axis (with positive or negative polarity), and the crystal maintains the magnetization, unlike superparamagnetic magnetite (see below). Single-domain magnetite (size: less than 100 nm) or greigite are the elements of magnetotactic bacteria [44]. There are suggestions that these crystals form the basic functional components of higher magnetosensitive animals. Based on re-magnetization experiments, there are good reasons to believe that permanent ferromagnets can be involved in the physical transduction [45, 46]. Physical models utilizing single-domain crystals have been discussed by Kirschvink et al. [44].

Edmonds [47] proposed a sensitive biological magnetic compass by examining the behavior of a cluster of needle-shaped magnetite crystals in a nematic fluid. The argument is that this system would be able to respond to the orientation of the magnetic field with relatively high resolution, given enough crystals in the cluster, and useful detection could be achieved optically.

2.3.2 Superparamagnetic Magnetite and Other Possibilities

Superparamagnetic magnetite grains are too small to have a stable magnetic moment impressed, but they do respond to an externally applied field. Clusters (1-3 ìm in diameter) of superparamagnetic nanocrystals (2-5 nm in diameter) have been reported in the upper beak of homing pigeons [40, 48]. Single-domain features were ruled out in these studies.

There are suggestions that there are possibilities other than magnetite for ferromagnetic inclusions in bacterial and archaeal cells [49]. The detection of these reported structures was achieved by magnetophoresis in a tesla-level field. The structures did not show the crystalline signatures of magnetite.

2.3.3 Experimental Support for Magnetite-Based Mechanisms

The issue of animal navigation is a relatively well worked-out area of experimental research, and a substantial amount of effort has gone into a search for the anatomical structures responsible for detecting and processing magnetic-field information. Phillips [35] outlined some of the theoretical challenges and possible testable hypotheses.

Pulse re-magnetization [45] is a way to critically test magnetite models. Magnetic remanence measurements have provided evidence that ferromagnetic materials are available in isolated anatomical structures [38, 44]. Another aspect of animal navigation that is consistent with magnetite detection is the existence of an inclination compass [43, 50]. Light dependence has provided mechanistic evidence that is more biological/physiological in nature, and this has proven to be a fertile ground for research that does address the primary physical transduction, as well [34]. Nerve-path physiology is another way that magnetic sense has been mapped in animals [37, 51].

2.4 Magnetic Resonance

The Larmor frequency for an un-hydrated ion in a typical geomagnetic static field lies in the vicinity of that of power-frequency fields, and this has been utilized for a range of models trying to capitalize on this match in timescales [52-55]. This type of model suffers from serious physical deficiencies, particularly the requirement of extremely long-lived atomic and molecular states in the presence of thermal noise [56-58]. In order to create and observe resonance- or interference-based systems, the lifetime of the fundamental state of the physical model must exceed, or at least be comparable to, the period of the field stimulus.

Another attempt at utilizing this characteristic timescale of ions in magnetic fields is the quantum interference model by Binghy [59, 60] This model has been used to provide predictions for static magnetic fields, as well [61]. A recent extension to this framework involves molecular gyroscopes as one suggestion for how a molecular dynamical system can be shielded from very rapid thermalization [62].

The original work on biological magnetic resonance by Lednev et al. [52] has inspired much experimental work. The basic assumptions of the physical model are still quite dubious, but some experimental work supports the predictions of the model [63, 64]. The consequences of experimental verification of this model would be very interesting for many reasons, but, as discussed above: from a physical point of view it would be extraordinary to have a quantum-based biological resonance in the millisecond range if the mechanism couples strongly to thermally-driven collisions.

Much experimental work done in support of various magnetic-resonance models has been carried out with an assumed resonant frequency, using the oscillating-field amplitude as the primary experimental variable [65]. This is a reasonable approach, since this parameter is a prominent feature with detailed predictions in the theory, but it does not critically test the resonance character of the mechanism. The studies that did report estimates of the bandwidth (which is inversely related to the coherence time of the exited state) reported values of $\Delta f / f$ in the range of 1% [60, 66] to 10% [67].

2.5 Free Radical Recombination Rates

Spin-correlated free-radical pair chemistry has long been a consideration for magnetic-field effects in chemistry and biology [68-71]. A spin-correlated radical pair may be formed as a result of a chemical reaction, or, if radicals encounter each other at random, spin-correlation can be achieved by a spin-selective recombination reaction. Coherent hyperfine interactions must be the dominant source of spin inter-conversion. If singlet-to-triplet inter-conversion rates are relatively slow, it is possible to have a magnetic field interfere with the singlet/triplet conversion ratio by various mechanisms (see below). Depending on the diffusion properties and the requirement that singlet and triplet pairs have different chemical impact, we have a basis for a magnetosensitive chemical reaction with possible impact on both yield (depending on the pair re-conversion rate) and the fraction of singlet and triplet states in the product. There are several mechanisms within this general framework [72, 73].

If the two radicals have different *g*-factors, they will precess differentially and oscillate in and out of triplet and singlet states, allowing for a high rate of re-conversion in the short interval after the pair generation when the re-encounter probability is high. This process becomes dominant at high fields (> 1 T), and is generally referred to as the Δg mechanism.

At intermediate field strengths (down to the mT range), spin mixing due to hyperfine interactions dominates the singlet-triplet inter-conversion. The rate of this type of spin conversion is higher when the nuclear states involved are significantly different. The magnetic field has an effect in this regime because it separates the degenerate energy levels of the triplet state, leading to enhanced spin conversion as the T_{-1} state experiences an enhanced ability to mix into the singlet state. At higher field strengths, the $T_{\pm 1}$ states become decoupled from any interaction with the singlet state, and a reduction in the inter-conversion rate occurs. This mechanism is fairly well understood, and is experimentally supported with detailed experiments in the chemical literature [74].

There is also a low-field effect, based on the fact that selection rules of hyperfine-induced mixing are more restrictive in zero field, and one might see a reduction in spin conversion rates for low fields [72]. Given a reaction environment that imposes spatial constraints on the radical-pair diffusion so that long recombination times (several hundred ns) can be possible, this free-radical low-field effect (LFE) is predicted to achieve significant responses (10%-40%) to magnetic fields in the ì T region [73, 75]. Further structure in the response to varying magnetic-field amplitude has been predicted if anisotropic hyperfine structures are considered [76].

It should be noted that the radical-pair mechanism depends on having the two radicals be spin-correlated. If they are not statistically correlated with each other a magnetic field will still rotate the species, but no coherent change in recombination rates will occur. This applies to uncorrelated, freely diffusing radicals, and it is important to exclude these chemical species from consideration as a magnetic-field target [77].

Since the radicals stay spin-correlated for a relatively short time, it has been argued that an effect of low-frequency magnetic fields should be equivalent to a static field with appropriate amplitude [78]. However, this may not be true if the dynamics of the biological system responding to the time-varying field are frequency specific in the appropriate range [79, 80]. The notion that the dynamical character of a chemical system may modify (and increase) its sensitivity to magnetic fields is supported by experiments in the peroxidase-oxidase system [81, 82]. The timescale of the transductive mechanism seen as an integrated unit can be queried with appropriate experiments [83, 84].

The free-radical mechanism has been proposed as the foundation for magnetically-aided animal homing and navigation [36, 85]. The low-field effect (LFE) has only recently been developed as a general mechanism for field levels in the microtesla region. It is not yet clear how a detector operating at threshold field amplitudes will be capable of the very fine angular resolution that was observed in some experiments [33, 86], but it is promising that new physical routes for explaining these compelling behavioral data are being pursued. Experiments involving combined static magnetic fields and radio-frequency fields provide additional support for the hypothesis that animal magnetic-field sensitivity may be based on a free-radical mechanism [87].

2.6 Biological Electron Transfer: Tunneling

Electron tunneling can be directly affected by magnetic fields [88]. While there have been some attempts to examine possibilities for field interaction [89], few consequences or limits have been usefully applied to biological systems at this point.

2.7 Mechanistic Co-Factors and Other Mechanisms

There are co-factors in some experimental work of static and low-frequency magnetic-field studies that might provide clues about low-level mechanisms. Three prominent ideas are briefly included here: light as an influence, either direct or indirect; modulation of a field-detection mechanism based on cell or tissue states; the idea that the properties of water itself are directly affected by the field and, hence, many biological systems, since water is a ubiquitous component of these systems.

Nociceptive behavior in snails and rats has been extensively studied [65, 90, 91] as a model of animal response to low-frequency magnetic fields. Interesting work on how the absence of fields due to shielding can affect mice behavior has also been reported [92-94]. That shielding the ambient field has an effect implies that geomagnetic field levels have some physiological effects on these mice, but an even more intriguing aspect from a mechanistic perspective is that attempts at actively zeroing the field with coils, or shielding the ambient electric fields with electrically conducting but magnetically transparent material, do not yield the same results (albeit this work has not yet been independently repeated) [92].

2.7.1 Light as a Co-Factor

One recurring theme in the bioelectromagnetics literature is that of light-sensitive magnetic-field detection [95]. It has been shown that wavelength-specific effects occur in avian and reptile magnetic navigation [34], and that the light dependence is closely linked to the magnetic-field detection [39]. In salamanders, a model was proposed in which two separate and antagonistic magnetic-field sensitive systems are activated by short-wavelength light (< 450 nm) and long-wavelength light (> 500 nm), respectively [42].

Animal models have been used to investigate the relationship between magnetic-field detection and light by forming hypotheses that can be tested by training – and later testing – behavioral responses in various light conditions, varying with respect to wavelength [39] and polarization [96]. Another consistent series of papers on light-dependent magnetic-field-sensitive systems was a snail behavioral model, in which nociceptive responses were modulated by magnetic fields only in the presence of light [91, 97, 98].

Light sensitivity has also been reported in the peroxidase-oxidase oscillator system [99]. This strictly biochemical system is widely studied. Spectroscopic methods are often used to study the peroxidase-oxidase oscillator, so extra care is warranted in doing these experiments since the measurement apparatus may influence the system. It is not clear at this point whether the light-dependent part of the biological mechanism at work is integrated with the magnetic-field transduction. It is uncommon in sensory physiology that two independent detectors become tightly integrated, but one model for the avian magnetic-field detection embeds the detection organ in the bird's eye [36]. It could also be that light is enabling a physical detection mechanism, either on a behavioral level, or directly, as suggested by Leask [100].

2.7.2 State Dependence

Many reported effects have proven difficult to reproduce reliably in the ELF area of magnetic-field research on biological systems, despite some dedicated efforts to exact replication and exploration of confounding factors. In the pursuit of understanding the poor reproducibility of experiments, it has been noted that seemingly subtle differences may play a role [101, 102]. Differences between strains of animals, batches of serum, and cell lines have all been considered as possible sources of variability. In addition to these factors, it is important to consider the state of the system under study, and how to properly prepare an assay for study. If only a subpopulation of cells responds to the magnetic-field stimulus, it becomes essential to control or at least estimate the distribution into different states. Examples of this come from the work on human lymphocytes [103, 104] and also in Jurkat cells [105, 106], in which cells were screened for belonging to a "responder population" before being selected for experimentation. A direct correlation to cell-cycle and magnetic-field responsiveness has also been reported [107]. Not surprisingly, these concerns propagate all the way to the organism level. The human EEG is one example where even personality factors play a role in determining the experimental baseline [108].

State- and activation-dependent factors have been examined theoretically in a model of free-radical responses in enzyme systems [e.g., 109]. Experimentally, it has been observed that the sign of the response of Na-K-ATPase depends on its activation state [20]. The real problem this idea presents is the possibility of overlooked parameters that are simply not controlled for in an experiment, naturally giving rise to unexpected variation. This is a general problem in science, but perhaps more urgent in the field of bioelectromagnetics, due to its history of problems with reproducibility.

2.8 Structured Water

A controversial but recurring suggestion for how magnetic fields interact with biological systems is that long-lived water structures are somehow influenced by field exposures. An extreme theoretical version of this suggests the existence of large-scale coherence domains in water [110, 111]. Incidentally, this proposal claims to provide answers to some experiments previously attributed to ion-resonance phenomena [112, 113].

There are persistent (> 24 h) effects of magnetic-field exposure of colloids and solutions on zeta potential and diffusivity [114-116] at field strengths in the range of 50 mT to 500 mT. Similar effects using RF fields have indicated a role for the liquid-gas interface as deduced by de-gassing the experimental solutions [117], but it is not clear that there is any mechanistic relation between these experiments.

Related to the work on colloids are a number of experiments claiming that exposure of water or solutions is capable of inducing chemical changes that sometimes are able to persist for many hours [118]. One study that has relevance for biology was the report that dissolved oxygen levels in solution can be affected by a 200 mT magnetic field [119].

Magnetic water treatment for scale prevention falls in this category, and there is a substantial – albeit not "mainstream" – literature on this subject [120-124].

3. Discussion

Basic consequences of Maxwell's equations and (quasi-) static magnetic theory provide well-understood mechanisms for how magnetic fields might influence biology. The problem with this approach is that on the microscopic level, thermal noise tends to overwhelm the physical-detection step, and it is difficult to build functional mechanisms based on simple models. Looking to nature for solution of how the detection of weak fields is accomplished, we see, or expect to see, complex sensory systems with the added help of nerve-based signal processing. This is not going to be universally true, however: there are many examples of low-level field detection accomplished by cell cultures [125-128], and even in cell-free systems [129,130].

Magnetic resonance/interference is still a weak explanation of biological field effects from magnetic-field exposure, primarily due to the complications with constructing a believable physical model from these concepts. It is a very good model from the point of view of experimental verification/rejection since it is highly predictive. With experiments that critically test the expected resonance behavior of this model, it would be possible to build a strong case for the existence of the necessary long-lived microscopic states, or, alternatively, to reject this class of models as an explanation for the behavior of a particular experimental system. The parametric resonance model (PRM) [131] was able to explain experiments on neurite outgrowth [132]. However, this model has a phenomenological component, which introduces a factor of two that is needed for prediction of the experimental behavior, whereas a physically derived model does not. A very limiting problem for all this work is the availability of reliable experimental models that can be examined with exposures selected from a large parameter space in a reasonable time.

The most encouraging recent progress in theoretical possibilities for biological detection of magnetic fields is the development of the low-field effect for radical-pair recombination rates [73, 75, 76]. It is significant that this model has been elaborated with the aim of understanding animal navigation data, just as the other theoretical model with broad physical credibility before it, magnetite. While these models are able to reach the threshold of detection for geomagnetic fields, both frameworks are at their current limits to explain how fields of this magnitude (50 mT) can have an effect in biology. The ability of animals to use an inclination compass with sub-degree resolution (and to compare it to a gravitational reference) is still largely a mystery [33]. Biogenic magnetite has been found in many species able to use magnetic fields for navigation and homing, and anatomical clues have been found, but a direct demonstration of a "magnetic sensor" is still not available.

3.1 Future Direction

The attempts at finding threshold constraints on magnetic-field detection in biological systems have generally addressed the disruptive influence of thermal noise. The only general way of approaching this subject so far has been by considering systems operating near a stationary point that can be modeled with linear excursions around equilibrium. More "interesting" dynamical systems, far away from equilibrium, provide alternatives that can be both more sensitive and more resistant to stochastic perturbations. Determining threshold sensitivities for various theoretical models is very important, but it is also important to keep an open mind to the possible interpretations of experimental data. If a particular theoretical model rules out magnetic field detection below a threshold "X," two possibilities exist if an correctly executed experiment shows effects below X: (1) the experiment is a false positive, or (2) the theory is not applicable to this experiment. The latter can be the case if assumptions for the theory are violated, or if the theory lacks detail or sophistication. The broader the scope of a theoretical limitation, the more important it becomes to consider the existence of misleading experimental results versus violations of a theoretical construct. It is likely that some absolute threshold exists below which a magnetic-field effect cannot occur, but at this juncture, it is probably safer to look to the experimental record for an estimate of this threshold. Consider "Y" as a

threshold below which we have reason to believe that no detectable magnetic-field interaction can occur. A logical implication of accepting the level Y is that all experiments that report effects below this threshold must be incorrect. At some level Y, this becomes an untenable position by the statistical argument that it would be unlikely that a large number of reports should all be false.

Just as finding limiting thresholds is important, it is also important to optimize theoretical models for field detection. It is my opinion that the answer to biological field detection may lie in detector aggregates on mesoscopic scales and larger. Larger size takes advantage of the coherent nature of the applied stimulus, and it also allows the creation of more complex dynamics, including feedback loops that can contribute frequency-specific amplification.

While it is very important to understand the entire chain of events from field detection to behavioral change, it is generally true that the more global the experimental model one observes, the less mechanistic information will be gained from equal efforts. Epidemiology is the only way to obtain definite knowledge about the true health impact of magnetic fields in humans, but it also ranks among the bluntest of tools to investigate what physical mechanism induced the initial change. Generally, smaller systems are better for investigating the physical aspects of field transduction. As long as the integrity of the biological system that contains the transduction mechanisms is maintained, measuring the response as close to the "antenna" as possible is clearly a goal for which to strive.

It is natural for a biologist to try to understand biological structures, and to design experiments for this purpose. However, if progress is to be made in understanding the initial transduction of magnetic fields in biology, physical issues must be addressed, not only theoretically but also experimentally. This calls for stronger interaction and collaboration among scientists of disciplines ranging from physics to biology, so that biological experiments are designed to decisively test physical ideas, and physical models are built with relevant features of living systems.

4. References

1. V. N. Binhi and A. V. Savin, "Effects of Weak Magnetic Fields on Biological Systems: Physical Aspects," *Physics-Uspekhi*, **46,** 3**,** 2003, pp. 259-291.

2. V. N. Binhi, *Magnetobiology: Underlying Physical Problems*, San Diego, CA**,** Academic Press, 2002.

3. M. N. Zhadin, "Review of Russian Literature on Biological Action of DC and Low-Frequency AC Magnetic Fields," *Bioelectromagnetics*, **22,** 2001, pp. 27-45.

4. R. K. Adair, "Static and Low-Frequency Magnetic Field Effects: Health Risks and Therapies," *Rep. Prog. Phys.*, **63,** 2000, pp. 415-454.

5. R. Matthes, A. F. McKinlay, J. H. Bernhardt, P. Vecchia, and B. Veyret, "Exposure to Static and Low Frequency Electromagnetic Fields, Biological Effects and Health Consequences (0-100 kHz)," UNEP-ICNIRP, 2004.

6. F. Bezanilla, "The Voltage Sensor in Voltage-Dependent Ion Channels," *Physiological Reviews*, **80,** 2**,** 2000, pp. 555-592.

7. B. Farboud, R. Nuccitelli, I. R. Schwab, and R. R. Isseroff, "DC Electric Fields Induce Rapid Directional Migration in Cultured Human Corneal Epithelial Cells," *Experimental Eye Research*, **70,** 5**,** 2000, pp. 667-673.

8. J. G. R. Jefferys, J. Deans, M. Bikson, and J. Fox, "Effects of Weak Electric Fields on the Activity of Neurons and Neuronal Networks," *Radiation Protection Dosimetry*, **106,** 4**,** 2003, pp. 321-323.

9. J. D. Jackson, *Classical Electrodynamics, Third Edition*, New York, NY**,** Wiley, 1999.

10. N. G. Ptitsyna, G. Villoresi, L. I. Dorman, N. Iucci, and M. I. Tyasto, "Natural and Man-Made Low-Frequency Magnetic Fields as a Potential Health Hazard," *Physics - Uspekhi*, **41,** 1998, pp. 687-709.

11. R. Czopnik and P. Garbaczewski, "Brownian Motion in a Magnetic Field," *Physical Review E*, **6302,** 2**,** 2001, pp. art-021105.

12. J. L. Kirschvink, M. M. Walker, and C. E. Diebel, "Magnetite-Based Magnetoreception," *Current Opinion in Neurobiology*, **11,** 4**,** 2001, pp. 462-467.

13. W. Bras, G. P. Diakun, J. F. Diaz, G. Maret, H. Kramer, J. Bordas, and F. J. Medrano, "The Susceptibility of Pure Tubulin to High Magnetic Fields: A Magnetic Birefringence and X-Ray Fiber Diffraction Study," *Biophysical Journal*, **74,** 3**,** 1998, pp. 1509-1521.

14. J. M. Valles, K. Lin, J. M. Denegre, and K. L. Mowry, "Stable Magnetic Field Gradient Levitation of Xenopus Laevis: Toward Low-Gravity Simulation," *Biophys .J.*, **73,** 1997, pp. 1130-1133.

15. E. Beaugnon and R. Tournier, "Levitation of Water and Organic-Substances in High Static Magnetic-Fields," *J. Phys. III*, **1,** 1991, pp. 1423-1428.

16. A. Kangarlu and P. M. L. Robitaille, "Biological Effects and Health Implications in Magnetic Resonance Imaging," *Concepts in Magnetic Resonance*, **12,** 5**,** 2000, pp. 321-359.

17. M. J. McLean, R. R. Holcomb, A. W. Wamil, J. D. Pickett, and A. V. Cavopol, "Blockade of Sensory Neuron Action Potentials by a Static Magnetic Field in the 10 mT Range," *Bioelectromagnetics*, **16,** 1995, pp. 20-32.

18. A. V. Cavopol, A. W. Wamil, R. R. Holcomb, and M. J. McLean, "Measurement and Analysis of Static Magnetic Fields that Block Action Potentials in Cultured Neurons," *Bioelectromagnetics*, **16,** 1995, pp. 197-206.

19. M. Blank and L. Soo, "The Threshold for Alternating Current Inhibition of the Na,K-ATPase," *Bioelectromagnetics*, **13,** 1992, pp. 329-333.

20. M. Blank and L. Soo, "The Threshold for Na,K-ATPase Stimulation by Electromagnetic Fields," *Bioelectrochem. Bioenerg.*, **40,** 1996, pp. 63-65.

21. S. Engstrom, M. S. Markov, M. J. McLean, R. R. Holcomb, and J. M. Markov, "Effects of Non-Uniform Static Magnetic

Fields on the Rate of Myosin Phosphorylation," *Bioelectromagnetics*, **23,** 2002, pp. 475-479.

22. G. Maret and K. Dransfeld, "Macromolecules and Membranes in High Magnetic-Fields," *Physica B & C*, **86,** 1977, pp. 1077-1083.

23. L. F. Braganza, B. H. Blott, T. J. Coe, and D. Melville, "The Superdiamagnetic Effect of Magnetic-Fields on One and 2 Component Multilamellar Liposomes," *Biochimica et Biophysica Acta*, **801,** 1, 1984, pp. 66-75.

24. W. Helfrich, "Lipid Bilayer Spheres – Deformation and Birefringence in Magnetic-Fields," *Phys. Lett. A*, **43,** 5, 1973, pp. 409-410.

25. T. S. Tenforde and R. P. Liburdy, "Magnetic Deformation of Phospholipid-Bilayers – Effects on Liposome Shape and Solute Permeability at Prephase Transition-Temperatures," *Journal of Theoretical Biology*, **133,** 3, 1988, pp. 385-396.

26. B. J. Gaffney, H. M. McConnell, "Effect of a Magnetic-Field on Phospholipid Membranes," *Chemical Physics Letters*, **24,** 3, 1974, pp. 310-313.

27. M. J. Azanza and A. del Moral, "Cell Membrane Biochemistry and Neurobiological Approach to Biomagnetism," *Progress in Neurobiology*, **44,** 1994, pp. 517-601.

28. A. del Moral and M. J. Azanza, "Model for the Effect of Static Magnetic-Fields on Isolated Neurons," *Journal of Magnetism and Magnetic Materials*, **114,** 3, 1992, pp. 240-242.

29. J. M. Denegre, J. M. Valles, K. Lin, W. B. Jordan, and K. L. Mowry, "Cleavage Planes in Frog Eggs are Altered by Strong Magnetic Fields," *Proceedings of the National Academy of Sciences of the United States of America*, **95,** 25, 1998, pp. 14729-14732.

30. J. M. Valles, "Model of Magnetic Field-Induced Mitotic Apparatus Reorientation in Frog Eggs," *Biophysical Journal*, **82,** 3, 2002, pp. 1260-1265.

31. R. Blakemore, "Magnetotactic Bacteria," *Science*, **190,** 4212, 1975, pp. 377-379.

32. J. H. Fischer, M. J. Freake, S. C. Borland, and J. B. Phillips, "Evidence for the Use of Magnetic Map Information by an Amphibian," *Animal Behaviour*, **62,** 2001, pp. 1-10.

33. J. B. Phillips, M. J. Freake, J. H. Fischer, and S. C. Borland, "Behavioral Titration of a Magnetic Map Coordinate," *Journal of Comparative Physiology A-Neuroethology Sensory Neural and Behavioral Physiology*, **188,** 2, 2002, pp. 157-160.

34. M. E. Deutschlander, J. B. Phillips, and S. C. Borland, "The Case for Light-Dependent Magnetic Orientation in Animals," *J. Exp. Biol.*, **202,** 1999, pp. 891-908.

35. J. B. Phillips, "Magnetic Navigation," *Journal of Theoretical Biology*, **180,** 4, 1996, pp. 309-319.

36. T. Ritz, S. Adem, and K. Schulten, "A Model for Photoreceptor-Based Magnetoreception in Birds," *Biophysical Journal*, **78,** 2, 2000, pp. 707-718.

37. R. C. Beason and P. Semm, "Does the Avian Ophthalmic Nerve Carry Magnetic Navigational Information?," *Journal of Experimental Biology*, **199,** 5, 1996, pp. 1241-1244.

38. J. Brassart, J. L. Kirschvink, J. B. Phillips, and S. C. Borland, "Ferromagnetic Material in the Eastern Red-Spotted Newt Notophthalmus Viridescens," *Journal of Experimental Biology*, **202,** 22, 1999, pp. 3155-3160.

39. M. E. Deutschlander, S. C. Borland, and J. B. Phillips, "Extraocular Magnetic Compass in Newts [letter]," *Nature*, **400,** 1999, pp. 324-325.

40. M. Hanzlik, C. Heunemann, E. Holtkamp-Rotzler, M. Winklhofer, N. Petersen, and G. Fleissner, "Superparamagnetic Magnetite in the Upper Beak Tissue of Homing Pigeons," *Biometals*, **13,** 4, 2000, pp. 325-331.

41. K. J. Lohmann and S. Johnsen, "The Neurobiology of Magnetoreception in Vertebrate Animals," *Trends in Neurosciences*, **23,** 4, 2000, pp. 153-159.

42. J. B. Phillips, M. E. Deutschlander, M. J. Freake, and S. C. Borland, "The Role of Extraocular Photoreceptors in Newt Magnetic Compass Orientation: Parallels Between Light-Dependent Magnetoreception and Polarized Light Detection in Vertebrates," *Journal of Experimental Biology*, **204,** 14, 2001, pp. 2543-2552.

43. W. Wiltschko and R. Wiltschko, "Magnetic Compass Orientation in Birds and its Physiological Basis," *Naturwissenschaften*, **89,** 10, 2002, pp. 445-452.

44. J. L. Kirschvink, A. Kobayashi-Kirschvink, J. C. Diaz-Ricci, and S. J. Kirschvink, "Magnetite in Human Tissues: A Mechanism for the Biological Effects of Weak ELF Magnetic Fields," *Bioelectromagnetics*, **13,** 1992, pp. 101-113.

45. R. C. Beason, R. Wiltschko, and W. Wiltschko, "Pigeon Homing: Effects of Magnetic Pulses on Initial Orientation," *Auk*, **114,** 3, 1997, pp. 405-415.

46. U. Munro, J. A. Munro, J. B. Phillips, R. Wiltschko, and W. Wiltschko, "Evidence for a Magnetite-Based Navigational 'Map' in Birds," *Naturwissenschaften*, **84,** 1, 1997, pp. 26-28.

47. D. T. Edmonds, "A Sensitive Optically Detected Magnetic Compass for Animals," *Proc. Royal Soc. London B Biol. Sci.*, **263,** 1996, pp. 295-298.

48. M. Winklhofer, E. Holtkamp-Rotzler, M. Hanzlik, G. Fleissner, and N. Petersen, "Clusters of Superparamagnetic Magnetite Particles in the Upper- Beak Skin of Homing Pigeons: Evidence of a Magnetoreceptor?," *European Journal of Mineralogy*, **13,** 4, 2001, pp. 659-669.

49. M. Vainshtein, N. Suzina, E. Kudryashova, and E. Ariskina, "New Magnet-Sensitive Structures in Bacterial and Archaeal Cells," *Biology of the Cell*, **94,** 1, 2002, pp. 29-35.

50. W. Wiltschko and R. Wiltschko, "Light-Dependent Magnetoreception in Birds: The Behaviour of European Robins, Erithacus Rubecula, Under Monochromatic Light of Various Wavelengths and Intensities," *Journal of Experimental Biology*, **204,** 19, 2001, pp. 3295-3302.

51. C. E. Diebel, R. Proksch, C. R. Green, P. Neilson, and M. M. Walker, "Magnetite Defines a Vertebrate Magnetoreceptor," *Nature*, **406,** 6793, 2000, pp. 299-302.

52. V. V. Lednev, "Possible Mechanism for the Influence of Weak Magnetic-Fields on Biological-Systems," *Bioelectromagnetics*, **12,** 1991, pp. 71-75.

53. A. Chiabrera, M. Grattarola, and R. Viviani, "Interaction Between Electromagnetic-Fields and Cells – Microelectrophoretic Effect on Ligands and Surface-Receptors," *Bioelectromagnetics*, **5,** 1984, pp. 173-191.

54.A. Chiabrera, B. Bianco, E. Moggia, and T. Tommasi, "Interaction Mechanism Between Electromagnetic-Fields and Ion Adsorption – Endogenous Forces and Collision Frequency," *Bioelectrochem. Bioenerg.*, **35,** 1994, pp. 33-37.

55.D. T. Edmonds, "Larmor Precession as a Mechanism for the Detection of Static and Alternating Magnetic Fields," *Bioelectrochemistry and Bioenergetics*, **30,** 1993, pp. 3-12.

56.R. K. Adair, "A Physical Analysis of the Ion Parametric Resonance Model," *Bioelectromagnetics*, **19,** 1998, pp. 181-191.

57.R. K. Adair, "Criticism of Lednev Mechanism for the Influence of Weak Magnetic-Fields on Biological-Systems," *Bioelectromagnetics*, **13,** 1992, pp. 231-235.

58.D. J. Muehsam and A. A. Pilla, "Lorentz Approach to Static Magnetic Field Effects on Bound-Ion Dynamics and Binding Kinetics: Thermal Noise Considerations," *Bioelectromagnetics*, **17,** 1996, pp. 89-99.

59.V. N. Binghy, "Interference of Bounded Ions in Proteins in Weak Magnetic Fields," *Biofizika*, **42,** 1997, pp. 1186-1191.

60.V. N. Binghy, "Interference of Ion Quantum States Within a Protein Explains Weak Magnetic Field's Effect on Biosystems," *Electro. Magnetobiol.*, **16,** 1997, pp. 203-214.

61.V. N. Binhi, Y. D. Alipov, and I. Y. Belyaev, "Effect of Static Magnetic Field on E-Coli Cells and Individual Rotations of Ion-Protein Complexes," *Bioelectromagnetics*, **22,** 2001, pp. 79-86.

62.V. N. Binhi and A. V. Savin, "Molecular Gyroscopes and Biological Effects of Weak Extremely Low-Frequency Magnetic Fields," *Physical Review E*, **65,** 2002, pp. 51912.

63. C. L. M. B. Koch, M. Sommarin, B. R. R. Persson, L. G. Salford, and J. L. Eberhardt, "Interaction Between Weak Low Frequency Magnetic Fields and Cell Membranes," *Bioelectromagnetics*, **24,** 6, 2003, pp. 395-402.

64.F. S. Prato, M. Kavaliers, and A. W. Thomas, "Extremely Low Frequency Magnetic Fields can Either Increase or Decrease Analgaesia in the Land Snail Depending on Field and Light Conditions," *Bioelectromagnetics*, **21,** 4, 2000, pp. 287-301.

65.F. S. Prato, M. Kavaliers, and J. J. L. Carson, "Behavioural Evidence that Magnetic Field Effects in the Land Snail, Cepaea Nemoralis, Might Not Depend on Magnetite or Induced Electric Currents," *Bioelectromagnetics*, **17,** 2, 1996, pp. 123-130.

66.V. V. Lednev, L. K. Srebnitskaya, E. N. Ilyasova, Z. E. Rozhdestvenskaya, A. A. Klimov, and H. P. Tiras, "Weak Combined Magnetic Field Tuned to the Parametric Resonance of the Nuclear Spins of Hydrogen Atoms Increases the Proliferation of Neoblasts in Regenerating Planarians Dugesia Tigrina," *Doklady Akademii Nauk*, **348,** 6, 1996, pp. 830-833.

67.C. F. Blackman, J. P. Blanchard, S. G. Benane, and D. E. House, "Experimental Determination of Hydrogen Bandwidth for the Ion Parametric Resonance Model," *Bioelectromagnetics*, **20,** 1, 1999, pp. 5-12.

68.C. B. Grissom, "Magnetic-Field Effects in Biology – A Survey of Possible Mechanisms with Emphasis on Radical-Pair Recombination," *Chemical Reviews*, **95,** 1, 1995, pp. 3-24.

69.K. M. Salikhov, Yu. N. Molin, R. Z. Sagdeev, and A. L. Buchachenko, *Spin Polarization and Magnetic Effects in Radical Reactions*, Amsterdam, Elsevier, 1984.

70.U. E. Steiner, T. Ulrich, "Magnetic-Field Effects in Chemical-Kinetics and Related Phenomena," *Chemical Reviews*, **89,** 1, 1989, pp. 51-147.

71.B. Brocklehurst, "Magnetic Fields and Radical Reactions: Recent Developments and their Role in Nature," *Chemical Society Reviews*, **31,** 5, 2002, pp. 301-311.

72.K. A. McLauchlan and U. E. Steiner, "The Spin-Correlated Radical Pair as a Reaction Intermediate," *Molecular Physics*, **73,** 1991, pp. 241-263.

73.C. R. Timmel, U. Till, B. Brocklehurst, K. A. McLauchlan, and P. J. Hore, "Effects of Weak Magnetic Fields on Free Radical Recombination Reactions," *Molecular Physics*, **95,** 1998, pp. 71-89.

74.T. T. Harkins, C. B. Grissom, "The Magnetic-Field Dependent Step in Bit Ethanolamine Ammonia-Lyase Is Radical-Pair Recombination," *Journal of the American Chemical Society*, **117,** 1, 1995, pp. 566-567.

75.U. Till, C. R. Timmel, B. Brocklehurst, and P. J. Hore, "The Influence of Very Small Magnetic Fields on Radical Recombination Reactions in the Limit of Slow Recombination," *Chem. Phys. Lett.*, **298,** 1998, pp. 7-14.

76.C. R. Timmel, F. Cintolesi, B. Brocklehurst, and P. J. Hore, "Model Calculations of Magnetic Field Effects on the Recombination Reactions of Radicals with Anisotropic Hyperfine Interactions," *Chem. Phys. Lett.*, **334,** 2001, pp. 387-395.

77.B. Brocklehurst and K. A. McLauchlan, "Free Radical Mechanism for the Effects of Environmental Electromagnetic Fields on Biological Systems," *International Journal of Radiation Biology*, **69,** 1, 1996, pp. 3-24.

78.J. C. Scaiano, F. L. Cozens, and N. Mohtat, "Influence of Combined AC-DC Magnetic Fields on Free Radicals in Organized and Biological Systems. Development of a Model," *Photochem. Photobiol.*, **62,** 1995, pp. 818-829.

79.C. Eichwald and J. Walleczek, "Magnetic field Perturbations as a Tool for Controlling Enzyme-Regulated and Oscillatory Biochemical Reactions," *Biophysical Chemistry*, **74,** 3, 1998, pp. 209-224.

80.J. Walleczek, "Magnetokinetic Effects on Radical Pairs: A Paradigm for Magnetic Field Interactions with Biological Systems at Lower than Thermal Energy," *Electromagnetic Fields*, **250,** 1995, pp. 395-420.

81.A. C. Moller and L. F. Olsen, "Effect of Magnetic Fields on an Oscillating Enzyme Reaction," *Journal of the American Chemical Society*, **121,** 27, 1999, pp. 6351-6354.

82.A. C. Moller, A. Lunding, and L. F. Olsen, "Further Studies of the Effect of Magnetic Fields on the Oscillating Peroxidase-Oxidase Reaction," *Physical Chemistry Chemical Physics*, **2,** 15, 2000, pp. 3443-3446.

83.S. Engstrom and R. J. Fitzsimmons, "Five Hypotheses to Examine the Nature of Magnetic Field Transduction in Biological Systems," *Bioelectromagnetics*, **20,** 1999, pp. 423-430.

84.S. Engstrom, "What is the Time Scale of Magnetic Field Interaction in Biological Systems?," *Bioelectromagnetics*, **18,** 3**,** 1997, pp. 244-249.

85.F. Cintolesi, T. Ritz, C. W. M. Kay, C. R. Timmel, and P. J. Hore, "Anisotropic Recombination of an Immobilized Photoinduced Radical Pair in a 50-mu T Magnetic Field: A Model Avian Photomagnetoreceptor," *Chemical Physics*, **294,** 3**,** 2003, pp. 385-399.

86.J. B. Phillips, S. C. Borland, M. J. Freake, J. Brassart, and J. L. Kirschvink, "'Fixed-Axis' Magnetic Orientation by an Amphibian: Non-Shoreward-Directed Compass Orientation, Misdirected Homing or Positioning a Magnetite-Based Map Detector in a Consistent Alignment Relative to the Magnetic Field?," *Journal of Experimental Biology*, **205,** 24**,** 2002, pp. 3903-3914.

87.T. Ritz, P. Thalau, J. B. Phillips, R. Wiltschko, and W. Wiltschko, "Resonance Effects Indicate a Radical-Pair Mechanism for Avian Magnetic Compass," *Nature*, **429,** 6988**,** 2004, pp. 177-180.

88.T. Sharpee, M. I. Dykman, and P. M. Platzman, "Tunneling Decay in a Magnetic Field," *Phys. Rev. A*, **65,** 2002, pp. art-032122.

89.E. G. Petrov, "Influence of a Periodic Field an the Distant Electron Transfer in Biological Systems," *Bioelectrochem. Bioenerg.*, **48,** 1999, pp. 333-337.

90.K. P. Ossenkopp, M. Kavaliers, F. S. Prato, and M. Hirst, "Effects of Magnetic-Fields from NMR Imaging and other Sources on Opioid Analgesia in Mice," *Federation Proceedings*, **43,** 3**,** 1984, pp. 748-748.

91.F. S. Prato, M. Kavaliers, A. P. Cullen, and A. W. Thomas, "Light-Dependent and -Independent Behavioral Effects of Extremely Low Frequency Magnetic Fields in a Land Snail are Consistent with a Parametric Resonance Mechanism," *Bioelectromagnetics*, **18,** 3**,** 1997, pp. 284-291.

92.E. Choleris, C. D. Seppia, A. W. Thomas, P. Luschi, S. Ghione, G. R. Moran, and F. S. Prato, "Shielding, but not Zeroing of the Ambient Magnetic Field Reduces Stress-Induced Analgesia in Mice," *Proceedings of the Royal Society of London. Series B. Biology*, **269,** 2002, pp. 193-201.

93.F. S. Prato, J. A. Robertson, D. Desjardins, J. Hensel, and A. W. Thomas, "Daily Repeated Magnetic Field Shielding Induces Analgesia in Cd-1 Mice," *Bioelectromagnetics*, 2004 (in press).

94.C. Del Seppia, P. Luschi, S. Ghione, E. Crosio, E. Choleris, and F. Papi, "Exposure to a Hypogeomagnetic Field or to Oscillating Magnetic Fields Similarly Reduce Stress-Induced Analgesia in C57 Male Mice," *Life Sciences*, **66,** 14**,** 2000, pp. 1299-1306.

95.T. Ritz, D. H. Dommer, and J. B. Phillips, "Shedding Light on Vertebrate Magnetoreception," *Neuron*, **34,** 4**,** 2002, pp. 503-506.

96.K. P. Able and M. A. Able, "Daytime Calibration of Magnetic Orientation in A Migratory Bird Requires A View of Skylight Polarization," *Nature*, **364,** 6437**,** 1993, pp. 523-525.

97.F. S. Prato, M. Kavaliers, A. W. Thomas, and K. P. Ossenkopp, "Modulatory Actions of Light on the Behavioural Responses to Magnetic Fields by Land Snails Probably Occur at the Magnetic Field Detection Stage," *Proceedings of the Royal Society of London Series B-Biological Sciences*, **265,** 1394**,** 1998, pp. 367-373.

98.F. S. Prato, M. Kavaliers, and J. J. L. Carson, "Behavioural Responses to Magnetic Fields by Land Snails are Dependent on both Magnetic Field Direction and Light," *Proceedings of the Royal Society of London Series B-Biological Sciences*, **263,** 1376**,** 1996, pp. 1437-1442.

99.J. J. L. Carson and J. Walleczek, "Response of the Peroxidase-Oxidase Oscillator to Light is Controlled by MB+-NADH Photochemistry," *Journal of Physical Chemistry B*, **107,** 33**,** 2003, pp. 8637-8642.

100. M. J. M. Leask, "Physicochemical Mechanism for Magnetic-Field Detection by Migratory Birds and Homing Pigeons," *Nature*, **267,** 5607**,** 1977, pp. 144-145.

101.W. Loscher, "Do Cocarcinogenic Effects of ELF Electromagnetic Fields Require Repeated Long-Term Interaction with Carcinogens? Characteristics of Positive Studies Using the DMBA Breast Cancer Model in Rats," *Bioelectromagnetics*, **22,** 8**,** 2001, pp. 603-614.

102.L. E. Anderson, J. E. Morris, L. B. Sasser, and W. Loscher, "Effects of 50-or 60-hertz, 100 mu T Magnetic Field Exposure in the DMBA Mammary Cancer Model in Sprague-Dawley Rats: Possible Explanations for Different Results from Two Laboratories," *Environmental Health Perspectives*, **108,** 9**,** 2000, pp. 797-802.

103.P. Conti, G. E. Gigante, M. G. Cifone, E. Alesse, C. Fieschi, M. Bologna, and P. U. Angeletti, "Mitogen Dose-Dependent Effect of Weak Pulsed Electromagnetic-Field on Lymphocyte Blastogenesis," *Febs Letters*, **199,** 1**,** 1986, pp. 130-134.

104.J. Walleczek, "Electromagnetic-Field Effects on Cells of the Immune-System – The Role of Calcium Signaling," *Faseb Journal*, **6,** 13**,** 1992, pp. 3177-3185.

105.E. Lindstrom, P. Lindstrom, A. Berglund, E. Lundgren, and K. H. Mild, "Intracellular Calcium Oscillations in a T-Cell Line After Exposure to Extremely-Low-Frequency Magnetic-Fields with Variable Frequencies and Flux Densities," *Bioelectromagnetics*, **16,** 1**,** 1995, pp. 41-47.

106.M. O. Mattsson, E. Lindstrom, M. Still, P. Lindstrom, K. H. Mild, and E. Lundgren, "[Ca2+](i) rise in Jurkat E6-1 Cell Lines from Different Sources as a Response to 50 Hz Magnetic Field Exposure is a Reproducible Effect and Independent of poly-L-lysine Treatment," *Cell Biology International*, **25,** 9**,** 2001, pp. 901-907.

107.C. R. McCreary, A. W. Thomas, and F. S. Prato, "Factors Confounding Cytosolic Calcium Measurements in Jurkat E6.1 Cells During Exposure to ELF Magnetic Fields," *Bioelectromagnetics*, **23,** 4**,** 2002, pp. 315-328.

108.C. M. Cook, A. W. Thomas, and F. S. Prato, "Human Electrophysiological and Cognitive Effects of Exposure to ELF Magnetic and ELF Modulated RF and Microwave Fields: A Review of Recent Studies," *Bioelectromagnetics*, **23,** 2**,** 2002, pp. 144-157.

109.C. Eichwald and J. Walleczek, "Activation-Dependent and Biphasic Electromagnetic Field Effects: Model Based on Cooperative Enzyme Kinetics in Cellular Signaling," *Bioelectromagnetics*, **17,** 1996, pp. 427-435.

110.E. Del Giudice, M. Fleischmann, G. Preparata, and G. Talpo, "On the 'Unreasonable' Effects of ELF Magnetic Fields Upon

a System of Ions," *Bioelectromagnetics*, **23,** 7**,** 2002, pp. 522-530.

111.E. Del Giudice, G. Preparata, and M. Fleischmann, "QED Coherence and Electrolyte Solutions," *Journal of Electroanalytical Chemistry*, **482,** 2**,** 2000, pp. 110-116.

112.M. N. Zhadin, V. V. Novikov, F. S. Barnes, and N. F. Pergola, "Combined Action of Static and Alternating Magnetic Fields on Ionic Current in Aqueous Glutamic Acid Solution," *Bioelectromagnetics*, **19,** 1**,** 1998, pp. 41-45.

113.V. V. Novikov and M. N. Zhadin, "Combined Action of Weak Static and Alternating Low-Frequency Magnetic-Fields on Ionic Currents in Aqueous Amino-Acid Solutions," *Biofizika*, **39,** 1**,** 1994, pp. 45-49.

114.J. Oshitani, D. Yamada, M. Miyahara, and K. Higashitani, "Magnetic Effect on Ion-Exchange Kinetics," *J. Colloid Interface Sci.*, **210,** 1999, pp. 1-7.

115.K. Higashitani, H. Iseri, K. Okuhara, A. Kage, and S. Hatade, "Magnetic Effects on Zeta-Potential and Diffusivity of Nonmagnetic Colloidal Particles," *J. Colloid. Interface. Sci.*, **172,** 1995, pp. 383-388.

116.L. Holysz, E. Chibowski, and A. Szczes, "Influence of Impurity Ions and Magnetic Field on the Properties of Freshly Precipitated Calcium Carbonate," *Water Research*, **37,** 14**,** 2003, pp. 3351-3360.

117.M. Colic and D. Morse, "Mechanism of the Long-Term Effects of Electromagnetic Radiation on Solutions and Suspended Colloids," **14,** 1998, pp. 783-787.

118.S. N. Ayrapetyan, K. V. Grigorian, A. S. Avanesian, and K. V. Stamboltsian, "Magnetic Fields Alter Electrical Properties of Solutions and their Physiological Effects," *Bioelectromagnetics*, **15,** 1994, pp. 133-142.

119.H. Sakurai, H. Yasui, K. Kunitomi, M. Kamatari, N. Kaneko, and A. Nakayama, "Effects of Static Magnetic Field on Dissolved Oxygen Levels in Aqueous Solutions Containing Copper(II), Iron(II), and Heme Iron(III) Complexes," *Pathophysiology*, **7,** 2000, pp. 93-99.

120.J. S. Baker and S. J. Judd, "Magnetic Amelioration of Scale Formation," *Water Res.*, **30,** 1996, pp. 247-260.

121.J. M. D. Coey, S. Cass, "Magnetic Water Treatment," *Journal of Magnetism and Magnetic Materials*, **209,** 2000, pp. 71-74.

122.A. Goldsworthy, H. Whitney, and E. Morris, "Biological Effects of Physically Conditioned Water," *Water Res.*, **33,** 1999, pp. 1618-1626.

123.S. Kobe, G. Drazic, P. J. Mcguiness, and J. Strazisar, "The Influence of the Magnetic Field on the Crystallisation Form of Calcium Carbonate and the Testing of a Magnetic Water-Treatment Device," *Journal of Magnetism and Magnetic Materials*, **236,** 2001, pp. 71-76.

124.A. Szkatula, M. Balanda, and M. Kopec, "Magnetic Treatment of Industrial Water. Silica Activation," *European Physical Journal-Applied Physics*, **18,** 1**,** 2002, pp. 41-49.

125.R. P. Liburdy, J. D. Harland, and S. M. J. Afzal, "Inhibition of Melatonin's Action on MCf-7 Cell Proliferation by Magnetic Fields," *Molecular Biology of the Cell*, **7,** 1996, pp. 1057-1057.

126.Liburdy, R. P., "Electromagnetic Fields and Control of Cell Growth. Drugs, Hormones and Human Tumor Cells: A Summary of Replication Studies at Five Laboratories," in M. J. McLean, S. Engstrom, and R. Holcomb (eds.), *Magnetotherapy: Potential Therapeutic Benefits and Adverse Effects*, 2003, pp. 57-88.

127. C. F. Blackman, S. G. Benane, and D. E. House, "The Influence of 1.2 mu T, 60 Hz Magnetic Fields on Melatonin- and Tamoxifen-Induced Inhibition of MCF-7 Cell Growth," *Bioelectromagnetics*, **22,** 2**,** 2001, pp. 122-128.

128.J. D. Harland and R. P. Liburdy, "Environmental Magnetic Fields Inhibit the Antiproliferative Action of Tamoxifen and Melatonin in a Human Breast Cancer Cell Line," *Bioelectromagnetics*, **18,** 8**,** 1997, pp. 555-562.

129.M. S. Markov, S. Wang, and A. A. Pilla, "Effects of Weak Low Frequency Sinusoidal and DC Magnetic Fields on Myosin Phosphorylation in a Cell-Free Preparation," *Bioelectrochem. and Bioenerg.*, **30,** 1993, pp. 119-125.

130.M. S. Markov and A. A. Pilla, "Modulation of Cell-Free Myosin Light Chain Phosphorylation with Weak Low Frequency and Static Magnetic Fields," 1994.

131.J. P. Blanchard and C. F. Blackman, "Clarification and Application of an Ion Parametric Resonance Model for Magnetic-Field Interactions with Biological-Systems," *Bioelectromagnetics*, **15,** 3**,** 1994, pp. 217-238.

132.C. F. Blackman, J. P. Blanchard, S. G. Benane, and D. E. House, "Empirical-Test of an Ion Parametric Resonance Model for Magnetic-Field Interactions with Pc-12 Cells," *Bioelectromagnetics*, **15,** 3**,** 1994, pp. 239-260.

Radio-Frequency Radiation Safety and Health

James C. Lin

A Research Program on the Human Impact of the Wireless Telecommunications and Other Electromagnetic-Field-Emitting Systems

Abstract

The Italian government – specifically, the Ministry for the Instruction, University, and Research – is to be applauded for its decision to provide the financial support for a comprehensive research program. A three-day conference was convened at the official conclusion of the coordinated research program, which was devoted to the assessment of the biological and environmental impact of wireless telecommunication systems and other systems that emit electromagnetic energy, and the development of new knowledge and techniques for the control and mitigation of already existing electromagnetic-field-emitting sources. It is interesting to note that within the past few years – in contrast to the United States – several counties in Europe have initiated nationwide research programs to investigate the biological effects and health implications of electromagnetic fields from wireless telecommunication systems. Comprehensive interdisciplinary research programs, which take into account field emissions both from base stations and personal handsets, are found in Finland, Germany, and the United Kingdom. Indeed, at this moment in time, there are a far greater number of research projects taking place in Japan and several countries in Europe than in the US.

Rome, Italy is a wonderful place to be at any time of the year. Autumn is an especially splendid time to visit. The summer's heat has abated, most of the tourists have gone home, the restaurants that were closed in August have reopened. One can easily find a spot to relax in front the 2000-year-old Pantheon in the Piazza della Rotonda, to admire the unrivaled Trevi Fountain, or to throw coins in the fountain to guarantee a return visit to Rome.

On just such a warm autumn day, Rome was the venue for an important gathering to evaluate progress made in protecting humans and the environment from electromagnetic emissions. A three-day conference was held at the Italian National Research Council (CNR) on October 25-27, 2004. It was convened at the official conclusion of a coordinated research program on Human and Environmental Protection From Electromagnetic Emissions, funded by the Italian Ministry for the Instruction, University, and Research (MIUR). The comprehensive research program, started in June, 2000, was under the leadership of Prof. Paolo Bernardi of the University of Rome "La Sapienza." It was devoted to the assessment of the biological and environmental impact of wireless telecommunication systems and other systems that emit electromagnetic energy, and the development of new knowledge and techniques for the control and mitigation of already existing electromagnetic-field-emitting sources.

The research program was organized into five categories, including: (1) Characterization and modeling of electromagnetic fields and their sources, (2) measurement of electromagnetic field values in the environment, (3) interaction between electromagnetic field sources and exposed subjects, (4) electromagnetic field reduction and mitigation methods and technology, and (5) coordination and dissemination of results.

The program enjoyed a wide and diverse participation, which involved researchers from 14 universities; six public research agencies; seven CNR institutes; three from divisions of the Italian National Agency for New Technologies, Energy, and the Environment (ENEA); and seven industry or private organizations; for a total of 37 research groups, all from Italy.

I was fortunate to be invited to take part in the conference. I will highlight, from my vintage point, some accomplishments of the research program. Among the projects were the development of software packages for the evaluation of electromagnetic fields under various environmental and operating conditions. Some of the projects addressed the problem of characterization of electromagnetic field sources, including electromagnetic fields near railroad tracks and the modeling of field values within train cars, as well as electromagnetic fields in airline terminals. Other

James C. Lin is with the University of Illinois at Chicago 851 South Morgan Street (M/C 154), Chicago, Illinois 60607-7053 USA; Tel: +1 (312) 413-1052 (direct); +1 (312) 996-3423 (main office); Fax: +1 (312) 996-6465; E-mail: lin@uic.edu

This contribution originally appeared in the *IEEE Antennas and Propagation Magazine*, **46**, 6, December, 2004, pp. 161-163, and is copyright ©2004 by the IEEE.

projects were concerned with the computation of electromagnetic fields in human subjects, exposed to the radio-frequency fields from wireless communication devices and systems.

A mobile electromagnetic field monitoring platform was developed for measuring electromagnetic fields in the environment. This effort involved the development of electromagnetic field sensors and associated signal-processing instrumentation and algorithms. The system has been used to measure ambient electromagnetic fields, including simultaneously emitting sources. Moreover, a foot current meter was developed to measure the foot current in humans exposed to the fields in typical open environments.

The studies on the interaction between electromagnetic fields and biological subjects have included the influence of both low- and high-frequency electromagnetic fields on proliferation and differentiation of cells, *in vitro*, and the cyto- and geno-toxic effects. The program also supported several dosimetric studies, namely, the development of a small sensor for the measurement of electromagnetic fields inside phantom models, and the development of a model of female anatomy. Studies on mechanisms that could underlie biological interactions formed another part of the program.

A significant part the research program was devoted to methods and technology for the reduction and mitigation of electromagnetic fields in different environments. The work involved the evaluation of potential exposures and the reduction of risk from electromagnetic field sources in research laboratories, hospitals, work environments, and, in private homes, the control of field emissions and the reduction of the environmental impact of industrial use of electromagnetic fields. Some of the projects were aimed at low-SAR antennas for mobile phones, and the development of highly field-immune cardiac pacemakers. Codes were developed to optimize the location of wireless-system transmitters in urban areas and in areas where multiple transmitters are present, to minimize human exposure. With respect to the 50 Hz frequency, a low-emission cable for electric power distribution was developed and demonstrated.

Bioelectromagnetics research is a multidisciplinary endeavor. It thrives on collaborative efforts and insights among scientists. In fact, viewing it from a higher level, we should be vigilant in guarding against any inclinations directed otherwise. For without effective participation of biological and medical colleagues, the most skilled engineers or physical scientists can be like sheep that go astray. Without meaningful participation of engineers and physical scientists, the most expert biologist or physician can fair no better. The interdisciplinary approach would most definitely enhance the progress of bioelectromagnetics research.

A comprehensive research program may be organized in various ways, depending on its type and level of complexity [1]. There are two major categories of organized research: exploratory and mission-oriented research. The Italian research program falls under the category of mission-oriented research. It had a specific goal. It followed the key steps in this type of research endeavor, namely, (1) definition of issues, (2) identification a research agenda, (3) dissemination of agenda, (4) call for proposals, (5) selection of projects, (6) execution of projects, and (7) reporting of results. Each step is crucial for successful completion of the research. Leadership style and management to ensure proper execution of each step are fundamental for success.

The public has become apprehensive and skeptical of research results and conclusions if they suspect a breach of the arms-length or firewall procedure between the sponsor that provides funding for the selected projects and the execution and reporting of results from the projects. Likewise, if there is a lack of demonstrated transparency in the seven key steps outlined above, public perception and acceptance of the resulting research or conclusions would be checked and restrained. In this regard, the Italian government – specifically, the Ministry for the Instruction, University, and Research – is to be applauded for its decision to provide the financial support for the research program. It removed the public concern – perceived or otherwise – about vested interests of the affected industry. In addition, the management of the research program by a university professor fulfilled the firewall arrangement, in this case, to further enhance the acceptance of the results, and to help mitigate against fears of personal injury and threat to public health.

The interdisciplinary approach is essential to the investigation of health effects of electromagnetic fields. It demands the collective efforts of investigators who are knowledgeable and experienced with specific training in this specialized field of study.

The comprehensiveness of the scope of the Italian research program is obvious. The research program spanned the disciplines of biology, engineering, physics, and medicine. Many of the 30-some projects involved teams of experts in such specialties as electronics, electromagnetic engineering, signal processing, medicine, physiology, cellular and molecular biology, physics, biophysics, material science and engineering, electric power transmission, high-speed railways, and wireless telecommunication from industry, government, academic, and research institutions. It truly was a multidisciplinary effort. It is my sincere hope that the efforts will benefit not only Italy, but all regions of the globe in terms of public well-being, industrial development, commercial exploitation, and for health care and safety.

It is interesting to note that within the past few years, in contrast to the United States, several counties in Europe have initiated nationwide research programs to investigate the biological effects and health implications of electromagnetic fields from wireless telecommunication systems. In particular, comprehensive research programs in Finland, Germany, and the United Kingdom take into account field emissions both from base stations and personal handsets. Indeed, at this moment in time, there are a far greater number of research projects taking place in Japan and several countries in Europe than in the US.

Reference

1. J. C. Lin, "Research on Health Effects from Cell Phone Radiation," *IEEE Antennas and Propagation Magazine*, **42**, 4, August 2000, pp. 142-144.

URSI'S SCT

URSI's SCT

The prime objective of URSI's SCT (Scientific Committee on Telecommunications) is to communicate results of research by scientists active in URSI for use by "user" organizations – such as ITU, CISPR, and WHO – needing to apply such information. In addition, the SCT should make URSI aware of the needs of these organisations. There is a priority list for the types of information required by these user organisations, which is spelt out in some detail in Appendix 1 of the SCT website: (http://www.ursi.org/SCT.htm).

The SCT has existed for many years, with a progressive evolution, but had difficulty making an impact on its prime objective, as above. If this now begins to develop, it may be possible to also act through "Associated Meetings" with user organisations and also an "SCT Lecture Team."

An example of Associated Meetings has been where a small specialist meeting of URSI scientists, active in examining the use of climatic parameters in the prediction of radiowave performance, has been held immediately before a related Working Party meeting of ITU-R SG3. Some of each community also attended the related meeting and there was a useful exchange of information. The most recent meeting, which extended the earlier scope, was reported in the *Radio Science Bulletin*, **308**, March 2004, pp. 59-62.

An SCT Lecture Team has not yet been attempted due to other priorities, but the intention would be to have (i) a directory of URSI-related speakers and topics alongside (ii) a directory of "user" organizations and topics on which having lectures would be felt advantageous. Costs and expenses would be borne by the local hosts or organizers.

The "User" Organizations

Whereas URSI is concerned with promoting research in radio science, the ITU (International Telecommunications Union), the CISPR (International Special Committee on Radio Interference, which is a Technical Committee of the IEC), and the WHO (World Health Organisation) are anxious to use recent research results in their work to help the international community. The ITU has three Sectors: Radiocommunication (ITU-R), Telecommunication Standardisation (ITU-T), and Telecommunication Development (ITU-D).

The ITU-R coordinates the efficient use of the radio-frequency spectrum and satellite orbits, which is done largely through the means of Radiocommunication Conferences, producing the Radio Regulations, and by Study Groups producing technical Recommendations and Handbooks.

The aims of the CISPR are to promote international agreements on the various aspects of radio interference, thereby facilitating international trade. These agreements are expressed in International Standards.

How Can You Help?

If you know of individuals active in the fields of research mentioned in the Appendix 1 list, or are active in one of them yourself, please get in touch with your Commission Representative on the SCT, or the SCT Chair (as below), to discuss how best to communicate recent results to the body concerned. Although those bodies have cooperated in spelling out the list of topics, they do not have individuals able to scan the scientific journals for results of relevant research, or indeed to put those results into documentation that can be applied into their methods of working. Hopefully, those of us active in the SCT can help produce this communication through national URSI or user-organisation representatives.

If you can help, please send to myself, SCT Chair, or, better, to your Commission Representative, as below: (1) your name, (2) your e-mail address, (3) the name of your organisation and country, (4) the topic number and description in SCT Web site Appendix 1 where you are expecting to be able to find/supply suitable research material, and (5) any further helpful comments.

In addition, it would be helpful if you could distribute at URSI meetings copies of a leaflet describing most of what is written here. The text of the leaflet (which should be folded into three columns) may be downloaded from http://www.ursi.org/SCTlfA4.doc (A4 size) or http://www.ursi.org/SCTlfUS2.doc (US letter size).

SCT Commission Representatives

A Dr. Quirino BALZANO: qbalzano@eng.umd.edu, qbfree01@aol.com
B Prof. Lot SHAFAI: shafai@ee.umanitoba.ca
C Prof. Masami AKAIKE: akaike@ee.kagu.sut.ac.jp
D Prof. Peter RUSSER: P.Russer@t-online.de
E Dr. Ahmed ZEDDAM: ahmed.zeddam@francetelecom.com
F Dr. Jean ISNARD: jisnard-isti@club-internet.fr
G Dr. Patrick LASSUDRIE-DUCHESNE: patrick.lassudrieduchesne@enst-bretagne.fr
H Dr. Bo THIDÉ: bt@irfu.se
J Dr. Willem BAAN: willem@astron.nl, baan@astron.nl
K Prof. Bernard VEYRET: b.veyret@enscpb.fr

Your help will be much appreciated.

Martin Hall
E-mail: Martin.Hall@rl.ac.UK

Conferences

CONFERENCE REPORT

COSPAR 2004

Session C4.2, Advances in Specifying Plasma Temperatures and Ion Composition in the Ionosphere

This session was organized by the International Reference Ionosphere (IRI) Working Group with the goal of improving the description of the electron and ion temperature and the ion composition in the IRI model. The 62 presentations were divided into sessions entitled: Plasma Temperatures – Measurements and Models I, II, Modeling the Ionospheric Ion composition, Topside Ionosphere and TEC, Electron Density Below the Peak, Description of Disturbed Conditions, and Posters. A wide array of data sources was used in these studies including satellite data from SROSS C2, CHAMP, GPS, SNOE, SORCE, TIMED, COSMOS 1809, Interkosmos 19, Rocsat, Kompsat 1, Akebono, ACTIVE, ISS-b, DE, AE-C,D,E, OGO-6, AEROS, ISIS, Alouette, Incoherent Scatter Radar (ISR) data from Saint Santin, Millstone Hill, Irkutsk, and EISCAT, MST Radar data, Ionosonde data, and Rocket measurements. The global reach of the IRI effort was documented by presentations from many different countries including Argentina, Austria, Brazil, Bulgaria, China, Czech Republic, France, Germany, Greece, India, Italy, Ivory Coast, Japan, Korea, Poland, Russia, South Africa, Taiwan, UK, and USA. Financial support was provided by the Committee on Space Research (COSPAR) and by the International Union of Radioscience (URSI).

Plasma temperatures

Several new models were presented for the electron temperature (Te) and ion temperature (Ti). Bhuyan et al. (India) used data from SROSS C2 to study variation of Te with local time, season and solar activity in the area covered by the satellite (~400 km, low latitudes, 1994-1998) and to develop a model for solar cycle minimum conditions. The climatology of Te and Ti recorded by the French Incoherent Scatter Radar in Saint Santin over more than 2 decades was represented in an empirical model by S.R. Zhang et al. (USA). Data from the first Taiwanese satellite, ROCSAT-1 were used by Chao et al. (Taiwan) to construct a Ti model including seasonal, diurnal, longitudinal, and latitudinal variations at 600 km. Truhlik et al. (Czech Republic) pointed out ways of improving the IRI plasma temperature models in particular including the dependence on solar activity.

Nighttime data from the Korean KOMPSAT-1 satellite at 685 km are 200 to 400 K higher than the IRI predictions, whereas the electron densities are somewhat lower than IRI (Min et al., Korea). Oyama et al. (Japan) succeeded in taking on of the first Te measurements within a sporadic E layer and reported a lowering of Te within the thin layer. Studying polar conditions with Akebono data, Abe et al. (Japan) find a positive gradient for Te increasing with altitude and Bz. Data from a rocket launched in Norway up to 767 km, show elevated electron temperatures associated with energetic particle precipitation in the cusp (Steigies et al., Germany). Murilakrishna's (Brazil) rocket measurements show larger Te within plasma bubbles than outside. Proelss et al. (Germany) noted the importance of including the Te enhancement in IRI that is observed under the magnetospheric cleft region and they presented first modeling results.

Richards (USA) focused on the nighttime behavior of Te and Ne at mid-latitudes (Millstone Hill) and studied how well his Field Line Interhemispheric Plasma (FLIP) model and the IRI model reproduce the observed features. The main un-modeled feature is a post-midnight Ne enhancement that correlates with a sharp drop in Te. A possible explanation might be a large downward flow of ions facilitated by the decreasing temperatures.

IRI efforts are now focusing on including a full description of solar cycle variations for the plasma temperatures, on developing an independent Ti model, and on coupling with plasmaspheric temperature models.

Ion Composition and Densities

Triskova et al. (Czech Republic) presented models for the absolute ion densities of O^+, H^+, and He^+ based on data from ACTIVE, AE, and OGO-6 and showed discrepancies with the current IRI model. Many of these discrepancies are due to shortcomings of the IRI electron density topside model (see next section), which is used to obtain the individual ion densities from the IRI ion composition percentages. Another source of error is the constant light ion ratio n(He+)/n(H+)=1/9 currently assumed

in IRI. This was also pointed out by Sidorova (Russia), who found large differences between the He+ densities measured by ISS-b and predicted by IRI. A better description of the light ion ratio was proposed at an earlier IRI Workshop by Truhlik et al. (Czech Republic) and is now being considered for inclusion in IRI.

In the F-region which is dominated by O+ ions IRI performs generally quite well. This was also confirmed by Bhuyan (India) who studied the diurnal, seasonal and latitudinal variations of SROSS-C2 ion densities and compared them with IRI. Lathuillere and Kofman (France) discussed the different EISCAT measurement programs, the accuracy of deduced ion densities, and how these data can be used for studying the ion composition behavior in the auroral and polar ionosphere

Electron Density – Topside and TEC

The ISIS/Alouette topside sounder Ne data sets available from the National Space Science Data Center (NSSDC) were used for a variety of studies. Kutiev et al. (Bulgaria) developed a new model for the topside ionosphere scale height (TISH) as a function of month, local time, latitude, longitude and solar flux F10.7. Comparisons by Belehaki et al. (Greece) show that TISH is in general agreement with scale heights deduced from ground ionosondes but the model predicts post-midnight and afternoon maxima whereas the ionosonde data show a noon maximum. Webb et al. (USA) reported on their effort to deduce changes in the plasma temperature and ion composition from changes in the ISIS/Alouette topside profiles. Using the sounder data Coisson et al. (Italy) discussed limitations and possible improvements of the IRI topside model and the NeQuick model.

Reinisch and Huang (USA) showed how the topside scale height for IRI can be obtained from the bottomside profile using the technique developed for their Digisonde measurements. Stankov (Bulgaria) and Jakowski (Germany) used CHAMP radio occultation data to deduce topside scale heights and plan to develop a model based on these data.

M.L. Zhang et al., (PR China) compared TEC derived from Digisonde measurements at a low latitude station in China with GPS maps (IGS) and with IRI predictions. The Digisonde TEC shows a somewhat better agreement with the IGS values. Of course, the IGS TEC includes also a plasmaspheric contribution that is not included with the other two methods. The properties of the TEC in the equator anomaly region were studied with GPS data by Wan et al. (PR China).

The main focus of future IRI activities is on improvements of the topside electron density profile using a Chapman approach with variable scale height and on merging the topside profile with a plasmaspheric model.

Electron Density – F peak

Abdu et al. (Brazil) compared the evening F layer peak height and vertical drift from several Brazilian ionosonde stations with the IRI predictions and find that the ion drift peak is often underestimated by IRI whereas the F peak density is overestimated. Comparisons with Japanese ionosonde data show good agreement with IRI except for small discrepancies of the electron density at sunset (Tsujita et al., Japan).

Real-time updating of IRI bottomside profiles for the European sector with ionosonde data was discussed by Buresova et al. (Czech Republic) and Stanislawska et al. (Poland). An improved algorithm for IRI-TEC updating was presented by Pelevin et al. (Russia)

Studies of ionospheric variability continued with data from ionosondes in Africa (Obrou et al., Ivory Coast), Europe (Mosert et al., Argentina) and Japan (Ezquer et al., Argentina). A first order variability model for IRI is currently under development based on inputs from the ground and topside ionosondes.

"A first order variability model for IRI is currently under development based on input from the ground ionosondes (Fotiadis and Kouris) and topside ionosondes." I have presented a paper on : relation between TEC and peak density which I submitted for consideration and publication in Adv.Space Res. In this work there was reported the results on the diurnal and seasonal variations of slab thickness and the variability of TEC , using mainly hourly daily GPS data from Matera (Italy) and Hailsham (England) . Specifications on these variations are also given in relation with those in foF2.

Electron Density – Bottomside and Below

New models for the electron density in the lower ionosphere at auroral latitudes were presented by Danilov (Russia) and McKinnell (South-Africa). Danilov describes variations in the D-region in terms of solar zenith angle and daily sum of Kp based on rocket data from the Northern and Southern hemisphere. McKinnell applied a Neural Network approach to a combined data base of rocket and EISCAT ISR data. Friedrich et al. (Austria) have combined EISCAT-Svalbard data with polar-latitude rocket data to investigate the "true quiet" electron density profile in the D, E and F regions; this is the minimum envelope of all data.

Solomon (USA) investigated how well theoretical models represent the E-region ionosphere when fed with accurate solar irradiances. He found that the EUVAC solar irradiance model is in better agreement with SNOE, TIMED/SEE and SORCE measurements than the Hinteregger EUV model. But even with the EUVAC model the theoretical model still underestimates IRI and ionosonde E peak densities particularly at solar minimum.

IRI predictions agree overall quite well with data from the Irkutsk ISR (1997 - 2003) (Potekhin et al., Russia) and the Irkutsk ionosonde (Ratovsky et al., Russia), some overestimation is found during summer and underestimation during winter. Lei et al. (PR China) compared the bottomside parameters B0, B1 deduced from Millstone Hill and EISCAT measurements with IRI and pointed out needed improvements.

IRI Publications, Workshops, and New Members

Papers from the 2002 IRI session during the World Space Congress in Houston, USA have been published in Advances in Space Research (ASR), Volume 33, Number 6, 2004. The ASR issue with papers from the 2003 IRI Workshop in Grahamstown, South Africa has just come out as Volume 34, Number 9, 2004. A special session was held during the 2003 German URSI meeting in honor of Karl Rawer's 90th Birthday. The papers from this session are now published as the 2nd Volume of the Advances in Radioscience http://www.copernicus.org/URSI/ars/published_articles.htm (formerly "Kleinheubacher Berichte").

The 2005 IRI Workshop is now planned for the week of June 27 to July 1 at the Ebro Observatory in Roquetes, Spain (http://www.obsebre.es/w3/wsiri/index.php) and its theme will be "New Satellite and Ground Data for IRI, and Comparisons with Regional Models". For the 2006 COSPAR General Assembly in Beijing, PR China the IRI team has proposed a session on the "Solar Activity Variations of Ionospheric Parameters".

Three new members were welcome into the IRI working Group: Dr. O. Obrou from the University of Cocody in Abidjan, Ivory Coast; Dr. P.K. Bhuyan of the University of Dibrugarh in Dibrugarh, India; Dr. M.L. Zhang, Center for Space Science and Applied Research, Chinese Academy of Sciences, Beijing, PR China.

BIANISOTROPICS 2004

Meditation on Metamaterials in a Monastery

Ghent, Belgium, 22-24 September 2004

The 10th international conference on complex media and metamaterials, "Bianisotropics 2004," took place from September 22 to 24, 2004, in the beautiful medieval city of Ghent, in Flanders, Belgium. The meeting was held in the lofty halls of the Dominican monastery Het Pand. The monastery is presently owned by Ghent University and serves as a conference center, a faculty club, and a restaurant, and it also hosts part of the central university administration.

Bianisotropics meetings have been forums for discussion of interactions of electromagnetic waves with chiral and other materials with complicated response, including metamaterials. The first one was held in Espoo, Finland (February, 1993), followed by meetings in Gomel, Belarus (October, 1993); Perigueux, France (1994); State College, Pennsylvania, USA (1995); a river cruise between St. Petersburg and Moscow, Russia (1996); Glasgow, UK (1997); Braunschweig, Germany (1998); Lisbon, Portugal (2000); and Marrakesh, Morocco (2002).

This year's meeting was organized by the Electromagnetics Group in the Department of Information Technology of Ghent University. The co-Chairs were Frank Olyslager and Ann Franchois (Figure 1). The Université Catholique de Louvain also assisted in the organization. Advisory and scientific support came from the International Bianisotropics Conference Committee, and the always-needed financial assistance came from Fund for Scientific Research – Flanders (Belgium) and the Fonds National de Recherche Scientific. These are the Flemisch and Wallonien branches of the Belgian National Science Foundation. Three commercial sponsors also generously sponsored the meeting: Ansoft, Emerson and Cuming Microwave Products, and Agilent Technologies. Technical co-sponsorship, also very valuable, was provided by the IEEE Antennas and Propagation Society, URSI Commission B, and the new European Network of Excellence, METAMORPHOSE.

The scientific program was chaired by Ari Sihvola, from the Electromagnetics Laboratory at the Helsinki

Figure 1. The conference Chairwoman, Prof. Franchois, explaining how to characterize steel-fiber-reinforced concrete.

University of Technology, Finland. There were 50 presentations in the scientific program of the three days of the conference. This selection was made from the set of about 75 submitted papers. The program comprised 11 keynote lectures, in addition to ordinary contributed presentations. The review lectures were:

- Prof. John Arnold, Department of Electronics and Electrical Engineering, University of Glasgow, UK, "Homogenisation Theory for Nonlinear Optical Metamaterials"
- Dr. Giorgio Bertotti, Istituto Elettrotecnico Nazionale "Galileo Ferraris," Torino, Italy, "Micromagnetics and Non-Linear Magnetization Dynamics in Ferromagnetic Media"
- Prof. Nader Engheta, the Moore School of Electrical Engineering, University of Pennsylvania, USA, "Metamaterials and Plasmonic Media: Theory and Potential Applications"
- Prof. Christophe Craeye, Université Catholique de Louvain, Belgium, "Periodic Metamaterials Combining Ferromagnetic, Dielectric and/or Metallic Structures for Planar Circuits Applications"
- Prof. Gerhard Kristensson, Department of Electroscience, Lund Institute of Technology, Sweden, "Homogenization Techniques for Anisotropic Materials"
- Prof. Ismo Lindell, Electromagnetics Laboratory, Helsinki University of Technology, Finland, "Differential Forms and Bianisotropic Media" (Figure 2)
- Prof. Raj Mittra, Electromagnetic Communication Laboratory, the Pennsylvania State University, USA, "Techniques for Enhancement of Antenna Characteristics using EBG Materials as Superstrates"
- Prof. Sergei Tretyakov, Radio Laboratory, Helsinki University of Technology, Finland, "Exotic Materials and Thin Sheets for Near-Field Imaging and Detection"
- Prof. Vasundara V. Varadan, Research Center for the Engineering of Electronic & Acoustic Materials & Devices, the Pennsylvania State University, USA, "Random and Ordered Chirality and Negative Refractive Index – Experimental and Theoretical Studies"
- Prof. Keith Whites, Department of Electrical and Computer Engineering, South Dakota School of Mines and Technology, USA, "Survey of Developments in the Construction of Electromagnetic Media and Textured Surfaces"
- Prof. Richard W. Ziolkowski, Department of Electrical and Computer Engineering, University of Arizona, USA, "Double Negative Metamaterial Designs and Applications"

The field of electromagnetics of complex materials is in a state of great activity. New designs and applications are constantly being suggested. The activity seems to concentrate very much under the umbrella of so-called metamaterials, whatever this name may mean to different people. The research covers negative-phase-velocity media, electromagnetic crystals, bianisotropic materials, nonlinear effects, handed (chiral) media, magnetically active materials, and even zero-index and infinite-index media! It is clear that many proposed structures remain speculations, but it is important to let new ideas arise and be nurtured. More down-to-earth analyses will keep the proposals closer to reality.

The variety of the designs and studies is also a reflection of the multidisciplinary nature of the field of complex-media electromagnetics. In the community, we need and we have the contributions of not only electromagnetics people, but also physicists, chemists, mathematicians, and materials science and mechanical and processing engineering experts.

All this was reflected in the program of Bianisotropics 2004. The session names give a picture of the scope of the meeting:

- Electromagnetic Theory
- Numerical Modeling on Complex Materials
- Random, Complex, and Speculative Materials
- Metamaterials, Nanomaterials
- Applications of Complex Materials
- Photonic/Electromagnetic Bandgap Materials
- Modeling of Negative-Refractive-Index Media

Figure 2. Prof. Lindell introducing the audience to the magic formulas of differential geometry.

Figure 3. Prof. Mittra proves that metamaterials can be very useful in antenna design.

Figure 4. A bird's eye view of the audience in the garden of the monastery, enduring the Belgian rain without umbrellas....

In addition, Prof. Raj Mittra (Figure 3), from the Pennsylvania State University, organized a special session that focused on the applications of metamaterials to antenna problems.

There was also a panel discussion session, where the present status and future of the field of complex materials and metamaterials was discussed. There, questions were touched upon that dealt with the terminology of the various materials and media; the balance between theory and applications, on one hand, and the speculations versus immediately realizable designs, on the other. Also, there was a desire for so-called "killer applications" for metamaterials, which would give special push to the field. But detailed technical issues were also raised, like the bandwidth of the active region that can be achieved with the use of metamaterials.

In total, the conference hosted 82 scientists (Figure 4) from 21 different countries and four continents. The meeting clearly carried a very international character. Characteristic to the bianisotropics meetings is that the organizers make special efforts to provide financial assistance to participants from countries with difficulties in funding international travel. So it also was this time: 13 scientists from Russia, Belarus, Ukraine, Turkey, and Brazil were able to come to the meeting with the support from the conference budget.

Frank Olyslager and Ann Franchois
frank.olyslager@intec.ugent.be,
ann.franchois@intec.ugent.be

Ari Sihvola
ari.sihvola@hut.fi

VLF WORKSHOP 2004

ELF/VLF Radio Phenomena: Generation, Propagation and Consequences in Observations, Theory & Modelling

Sodankylä, Finland, 27 September - 1 October 2004

The VLF Workshop 2004 which took place last month at the Sodankylä Geophysical Observatory was sponsored by URSI Commission H and supported by the VERSIM IAGA/URSI joint working group. The workshop attracted 27 participants from 9 countries resulting in 36 presentations. There was a particularly strong series of presentations on chorus emissions observed by satellites (for example, Cluster) and subionospheric propagation studies undertaking remote sensing of the lower ionosphere (plus mineral prospecting underground). A full listing of abstracts can be found at: http://www.sgo.fi/Events/Workshops/vlf-2004/abstracts.php

Because of the relaxed nature of the timetable all the oral presentations were of a sensible length (~20-25 min), allowing good discussion time after most of the talks. In addition, there were also good-length coffee and lunch breaks in which participants could follow up with more

detailed discussions, or plan future scientific collaborations. The nature of the programme was one of the best features of the VLF Workshop, as it allowed excellent interactions between the participants.

The facilities and organisation was of a very high standard, and at the end of the 2004 Workshop the participants gave a vote of thanks to the Local Organising Committee for running the workshop so smoothly. Their efforts ranged from keeping the timetable realistic and picking up people at the airport to arranging for some of Sodankylä's souvenir shops and restaurants to open late for workshop participants.

There were a small number of invited talks at the 2004 VLF Workshop, lead off by Tauno Turunen on the use of VLF techniques in scientific studies. Prof. Tauno Turunen gave this presentation on behalf of Prof. Michael Rycroft, who could not attend the workshop due to an operation. Prof. David Nunn ("On the numerical modelling of VLF chorus") and Dr. Craig Rodger ("Testing the importance of precipitation loss mechanisms in the inner radiation belt") also gave invited presentations during the Workshop, generating some broad discussions afterwards.

The social program included a welcoming "Ice Breaker" function supported by the Sodankylä regional Government at the Sodankylä Municipality Hall. The primary social evening took place on 29 September 2004, when the conference participants travelled to the "Aurora House". There participants had the official dinner and the presentation which explain the wonders of the Aurora.

Some idea of the success of this session can be found on the Photos page of the 2004 Workshop: http://www.sgo.fi/Events/Workshops/vlf-2004/photos.php

At the end of the 2004 Workshop it was felt that the meeting had been a large success, providing a fresh venue for the VLF community to gather and exchange information. After discussions amongst the participants, it was decided to run another workshop in 2006 (as no URSI or IAGA meeting will take place that year), with the possibility of the VLF Workshop becoming a "standard" feature of our scientific community.

Dr. Craig Rodger noted that he would like to invite the participants to New Zealand for a future meeting, once it has become well established.

The Local Organisers of the 2004 Workshop announced that they would be happy to run another meeting at the Sodankylä Geophysical Observatory in 2006, which was widely supported by all present!

International Conference on Radar Systems

Toulouse, France, 18 - 22 October 2004

The International Conference on Radar Systems is organised in the frame of the international relations set up between the Institution of Electrical Engineers (IEE), the Institute of Electrical and Electronics Engineers (IEEE), the Chinese Institute of Electronics (CIE), the Verband Deutscher Elektroniker (VDE), the Institut Français de Navigation (IFN), the Institution of Engineers Australia (IE Aust) and SEE*.

The 2004 International Conference on Radar Systems organised by SEE was held in Toulouse (18-22 October, 2004). It received the sponsorship of URSI (Commission F).

Radar 2004 was also a historical event in Europe : the century of the radar invention by Christian Hülsmeyer (Telemobiloskop Patentscrift n° 165546, 30th of April 1904). It was commemorated in a special historical session.

Sessions covered all aspects of radar,
- Radar concepts (Low frequency, SAR, UWB, multi-static …),
- Technologies (Microwave sub-assembly, active modules, …),
- Techniques (Signal processing, antenna, detection,...)
- Applications.

The main areas of applications covered were,
- Forecasting of ocean thunderstorms
- Precipitation radar
- Electromagnetic scattering by oil slicks and oil spill detection on the sea surface
- Foliage penetration
- Detection of atmospheric and gravity waves using HF Doppler radar
- Radiometric calibration of radar (Exploration of the Earth)
- Imaging
- Earth cartography
- Modelling of sea clutter returns and sea spikes characterisation
- Propagation modelling
- VHF radar wave propagation inside forest
- Polarisation sensitivity analysis for developing soil moisture and surface roughness inversion model
- Horizon wind field and wake turbulence forecasting on airport.

The most discussed topics were :
- Synthetic Aperture Radar (SAR),
- Space-Time Adaptive Processing (STAP),
- Low-frequency Radar,
- Active antenna.

A few papers dealt with interference suppression using nulling and coherent estimation of the unwanted signal; polarisation filtering is also proposed for a dual-polarisation high-frequency surface wave radar. No doubt that the use of non-co-operative multi-static transmitters in low frequency bands and/or non directive systems will increase the number of research aiming at a better use of spectrum by the sharing of bands.

Active antenna technologies have also reached some maturity; their advantages in terms of light weight and lower power consumption should enlarge their applications : URSI members should be attentive to this development.

This edition of the International Conference on Radar Systems illustrates the growing diversity of applications which benefit from the slow but steady progress of technology, for example, the application of UWB radar in medicine for remote measuring of patients heart activity and respiration.

The 350 radar specialists from 29 countries participated in a Gala dinner given in the magnificent rooms of the Hôtel Dieu Saint Jacques along the Garonne river; it was preceded by a piano concert in the chapel by one of the Conference participants, Richard Klemm (FGAN, Germany).

During the dinner five young scientists were rewarded for the quality of their papers and one of them , Fabian Lapierre (Université de Liège, Institut de Montefiore), was distinguished as the best contributor.

All members of the Conference Board have to be thanked, specially Steering Committee (Chair, Michel Bon), Organising Committee (Chair, Florent Chritophe), Technical Programme Committee (Chair, Marc Lesturgie) and IEEE Radar Systems Panel and International Liaison Officer (François Le Chevalier).

Jean J. Isnard
jisnard-isti@club-internet.fr
*** SEE :** www.see.asso.fr

CONFERENCE ANNOUNCEMENTS

URSI 2005 COMMISSION F SYMPOSIUM
Symposium on Microwave Remote Sensing of the Earth, Oceans, Ice and Atmosphere

Barza d'Ispra, Italy, 20 - 21 April 2005

The URSI Commission F Symposium on Microwave Remote Sensing of the Earth, Oceans, Ice, and Atmosphere will build on the success of previous Commission F symposia dating back to the first one held in 1974 in Berne, Switzerland. The 2005 Symposium provides a premier forum for the scientific community to discuss the latest results and to identify developing trends. The conference programme will include a number of keynote presentations by leading researchers, intended to review the state of the art in the field of microwave remote sensing. No parallel sessions will be organised.

The venue will be the Conference Centre Casa Don Guanella in Barza d'Ispra, located close to the Lake Maggiore. The venue belongs to the Province Varese in the famous Lombardia Region in Northern Italy.

The Symposium is organised by the Sensors, Radar Technologies, and Cybersecurity Unit, Institute for the Protection and Security of the Citizen, EC DG Joint Research Centre.

The Symposium Chairman is Prof. Martti Hallikainen (URSI Commission F Chair; Finland), Honorary Chairman is Dr. Alois Sieber (JRC), and Programme and Organisation Committee Chairman is Dr. Joaquim Fortuny (JRC).

Topics

The Symposium will welcome contributions from all those working in the of microwave remote sensing using space-borne, airborne, and ground-based platforms.

The Symposium will cover the following topics:

* Passive and active microwave remote sensing
* Ground-based, aircraft, and satellite microwave instruments
* SAR interferometry
* Monitoring of snow and ice
* Radar polarimetry
* Ocean Surface and Winds
* Remote sensing of vegetation and soil moisture
* SAR modeling of ocean backscatter

Furthermore, papers presenting advances in the field of monitoring and forecasting techniques to enhance the preparedness and response against the landslide and avalanche risks will be especially welcome.

Full details about the registration procedure and the instructions to prepare the full papers will be published on the Symposium's website: http://ursi-f-2005.jrc.it

Deadlines

* Deadline for abstract submission: 25 February 2005
* Notification of acceptance: 25 March 2005
* Full paper submission: 20 April 2005

Contact

EC DG Joint Research Centre
Via E. Fermi no. 1, TP723
I-21020 Ispra (VA), Italy

Abstract Submission and Technical Information
Dr. Joaquim Fortuny
Joaquim.Fortuny@jrc.it

Tel: +39 0332 785104
Fax: +39 0332 785469

Registration
Ms. Marta Garotta
Marta.Garotta@cec.eu.int

Tel: +39 0332 785546
Fax: +39 0332 785469

International Symposium on Antennas and Propagation ISAP 2005

Seoul, Korea, 3 - 5 August 2005

The 2005 International Symposium on Antennas and Propagation (ISAP2005) will be held at the Seoul KyoYuk MunHwa HoeKwan, Korea, during August 3-5, 2005. This symposium, the tenth ISAP, is sponsored and organized by the Korea Electromagnetic Engineering Society (KEES). This symposium is cosponsored by the Communications Society of the Institute of Electronics, Information and Communication Engineers (IEICE). This symposium is held under the technical co-sponsorship of the Antennas and Propagation Society of the Institute of Electrical and Electronics Engineers (IEEE/AP-S) and in cooperation with the Chinese Institute of Electronics (CIE), the International Union of Radio Science (URSI), and the IEE Antennas and Propagation Professional Network.

The Organizing Committee Chair is Hyo Joon Eom (KAIST).

Topics

A. Antennas and Related Areas
B. Propagation and Related Areas
C. Electromagnetic Wave Theory
D. Systems and Related Areas

Deadlines

Papers Submission:	February 28, 2005
Notification of Acceptance:	April 28, 2005
Early Registration:	July 1, 2005

Contact

GENICOM Convention Service Co., Ltd.
5F, Daehan Bldg., #1018,
Dunsan-dong, Seo-gu,
Daejeon 302-120, Korea
Tel: +82-42-472-7458
Fax: +82-42-472-7459
E-mail: isap05@ee.kaist.ac.kr
http://www.isap05.org

URSI CONFERENCE CALENDAR

February 2005

EMC Zurich'05 - International Zurich Symposium & Technical Exhibition on Electromagnetic Compatibility
Zurich, Switzerland, 14-18 February 2005
Contact : EMC Zurich 2005, ETH Zentrum, Gloriastrasse 35, CH-8092 Zurich, Zwitzerland, Tel. +41 1-632 2951, Fax +41 1-632 1198, E-mail : info@emczurich.ethz.ch, http://www.emc-zurich.ch

March 2005

IWSE 2005 - International Workshop on Seismo Electromagnetics 2005
Tokyo, Japan, 15-17 March 2005
Contact : Prof. M. Hayakawa, Dept. of Electronic Engineering, The University of Electro-Communications, 1-5-1 Chofugaoka, Chofu City, 182-8585 TOKYO, JAPAN, Phone : +81 424-43 5159, Fax : +81 424-43 5783, E-mail iwse2005@whistler.ee.uec.ac.jp,http://www.iwse.ee.uec.ac.jp

TELECOM'2005 & JFMMA
Rabat, Morocco, 23-25 March 2005
Contact : Prof. Ahmed MAMOUNI, IEMN, Cité Scientifique, Av. Poincaré, BP. 69, 59652 Villeneuve d'Ascq, France, E-mail : Ahmed.Mamouni@iemn.univ-lille1.fr

ISSS-7 - 7th International School/Symposium for Space Simulations
Kyoto, JAPAN, 26 - 31 March 2005
cf. announcement in RSB September 2004, p. 117
Contact : ISSS-7 Secretariat, Research Institute for Sustainable Humanosphere, Kyoto University, Gokasho, Uji Kyoto 611-0011, Japan, Tel. +81-774-38-3811, Fax : +81-774-31-8463, E-mail: isss7@rish.kyoto-u.ac.jp, http://www.rish.kyoto-u.ac.jp/isss7/

May 2005

IES 2005 - 11th International Ionospheric Effects Symposium
Alexandria, Virginia, USA, 3-5 May 2005
Contact : JMG Associates Ltd., IES2005 Symposium Managers, 8310 Lilac Lane, Alexandria, VA 22308, USA, Fax: +1-703-360-3954, jm_good@cox.net, Web site : http://www.ies2005.com

4th European Workshop on Conformal Antennas
Stockholm, Sweden, 23-24 May 2005
Contact : Dr. Patrik Persson, Royal Institute of Technology, Alfvén Laboratory, Division of Electromagnetic Theory, SE-100 44 Stockholm, Sweden, E-mail : patrik.persson@alfvenlab.kth.se , http://www.ewca-home.org/

June 2005

ANTEM 2005
Saint Malo, France, 15-17 June 2005
Contact : Antem 2005 - IETR Université de Rennes 1, campus Beaulieu, Bât. 11D 35042 Rennes Cedex, France, Tel. +33 2 23 23 62 17 and +33 2 23 23 69 56, Fax +33 2 23 23 69 69, http://antem2005.ietr.org/home/index.htm

EMC2005 - VIth International Symposium on Electromagnetic Compatibility and Electromagnetic Ecology
St. Petersburg, Russia, 21-24 June 2005
Contact : Dr. Pavel Asovich, Prof. Popov Str. 5, St. Petersburg 197376, Russia, Fax +7 812 234-4840, E-mail : discone@vilan.spb.ru , http://www.eltech.ru/emc2005

IRI Workshop 2005 - New Satellite and ground data for IRI, and comparison with regional models
Roquetes, Spain, 27 June - 1 July 2005
Contact : IRI 2005 WORKSHOP "New satellite and ground data for IRI, and comparison with regional models", Observatori de l'Ebre, Roquetes, Spain, secretaria@obsebre.esn , http://www.obsebre.es/w3/wsiri/

July 2005

CEFBIOS 2005 - Coherence and Electromagnetic Fields in Biological Systems
Prague, Czech Republic, 1-4 July 2005
cf. announcement in RSB September 2004, p. 118
Contact : Dr. Jiri Pokorny, Inst. of Radioengineering and Electronics, Academy of Sciences of the Czech Republic, Chaberska 57, CZ-182 51 PRAGUE 8, Czech Republic, phone : +420 266 773 432, fax +420 284 680 222, pokorny@ure.cas.cz , http://www.ure.cas.cz/events/cefbios2005/

August 2005

ISAP'05 - International Symposium on Antennas and Propagation
Seoul, Korea, 3-5 August 2005
cf. announcement in RSB December 2004, p. 217
Contact : Prof. H.J. Eom, Department of Electrical Engineering and Computer Science, Korea Advanced Institute of Science and Technology (KAIST), 373-1, Guseong-dong, Yuseong-gu Daejeon, 305-701 Korea, Tel. +82 42-869 3436, Fax : +82 42-869 8036, E-mail : hjeom@ee.kaist.ac.kr, http://www/isap05.org

MAPE 2005 - International Symposium on Microwave, Antenna, Propagation, and EMC Technologies for Wireless Communications
Beijing, China, 8-12 August 2005
cf. announcement in RSB September 2004, p. 118
Contact : Mr. Mengqi Zhou, Secretary of IEEE Beijing Section, P.O. Box 165, Beijing 100036, China, E-mail : mqzhou@public.bta.net.cn , http://www.cie-china.org/mape2005/temp/main.html

ISMOT 2005 - 10th International Symposium on Microwave and Optical Technology
Fukuoka, Japan, 22-25 August 2005
Contact : Prof. Kiyotoshi YASUMOTO, Dpt. Comp. Sci. & Comm. Eng., Kyushu University, 6-10-1 Hakozaki, Higashi-ku, Fukuoka 812-8581, Japan, Phone: +81-92-642-4045, Fax: +81-92-632-5204, E-mail: yasumoto@csce.kyushu-u.ac.jp , http://ismot2005.fit.ac.jp

October 2005

XXVIIIth URSI General Assembly
New Delhi, India, 23-29 October 2005
Contact : URSI Secretariat, c/o INTEC, Sint-Pietersnieuwstraat 41, B-9000 Ghent, Belgium, Tel. : +32 9 264 3320, Fax : +32 9 264 4288, E-mail : ursi@intec.rug.ac.be, http://www.ursiga2005.org

News from the URSI Community

NEWS FROM THE MEMBER COMMITTEES

FINLAND

XXIX URSI National Convention on Radio Science

Espoo, Finland, 1-2 November 2004

The 29th URSI National Convention on Radio Science was held at Dipoli Congress Centre in Espoo, Finland, on 1-2 November 2004. VTT Information Technology and Finnish National Committee of URSI organised the convention with Nokia Corporation and Finland IEEE Section as sponsors. Professor Markku Sipilä (VTT) was Chair of the Organising Committee and Mr. Manu Liedes was its Secretary. Convention attendance was 75.

The annual convention provides a forum for discussion of advances in the broad field of radio science and radio communications. Traditionally, each convention highlights the topics of 3 to 4 URSI Scientific Commissions, thus allowing the fields of all 10 Commissions to be covered in the three-year URSI cycle of General Symposia. The programme includes both contributed and invited presentations.

The following topics were highlighted:

- RF microelectromechanical systems (RF-MEMS)
- 4th generation mobile communications (4G)
- Defence and security

Recipient of the Young Scientist Award Pekka Pursula (middle) with Chair of Organising Committee, Professor Markku Sipilä (left) and Chair of the Finnish National Committee of URSI, Professor Martti Hallikainen (right).

Contributions from other areas of radio science and radio communications technologies were also welcome. The Technical Committee reviewed all submitted papers and the final published paper was a 4-page summary. A total of 35 presentations were given in the following sessions:

- Future communication technologies
- Remote sensing (two sessions)
- Antennas (two sessions)
- Electromagnetic theory and materials
- Circuits and components
- Defence and security
- Wireless communications
- Sensors and applications

The programme included four invited presentations:

- Hannu Kattelus (VTT): Amorphous metals for RF-MEMS
- Hannu Kauppinen (Nokia Corporation): Spectrum sharing and flexible spectrum use
- Jukka Ruoskanen (PvTT): Radar signal processing
- Petri Jukkala (Ylinen Electronics Ltd.): Planck - mission and technology

The attendees received two copies of the Proceedings: a 155-page hardcopy and a CD-ROM. A pdf version of the Proceedings is available at http://www.vtt.fi/inf/pdf/symposiums/2004/S235.pdf. The Convention website is http://ursi2004.vtt.fi.

The convention is also intended to provide a forum for Young Scientists. Based on a tradition since 1997, the Awards Committee evaluated all presentations given by Young Scientists (under 35 years of age), based on the quality of both the written paper and the oral presentation. The winner of the Young Scientist Award was Pekka Pursula (VTT); the title of his presentation was “Antenna radiation characterization by backscattering modulation”.

Prof. M. Hallikainen

International Geophysical Calendar 2005

	S	M	T	W	T	F	S
JANUARY							1
	2	3 N	4	5	6	7	8
	9	10	11 *	12 *	13	14	15
	16	17	(18)	**19**	(20)	21	22
	23	24	25 F	26	27	28	29
	30	31	1	2	3	4	5
FEBRUARY	6	7	8 N *	9 *	10	11	12
	13	14	15	**16**	17	18	19
	20	21	22	23	24 F	25	26
	27	28	1	2	3	4	5
MARCH	6	7 +	8 +	9 * +	10 N * +	11 +	12 +
	13	14	15	**16**	17	18	19
	20	21	22	23	24	25 F	26
	27	28	29	30	31	1	2
APRIL	3	4	5	6 *	7 *	8 N	9
	10	11	(12)	**13**	(14)	15	16
	17	18	19	20	21	22	23
	24 F	25	26	27	28	29	30
MAY	1	2	3	4	5	6	7
	8 N	9	10 *	**11** *	12 *	13	14
	15	16	17	18	19	20	21
	22	23 F	24	25	26	27	28
	29	30	31	1	2	3	4
JUNE	5	6 N	7 *	**8** *	9	10	11
	12	13	14 +	15 +	16 +	17 +	18 +
	19	20	21	22 F	23	24	25
	26	27	28	29	30		
	S	M	T	W	T	F	S

	S	M	T	W	T	F	S
						1	2
JULY	3	4	5	6 N *	7 *	8	9
	10	11	(12)	**13**	(14)	15	16
	17	18	19	20	21 F	22	23
	24	25	26	27	28	29	30
AUGUST	31	1	2	3	4	5 N	6
	7	8	9 *	10 * +	11 +	12 +	13 +
	14	15	(16)	**17**	(18)	19 F	20
	21	22	23	24	25	26	27
SEPTEMBER	28	29	30	31	1 +	2 +	3 N +
	4 +	5 +	6 * +	7 * +	8 +	9 +	10 +
	11 +	12 +	(13) +	**14** +	(15) +	16 +	17 +
	18 F +	19 +	20 +	21 +	22 +	23 +	24 +
OCTOBER	25 +	26 +	27 +	28 +	29 +	30 F +	1
	2	3 N	4	5	6	7	8
	9	10	11 *	12 *	13	14	15
	16	17 F	(18)	**19**	(20)	21	22
	23	24	25	26	27	28	29
NOVEMBER	30	31	1	2 N	3	4	5
	6	7	8 * +	9 * +	10 +	11 +	12 +
	13	14	(15)	**16** F	(17) +	18 +	19 +
	20 +	21	22	23	24	25	26
DECEMBER	27	28	29	30 *	1 N *	2	3
	4	5	6	7	8	9	10
	11	12	13	14	15 F	16	17
	18	19	(20)	**21**	(22)	23	24
	25	26	27	28 *	29 *	30	31 N
2006	S	M	T	W	T	F	S
JANUARY	1	2	3	4	5	6	7
	8	9	10	11	12	13	14 F
	15	16	(17)	**18**	(19)	20	21
	22	23	24	25 *	26 *	27	28
	29 N	30	31				
	S	M	T	W	T	F	S

(18) Regular World Day (RWD)

19 Priority Regular World Day (PRWD)

16 Quarterly World Day (QWD)
also a PRWD and RWD

5 Regular Geophysical Day (RGD)

7 8 World Geophysical Interval (WGI)

\+ Incoherent Scatter Coordinated Observation Day

N NEW MOON F FULL MOON

8 Day of Solar Eclipse: Apr 8 and Oct 3

6 7 Airglow and Aurora Period

11* Dark Moon Geophysical Day (DMGD)

This Calendar continues the series begun for the IGY years 1957-58, and is issued annually to recommend dates for solar and geophysical observations, which cannot be carried out continuously. Thus, the amount of observational data in existence tends to be larger on Calendar days. The recommendations on data reduction and especially the flow of data to World Data Centers (WDCs) in many instances emphasize Calendar days. The Calendar is prepared by the *International Space Environment Service (ISES*) with the advice of spokesmen for the various scientific disciplines.

The **Solar Eclipses** are:

- **8 April 2005 (hybrid – total central section surrounded by annular sections) eclipse** visible within a narrow corridor that traverses the southern Pacific Ocean (30 km wide), begins as annular east of southern tip of New Zealand (5770 km SW of Tahiti), turns total 2200 km S of Tahiti (duration 45s), passes 1500 km W of Galapagos, turning annular 800 km N of Galapagos and 800 km W of Panama, ending annular in S tip of Costa Rica, Panama, Colombia, Venezuela. Partial eclipse in New Zealand, much of S. Pacific, U.S. north to line from San Diego, through mid-Kansas and mid Pennsylvania (40% in Florida), Caribbean, Central America, S. America to mid-Chile and Argentina, and bit of Antarctica.
- **3 October 2005 (annular) eclipse** with annularity 0.958 extending from N. Portugal, through Spain (duration 4m 10s), NE Africa (Algeria, Tunesia, Libya, Sudan (duration 4m 31s), Kenya, southern tip of Somalia). Partial visible in Europe, Africa (except southern tip), Middle East, and SE Asia, including India.

Description by Dr. Jay Pasachoff, Williams College, Chair of IAU WG on Solar Eclipses, jmp@williams.edu, based on maps from Fred Espenak, NASA GSFC. See http://sunearth.gsfc.nasa.gov/eclipse/SEcat/SEdecade2001.html and http://www.williams.edu/Astronomy/IAU_eclipses. See also International Astronomical Union Program Group on Public Education at the Times of Eclipses: http://www.eclipses.info.

Meteor Showers (selected by R. Hawkes, Mount Allison Univ., Canada, rhawkes@mta.ca) include important visual showers and also unusual showers observable mainly by radio and radar techniques. The dates are given in Note 1 under the Calendar.

Definitions of Terms:

Time = Universal Time (**UT**);
Regular Geophysical Days (**RGD**) = each Wednesday;
Regular World Days (**RWD**) = Tuesday, Wednesday and Thursday near the middle of the month (see calendar);
Priority Regular World Days (**PRWD**) = the Wednesday **RWD**;
Quarterly World Days (**QWD**) = **PRWD** in the **WGI**;
World Geophysical Intervals (**WGI**) = 14 consecutive days each season (See calendar);
ALERTS = occurrence of unusual solar or geophysical conditions, broadcast once daily soon after 0400 UT;
STRATWARM = stratospheric warmings
Retrospective World Intervals (**RWI**) = MONSEE study intervals.

For more detailed explanations of the definitions, please see one of the following or contact H. Coffey (address below): ISES Synoptic Codes for Solar and Geophysical Data; URSI Information Bulletin; COSPAR Information Bulletin; IAGA News; IUGG Chronicle; WMO Bulletin; IAU Information Bulletin; and the Journal of Atmospheric and Terrestrial Physics (UK). WWW homepage **http://www.ises-spaceweather.org.**

Priority recommended programs for measurements not made continuously — (in addition to unusual ALERT periods):

Aurora and Airglow — Observation periods are New Moon periods, especially the
7 day intervals on the calendar;

Atmospheric Electricity — Observation periods are the RGD each Wednesday,
beginning on 5 January 2005 at 0000 UT, 12 January at 0600 UT,
19 January at 1200 UT, 26 January at 1800 UT, etc. Minimum
program is PRWDs.

Geomagnetic Phenomena — At minimum, need observation periods and data reduction on RWDs and during MAGSTORM Alerts.

Ionospheric Phenomena — Quarter-hourly ionograms; more frequently on RWDs, particularly at high latitude sites; ionogram scaled parameters to WDCs; continuous observations for solar eclipse in the eclipse zone. See **Airglow and Aurora**.

Incoherent Scatter — Observations on Incoherent Scatter Coordinated Days; also intensive series on **WGIs** or **Airglow and Aurora** periods.

Special programs: Dr. Wes Swartz, 316 Rhodes Hall, School of Electrical and Computer Engineering, Cornell University, Ithaca, NY 14853 Tel. 607-255-7120, Fax 607-255-6236, e-mail wes@ece.cornell.edu, URSI Working Group G.5. See http://people.ece.cornell.edu/wes/URSI_ISWG/.

Ionospheric Drifts — During weeks with RWDs.

Traveling Ionosphere Disturbances — special periods, probably PRWD or RWDs.

Ionospheric Absorption — Half-hourly on RWDs; continuous on solar eclipse days for stations in eclipse zone and conjugate area. Daily measurements during Absorption Winter Anomaly at temperate latitude stations (Oct-Mar Northern Hemisphere; Apr-Sep Southern Hemisphere).

Backscatter and Forward Scatter — RWDs at least.

Mesospheric D region electron densities — RGD around noon.

ELF Noise Measurements of earth-ionosphere cavity resonances — WGIs.

All Programs — Appropriate intensive observations during unusual meteor activity.

Meteorology — Especially on RGDs. On WGIs and STRATWARM Alert Intervals, please monitor on Mondays and Fridays as well as Wednesdays.

GAW (Global Atmosphere Watch) — WMO program to integrate monitoring of atmospheric composition.

Early warning system of changes in atmospheric concentrations of greenhouse gases, ozone, and pollutants (acid rain and dust particles). WMO, 7 via avenue de la Paix, P.O. Box 2300, 1211 Geneva, Switzerland.

Solar Phenomena — Solar eclipse days, RWDs, and during PROTON/FLARE ALERTS.

CAWSES (Climate and Weather of the Sun-Earth System) — Program within the SCOSTEP (Scientific Committee on Solar-Terrestrial Physics): 2004-2008. Its focus is to mobilize the community to fully utilize past, present, and future data; and to produce improvements in space weather forecasting, the design of space- and Earth-based technological systems, and understanding the role of solar-terrestrial influences on Global Change. Contact is Su. Basu (sbasu@bu.edu), Chair of CAWSES Science Steering Group. Program "theme" areas are: Solar Influence on Climate – M. Lockwood and L. Gray (UK); Space Weather: Science and Applications – J. Kozyra (USA) and K. Shibata (Japan); Atmospheric Coupling Processes – F. Luebken (Germany) and J. Alexander (USA); Space Climatology – C. Frolich (Switzerland) and J. Sojka (USA); and Capacity Building and Education, M.A. Geller (USA). See http://www.bu.edu/cawses/.

Space Research, Interplanetary Phenomena, Cosmic Rays, Aeronomy — QWDs, RWD, and Airglow and Aurora periods.

The **International Space Environment Service (ISES)** is a permanent scientific service of the International Union of Radio Science (URSI), with the participation of the International Astronomical Union and the International Union Geodesy and Geophysics. ISES adheres to the Federation of Astronomical and Geophysical Data Analysis Services (FAGS) of the International Council for Science (ICSU). The ISES coordinates the international aspects of the world days program and rapid data interchange.

This Calendar for 2005 has been drawn up by H.E. Coffey, of the ISES Steering Committee, in association with spokesmen for the various scientific disciplines in SCOSTEP, IAGA and URSI. Similar Calendars have been issued annually beginning with the IGY, 1957-58, and have been published in various widely available scientific publications. PDF versions are available online (ftp://ftp.ngdc.noaa.gov/STP/SOLAR_DATA/IGC_CALENDAR).

Published for the International Council for Science and with financial assistance of UNESCO.

Additional copies are available upon request to ISES Chairman, Dr. David Boteler, Geological Survey of Canada National Geomagnetism Program, #7 Observatory Crescent, Ottawa, Ontario, Canada, K1A 0Y3 FAX (613) 824-9803, e-mail Boteler@geolab.NRCan.gc.ca, or ISES Secretary for World Days, Ms. H.E. Coffey, WDC-A for Solar-Terrestrial Physics, NOAA, E/GC2, 325 Broadway, Boulder, Colorado 80305, USA, FAX (303)497-6513, e-mail Helen.E.Coffey@noaa.gov.

NOTES on other dates and programs of interest:

1. Days with **significant meteor shower** activity are: Northern Hemisphere 4 Jan; 21-23 Apr; 4-5 May; 6-11, 27-29 Jun; 11-13 Aug; 21-22 Oct; 13-15, 21-23 Dec 2005. Southern Hemisphere 4-5 May; 6-11, 27-29 Jun; 27 Jul-2 Aug; 21-22 Oct; 13-15 Dec 2005. These can be studied for their own geophysical effects or may be "geophysical noise" to other experiments.
2. **GAW (Global Atmosphere Watch)** — early warning system for changes in greenhouse gases, ozone layer, and long range transport of pollutants. (See Explanations.)
3. **CAWSES (Climate and Weather of the Sun-Earth System) —** SCOSTEP Program 2004-2008. Theme areas: Solar Influence on Climate; Space Weather: Science and Applications; Atmospheric Coupling Processes; Space Climatology; and Capacity Building and Education. (See Explanations.)
4. **+ Incoherent Scatter Coordinated Observations Days** (see Explanations) starting at 1300 UT on the first day of the intervals indicated, and ending at 1600 UT on the last day of the intervals: 7-12 March **M-I Coupling** (or 28 Mar-2 Apr **Synoptic** or 18-23 Apr **GPS-Radar**) & **CPEA**; 14-18 Jun **LTCS—MST**; 10-13 Aug **Meteoric Ionization**; 1-30 Sep **LTCS—MST** for long period waves (**World Week**); 8-12 Nov **C/NOFS** wide F-region coverage; and 17-20 Nov **Meteoric Ionization**. See **http://people.ece.cornell.edu/wes/URSI_ISWG/2005WDschedule.htm**.
   where
   C/NOFS = Communications/Navigation Outage Forecasting System (O. delaBeaujardiere – Odile.delaBeaujardiere@hanscom.af.mil);
   CPEA = Coupling Processes in the Equatorial Atmosphere (S. Fukao — fukao@kurasc.kyoto-u.ac.jp); See http://www.kurasc.kyoto-u.ac.jp/~yamamoto/CPEA-panf2.pdf
   GPS-Radar = Global Plasma Structuring-Radar Experiment (J. Foster — jcf@haystack.mit.edu);
   LTCS = Lower Thermosphere Coupling Study (L. Goncharenko - lpg@haystack.mit.edu);
   Meteoric Ions = Global observations of ionization created by the Perseids and Leonids (I. Haggstrom — ingemar@eiscat.se)
   M-I Coupling = Magnetosphere-Ionosphere Coupling-Storm/Substorm Effects Mid & Low Latitude Iono. (C. Huang — cshuang@haystack.mit.edu);
   MST = Studies of the Mesosphere, Stratosphere, and Troposphere—Coordinated D- and E-region campaigns in high resolution MST mode (G. Lehmacher — glehmac@clemson.edu)
   Synoptic = Wide coverage of the F-region augmented with topside or E-region measurements (W. Swartz — wes@ece.cornell.edu)

URSI Publications

Modern Radio Science 1999

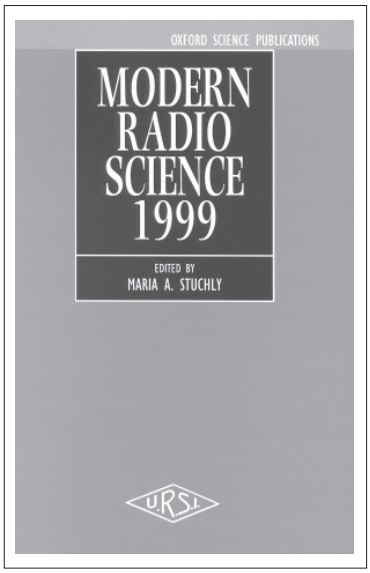

Editor: Maria Stuchly
ISBN 0-7803-6002-8
List Price : USD 49.95 Member Price : USD 45.00
IEEE Product No. PC5837

Published by Oxford University Press
in cooperation with URSI and IEEE Press
Order 24 hours a day, 7 days a week :
1-732-981 0060 (Worldwide)
1-800-678 4333 (USA & Canada)
Fax 1-732 981 9667
E-mail : customer-service@ieee.org

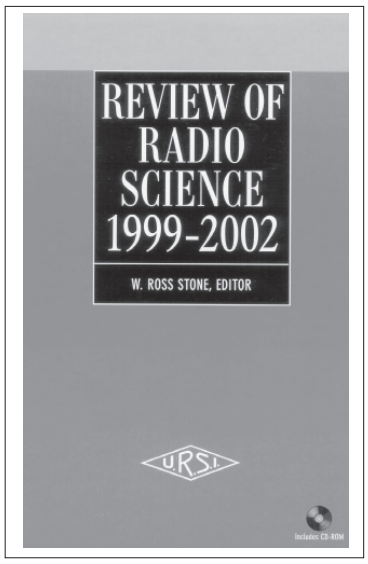

Review of Radio Science 1999-2002

Editor: W. Ross Stone
July 2002/Hardcover/977 pp
ISBN 0-471-26866-6
List Price : USD 125.00 Member Price : USD 106.25
IEEE Product No. #18493

Published by Wiley-Interscience
in cooperation with URSI and IEEE Press
Order can be sent to John Wiley & Sons, Inc.
from 8.30 a.m. to 5.30 p.m. :
1-732-469-4400 (Worldwide)
1-800-225-5945 (USA & Canada)
Fax 1-732 302-2370
E-mail : customer@wiley.com

Handbook on Radiopropagation Related to Satellite Communications in Tropical and Subtropical Countries

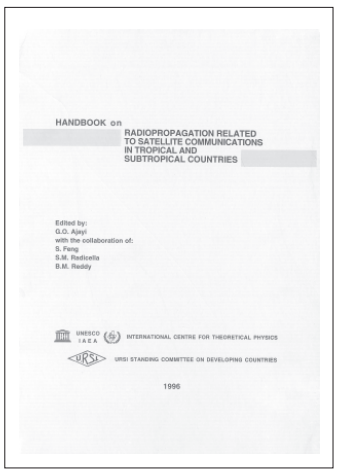

Editor: G.O. Ajayi
with the collaboration of :
S. Feng, S.M. Radicella, B.M. Reddy

Available from the URSI Secretariat
c/o Ghent University (INTEC)
Sint-Pietersnieuwstraat 41
B-9000 Gent, Belgium
tel. +32 9-264-33-20
fax +32 9-264-42-88
e-mail : ursi@intec.rug.ac.be

Wireless Networks

The journal of mobile communication, computation and information

Editor-in-Chief:
Imrich Chlamtac
Distinguished Chair in Telecommunications
Professor of Electrical Engineering
The University of Texas at Dallas
P.O. Box 830688, MS EC33
Richardson, TX 75083-0688
email: chlamtac@acm.org

Aims & Scope:
The wireless communication revolution is bringing fundamental changes to data networking, telecommunication, and is making integrated networks a reality. By freeing the user from the cord, personal communications networks, wireless LAN's, mobile radio networks and cellular systems, harbor the promise of fully distributed mobile computing and communications, any time, anywhere. Numerous wireless services are also maturing and are poised to change the way and scope of communication. WINET focuses on the networking and user aspects of this field. It provides a single common and global forum for archival value contributions documenting these fast growing areas of interest. The journal publishes refereed articles dealing with research, experience and management issues of wireless networks. Its aim is to allow the reader to benefit from experience, problems and solutions described. Regularly addressed issues include: Network architectures for Personal Communications Systems, wireless LAN's, radio , tactical and other wireless networks, design and analysis of protocols, network management and network performance, network services and service integration, nomadic computing, internetworking with cable and other wireless networks, standardization and regulatory issues, specific system descriptions, applications and user interface, and enabling technologies for wireless networks.

Wireless Networks is a joint publication of the ACM and Baltzer Science Publishers. Officially sponsored by URSI

For a complete overview on what has been and will be published in Telecommunication Systems please consult our homepage:

BALTZER SCIENCE PUBLISHERSHOMEPAGE
http://www.baltzer.nl/winet

Special Discount for URSI Radioscientists

Euro 62 / US$ 65
(including mailing and handling)

Wireless Networks ISSN 1022-0038
Contact: Mrs. Inge Heleu
Fax +32 9 264 42 88 E-mail ursi@intec.rug.ac.be
Non members/Institutions: contact Baltzer Science Publishers

BALTZER SCIENCE PUBLISHERS
P.O.Box 221, 1400 AE Bussum, The Netherlands
Tel: +31 35 6954250 Fax: +31 35 6954 258 E-mail: publish@baltzer.nl

The Journal of Atmospheric and Solar-Terrestrial Physics

SPECIAL OFFER TO URSI CORRESPONDENTS

AIMS AND SCOPE

The *Journal of Atmospheric and Terrestrial Physics* (JASTP) first appeared in print in 1951, at the very start of what is termed the "Space Age". The first papers grappled with such novel subjects as the Earth's ionosphere and photographic studies of the aurora. Since that early, seminal work, the Journal has continuously evolved and expanded its scope in concert with - and in support of - the exciting evolution of a dynamic, rapidly growing field of scientific endeavour: the Earth and Space Sciences. At its Golden Anniversary, the now re-named *Journal of Atmospheric and Solar-Terrestrial Physics* (JASTP) continues its development as the premier international journal dedicated to the physics of the Earth's atmospheric and space environment, especially the highly varied and highly variable physical phenomena that occur in this natural laboratory and the processes that couple them. The *Journal of Atmospheric and Solar-Terrestrial Physics* is an international journal concerned with the inter-disciplinary science of the Sun-Earth connection, defined very broadly. The journal referees and publishes original research papers, using rigorous standards of review, and focusing on the following: The results of experiments and their interpretations, and results of theoretical or modelling studies; Papers dealing with remote sensing carried out from the ground or space and with in situ studies made from rockets or from satellites orbiting the Earth; and, Plans for future research, often carried out within programs of international scope. The Journal also encourages papers involving: large scale collaborations, especially those with an international perspective; rapid communications; papers dealing with novel techniques or methodologies; commissioned review papers on topical subjects; and, special issues arising from chosen scientific symposia or workshops. The journal covers the physical processes operating in the troposphere, stratosphere, mesosphere, thermosphere, ionosphere, magnetosphere, the Sun, interplanetary medium, and heliosphere. Phenomena occurring in other "spheres", solar influences on climate, and supporting laboratory measurements are also considered. The journal deals especially with the coupling between the different regions. Solar flares, coronal mass ejections, and other energetic events on the Sun create interesting and important perturbations in the near-Earth space environment. The physics of this subject, now termed "space weather", is central to the Journal of Atmospheric and Solar-Terrestrial Physics and the journal welcomes papers that lead in the direction of a predictive understanding of the coupled system. Regarding the upper atmosphere, the subjects of aeronomy, geomagnetism and geoelectricity, auroral phenomena, radio wave propagation, and plasma instabilities, are examples within the broad field of solar-terrestrial physics which emphasise the energy exchange between the solar wind, the magnetospheric and ionosphericplasmas, and the neutral gas. In the lower atmosphere, topics covered range from mesoscale to global scale dynamics, to atmospheric electricity, lightning and its effects, and to anthropogenic changes. Helpful, novel schematic diagrams are encouraged. Short animations and ancillary data sets can also be accommodated. Prospective authors should review the *Instructions to Authors* at the back of each issue.

Complimentary Information about this journal:
http://www.elsevier.com/locate/JASTP?
http://earth.elsevier.com/geophysics

Audience:
Atmospheric physicists, geophysicists and astrophysicists.

Abstracted/indexed in:
CAM SCI Abstr
Curr Cont SCISEARCH Data
Curr Cont Sci Cit Ind
Curr Cont/Phys Chem & Sci
INSPEC Data
Meteoro & Geoastrophys Abstr
Res Alert

Editor-in-Chief:
T.L. Killeen, National Centre for Atmospheric Research, Boulder, Colorado, 80307 USA

Editorial Office:
P.O. Box 1930, 1000 BX Amsterdam, The Netherlands

Special Rate for URSI Radioscientists 2003:
Euro 149.00 (US$ 149.00)
Subscription Information
2002: Volume 65 (18 issues)
Subscription price: Euro 2659 (US$ 2975)
ISSN: 1364-6826

CONTENTS DIRECT:
The table of contents for this journal is now available pre-publication, via e-mail, as part of the free ContentsDirect service from Elsevier Science. Please send an e-mail message to cdhelp@elsevier.co.uk for further information about this service.

For ordering information please contact Elsevier Regional Sales Offices:

Asia & Australasia/ e-mail: asiainfo@elsevier.com
Europe, Middle East & Africa: e-mail: nlinfo-f@elsevier.com
Japan: Email: info@elsevier.co.jp
Latin America : e-mail: rsola.info@elsevier.com.br
United States & Canada : e-mail: usinfo-f@elsevier.com